DOCTOR OF PHILOSOPHY

Temporal variability of suspended particulate matter in a tidal estuary

Todd, David

Award date:
2014

Awarding institution:
Bangor University

Temporal variability of suspended particulate matter in a tidal estuary

David Todd

Thesis submitted in accordance with the requirements for the degree of

Doctor of Philosophy

Bangor University

School of Ocean Sciences

22nd September 2014

Acknowledgements

Many people made this Thesis possible. Principal amongst them my supervisors Prof. Colin Jago & Prof. Alex Souza. For their years of help, support, questions, dark humour and fear-inducing stories – with a few well-timed beers along the way – I will always be grateful. Secondly, the Captain and Crew of the RV Prince Madog, in addition to the Bangor University and NOC-L scientists and technicians for planning and conducting the cruises and collecting the data for this project. Prof. Alan Davies for his encouragement to apply for this Ph.D, and Dr. Katrien van Langdeghem for her unwavering support – teaching me during my Undergraduate Degree, supervising my Undergraduate Dissertation, and providing invaluable help and advice for my Ph.D Interview. "Room 203" from Bangor: Suzie Jackson, Iris Verhagen, Martin Roberts, Holly Pelling, Sophie Ward, Mike Tetley, Ben Lincoln, Ollie Way, Sophie Wilmes and Jon Wright and more recently at HR Wallingford Prof. Richard Whitehouse, who is an inspiration, Jon Taylor for his invaluable, extensive knowledge and Kerry Marten and Jenny Semmence for their great science and unwavering support.

Outside of the office: Beth, for always believing in me, even when I didn't. Mez, Smasher and Gemstar for opening their homes to me so I could finally finish. Ryan, who inspires me, and filled my Undergraduate years with so much humour, usually at his own expense. The TLC (CBear, RPorts, Smasher, McLovin, Crazy Joe, & Mange Tout), Joan and Tim provided both a job and endless amounts of recreational activity, and the dancers of BU Dance, Bangor Salsa & the Liverpool BBoys for giving me places to vent my frustration productively.

Stef, my oldest friend, and Harry, who has always been a destructive distraction. And Joy, for putting up with me, quietly, patiently, always believing that I would one day achieve success. Thank you for believing in me, your faith in me has finally been rewarded.

Finally, to Prof. Dave Bowers and Dr. Jim Bennell. Their teaching was crucial to me during my Undergraduate years. Without their encouragement and hours spent coaching me through the finer points of their subject areas I would never have made it through.

Thanks also to NERC for supplying the studentship for this project, PML for supplying the satellite data, and CEFAS for supplying the buoy data.

Abstract

Observations are presented of interactions between hydrodynamics and suspended particulate matter (SPM) on tidal, spring-neap and seasonal timescales from data collected in the Hilbre Channel at the mouth of the Dee Estuary (N.W. United Kingdom). Emphasis is placed upon the relationships between SPM and hydrodynamic controls, and the impact of specific biological components.

Moored ADCP (Acoustic Doppler Current Profiler), temperature, salinity and LISST (Laser In-Situ Scattering Transmissometer) data were collected during February-March and May-June 2009, supplemented by ship-deployed 25h vertical profiles of transmissometer, LISST, CTD, and fluorescence data taken at the beginning and end of each mooring deployment.

The Dee Estuary is a hypertidal estuary with a mean spring tidal range of 7.7 m and strong, near-rectilinear currents dominated by the M_2 and S_2 tidal components. During May-June, flood-dominant current velocities resulted in flood-dominant SPM flux (63% by volume, 39% by mass). During February-March, a strong horizontal SPM concentration gradient reduced the flood dominant SPM flux to 16 % by volume and 39 % by mass. It is proposed that low biological activity (measured using low fluorescence as a proxy) enabled erosion of fine sediments from mud flats and saltmarsh within the estuary, thus causing a large horizontal concentration gradient of the fine particle component of SPM. By contrast, during May-June, it is proposed that biological activity and atmospheric forcing increased the bed sediment erosion threshold, thus suppressing the fine particle concentration gradient. Furthermore, it is proposed that this biological activity mediated the observed increases in the strength, size, density and settling velocity of the flocs that made up SPM. In May-June, SPM composition changed due to a contribution of particles of uniform density but variable size, suspected to be either diatoms or aggregates ripped from the bed sediment of the intertidal areas.

During February-March, flocs ruptured under the high turbulence conditions of flood and ebb tides, and reformed at high and low slack waters. By contrast, during May-June under comparable turbulence conditions, flocs resuspended on flood and ebb tides without significant breakup due to their increased strength.

Seasonal changes to SPM properties potentially influence SPM flux via two different mechanisms:

1. Biological and atmospheric suppression of resuspension in May-June reduces the horizontal concentration gradient that is observed in February-March. Consequently, flood dominance of SPM flux is greater in May-June. This must increase net up-estuary transport in May-June.
2. SPM undergoes rupture and flocculation due to reduced floc strength in February-March. Flocculation and enhanced settling are greatest over an extended low water, so that flocs are deposited further up the estuary than their original starting point when they were resuspended by the flood. This should increase net up-estuary transport in February-March.

These observations suggest that seasonal variations of SPM properties are important for net transport within estuaries characterized by large intertidal flats.

Contents

List of Figures

List of Tables

Chapter 1

Introduction

1.1 Background

The coastal ocean provides us with food, water, salt, energy, and leisure facilities, making the understanding of our coastal oceans vital to enable us to exploit this vast resource in a sustainable manner. Today more than 634 million people live less than 60 miles from the coast. This is in excess of 10 % of the world's population occupying an area which forms just 2 % of the global land surface area (McGranaham, et al., 2007).

Within the coastal region, estuaries provide a connection between the continents and oceans; a zone of transition between the river and marine environments, and are subject to influences including fresh and saline water, waves, tides, and sediment (McLusky & Elliott, 2004). Estuaries transport nutrients, anthropogenic pollutants, and carbon (Ridgway & Shimmield, 2002), while most sediment derived from the land that is deposited in the oceans is transported via estuaries and as such, these areas are of particular importance to the health of the coastal ocean. Many temperate estuaries are still recovering from the last glacial event, where lower sea levels caused the over-deepening of river valleys, and many modern-day estuaries are these river valleys, inundated by rising sea levels, and are therefore sinks of sedimentary material as they infill in order to restore equilibrium (Lesourd, et al., 2001).

Within estuaries, suspended particulate matter (particles which are held in the water column due to water motion – known as SPM) is transported in various forms and involved in many processes, with wide-ranging impacts. SPM affects primary production (Turner & Millward, 2002) through light (van de Hulst, 1957) and heat (Jago & Jones, 2002) attenuation, impacts shellfish growth through the clogging of gills and dilution of the food source (Essink & Bos, 1985), and plays a vital role in biogeochemical cycling (Turner & Millward, 2002) as it may carry important biogeochemical components (e.g. carbon, nitrogen) and pollutants (Zonta, et al., 2005). SPM may also impact upon re-mineralisation

(Suzuki, et al., 1985), while high levels can suppress bed shear stress (Gust & Walger, 1976), preventing the resuspension of sediment from the bed. A large part of estuarine SPM occurs in the form of flocs (collections of dead and living organic matter, cohesive inorganic matter, and water), which are easily disturbed by conventional sampling methods as they may be ruptured and/or flocculated during sampling (Jago, et al., 2006). Floc properties may change over multiple time scales: tidally due to resuspension and advection, over the lunar (spring-neap) cycle due to changes in the turbulence regime and seasonally due to river flow, storm resuspension and biological production (Manning, et al., 2010).

SPM affects all realms of an estuary: the biology, chemistry, and physics; making it a crucial system component. To understand the variations in SPM properties (size, concentration, settling velocity), one must understand the processes that control it.

The coastal zone, including estuaries, is a critical region of human influence that is highly susceptible to both climate change and anthropogenic impacts. As such, estuarine environments provide a challenging backdrop against which to conduct scientific investigations as particulate matter and particulate-associated biogeochemical components must pass through the estuary mouth to reach the coastal zone.

1.2 Aims

This study uses data collected at the mouth of the Dee Estuary in the United Kingdom to investigate how SPM within the Dee Estuary is modulated and controlled over tidal, spring-neap, and seasonal timescales. The main aims of this study are to:

- Investigate how the structure of the water column varies over tidal, spring-neap, and seasonal timescales and to identify the processes controlling these variations;
- Identify the main forcings responsible for SPM fluctuations within the estuary;
- Investigate how SPM size and concentration vary throughout the water column, and establish whether this can be explained as a response to tidal processes (i.e. turbulence and advection);

- Establish the properties and behaviour of suspended particles within the water column (sizes, densities, strength, settling velocities) and how these change according to tidal and seasonal variations.

This study aims to investigate the seasonally varying SPM characteristics of the Dee Estuary. With this objective in mind, the majority of data collected within the present study are recorded within the water column. For the first time, data have been collected during both February-March and May-June in the Hilbre Channel of the Dee Estuary as this channel will display the greater river influence of the two channels owing to the effects of the Earth's rotation. This data set allows a unique insight into the changes in SPM dynamics of the river-influenced region of the estuary between the February-March (winter) and May-June (summer) time periods. Data from February 2008 in the Welsh Channel have been analysed by Ramirez-Mendoza et al. (2014), but cross-seasonal analysis has yet to be undertaken in any form within the Dee Estuary.

The two critical controls on the flocculation of suspended cohesive sediments are known to be turbulence (Winterwerp, 2002) and the presence of biological substances such as polysaccharides (Dyer, 1986). The turbulence regime, controlled by the current speeds and therefore the tidal forcing, is constant between seasons. The variable inter-seasonal parameters are therefore the impact of changes in river discharge and biological activity between seasons. The impact of a reduction in river discharge on SPM should be small as the Dee Estuary is a hypertidal environment with a large tidal prism in comparison to the small river flow. However, impact on stratification is potentially large. The seasonal variation in biological activity will be large, with low productivity during February-March, and greatly increased productivity in May-June, particularly in the salt marsh and mud flat regions. As a result of these factors, the seasonal variations in the behaviour of suspended sediment between the February-March and May-June time periods will be large.

Changes in temperature and solar radiation between the February-March and May-June deployment periods may constrain the availability of material for flocculation by increasing the shear strength of intertidal sediments, while increasing the potential for flocculation as rates of flocculation have been shown to be lower under low temperature conditions. In addition, the increase in biological activity may increase sediment binding.

This study aims to characterise and quantify these changes by looking at how turbulence and biological activity impact upon SPM flux, particle characteristics and particle behaviour across seasons in the hypertidal estuarine environment of the Dee Estuary. The physical characteristics of the Dee make it an ideal location for studying biological-turbulence-suspended sediment interactions and flocculation: It experiences strong tidal forcing, has a large tidal prism, high tidal range and abundant amounts of cohesive sediment. In addition, the freshwater input creates a horizontal density gradient that, through interaction with tidal forcing, creates both periodic stratification and a residual, gravity-driven circulation.

1.3 Outline of thesis

This study is split into nine chapters. In the current chapter, the reasoning for undertaking the study and the aims of the research have been expressed. Chapter 2 presents a background literature review recounting the current understanding of the dynamics of estuaries with regard to hydrodynamics and turbulence. Chapter 3 presents a background literature review focusing on the current understanding with regard to SPM and, in particular, flocculation. Chapter 4 presents a background to the study location, while Chapter 5 presents the methodology and details of the observational strategy employed, and highlights the properties and calibrations of each instrument used. Data analysis begins in Chapter 6 with the meteorological conditions encountered, and details the harmonic analyses of both tidal elevations and current velocities. The water column structure is investigated with regard to velocity, turbulence, salinity, temperature, SPM, fluorescence and chlorophyll, while the time evolution of particle concentrations and sizes are shown and the potential origins of a fluorescence signal are discussed. Chapter 7 investigates the relative contributions of quarter-diurnal resuspension and semi-diurnal advection in relation to spring-neap and seasonal variation in small particle concentrations of SPM. This is done through harmonic analysis of the SPM time series by the fitting of quarter- and semi-diurnal harmonic frequencies to the time series and analysis of the variation in amplitude of the applied harmonics over both spring-neap and seasonal time scales, showing how varying small particle input affects both the net volume, and the net mass, flux of SPM in the estuary. Chapter 8 determines if the Dee Estuary is a flocculating system and the nature of

the particles, including sizes, densities, settling velocities, strengths and the identity of a potential primary particle are investigated, with the causes of the observed variations in particle characteristics and behavior discussed. Finally, Chapter 9 integrates the observations, providing conclusions and suggestions for future work to extend the study.

Chapter 2

Estuarine hydrodynamics and turbulence

2.1 Introduction

An estuary, as classified by Cameron and Pritchard, (1963), is a semi-enclosed coastal body of water that has free communication to the ocean, and within which oceanic water is diluted by land-derived freshwater. This definition is applicable to temperate estuaries such as the Dee Estuary, which will be considered herein, but not to subtropical basins, tropical, or arid estuaries (Valle-Levison, 2010). The first modern, systematic experiments into the dynamics of estuaries were conducted by Fleming (1818) in the Firth of Tay, Scotland using an anchored boat and bottles attached to string. Fleming collected water samples from the top, middle and bottom of the water column at different times during the tidal cycle. The resulting samples were evaporated, and the dry residue tasted to determine salinity. Despite the primitive nature of these observations, vertical salinity stratification was determined during slack water, and vertical mixing during both flood and ebb. Since these first, primitive observations, estuaries have been studied all over the world.

The current chapter provides an introduction to estuaries, considering the hydrodynamics, including classification by structure and circulation patterns, and the impact of the Earth's rotation. As the Dee Estuary is a hypertidal (Dyer, 2001; Archer, 2013), temperate estuary, a section on hypertidal estuaries highlights key aspects, and provides examples, of this estuary type. Hypertidal estuaries, with their high tidal ranges and fast currents, tend to be high energy environments (Archer, 2013) and therefore regions of high turbulence. Turbulence often controls suspended particulate matter (SPM) within estuaries (Hill, et al., 2001; Fugate & Friedrichs, 2002), and therefore a section on our current understanding of turbulence is also included.

2.2 Estuaries

2.2.1 Hydrodynamics

Classification by structure

Estuaries are commonly classified into four categories based upon their level of vertical stratification: vertically mixed, weakly stratified, strongly stratified, or salt wedge (Cameron & Pritchard, 1963; Hansen & Rattray, 1965; Hansen & Rattray, 1966; Valle-Levison, 2010). Differences in the level of stratification arise from the balance between the buoyancy force induced by freshwater from the river, and mixing due to tidal forcing, illustrated in Fig. 2.1. The tidal forcing is often proportional to the tidal prism – the volume of water transported into the estuary during each tidal period. Where the tidal forcing is large and river flow small, an estuary will be well mixed, with almost uniform vertical salinity distribution and mean flow by depth. Conversely, where the tidal forcing is small and the river flow large (e.g. the Mississippi), an estuary will be a salt wedge type with strong stratification and the presence of a sharp pycnocline occurring during the flood tide. Between these states, strongly stratified and weakly stratified estuaries (e.g. the James River, Chesapeake Bay) exist, which generally maintain their stratification throughout the tidal cycle (Valle-Levison, 2010). The Dee Estuary is well mixed for most of the tidal cycle, but experiences periodic density stratification during low water.

Estuarine circulation

Pritchard (1952; 1954; 1956) averaged the estuarine circulation of the James River (flowing into the south of Chesapeake Bay, USA) over a full tide, and used measurements of the freshwater-induced horizontal density gradient to show that a gravitational flow containing two separate layers was occurring (Fig. 2.1 top right). The freshwater input at the head of an estuary means a residual circulation may exist as the horizontal salinity-induced gradient is always present and therefore the density gradient is unable to equilibrate.

Horizontal density gradients (Valle-Levison, 2010), which occur when a location contains water of a higher or lower density relative to its neighborhood (caused by a difference in temperature, salinity or sediment concentration), which may result in density-driven flow between locations. This is known as “gravitational circulation” since it occurs due to the

natural tendency of fluid to adjust under gravity in order to minimize potential energy. The strength of the gradient may be time-varying and is influenced by the characteristics (including the degree of mixing) of the estuary (Linden & Simpson, 1988).

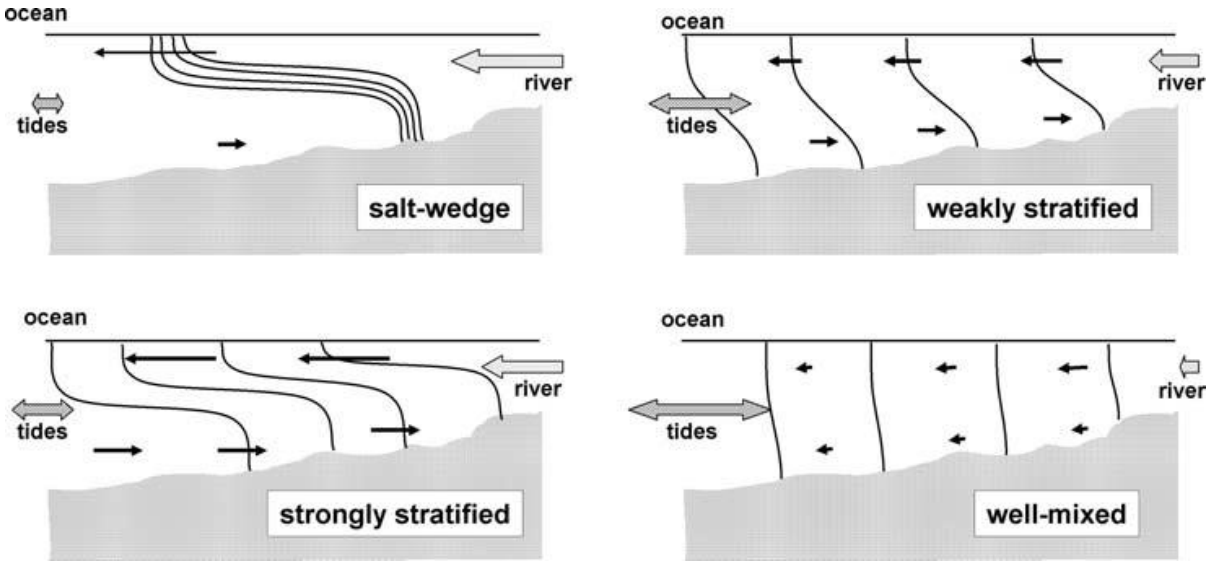

Fig. 2.1 – Averaged salt structure along an estuary showing examples of salt wedge (top left), strongly stratified (bottom left), weakly stratified (top right) and well-mixed (bottom right) estuaries. Black arrows indicate direction of residual flow. Lines shown are salinity contours. Reproduced from Valle-Levison (2010)

The total residual estuarine circulation is a result of the horizontal density gradient and the baroclinic pressure gradient it generates (since the flow is moving between a zone of higher pressure, to one of lower pressure), and the barotropic pressure gradient induced by the hydrodynamic processes associated with the propagating and oscillating tidal signal, in addition to the freshwater of the river inflow. This total residual circulation can be expressed as:

$$\frac{1}{\rho}\frac{p}{\partial x} = g\frac{\partial \eta}{\partial x} + \beta g\frac{\partial s}{\partial x}(h - z) \tag{2.1}$$

in which ρ is the water density, β the coefficient of saline contraction, g gravitational acceleration, h water depth, η surface elevation, s salinity, and z the vertical height of the observation (Geyer, 2010). The net result is that the pressure gradient drives the estuarine

surface waters toward the sea, and the bottom waters toward the estuary head – causing a residual estuarine circulation. If this residual current is of sufficiently high velocity, turbulence may result.

Circulation may also be caused by strain-induced periodic stratification (SIPS – Simpson, et al., (1990)) in which the flood tide strains the density field through the process of advection as higher density water advects over lower density water, causing destabilisation of the water column, while the opposite effect occurs during the ebb. This enhances vertical mixing through convective turbulence during the flood tide as stratification is broken down on the incoming flood tide, resulting in a fully-mixed water column at high water (Thurston, 2009). During the ebb, stratification gradually increases, reaching a maximum at low water. This results in a circulation of inflowing water at the sea bed, with outflow at the surface, reinforcing the residual estuarine circulation. The SIPS mechanism is considered further in Section 2.3.7.

2.2.2 Effects of the Earth's rotation

The effect of the Earth's rotation on objects moving over the Earth's surface was first observed by Coriolis (Coriolis, 1835). This force affects estuaries and coastal circulation by rotating currents clockwise in the northern hemisphere (Fig. 2.2), causing flow velocities, and therefore SPM concentrations, to be higher on one side of the estuary (Bowden, 1967; Fugate, et al., 2007). The classic interpretation of the impact of the Coriolis effect on a system is that it is the width of the basin that determines the scale of the impact of the rotational effects (Pritchard, 1952), and therefore the Kelvin number (Eq. (2.2)), which uses the internal Rossby radius of the system (Eq. (2.3)), gives a good indication of the importance of the Coriolis effect to a system. Rotational effects are deemed to be important when $K_e > 1$.

$$K_e = B/R_r \tag{2.2}$$

where B is basin width, and R_r the Rossby radius, given by:

$$R_r = \frac{(g'h)^{1/2}}{f} \tag{2.3}$$

in which g' is reduced gravity:

$$g' = g\Delta\rho/\rho_0 \tag{2.4}$$

composed of the gravitational acceleration (g), a reference water density (ρ_0), and the difference between the buoyant surface water and the density of water beneath ($\Delta\rho$), and f is the Coriolis parameter:

$$f = 2\Omega \sin \varphi \tag{2.5}$$

in which Ω is the rotation rate of the Earth and φ the latitude of the observations.

However, the depth of the water column may also be a determining factor with regard to the impact of Earth's rotation (Valle-Levison, 2008), and therefore the Ekman number (Eq. (2.6) – A_z is the eddy viscosity of the flow) must also be considered.

$$E_k = \frac{A_z}{fh^2} \tag{2.6}$$

For SPM, the impact of the Coriolis effect is source-dependent. In an idealised, northern hemisphere scenario where frictional forces are small (e.g. a wide, deep estuary), if the majority of SPM arrives from the sea, the highest concentrations are found on the left of the estuary (when facing seawards, and dependent upon the effects of stratification). However, if SPM is river dominant, the highest concentrations are found on the right. The outflow from the estuary is also affected, with flow turning towards the right on exit. When frictional forces are moderate to high (a narrow, shallow estuary), the horizontal density gradient dominates, trapping sediment in areas of fresher water (Huijts, et al., 2006). Frictional effects still occur, but the signal is small in comparison to other forces. The impact of the Coriolis effect within the study region of the Dee Estuary is considered through the use of the Ekman and Kelvin numbers in Chapter 4.

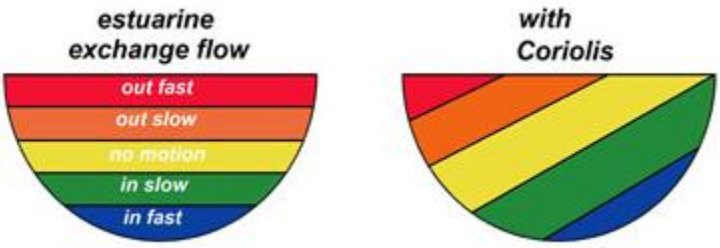

Fig. 2.2 – Estuarine circulation without Coriolis (left) and with Coriolis (right) [Source: http://www.po.gso.uri.edu/~codiga/foster/images/ResidualsLabeled.jpg]

2.2.3 Hypertidal estuaries

Estuaries with a mean spring tidal range in excess of 6m, such as the Dee, are classified as "hypertidal" (Dyer, 2001; Archer, 2013). These high tidal ranges often result in high energy estuaries with large intertidal areas, and sediment dynamics (including erosion, transport and deposition) that are subject to extreme short-term variability (Archer, 2013). There are many examples of hypertidal estuaries around the UK, and some of these systems, with their associated tidal ranges and maximum depth-averaged SPM concentrations, are presented in Table 2.1 (taken from Uncles, et al., (2002) and Uncles, et al., (2013)). The large number of hypertidal estuaries around the UK, combined with the need to move away from fossil fuel energy production, makes the understanding of hypertidal estuaries of great importance as their high current speeds and large tidal ranges makes hypertidal estuaries a potential untapped source of clean, renewable energy (Archer, 2013).

The maximum depth-averaged SPM concentration of an estuary has been shown to be related to the tidal range and estuary length (Uncles, et al., 2002), with long estuaries that have large tidal ranges generally having high maximum depth-averaged SPM concentrations. Therefore, hypertidal estuaries are more likely than other types of estuary to be areas of high SPM concentration.

Table 2.1 – Hypertidal estuaries in the UK including tidal range and depth-averaged SPM concentration

Estuary	Tidal range (m)	Max depth averaged SPM (mgl^{-1})
Bristol Avon	12.2	10900
Yeo	11.7	171
Somerset Axe	11.2	267
Parrett	11	32300
Kent	8.9	400
Mersey	8.4	12000
Leven	8.4	200
Waver	8.4	140
Wampool	8.4	300
Wyre	8.3	500
Lune	8.3	200

2.3 Turbulence

2.3.1 What is turbulence

Turbulence was first comprehensively studied by Reynolds (1883), who observed the flow properties of water moving through tubes. Reynolds realised that a transition occurred in the tube; linked to water viscosity and tube diameter, and that at some critical value (Re_{Crit}) laminar flow became turbulent. Using the ratio between the viscous and inertial forces within a fluid flow, Reynolds created the non-dimensional Reynolds number (Eq. (2.7)) in which U (ms^{-1}) and L (m) are length scales within the system, ν (with units of m^2s^{-1}) is kinematic viscosity (μ/ρ where μ is the dynamic viscosity and ρ the water density). Each flow has a critical Reynolds number, above which flow becomes turbulent. Under low Reynolds number conditions ($Re < Re_{Crit}$), viscous forces prevent turbulent eddies from forming. When $Re > Re_{Crit}$, inertial forces overcome the viscous damping, and turbulent flow results.

$$Re = \frac{UL}{\nu} \tag{2.7}$$

Turbulence is a random, irregular process that exists over a wide range of both temporal and spatial scales and as such, statistical properties must be recognised and used for its analysis (Huschke, 1959). Turbulent motions are rotational and energetic, forming eddies

which disperse material and transfer solutes, heat and momentum faster than would be experienced through only molecular processes (Thorpe, 2007). It is the principal sink for both wind-forced and tidal energy in the ocean, and although a high-frequency process, turbulence occurs on a small scale. It is inherently dissipative (Howarth & Souza, 2005), and driven by vertical current shear (Lorke & Wüest, 2005), causing motions on different spatial scales to interact and progressively spread to both smaller and larger length scales. In addition, turbulence is influenced by boundary effects (such as bottom topography, stresses at the sea surface etc.), stratification, and shear (Smyth & Moum, 2000a).

2.3.2 The derivation of the Reynolds stress tensor

The Reynolds stress, which accounts for turbulent fluctuations and defines the momentum transported between background shear and turbulent eddies by turbulence, can be used as a measure of the turbulence occurring within a turbulent flow and can be derived through the Reynolds averaging of the Navier-Stokes equations.

As water represents an incompressible flow, the average of the momentum must be equal to zero, resulting in a continuity equation (an equation which describes the transport of a conserved quantity) which can be written as:

$$\frac{\partial u}{\partial x} + \frac{\partial v}{\partial y} + \frac{\partial w}{\partial z} = 0 \tag{2.8}$$

in which x, y and z are the three components of direction, and u, v and w the three components of velocity in these directions, respectively.

In addition, turbulent fluctuations can be time averaged to yield a mean ($\bar{u}$) and a fluctuating, or turbulent, component (u') in a process known as Reynolds decomposition:

$$u = \bar{u} + u', v = \bar{v} + v', w = \bar{w} + w' \tag{2.9}$$

Further, since turbulent fluctuations are random in all directions, the mean of these turbulent fluctuations must also be zero, and therefore:

$$\overline{u'} = 0, \overline{v'} = 0, \overline{w'} = 0 \tag{2.10}$$

Substituting the expressions for the velocities from Eq. (2.9) into the continuity equation (Eq.(2.8)) yields:

$$\frac{\partial \bar{u}}{\partial x} + \frac{\partial u\prime}{\partial x} + \frac{\partial \bar{v}}{\partial y} + \frac{\partial v\prime}{\partial y} + \frac{\partial \bar{w}}{\partial z} + \frac{\partial w\prime}{\partial z} = 0 \tag{2.11}$$

The time-averaged x-direction momentum equation from the three-dimensional Navier-Stokes equations can be written as:

$$\frac{\partial u}{\partial t} + u\frac{\partial u}{\partial x} + v\frac{\partial u}{\partial y} + w\frac{\partial u}{\partial z} = -\frac{1}{\rho}\frac{\partial \rho_e}{\partial x} + \mu\left(\frac{\partial^2 u}{\partial x^2} + \frac{\partial^2 u}{\partial y^2} + \frac{\partial^2 u}{\partial z^2}\right) \tag{2.12}$$

in which ρ_e is the pressure force. The continuity equation (Eq. (2.8)) is multiplied by u, and added to Eq. (2.12) to give:

$$\frac{\partial u}{\partial t} + \frac{\partial u^2}{\partial x} + \frac{\partial (uv)}{\partial y} + \frac{\partial (uw)}{\partial z} = -\frac{1}{\rho}\frac{\partial \rho_e}{\partial x} + \mu\left(\frac{\partial^2 u}{\partial x^2} + \frac{\partial^2 u}{\partial y^2} + \frac{\partial^2 u}{\partial z^2}\right) \tag{2.13}$$

which can be averaged over a time period, t, giving:

$$\frac{\partial \bar{u}}{\partial t} + \frac{\partial \bar{u}^2}{\partial x} + \frac{\partial \overline{(uv)}}{\partial y} + \frac{\partial \overline{(uw)}}{\partial z} = -\frac{1}{\rho}\frac{\partial \overline{\rho_e}}{\partial x} + \mu\left(\frac{\partial^2 \bar{u}}{\partial x^2} + \frac{\partial^2 \bar{u}}{\partial y^2} + \frac{\partial^2 \bar{u}}{\partial z^2}\right) \tag{2.14}$$

$\frac{\partial u}{\partial t}$ = 0, and is therefore eliminated from the equation. Substituting Eq. (2.9), averaged over time, into Eq. (2.14) yields:

$$\left[\frac{\partial (\bar{u})^2}{\partial x} + \frac{\partial \overline{(u')}^2}{\partial x}\right] + \left[\frac{\partial (\overline{\bar{u}\bar{v}})}{\partial y} + \frac{\partial \overline{(u\prime v\prime)}}{\partial y}\right] + \left[\frac{\partial (\overline{\bar{u}\bar{w}})}{\partial z} + \frac{\partial \overline{(u\prime w\prime)}}{\partial z}\right] = -\frac{1}{\rho}\frac{\partial \overline{\rho_e}}{\partial x} + \mu\left(\frac{\partial^2 \bar{u}}{\partial x^2} + \frac{\partial^2 \bar{u}}{\partial y^2} + \frac{\partial^2 \bar{u}}{\partial z^2}\right) \tag{2.15}$$

in which:

$$\frac{\partial (\bar{u})^2}{\partial x} = 2\bar{u}\frac{\partial \bar{u}}{\partial x};\ \frac{\partial (\overline{\bar{u}\bar{v}})}{\partial y} = \bar{u}\frac{\partial \bar{v}}{\partial y} + \bar{v}\frac{\partial \bar{u}}{\partial y};\ \frac{\partial (\overline{\bar{u}\bar{w}})}{\partial z} = \bar{u}\frac{\partial \bar{w}}{\partial z} + \bar{w}\frac{\partial \bar{u}}{\partial z} \tag{2.16}$$

Therefore, substituting Eq. (2.16) into Eq. (2.15) gives:

$$\left[2\bar{u}\frac{\partial \bar{u}}{\partial x} + \frac{\partial (\overline{u\prime})^2}{\partial x}\right] + \left[\bar{u}\frac{\partial (\bar{v})}{\partial y} + \bar{v}\frac{\partial \bar{u}}{\partial y} + \frac{\partial \overline{(u\prime v\prime)}}{\partial y}\right] + \left[\bar{u}\frac{\partial \bar{w}}{\partial z} + \bar{w}\frac{\partial \bar{u}}{\partial z} + \frac{\partial \overline{(u\prime w\prime)}}{\partial z}\right] = -\frac{1}{\rho}\frac{\partial \overline{\rho_e}}{\partial x} + \mu\left(\frac{\partial^2 \bar{u}}{\partial x^2} + \frac{\partial^2 \bar{u}}{\partial y^2} + \frac{\partial^2 \bar{u}}{\partial z^2}\right) \tag{2.17}$$

Subtracting the continuity equation (Eq. (2.8)) after time averaging and multiplication by $\bar{u}$ gives:

$$\left[\bar{u}\frac{\partial\bar{u}}{\partial x}+\frac{\partial(\overline{u\prime})^2}{\partial x}\right]+\left[\bar{v}\frac{\partial\bar{u}}{\partial y}+\frac{\partial\overline{(u\prime v\prime)}}{\partial y}\right]+\left[\overline{w}\frac{\partial\bar{u}}{\partial z}+\frac{\partial\overline{(u\prime w\prime)}}{\partial z}\right]=-\frac{1}{\rho}\frac{\partial\overline{\rho_e}}{\partial x}+\mu\left(\frac{\partial^2\bar{u}}{\partial x^2}+\frac{\partial^2\bar{u}}{\partial y^2}+\frac{\partial^2\bar{u}}{\partial z^2}\right) \quad (2.18)$$

which can be rearranged into:

$$\bar{u}\frac{\partial\bar{u}}{\partial x}+\bar{v}\frac{\partial\bar{u}}{\partial y}+\overline{w}\frac{\partial\bar{u}}{\partial z}+\frac{1}{\rho}\frac{\partial\overline{\rho_e}}{\partial x}=\mu(\nabla^2\bar{u})-\frac{\partial(\overline{u\prime})^2}{\partial x}-\frac{\partial(\overline{u\prime})^2}{\partial y}-\frac{\partial(\overline{u\prime})^2}{\partial z} \quad (2.19)$$

where:

$$(\nabla^2\bar{u})=\frac{\partial^2\bar{u}}{\partial x^2}+\frac{\partial^2\bar{u}}{\partial y^2}+\frac{\partial^2\bar{u}}{\partial z^2} \quad (2.20)$$

This is the x-directional momentum equation. y- and z-directional momentum equations can be derived in a similar fashion.

In a two-dimensional turbulent boundary layer therefore, the momentum equation in the x-direction is:

$$\bar{u}\frac{\partial(\bar{u})}{\partial x}+\bar{v}\frac{\partial\bar{u}}{\partial y}+\frac{1}{\rho}\frac{\partial\overline{\rho_e}}{\partial x}=\mu\frac{\partial^2\bar{u}}{\partial y^2}-\frac{\partial\overline{(u\prime v\prime)}}{\partial y} \quad (2.21)$$

This can be rearranged to give:

$$\bar{u}\frac{\partial(\bar{u})}{\partial x}+\bar{v}\frac{\partial\bar{u}}{\partial y}+\frac{1}{\rho}\frac{\partial\overline{\rho_e}}{\partial x}=\frac{\partial}{\partial y}\left(\mu\frac{\partial\bar{u}}{\partial y}-\rho\overline{u'v'}\right) \quad (2.22)$$

Within this equation, $\mu\frac{\partial\bar{u}}{\partial y}$ is the molecular shear stress, and $-\rho\overline{u'v'}$ the Reynolds stress.

Shear between regions of flow moving at different velocities may form turbulent eddies, disrupting isotropy. The resultant anisotropy causes energy exchange via these Reynolds stresses (shown in Eq. (2.23) in tensor notation). In Eq. (2.23), u'_i represents the fluctuating, turbulent part of the velocity in the "i" direction, with the overbar indicating that $u'_i u'_j$ has been averaged by ensemble, spatially, or over time.

$$\tau'_{ij} = -\rho\overline{u'_\iota u'_j} \tag{2.23}$$

2.3.3 The turbulent energy cascade

Kolmogorov (1991) investigated high Reynolds number (turbulent) flows, quantifying the energy input at large scales, transferred via turbulent eddies, and ending with dissipation to viscosity. This is known as the turbulent energy cascade and is illustrated diagrammatically in Fig. 2.3. High-level energy cascades down the energy spectrum until it is dissipated through molecular viscosity at the lowest level (Smyth & Moum, 2000a). Kolmogorov believed that transferring energy to smaller scales involved losing information about the geometry of the larger scales, so that small-scale eddy structure was independent of both boundary and initial conditions (Smyth & Moum, 2000b). To test this, Kolmogorov made two assumptions about kinetic energy distribution over the range of turbulent eddies. The first was that for the smallest eddies, turbulence depends upon fluid viscosity and dissipation rate. This led to a relationship for the lengthscale of a flow (Eq. (2.24) in which ε is the turbulent dissipation rate, and λ the Kolmogorov length scale, which is the size of smallest turbulent eddies within a system).

$$\lambda = \left(\frac{\nu^3}{\varepsilon}\right)^{\frac{1}{4}} \tag{2.24}$$

The second was that viscous friction only exerts influence on these smallest eddies, where it dissipates energy. Thus, using dimensional analysis, the -5/3 power law was established (Eq. (2.25)), giving the inertial subrange of the energy spectrum in which the net energy being received from the large energy-containing eddies is in equilibrium with the net energy that is dissipated by the smallest eddies. k is the wavenumber corresponding to the wavelength r in the form $k = 2\pi/r$, and C_K a constant:

$$E(k) = C_K \varepsilon^{\frac{2}{3}} k^{-\frac{5}{3}} \tag{2.25}$$

Eq. (2.25) applies to eddies larger than the smallest (the size of which is given by Eq. (2.24)), from which energy is viscously dissipated, but smaller than the largest eddies which receive energy from the flow. There is no net gain or loss of energy from these eddies – the energy

received from larger eddies is equivalent to that lost to smaller eddies. Therefore, turbulence in this region can be considered as a conservative material, and the continuity equation becomes applicable.

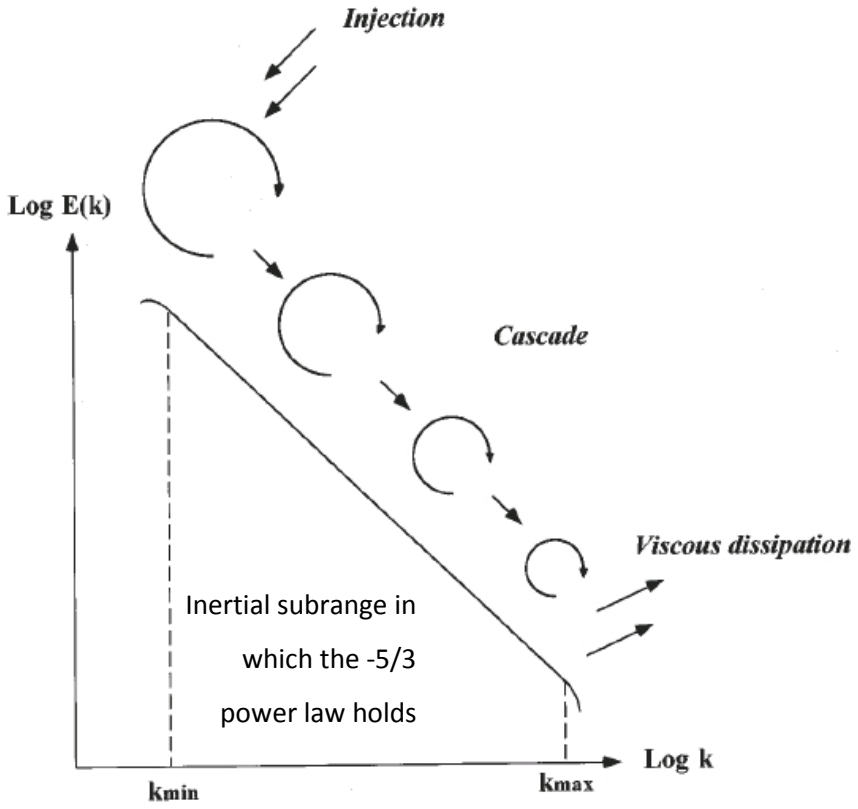

Fig. 2.3 – The Kolmogorov turbulent energy cascade, showing energy injection at large scales, cascading down into smaller turbulent eddies and viscously dissipating to friction at the smallest scales. k is the wavenumber, E(k) is defined in Eq. (2.25)

2.3.4 Turbulence as a mixing agent

Turbulence can cause the mixing of dissolved and suspended matter, momentum, gases, salt, and heat (Burchard, et al., 2008). Fig. 2.4 shows the difference that turbulent mixing can make to a system: In the diffusion-only system, spreading occurs at the rate of random particle perturbations, and (theoretically) in a regular, circular manner (in two dimensions; in three dimensions spreading is spherical) as the high concentration (red) region diffuses into the low concentration (white) region. With the addition of turbulence, the rate of mixing may be increased by several orders of magnitude as turbulent eddies break up the high concentration region. Over time, both diffusion and turbulence result in homogeneity,

and diffusion may still be required to remove small-scale variations including variations in particle distribution, but equilibrium is reached faster with turbulence, making this the more efficient process (Tennekes & Lumley, 1972).

Shear diffusion, which may occur in both turbulent and laminar flows (Hannah & Wright, 1995), is responsible for much of the horizontal mixing in the ocean (Bowles, et al., 1958) that occurs in low Reynolds number flows. In shear diffusion, shear between fluid layers causes mixing, without the creation of turbulent eddies. This results in faster mixing than molecular diffusion, but is slower than turbulent mixing.

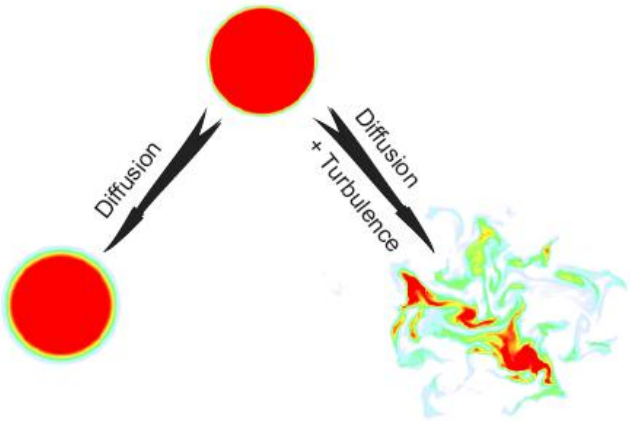

Fig. 2.4 – Spreading by diffusion and spreading by turbulent processes (Smyth & Moum, 2000b)

Turbulence performs two operations: momentum transport and scalar mixing. Where turbulence transports momentum, it reduces differences in velocity between two flow regions in a similar way to molecular viscosity, and, provided the fluid is Newtonian, in accordance with Newton's law of viscosity:

$$\tau \propto \partial u / \partial y \tag{2.26}$$

which states that the shear stress in a fluid is proportional to the velocity gradient. In scalar mixing, fluid properties such as temperature are homogenised by random turbulent motions.

Turbulent mixing occurs via strain and vorticity (Fig. 2.5 & Fig. 2.6), two interconnected processes which occur in separate, connected regions within a flow. Vorticity is the rotation of fluid parcels without the alteration of their shape, while strain, in which fluid parcels are stretched in one direction, leading to compression in the orthogonal direction due to mass conservation, occurs between regions undergoing vorticity (Fig. 2.5). Little deformation or mixing occurs within vortices, with most occurring between adjacent vortices, where strain deforms the fluid parcels, enlarging gradients, and enhancing mixing (Fig. 2.6, Smyth & Moum, (2000a)).

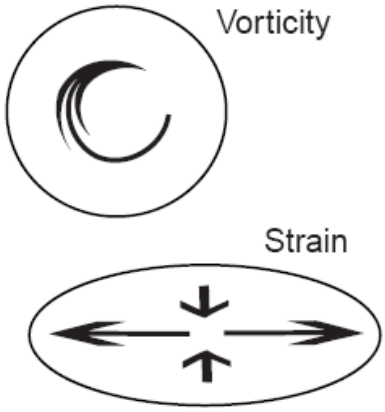

Fig. 2.5 – Vorticity (top) involves the rotation of a fluid parcel without altering its shape, while strain (bottom) involves stretching a fluid parcel in one direction, resulting in compression in the orthogonal direction in order to conserve mass (Smyth & Moum, 2000b)

2.3.5 Turbulence in the bottom boundary layer

Definition of the bottom boundary layer

Where a fluid flows over a solid, stationary boundary (e.g. the sea bed), the fluid that touches the boundary has a zero velocity due to the shear stress (τ_0) at the boundary. Above this point, the velocity of the fluid becomes non-zero, and at some height above the boundary the velocity may reach the free stream velocity ($\bar{u}_0$), the constant velocity that is free from the influence of any boundary (Bruley, 1965). Between the zero flow at the

boundary and 99% of $\bar{u}_0$, the velocity varies with the vertical coordinate. This is known as the benthic boundary layer and was first explained by Stokes (1851).

All boundary layers contain a laminar flow region immediately above the stationary fluid that contacts the sea bed, known as the viscous sub-layer, while the outer regions of the boundary layer may be laminar or turbulent dependent upon the characteristics of the flow. For the Dee Estuary, the flow characteristics are such that the boundary layer is almost always turbulent, and therefore we will consider turbulent boundary layers in more detail.

Shear stress in the boundary layer

In a horizontally homogeneous flow (in which $\frac{\partial}{\partial_y} = 0$, $\frac{\partial}{\partial_x} = 0$), the Reynolds averaged Navier-Stokes equation (as shown in Eq. (2.22)) can be written as:

$$\bar{w}\frac{\partial \bar{u}}{\partial z} = \frac{\partial}{\partial z}\left(\mu\frac{\partial u}{\partial z} - \overline{w'u'}\right), \frac{\partial \bar{w}}{\partial z} = 0 \tag{2.27}$$

assuming that there is no flow through the boundary, $\bar{w} = w' = 0$ at $z = 0$. Therefore, at the boundary:

$$\frac{\partial}{\partial z}\left(\mu\frac{\partial u}{\partial z} - \overline{w'u'}\right) = 0 \tag{2.28}$$

and the shear stress (τ) will be:

$$\tau = \nu\frac{\partial \bar{u}}{\partial z} - \overline{w'u'} = \left(\mu\frac{\partial u}{\partial z}\right)_{z=0} \tag{2.29}$$

In the viscous sub-layer there is no turbulence to account for since flow is laminar, and therefore τ reduces to just the viscous term ($\mu\frac{\partial u}{\partial z}$). Away from the boundary layer, viscous forces become negligible and therefore Eq. (2.29) reduces to Eq. (2.23).

The velocity scale that can be defined from this stress is:

$$u_*{}^2 = \tau/\rho \tag{2.30}$$

u_* is known as the friction, or shear, velocity. Away from the effects of the boundary, u_* is the magnitude of the turbulent velocity fluctuations.

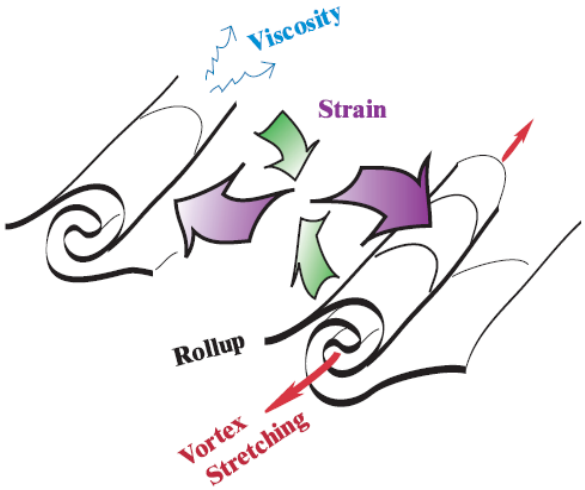

Fig. 2.6 – Strain occurring in between regions of vorticity (Smyth & Moum, 2000a)

Regions of a turbulent bottom boundary layer

Turbulent boundary layers can be divided into several sections based upon distance from the solid boundary. The regions of a smooth turbulent boundary layer (Fig. 2.7) are:

- The viscous sub-layer

  The viscous sub-layer occupies the region in which $z < z_f$, where z is distance from the solid boundary and z_f is the distance at which Re = 1. It is the region of high viscosity adjacent to the boundary where friction is important. Reynolds stress is negligible, and therefore there is no turbulence. Flow is laminar, with flow velocity increasing with distance away from the solid boundary as shown in Eq. (2.31).

$$\frac{\bar{u}}{u_*} = \frac{u_* z}{\nu} \tag{2.31}$$

  As the Reynolds number of the freestream flow increases, this region decreases in size. At Re = 1, the top of the viscous sub-layer, the turbulent and viscous stresses are around the same magnitude and therefore $z_f = \frac{\nu}{u_*}$.

- The velocity defect region

  The thickness of this region is determined by the maximum attainable size of the turbulent eddies. Viscosity can be neglected due to the size of the turbulent fluctuations, and therefore this region is dependent upon u_* (Eq. (2.30)), *M* (total

boundary layer depth), and *z*. The change in mean velocity with change in distance from the solid boundary (the mean velocity gradient) can be represented as:

$$\frac{\partial \bar{u}}{\partial z} = \frac{u_*}{\partial} g\left(\frac{z}{M}\right) \tag{2.32}$$

Although not included in this formula, the mean velocity is also dependent upon the freestream velocity ($\bar{u}_0$), and as *z/M* → ∞, $\bar{u} \rightarrow \bar{u}_0$.

Integrating from *z* = ∞ inwards toward the solid boundary in order to calculate $\bar{u}$ gives:

$$\int_z^\infty \frac{\partial \bar{u}}{\partial z'} \delta z' = \frac{u_*}{\partial} \int_z^\infty g\left(\frac{z'}{M}\right) \delta z' \tag{2.33}$$

which can be simplified, to find $\bar{u}$, to:

$$\bar{u}(z) - \bar{u}_0 = u_* F\left(\frac{z}{M}\right) \tag{2.34}$$

in which *F* is a function. This is known as the velocity defect law and is not valid within the viscous sub-layer, as it does not satisfy $\bar{u} = 0$ at the solid boundary. Because of this, other regions must exist which provide a transition between the viscous sub-layer and the fully turbulent velocity defect layer.

If the velocity defect layer reaches the surface, the water column will be well mixed, since it is an area of high turbulence. If the velocity defect layer does not reach the surface, stratification may occur; dependent upon whether any surface mixed layer is sufficiently deep for the boundary layers to overlap (Prandle, 1982; Souza, 2013).

- The inertial sub-layer

  In this transition region between the viscous sub-layer and velocity defect region, flow is independent of the size of the boundary layer (M) and viscosity. It is located at $z_f << z << M$. Within this layer, turbulence production balances turbulence dissipation and velocity increases logarithmically with height above the boundary according to the equation:

$$\frac{\bar{u}}{u_*} = \frac{1}{\kappa} \ln\left(\frac{z u_*}{v}\right) + b \tag{2.35}$$

Where κ is the von Karmen constant (approximately equal to 0.41), and b is a constant (approximately equal to 5). Due to the logarithmic increase in velocity with height, this region is often referred to as the "log layer."

- The buffer layer

  Between the viscous sub-layer and the inertial sub-layer (logarithmic layer) is a fourth region, the buffer region, in which the turbulent and viscous forces are of the same order of magnitude.

Types of boundary layer flow

A turbulent boundary layer may undergo either rough or smooth turbulent flow dependent upon the bed roughness (Nikuradse, 1932; 1933), which may influence the boundary layer velocity profile. Nikuradse classified three types of boundary based upon their boundary Reynolds number value:

$$\frac{k_S u_*}{v} \tag{2.36}$$

in which k_S is the roughness length. These regions are:

- Hydraulically smooth wall

  This occurs when $\frac{k_S u_*}{v} < 5$, and therefore the roughness elements remain entirely immersed within the viscous sub-layer. The roughness elements are not exposed to the non-laminar flow and therefore although the bed may be rough, the boundary acts as a smooth wall.

- Hydraulically rough wall

  When $\frac{k_S u_*}{v} > 70$, the roughness elements are larger than the viscous sub-layer, and therefore the viscous sub-layer effectively wraps around the roughness elements.

- Transitional wall

  When $5 < \frac{k_S u_*}{v} < 70$. In this region, the roughness elements have an effect upon the characteristics of the viscous sub-layer but do not fully deform it as occurs with a fully hydraulically rough wall.

Fig. 2.7 shows the regions of the benthic boundary layer under smooth turbulent flow – indicated by the presence of a viscous sub-layer which displays no impacts of roughness elements.

Boundary layer development

The thickness of the benthic boundary layer in estuarine regions is time dependent. Under oscillating tidal flow conditions, the boundary layer grows under accelerating flow, and reduces under decelerating flow, disappearing completely at flow reversal. In addition, the thickness of the benthic boundary layer is influenced by other factors including sediment transport, and potentially wind & wave action (Dyer, 1986).

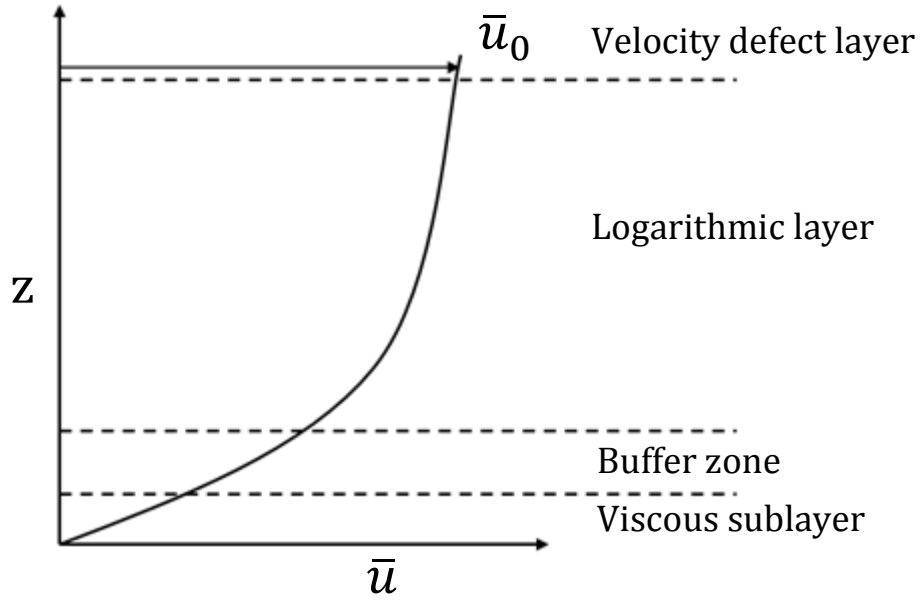

Fig. 2.7 – Regions of the benthic boundary layer under smooth turbulent flow

As tidal currents increase from high or low water to peak ebb or flood respectively, the bed stress increases (Feddersen, et al., 2006; Burchard, et al., 2008). The increasing stress causes vertical shear and the expansion of the benthic boundary layer at a rate influenced primarily by current speed, but also by horizontal density gradients, the time available for development, and bed roughness (Burchard, et al., 2008).

The development of the boundary layer can be expressed as laminar when the Reynolds number of the flow is less than 5 x 10^5, and turbulent when the Reynolds number is greater than this (Liu, 2001). Liu, (2001) gives equations to determine the distance at which

boundary layer flow starts to fill the whole water depth Eq. (2.37) and the type of boundary layer flow (Eq. (2.38)).

$$x_{\delta=h} = \left(\frac{(u/v)^{0.25}}{0.4^{1.25}} h^{1.25}\right) \tag{2.37}$$

$$Re_x = \frac{u\,x}{v} \tag{2.38}$$

Wave and current boundary layers

Current boundary layers tend to be less turbulent and thicker, of the order meters to tens of meters, than wave boundary layers, which tend to be highly turbulent, and a few to tens of centimetres in thickness (Liu, 2001; Sahin, 2014) due to the rapid velocity oscillations and steep velocity gradients associated with wave motion. Where wave effects are felt at the seabed, a wave-current boundary layer may exist, which is in effect a steady current-driven component in combination with an oscillatory wave component. If the flow in this boundary layer is turbulent, the turbulence generated by the current and wave boundary layers interacts in a non-linear fashion, and the resultant bed shear stress is larger than would be found from the addition of the independent current and wave stress values (Souza, et al., 2012). This is frequently observed in the shallow nearshore region (< 5 m depth), where the boundary layer reaches the sea surface (Feddersen, et al., 2006), which may occur within the intertidal and shallow subtidal regions of the Dee Estuary and affect the erosion and entrainment of sediment in these regions.

What constitutes a boundary

Any obstacle that impinges upon the flow can be considered a boundary (e.g. seamounts, islands, or smaller objects such as bedforms). These objects may create additional skin friction (the friction arising from the movement of the fluid against the “skin” of an object such as individual sediment grains), form drag (the friction arising due to the shape of an object – such as bedforms etc. Objects with larger presented cross-sections usually cause more drag), or reduce drag (as with mobile sediment grains under bedload transport). Additional turbulence may be created by the boundary layer that results from an object that extends into the flow. Generally, these objects enhance mixing, with the size of an obstacle relating to its impact on mixing (Burchard, et al., 2008).

2.3.6 Sea surface generated turbulence

The majority of momentum transferred to the sea surface comes from wind stress, which creates a wall layer over time, similar to the bottom boundary layer, extending down from the air-water interface (Jones & Monismith, 2008b). Wind stress causes stirring and mixing through the addition of energy to the surface of the water in the form of currents, indirect currents caused by the creation of a pressure gradient, and the creation of surface waves (Sverdrup, et al., 1942). This results in a homogenised region of fully mixed water known as the "surface mixed layer" which is maintained by turbulent mixing and can extend for many metres below the surface dependent upon the strength of the wind stress acting upon it.

Wind also creates white-capping and breaking waves, particularly in shallow or intermediate-depth water and in the surf zone, where depth-limited wave breaking may be the primary turbulence-inducing force (Feddersen, et al., 2006). The TKE (turbulent kinetic energy) produced by white-capping and breaking waves may be sufficient for them to determine both the magnitude and distribution of water column TKE (Jones & Monismith, 2008b); however in the outer Dee Estuary this is unlikely to be the case due to the size of waves encountered by comparison with the water depth. However, wave-induced resuspension can be important in any region in which the water is sufficiently shallow (e.g. intertidal and salt marsh regions).

2.3.7 Turbulence generated within the water column

Turbulence may be generated within the water column through many mechanisms, and several of these will be considered individually here.

Tidal straining

Tidal currents in shallow areas are sensitive to bed roughness and fine-scale bathymetry (Prandle, et al., 2011), making them susceptible to change within estuarine environments (upon which they have a large impact). Tidal flows may cause vertical convection through a more dense fluid differentially advecting over a less dense fluid, as occurs in Liverpool Bay (Baumert, et al., 2005) as part of the SIPS tidal straining mechanism (Simpson, et al., 1990) which creates unstable stratification. Tidal straining occurs due to the presence of the

benthic boundary layer resulting in larger velocities in the near-surface (due to velocity shear). During the flood tide, this advects denser, higher salinity water over lower layers of fresher, less dense water. This process results in turbulent convective overturning and mixing through the production of shear as the water column restores buoyancy equilibrium (Simpson, et al., 1990). Tidal straining is enhanced when flow is towards water of lower density – i.e. the flood tide in estuaries – and suppressed during the reverse (Burchard, et al., 2008). The tidal straining process reinforces the residual estuarine circulation (see Section 2.2.1) by decreasing stratification on the flood, and increasing stratification on the ebb (Moore, 2009). This process depends upon the ratio between mixing and tidal straining, which can be represented by a modified version of the Richardson number (Eq. (2.39), in which N is the Brunt–Väisälä frequency, which can be used to provide a measure of the change in density over the vertical (Eq. (2.40)). This modified version is shown in Eq. (2.41), in which א is the coefficient of saline expansivity, Γ the salinity gradient (in ppt/km) and C_D the bottom drag coefficient. The tidal straining process also relies upon the ratio of the boundary depth to the total depth (represented by the Stokes Number – Eq. (2.42), in which a is a constant, u_* the shear velocity (Eq. (2.30)) and ω the tidal oscillatory frequency (Souza, 2013)), and the competition between friction and the Earth's rotation, represented by an inverse Ekman number (the non-inverse Ekman number is shown in Eq. (2.6)).

$$Ri = \frac{potential\ energy}{kinetic\ energy} = \frac{N^2}{(\delta u/\delta z)^2} \tag{2.39}$$

$$N^2 = -\frac{g}{\rho}\frac{\partial \rho}{\partial z} \tag{2.40}$$

$$Ri_E = \frac{\text{א} g \Gamma h^2}{C_D u^2{}_{max}} \tag{2.41}$$

$$St = \frac{a u_*}{\omega h} \tag{2.42}$$

Due to the velocity dependence of tidal straining, the spring-neap cycle impacts upon turbulent mixing, with more mixing occurring during spring tides (Prandle, et al., 2011) since mixing due to tidal forcing is proportional to the volume of water that enters the estuary from the ocean during each tidal cycle (Valle-Levison, 2010), while storm surges can also impact by increasing the tidal range.

Heat Flux

The thermal structure of the water column is usually controlled by the balance between the surface heat fluxes, caused by solar heating and a difference in temperature between the sea surface and air, and tidal and wind mixing (Simpson & Hunter, 1974). This heating enhances water column stability through the creation of positive buoyancy in the surface layer. Latent heat also aids stability, as although the water body may not increase in temperature, its density reduces due to the increase in volume associated with latent heat input. However, in strongly turbulent regions such as the Dee Estuary, the periodic full mixing of the water column means that stratification is unaffected by surface heating.

Solar heating may also cause the establishment of a frontal system (governed by the h/u^3 parameter (Simpson & Hunter, 1974)). Frontal regions are often highly productive areas with strong residual currents that occur parallel to the front edge. Fronts form the boundary between (i) a vertically stratified region, wherein turbulent mixing is insufficient to mix surface heating to lower layers resulting in thermal stratification with warmer, lower density water overlying colder, denser water, and (ii) a vertically mixed region, where turbulence is sufficient to mix heat throughout the water column, but will be affected by the Earth's rotation (Souza, 2013). A frontal region occurs offshore of the mouth of the Dee Estuary which is strongly affected by seasonal freshwater input. This frontal region may encroach on the mouth of the Dee (Hopkins & Polton, 2012), but due to the highly turbulent nature of the estuary, it is unlikely that the front edge progresses into the estuary itself.

Buoyancy

Buoyancy reacts to gravity, with denser fluids sinking downwards, and can therefore act to create or dampen turbulence. When unstable density stratification is present (i.e. a more dense fluid overlies a less dense fluid – usually caused by temperature or salinity variations between the fluids), turbulence occurs as the water bodies attempt to stabilise. Conversely, where light fluid overlies heavy, this stable stratification dampens turbulence (Smyth & Moum, 2000a). Heat flux is a major cause of buoyancy; however, as has been shown in the previous section, heat flux is not a strong factor in the Dee Estuary. River input tends to result in stable buoyancy, with lighter, fresher water overlying denser salt water (ignoring tidal effects).

Stirring & Mixing

Stirring due to turbulent motions deforms and advects fluid parcels, while mixing changes the physical properties of a fluid parcel and is greatly enhanced by stirring in turbulent flows (Fig. 2.4) (Smyth & Moum, 2000a). Stirring and the resulting mixing control many properties of the water column – including vertical stratification. Where depth is large in comparison to velocity, stratification takes place, and vice versa, where the water column is shallow in comparison to the velocity, turbulent mixing prevents stratification, even in deep regions, such as the North Channel of the Irish Sea (Bowers & Simpson, 1987). An estimation of the impact of mixing on the lateral buoyancy inputs is given by the horizontal Richardson number (Eq.(2.41)).

2.3.8 Measuring turbulence

Instruments

Historically, the most popular instruments for measuring turbulence were shear probes (Osborn & Crawford, 1980) point current meters (Bowden & Proudman, 1949; Gross & Nowell, 1983), and electromagnetic current meters (Bowden, 1955). However, in the last decade ADCPs (Acoustic Doppler Current Profilers), which are traditionally used for measuring flow velocities (see Section 5.2.2), have become increasingly popular. ADCPs transmit a fixed frequency sound and record echoes returned from particles in the water column. The Doppler shift of the echo provides the flow velocity by assuming that the particles are moving at the same speed as the flow (Lohrmann, et al., 1990; Lorke & Wüest, 2005).

Methods of turbulence measurement using ADCPs

3 methods of analysis have been used to determine turbulence using ADCPs:

The “large-eddy” method, first reported by Gargett, (1988), and expanded upon in Gargett, (1994), uses a narrow-band, modified ADCP, where one beam has been rotated to the vertical (with the others in the instance of Gargett, (1994) inclined at 30˚ to the vertical). The vertical beam is used to improve both the depth range of the instrument, and the

accuracy of the vertical velocity calculation as calculating the vertical velocity from beam pairs assumes that the vertical velocity is constant across the spread of the beams, where in fact, this assumption holds very close to the ADCP unit where the spread is small, but the relationship reduces with distance from the ADCP unit. Using a true vertical beam provides a direct measurement of the vertical velocity and removes the need for this assumption.

The true vertical beam is used to look for large vertical velocities in the data, as these are a characteristic of turbulent flows. Where large vertical velocities are present, investigation into the timescales of the fluctuations is required to distinguish turbulence from physical processes such as mean flows along sloping boundaries, internal waves etc. to provide an estimate of ε. Due to uncertainties in horizontal averaging, Gargett, (1994) defines the magnitude of TKE as:

$$1.5{W_r}^2 \tag{2.43}$$

where

$$W_r \equiv \langle w'^2 \rangle^{1/2} \tag{2.44}$$

is the rms (root mean squared) vertical velocity under averaging such that <w> = 0.

Using this rms vertical velocity, and assuming that only a small amount of the TKE works against buoyancy forces, the turnover time of an eddy (t) is approximately equal to its lengthscale (l) divided by the rms vertical velocity (W_r), and therefore:

$$\varepsilon \approx \frac{{W_r}^2}{t} + c_n \approx \frac{{W_r}^3}{l} + c_n \tag{2.45}$$

where c_n is an unknown constant. The lengthscale is determined through a time series analysis twice the length of time that w is greater than one standard deviation away from the mean, as this time period equates to half a wavelength.

More recently, the “variance technique” has been used to derive Reynolds stresses from the along-beam velocity variance (see Section 5.2.2), with these stresses used to calculate TKE production (Stacey, et al., 1999; Rippeth, et al., 2002; Howarth & Souza, 2005). This technique was developed by Lohrmann et al. (1990), who used a High Resolution Current

Profiler (HRCP – a pulse-to-pulse coherent sonar) with four beams inclined at 30° to the vertical in 90° azimuthal increments. Along-beam velocity data were decomposed into mean and fluctuating components using spectral analysis, and a logarithmic profile fitted to the mean component. From this, Reynolds stresses, and hence TKE production, were estimated (see Section 5.2.2). This technique was converted for use with a broadband ADCP by Stacey (1996), with full details published in Stacey et al. (1999). This is currently the most popular method for calculating TKE production from ADCP data since broadband ADCPs have a lower noise level during velocity profiling than is possible with narrow-band ADCPs. This, combined with their large profiling range, makes the broadband ADCP an ideal tool for use in turbulence calculations (Lu & Lueck, 1999). However, there are limitations to this method. Since it uses a conventional ADCP with no true vertical beam it suffers from an assumption of horizontal homogeneity between beams – a problem identified by Gargett (1994) with the large-eddy method.

The most recent method is the "structure function" method, based on a technique used in radar meteorology. In this method, a second order structure function, *D(z,r)*, is used (Wiles, et al., 2006), which can be defined as:

$$D(z,r) = \overline{\left(v_f'(z) - v_f'(z+r)\right)^2} \tag{2.46}$$

Where v_f' is the along-beam velocity fluctuation. *D(z,r)* is therefore the mean-square of the v_f' difference between two points that are separated by a distance (*r*). Using the Taylor cascade theory, which relates velocity scales and length scales to isotropic eddies results in the equation:

$$D(z,r) = C_c^{\,2}\epsilon^{2/3}r^{2/3} \tag{2.47}$$

where C_c^2 is a constant with a value between 2 and 2.2 (used in atmospheric studies, and generally applicable to marine studies, though these values may underestimate dissipation values (Souza, 2007)).

The structure function method is less applicable to estuaries such as the Dee as the size of the smallest resolvable eddies is approximately equal to the size of the ADCP bins. In estuaries such as the Dee (depths < 20 m), bin sizes > 0.25 m are commonly used, and

therefore the structure function method is not an appropriate method to use for estimations of TKE.

Necessary assumptions in measuring turbulence

Turbulence is intermittent in time, space and amplitude and as such is often quantified through indirect measurements such as Reynolds stresses (Eq. (2.23)). Because of its continuously varying nature, highly-resolved 4D (height (z), width (x), length (y), & time (t)) measurements must be made of the physical properties of the water column in order to calculate turbulence. These must be over a sufficient period and at a high enough resolution to resolve dissipation to TKE (Burchard, et al., 2008), with TKE often calculated from ε (Jones & Monismith, 2008a). Obtaining high resolution data over wide areas in the natural environment is seldom possible – most research covers only two dimensions – meaning temporal and spatial under-sampling is a constant problem. In addition, the range of spatial scales over which turbulence operates – from tiny dissipative eddies (cms) to large energy eddies (up to several metres) – means no single method can resolve the total turbulence of a system such as the Dee Estuary, necessitating certain assumptions (Burchard, et al., 2008):

i. Extrapolating from 2D to 4D assumes locally isotropy;
ii. It is assumed that large scale turbulent fluctuations have no significant impact on micro-scale turbulent fluctuations; and
iii. Small-scale turbulence does not significantly impact the large-scale.

Further, using ADCPs for measuring turbulence involves assuming that both turbulence and mean flow are horizontally homogeneous. The homogeneity of the vertical velocity – which can generally be used as a proxy for the homogeneity of the flow, dependent upon the sampling region, can be inferred using the error velocity that is calculated from the variance method of turbulence calculation (see Section 5.2.2). In addition, the ADCP must be fixed to prevent the ADCP unit moving and readings being contaminated by correlations between turbulent velocity fluctuations and instrument motion (Lu & Lueck, 1999).

Problems with measurements: Wave contamination

Outside of the need for assumptions due to the difficulty in making high spatial and temporal resolution measurements (see previous section); site-specific factors can make turbulence measurements difficult. Surface waves can create problems for the observation and interpretation of surface and near-surface turbulence (Burchard, et al., 2008) and instrument location may have to be compromised by moving instruments to more sheltered areas, or instrument sensitivity may need to be reduced or less sensitive, more robust instruments used due to the high velocities and pressures encountered in surface regions. These factors can hamper small spatial scale measurements and make it necessary to make more assumptions. In addition, complex variations in TKE can occur under waves, with turbulence under a wave crest up to 1.6 times greater than that under a trough – making the removal of wave signals a complicated process (Jones & Monismith, 2008b). Further, the scale over which turbulence operates under strong wave conditions is usually smaller than the surface wave velocity fluctuations. Turbulent velocity fluctuations are generally 10^{-2} – 10^{-1} ms^{-1}, 10 – 100 times smaller than the wave-induced velocities. This gives up to four orders of magnitude difference between the TKE induced by wave motion, and that produced by tidal currents (Burchard, et al., 2008), meaning each wave almost completely "masks" the turbulence signal.

Doppler noise

Uncertainties known as "Doppler noise" are present in the calculation of beam velocities in all Doppler backscatter systems. This noise within the detected signal is related to the hardware of the system, the velocity of the flow, particle scattering, beam divergence (in acoustic systems which include this, such as ADCPs), and the residence time of the particles in the sample volume (Khorsandi, et al., 2012; Richard, et al., 2013). When the level of the noise is comparable to the sampling frequency of the sensor, the signal becomes notably contaminated (Richard, et al., 2013). This cannot be corrected for in the time-series of measurements, and can cause bias in the estimation of Reynolds stresses if the noise is not equal in opposing beams. Low intensity turbulence is susceptible to Doppler noise as the noise level is constant, and therefore its influence is greater where the signal to noise ratio is low. This does not affect estimates of stress, provided the noise in opposing beams is

equal, however, stress estimate uncertainty may occur in very turbulent regions as stress errors are proportional to the turbulence values recorded and thus, as turbulence increases, the associated error bars also increase (Lu & Lueck, 1999).

Chapter 3

SPM

3.1 Introduction

Estuarine sediments have been studied for a similar length of time to estuarine hydrodynamics, with even Charles Darwin remarking upon them during his journey aboard the Beagle (Darwin, 1846). A more comprehensive study of estuarine SPM was undertaken by Sollas (1883), who investigated the origins of SPM in the Severn Estuary and its tributaries. An attempt to summarise SPM deposition (in a non-mathematical way) was made by Willis (1893), who believed SPM was held in suspension by regular currents in rivers, and that in estuarine regions "where the rivers and the tidal wave contend for supremacy, each trying to establish its own current, and where for hours the power of either of them trembles in the balance without any sensible movement in any direction that deposit copiously takes place."

Particles suspended within the water column in estuaries may originate from aeolian sources, be generated biologically in-situ (plankton), or nearby (organic detritus), arrive from rivers or the sea, or be the product of resuspension from the seabed. The major source of SPM in temperate NW European estuaries such as the Dee Estuary tends to be from resuspension, while Aeolian input in these regions is negligible.

In the following chapter, SPM will be considered in detail. The sources of SPM including resuspension, plankton, organic detritus and river and sea input will be considered, along with a brief discussion of why SPM is important and the various types and components likely to be found in an environment such as the Dee Estuary. The vertical distribution of SPM will be considered, as well as the settling and sinks of SPM and the mechanics of flocculation.

3.2 SPM processes

3.2.1 Sources of SPM

Plankton

Pelagic plankton – both phytoplankton and zooplankton – are considered part of the SPM. During the spring and autumn bloom periods plankton may form a major component of SPM, providing a pathway for carbon transfer from pelagic to benthic habitats (Jago, et al., 2002). Plankton can influence both the composition and concentration of SPM (Jones, et al., 1998), through their presence as particles, and their production of sticky polysaccharide substances (Krivtsov, et al., 2009).

The pelagic plankton cycle coincides roughly with the four seasons. Winter sees low production due to low light levels and low temperatures. The water warms during spring, and, over a period of one to two weeks, the spring bloom occurs (Graf, et al., 1982). Higher sunlight, plentiful nutrients and warmer water fuel rapid plankton growth (Weisse, et al., 1990), most of which reaches the sea bed (Graf, et al., 1982) and is resuspended many times during breakdown (Auffret, et al., 1994). In summer, stratification may occur in regions of weak currents (Simpson & Hunter, 1974; Souza, 2013), and the thermocline, if present, prevents nutrients from mixing into surface waters (Jago, et al., 1993). Subsequently, production rates are centered on the sub-surface chlorophyll maximum at the base of the thermocline region. Re-mineralisation and consumption dominate, with little organic matter reaching the sea bed (Graf, et al., 1982). Stratification may break down during autumn as temperatures decrease and wind energy increases, and, if sufficient sunlight is present, an autumn bloom occurs (Garcia-Soto & Pingree, 2009). This regime can influence estuarine regions as offshore plankton blooms may be advected into the estuary during the flood tide, while the nutrient-rich estuary outflow may increase plankton growth around the estuary mouth during the nutrient-limited summer period.

Organic detritus

Organic detritus may be defined as “all types of biogenic material in various stages of microbial decomposition, which represents a potential energy source for consumer species” (McLusky & Elliott, 2004). Much is composed of particulate, non-living organic material such

as fecal material or fragments of salt marsh plants and animals. The main sources of organic detritus tend to be the estuary river, the sea, or areas alongside the estuary such as the salt marshes. In regions with large salt marsh areas such as the Dee Estuary, detrital material can act to smooth out seasonal variations in primary production since the increase in storminess experienced during winter can increase the supply of organic detrital material to the estuary system during times when primary production is low (McLusky & Elliott, 2004).

The vertical distribution of detritus is dependent upon the sources and sinks of the material within the system. In estuarine systems, a river source bringing in abundant organic detritus would tend to result in higher concentrations in the surface regions, while an oceanic source would conversely result in higher concentrations toward the bed.

Rivers

Rivers are the principal source of inorganic SPM to the oceans, bringing a continuous, though seasonally varying supply of fine particles in suspension, with discharge often heightened during and after storm events (Krivtsov, et al., 2008). These particles often become trapped in the estuary as they flocculate and sink out, becoming part of the resuspension fraction.

Further components of SPM include resuspension, which will be considered in detail in the remainder of this chapter, as well as material ejected or washed out of the feeding mounds of burrowing organisms, and bacterial colonies growing on flocs, which re-mineralise organic matter as it settles through the water column (Jones, et al., 1998).

3.2.2 Why SPM is important

SPM is particularly important in estuarine regions due to its ability to transport adsorbed pollutants from the estuary to the shelf seas (Winkler, et al., 1998). In addition, SPM impacts upon both light and heat attenuation within the water column, and controls the net sediment flux of the estuary – determining whether an estuary is infilling or exporting material – which can be of great significance to ports, harbors and wildlife areas in and around estuarine regions. The sediment flux of the Dee Estuary is considered in detail in

Chapter 7, while the impact of SPM on light, heat and pollutant transport are considered below.

Light

SPM affects light availability (Jerlov, 1976) as particles convert photons into other forms of energy in addition to altering the angle of light propagation through scattering. Both absorption and scattering are dependent upon the shape, size, refractive index and internal structure of the particles, as well as the physical characteristics of the water column (Stramski, et al., 2004). It is because of the scattering afforded by SPM that we are able to use optical instruments to measure the volume concentration of particles in suspension. Particle type also plays an important role in light attenuation, with inorganic particles tending to scatter all wavelengths of light, while organic particles absorb short wavelength light (Bowers & Mitchelson-Jacob, 1996). The size of particles impacts on their ability to attenuate light; large concentrations of small particles attenuate light more efficiently than small concentrations of large particles (Krivtsov, et al., 2008), with submicron particles the most efficient scatterers (Stramski, et al., 2004).

SPM may impact primary production (Jago, et al., 2006) through light attenuation, since light is essential for photosynthesis. This impact is greatest in shallow water where pelagic phytoplankton and resuspension both affect the entire water column. In these regions, the SPM impact may be sufficient to regulate the timing of the spring bloom (Tian, et al., 2009), impacting upon the amount of biological material and polysaccharide substances in the water column.

Heat

Solar radiation is attenuated by particles in the water column (Jago & Jones, 2002), with the depth of heat penetration dependent upon the tidal mixing (Holt, et al., 2005). In the shelf seas, temperature is the controlling factor on stratification (Holt & Umlauf, 2008), however, in estuarine regions, salinity stratification tends to be dominant.

Pollutants

Organic, non-polar, anthropogenic substances such as chloropesticides, polychlorinated biphenyls, polycyclic aromatic hydrocarbons, and heavy metals can all be adsorbed onto, and widely dispersed by, SPM (Winkler, et al., 1998). Mercury in particular readily adsorbs to small particles, and SPM is frequently sampled in studies to determine the quantities of mercury and other heavy metal compounds in an area (Mirlean, et al., 2003). A good example of this is the long-term monitoring of mercury levels in the Mersey Estuary, UK (Harland, et al., 2000) while Cd, Co, Cu, Ni, Pb and Zn have all been found in bed sediment after transportation via SPM (Martino, et al., 2002). Sampling of SPM is particularly important as SPM has been shown to contain higher concentrations of heavy metal pollutants than both bed sediment and macroalgae (Sfriso, et al., 1995).

3.2.3 Types of SPM

Sediment is generally divided into two types: cohesive, and non-cohesive, though no clear boundary exists between the two, with the transition gradual and dependent upon particle size and characteristics (Huang, et al., 2006). Non-cohesive sediments, such as sands, tend to be unreactive, quasi-spherical particles such as quartz sand or feldspathic minerals which do not interact, or react, with each other or other types of particle and remain almost always as single grains (Vanoni, 2006). By contrast, cohesive sediments (muds and silts) comprise small, reactive, platy minerals such as kaolinite that have a tendency to flocculate under suitable conditions (Eisma, 1986).

The transition between non-cohesive and cohesive sediment is dependent upon the inter-particle forces. These forces generally increase as the surface area to volume ratio (specific surface area) of the particles increases, and therefore the adhesive forces increase, as particles get smaller (Kranenberg, 1994; Huang, et al., 2006; Bolanos & Souza, 2010; Cartwright, et al., 2011), and can be several orders of magnitude larger than the gravitational forces between particles (Hayter & Mehta, 1986). Therefore, smaller particles tend to be more cohesive. The ionic charging of cohesive particles can result in strong inter-particle forces, dependent upon the minerals involved. An exception to this is fine glacial

material, which is within the size range of cohesive sediment (< 63 μm), but may be unreactive.

The transition between non-cohesive and cohesive sediment is arbitrarily set at a diameter of 63 μm (Wentworth, 1922), with particles less than 63 μm considered cohesive, and those greater than 63 μm considered non-cohesive. Non-cohesive sediments are composed mainly of sands and gravels (> 63 μm), while cohesive sediments are composed mainly of silt (2 – 63 μm), and clay (< 2 μm) particles (Hayter, 1983), and organic matter (animal and plant detritus & bacteria) when available.

Despite making up the majority of sea shelf deposits (Jago & Jones, 2002), cohesive sediments are the least understood sediment fraction (Milligan & Hill, 1998; Black, et al., 2002) due to their widely changing characteristics of size, density, mineral and biological composition, interaction with other particles and tendency to flocculate and break up over a range of differing timescales. Cohesive sediment can also be a valuable resource, with the cohesive clay and silt particles found on muddy flood plains and river deltas forming some of the most fertile regions in the world, showing that cohesive sediment can play a vital role in productive ecosystems (Junk, et al., 1989; Tockner & Stanford, 2002; Winterwerp & van Kesteren, 2004).

3.2.4 Components of SPM

There are three main components which make up SPM: a background component, particles resuspended from the bed, and those advected into the area of interest. These three components are considered separately below, with the resuspension component subdivided into resuspension resulting from tidal forces, and that resulting from wave action.

Background

The background component of SPM contains microplankton, organo-minerals as fine-grained individual particles, and very small microflocs (Jago & Jones, 1998). These particles advect at the will of the prevailing currents and are so small, with settling velocities so low, that they are considered permanently in suspension (Bunt, et al., 1999; Jago & Bull, 2000). The background concentration can be difficult to determine as it may be time varying

(Sanford & Halka, 1993; Fugate & Friedrichs, 2002), and the slack water minima which are often used for determining the background level may be unequal (Jago and Jones (1998)). An inaccurately determined background concentration could also result from the use of filtered SPM samples in a flocculating environment as these filtered samples are unable to resolve the natural floc sizes as they appear to the instruments and therefore ignore the impact of floc size on instrument response (Bunt, et al., 1999).

Particle suspension

Sediment transport can be broadly separated into two components: bedload and suspended load. In bedload transport, particles remain in constant contact with the seabed – they slide, or roll. Suspended transport involves the movement of particles not in constant contact with the seabed – particles are lifted into the water column, travel some horizontal distance, before sinking back to the seabed. In-between these two states, saltation occurs in which particles "hop" into the water column before quickly returning to the sea bed. These particles are neither in constant contact with the bed, nor are they regarded as being in suspension (Grove, 1914). Despite not being in constant contact with the bed, this process is commonly classified as bedload transport.

The mechanism of transport is dependent upon the Rouse number (Eq. (3.1) in which w_s is the settling velocity), which relies upon the u_* (Eq. (2.30)): W_s ratio. Four transport regions exist dependent upon this ratio (Fryirs & Brierley, 2013; Hearn, 2008):

- Ro > 2.5 – Bed load transport dominates
- 1.2 < Ro < 2.5 – 50% of load suspended
- 0.8 < Ro < 1.2 – 100% of load suspended
- Ro < 0.8 – Wash load (particles move towards, and remain close to, the surface)

$$Ro = \frac{w_s}{\kappa u_*} \tag{3.1}$$

Suspension is the result of bottom stresses (due to waves or currents – tidal or residual) interacting with eroded particles on the sea bed and lifting them into the water column when these stresses exceed a critical value. For a particle to be suspended, the vertical component of turbulence must be greater than the particle settling velocity. In non-

cohesive sediments, the smallest particles (with the lowest settling velocities) are the first to move into suspension since they require the smallest vertical component of turbulence to overcome their low settling velocities (Bagnold, 1966), however, this is not always true of cohesive material, since the attractive forces between these particles means their threshold of erosion and suspension is often higher than that of similarly sized non-cohesive sediments due to the effects of particle cohesion (Mitchener & Torfs, 1996).

Factors affecting particle resuspension

1. Bed roughness

Sediment properties, including bed roughness, settling velocities and composition and hydrodynamic factors such as water column structure, tides, waves and currents also impact upon particle suspension (Jago & Jones, 1998). Near-bed flow interaction with bed roughness may enhance bed shear stresses, and therefore increase resuspension and, under conditions where bedforms may develop (where bedforms are defined as "a regularly repeated pattern [of sediment] which forms on a solid surface because of the shearing action of a fluid" (Wilson, 1972)), lead to bedform creation. The creation of bedforms can alter the bed roughness (Sherman & Greenwood, 1984), resulting in a feedback mechanism that changes the bedforms until equilibrium is established (which may take many hours (Baas, 2006)).

Bioturbation by benthic organisms can increase bed roughness. Re-working the top few centimetres of the sea bed can increase roughness by up to 400 times (Rhoads & Boyer, 1982) through the presence of burrows and excavation mounds (Howarth, 1998). However, an increase in roughness does not always increase erosion. The growth of algal and cyanobacterial mats and benthic diatoms on the seabed may increase roughness but have a stabilizing effect on the sediment (Neumann, et al., 1970; Holland, et al., 1974; Wright, et al., 1997; Karleskint Jr, et al., 2006) increasing the threshold shear stress required for erosion. The presence of diatoms may also decrease surface roughness (Lindahl, 1983). This is particularly prevalent in intertidal regions, where diatoms migrate through the surface sediments and fill the interstitial spaces with sticky polysaccharide substances (Paterson, 1989). Likewise,

polysaccharides secreted by various benthic organisms can reduce erodability (Sanford, 2008).

An increase in bed roughness may occasionally lead to a decrease in sediment resuspension. In situations where fine material is winnowed from a mixed, sandy bed by preferential suspension and transport, an upper layer of coarser sand grains is created, and roughness increases. This creates an “armour” layer of coarse, non-suspending grains above a mixture of coarse and finer particles. In this scenario, though bed roughness increases, suspension declines (Velegrakis, et al., 1997).

2. Biological activity

Sticky, organic, transparent exopolymers (TEP’s) such as carbohydrate-based polysaccharides play a key role in the stabilisation of bed sediment through sediment binding and biofilm formation, which can bind sediment together and prevent resuspension, despite being difficult to measure quantitatively in natural systems. Polysaccharides can be associated with a specific particle, or exist as a dispersed slime with no particular association to any one cell. In addition, polysaccharides can occur in both a particular or colloidal form dependent upon particle association (Decho, 1990), with colloidal polysaccharides often classified as part of the dissolved organic matter (DOM) as they pass through a 0.5 μm filter (Burney, 1986). These mucus-like substances are secreted by a variety of microbial flora and fauna throughout the marine environment (Rosen & Cornford, 1971), with studies showing that virtually all bacterial cells growing on marine sediments, detrital particles and flocs are surrounded by an extracellular layer of polysaccharides of varying thickness (Costerton, 1984).

Biofilms form on most submerged surfaces in the ocean such as water pipes, rocks and detritus. The environments of these surfaces often contain structured populations of microorganisms that are different from those within the water column and are embedded in a polysaccharide slime matrix generated by microalgae (when present) and bacteria which have the capability to alter the nutrient and physiochemical conditions present (Decho, 1990). Certain forms of polysaccharide that may form as part of a biofilm can remain across timescales of weeks if released

into the water column owing to their resistance to bacterial degradation (Engel, et al., 2004).

3. Atmospheric conditions

Temperature and precipitation may constrain the availability of material for resuspension as the shear strength of intertidal sediment may be affected by atmospheric effects, in addition to tidal controls such as exposure time (Amos, et al., 1988). Increases in air temperature between winter and summer, along with a concurrent decrease in precipitation levels can result in a change to surface mudflat sediments during exposure (Anderson & Howell, 1984), and these changes have been shown to increase the shear strength of the surface sediment by up to a factor of ten between winter and summer (Amos, et al., 1988).

Erosion and deposition

Erosion of bed sediment takes place once a critical bed shear stress is exceeded (C_e – Hayter and Mehta (1986)), with the erosion rate dependent upon the magnitude of the excess stress above this critical value. Classically, erosion has been thought to occur when the time-mean bed shear stress exceeds this critical threshold, however some experiments (e.g. Lavelle et al. (1984), Paintal (1971)) have shown that transport may occur under turbulent flow conditions irrespective of the time-mean bed shear stress, since the instantaneous turbulent stresses may be sufficient to initiate motion even if the time-mean bed stress is not (Lavelle & Mofjeld, 1987). The critical threshold for erosion may therefore be subjective, with erosion defined as having occurred once a certain level of transport is reached, a certain number of particles are in motion, or a certain rate of erosion is occurring since there is no consensus on what constitutes sediment transport (Lavelle, et al., 1984). It should be noted that a critical shear stress for the resuspension of particles will still exist, and that this lack of critical stress for erosion applies only to the initiation of motion.

Deposition may be continuous, or may take place only when the shear stress falls below a critical value for deposition (C_d), in what is a contentious subject within sediment transport (Sanford & Halka, 1993). When the bed shear stress (τ_b) exceeds this value, all sediment will remain in suspension; however, flocculation may increase the size of particles, increasing

the critical shear stress required to keep the particles in suspension, and enabling them to settle (Berlamont, et al., 1993). Erosion and deposition were widely regarded as mutually exclusive processes (Krone, 1962), making it possible therefore for the shear stress required to erode the bed to be larger than that required to keep all of the particles in suspension. This gives rise to an intermediate range of shear stresses for which neither deposition nor erosion occur (Sanford & Halka, 1993; Manning, et al., 2011). With erosion and deposition being mutually exclusive processes, it may also be possible for a regime to exist in which both erosion and deposition occur simultaneously. However, this paradigm of mutual exclusiveness has been challenged, with several papers arguing that it cannot be supported through any physical explanations or by model-data comparisons (Sanford & Halka, 1993; Winterwerp & van Kesteren, 2004; Amoudry & Souza, 2011), and therefore simultaneous erosion and deposition may not occur in the natural environment. In the classical approach, four scenarios are possible:

- Erosion ($C_d > \tau_b > C_e$)
- Neither erosion nor deposition ($C_d < \tau_b < C_e$)
- Settling ($C_d > \tau_b$, $C_e > \tau_b$)
- Both erosion and deposition ($C_e < \tau_b < C_d$)

For non-cohesive sediments, the critical stress for deposition (C_d) may be equal to, or greater than, the critical stress for erosion (C_e), and erosion and deposition may occur simultaneously, while a situation in which neither deposition nor erosion occurs does not exist (van der Perk, 2006). For cohesive sediments, the critical stress for erosion (C_e) is larger than that for deposition (C_d) and deposition and erosion may not occur simultaneously (Parchure & Mehta, 1995; Li & Amos, 2001).

Causes of resuspension

1. Tides

   Tidal currents exert shear stresses on the sea bed, and, if the necessary thresholds are exceeded, erosion and resuspension occur (Bagnold, 1966). Shear stress is proportional to the square of the velocity (Dyer, 1986) and therefore changes over the course of the spring-neap cycle. Peak current velocities are lower on neaps than

spring tides (Lindsay, et al., 1996), and these lower velocities may result in the accumulation of material on the sea bed during the transition from spring to neap tides as particles and flocs settle during each slack water, but not all are resuspended due to the decrease in peak shear stress as the tidal range decreases. Deposited material that is not re-entrained may undergo consolidation due to further sediment settling on top causing overburden, crushing the flocs below, combined with thixotropic effects (the rearrangement of deposited material caused by unbalanced internal stresses and internal energy (Hayter & Mehta, 1986)), making the material harder to erode (Hayter & Mehta, 1986; Ziegler & Lick, 1988). Conversely, as the tidal cycle progresses from neaps to springs, velocity and shear stress increase, causing resuspension to increase (in some areas 3 times more material is suspended during springs than during neaps (Velegrakis, et al., 1997)), provided sufficient material is available (Buchan, et al., 1967). Once the surface material is suspended, erosion of the recently deposited and partially consolidated portion of the bed deposited during the transition between spring and neap tides may take place. However, the higher shear stresses required to erode this partially consolidated material may mean not all of the material is eroded, and, if this sediment survives successive spring-neap cycles, a new sediment layer is formed (Clarke & Elliot, 1998). This process affects regions in which the peak bed shear stresses during the transition from spring to neap tides are insufficient to resuspend all of the recently deposited material, and is therefore more likely to occur in tidal flat regions than in estuary channels.

2. Waves

In shallow shelf areas (< 60 m), where wave effects may reach the seabed, high SPM concentrations often occur due to surface waves interacting with tidal currents and creating high bottom stresses, resulting in resuspension (Souza, et al., 2001) as waves can increase bed shear stress by several orders of magnitude (in comparison to currents), resulting in both the breakup of flocs (Agrawal & Traykovski, 2001; Hill, et al., 2001; Winterwerp, 2002) and the resuspension of material from the bed. Due to these instantaneously high shear stresses, waves in certain areas may have a greater impact upon SPM resuspension than tidal currents (Krivtsov, et al., 2009),

however, this is not anticipated to be the case in the mouth of the Dee Estuary due to the relatively sheltered nature of the site and small wave heights experienced in comparison to the water depth (Bolanos & Souza, 2010).

The size of a wave is determined by the wind intensity across the water surface, fetch distance, and water depth along the fetch. These determine the wave height, wave length and wave period, which, along with the water depth, determines the shear stress that a wave exerts upon the sea bed, with larger waves having a greater impact (Dean & Darymple, 1991). It is possible to calculate an approximation for the bottom wave orbital velocities (u_w) at the seabed from measurements of H_s (significant wave height) and T_p (wave period) from simple linear wave theory.

Firstly, the radian frequency, ω, is calculated through:

$$\omega = 2\pi/T_p \tag{3.2}$$

and this is used to formulate an initial estimation of the wave number, k, using:

$$\mathrm{k} = \omega/\mathrm{g} \tag{3.3}$$

As k is found twice in the dispersion equation (Eq. (3.4)), the dispersion equation and the derivative thereof can be used to calculate k iteratively until the values converge.

$$\omega^2 = \mathrm{gktanh(kh)} \tag{3.4}$$

This allows u_w to be calculated using the method of Soulsby (1997):

$$u_w = \frac{\pi H_s}{T_p \sinh(kh)} \tag{3.5}$$

As this technique assumes a frictionless bed, the bottom wave orbital velocities are, in reality, likely to be lower than the values calculated.

Storms can significantly enhance wave action; with SPM concentrations increasing by in excess of twenty times during storm events, particularly during times of weak tidal currents (Mehta, 1988). Sediment consolidation and proximity to previous resuspension events are also important in determining the amount of sediment resuspended from the bed due to wave action (Sanford, et al., 1991).

If concentrations reach high levels, drag reduction in the boundary layer may suppress turbulence, preventing further resuspension (Gust & Walger, 1976; Jago, et al., 1993). Amos et al. (1992) found that under a constant mean velocity, the friction velocity (Eq. (2.30)) may decrease by up to 10% as a concentration of clay particles increases to 200 mgl^{-1}. In this instance, waves do not enhance resuspension, but rather act to suppress deposition (Jago & Jones, 1998). Wave energy can penetrate the resuspended layer, causing turbulent motions, and maintaining the suspension of particles, but may not apply sufficient stress to the bed for further resuspension to occur. This process is site specific, and dependent upon the local critical shear stress for erosion (C_e), and that for deposition (C_d) (Parchure & Mehta, 1995).

Advection

Advection is a mechanism by which a conserved property or substance (e.g. SPM) is transported by the bulk motion of a fluid (Islam & Chaudry, 1997), and may therefore occur at any time while water is moving, potentially resulting in material entering or exiting an estuary. Suspended material within an estuary may be advected distances of up to several kilometers (Weekes, et al., 1993; Eggleston, et al., 1998; Jago & Jones, 2002) dependent upon the tidal excursion of the estuary. A horizontal concentration gradient may result from the advection of material (Jago & Bull, 2000), with diffusion and settling during transport reducing concentration levels with distance away from the source of material.

3.2.5 Sediment transport

Non-cohesive sediments

For non-cohesive sediments, the vertical concentration can be approximated as a Rouse profile, since concentration generally decreases with distance away from the bed (Burchard, et al., 2008):

$$\frac{C}{Ca} = \left[\frac{h-z}{h-h_r} \times \frac{h_r}{z}\right]^{W_s/\iota\kappa u_*} \tag{3.6}$$

in which C is concentration at height z, Ca a reference concentration at some depth (h_r), and ι a constant correlating eddy viscosity to eddy diffusivity (usually equal to 1).

The sediment flux is then controlled by the sediment concentration multiplied by the flow velocity, and thus integrating the current velocity (u) multiplied by the Rouse profile (c – Eq. (3.6)) from the bed (b) to the surface (h) plus a constant (e) provides the sediment flux (q):

$$q = \int_b^h uc \ \delta z + e \tag{3.7}$$

This is illustrated in Fig. 3.1, which shows that despite the highest concentrations being found at the seabed, the highest flux is often found higher up in the water column due to the sheared nature of the velocity profile close to the bed.

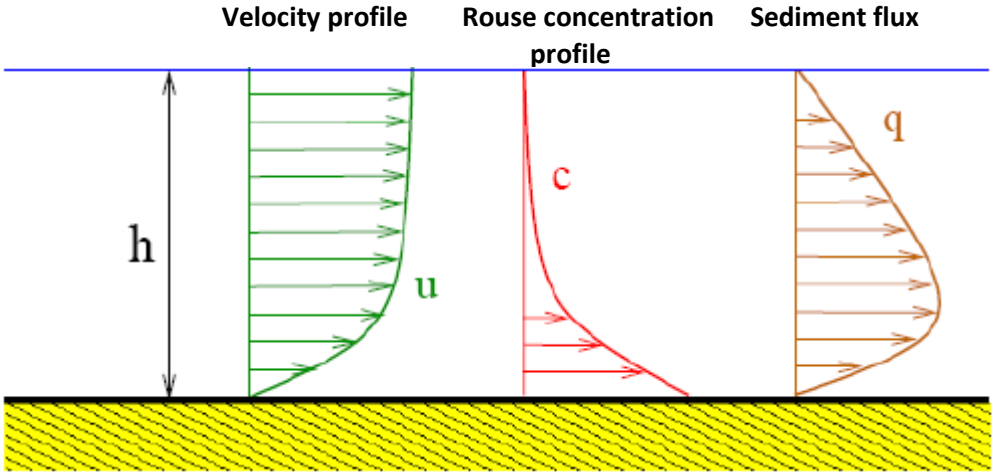

Fig. 3.1: Sediment flux calculated from the integral of the velocity profile multiplied by the concentration profile. Modified from Lund University, Sweden

Cohesive sediments

The Rouse profile has been applied to cohesive sediment (Agrawal & Pottsmith, 1994; Friedrichs, et al., 2008; Sanford, 2008), however, the concentration profile of suspended cohesive sediment includes complex processes such as flocculation and breakup, consolidation of the seabed whereby the required erosional shear stress increases down the sediment profile, the possible presence of a critical shear stress for deposition and, potentially, the liquefaction of the sea bed and the formation of fluid mud layers. Within estuarine regions, the potential effects of salinity stratification also need to be taken into account (Maa & Kwon, 2007) and therefore the Rouse profile is likely to be inaccurate.

The settling velocities for flocs tend to be smaller than those of equivalently sized sand particles, and because of this the concentration of cohesive sediments tends to be more uniform through the water depth, react slower to changes in current speeds, and be more susceptible to advection (Whitehouse, et al., 2000). Nevertheless, attempts have been made to parameterize the vertical cohesive sediment profile. Two such equations are those given by Soulsby (2000):

$$\frac{M_c}{C_b} = \left[1 + B\left(\frac{z}{h}\right)\right]^{-\frac{1}{m}} \tag{3.8}$$

in which $B = \frac{mw_{50b}}{0.0025\bar{u}}$, z is height above bed, M_c is the dry mass concentration at height z, C_b is the dry mass concentration of suspended mud immediately above the bed, w_{50b} is the median settling velocity of sediment immediately above the bed, h is water depth, and m is the mass of sediment eroded per unit area, and:

$$\frac{M_c}{C_b} = 1 - \frac{(R_c - 1)}{R_c}\frac{z}{h} \tag{3.9}$$

in which R_c is the ratio of the concentration in the near-bed region to the concentration in the near-surface region and it is assumed that concentration varies linearly with height above the bed. These formulae give an approximation of the sediment profile, however, neither is capable of taking salinity stratification into account, and are therefore less applicable to estuarine environments.

3.2.6 Vertical distribution of SPM

SPM is denser than water, and will therefore sink over a sufficiently long time period under quiescent conditions. The impact of SPM on the water column is dependent upon the method of sediment transport, which is determined by the Rouse number (see Section 3.2.4). Where the Rouse Number is small (< 1.2), suspended load transport dominates, and as the Rouse number decreases further, the tendency is for sediment to be mixed higher into the water column. Where the Rouse Number is large (> 2.5), bedload transport dominates, and therefore the tendency is for SPM within the water column to settle.

SPM impact upon the bottom boundary layer

The impact of SPM upon the bottom boundary layer is threefold:

1. Where SPM decreases with height above the bed, this has a stabilising effect on bottom boundary layer buoyancy, affecting both shear and turbulence in a similar way to thermohaline stratification (Souza & Friedrichs, 2005). Conversely, if SPM concentration increases with height above the bed, this can cause unstable stratification. Stratification effects can be site specific, and depth-varying, as in places only the upper part of the profile may be stratified (Whitehouse, 1995). The effects generally increase with flow speed, as the increase in concentration is greater than the increase in mixing, and are most effective with fine and very fine sand and coarse silt (Soulsby & Wainwright, 1987).
2. High concentrations of SPM adjacent to the bed cause stratification, suppressing near-bed turbulence and dampening vertical mixing. Even fine sediment in moderate concentrations (e.g. 1200 mgl^{-1} – Gross and Dade (1991)) can constrain the thickness of, and change velocity profiles within, the bottom boundary layer (Souza & Friedrichs, 2005; Baas, et al., 2009).
3. SPM adds density to the water body, and, just like temperature or salinity gradients, can create horizontal or vertical gradients that drive baroclinic flows. In regions of significant slope, (generally > 0.02° for currents to be self-accelerating) additional resuspension can be caused by this gravity current passing over the sediment-water interface, allowing the flow to be self-sustaining.

Impact of stratification

In strongly stratified waters, the presence of stratification may prevent resuspended particles from reaching the upper water column (Souza, et al., 2007). Water above the pycnocline becomes clearer than below as material sinks out of the upper layer, allowing light to penetrate deeper into nutrient-rich waters below. This may stimulate phytoplankton growth (Jago, et al., 1993), with 30-80% of euphotic plankton production in the coastal shelf seas occurring in the thermocline region, where the combination of light and nutrient abundance are able to fuel rapid and prolonged growth (Jago & Jones, 2002).

The vertical flux of SPM is considered to be dependent upon bed shear stress (resulting from currents, waves, or a combination of the two), which causes vertical mixing, and settling due to gravity, while the particles themselves are subject to other physical, biological and geological processes which can affect the settling velocities and size distributions of the SPM (Souza, et al., 2001).

The advection-dispersion equation

Sediment, in the context of sediment transport within estuaries, can be regarded as a conservative property in a similar way to both energy and momentum. Because of this, it is possible to define a continuity equation, known as the advection-dispersion equation, through the principal of the conservation of mass, to describe the spatial and temporal variations in sediment concentration, and the rate of sedimentation in an environment in which sediment transport is taking place.

The three-dimensional sediment dispersion equation can be written as:

$$\frac{\partial C}{\partial t} + u\frac{\partial C}{\partial x} + v\frac{\partial C}{\partial y} + (w - W_s)\frac{\partial C}{\partial z} = \frac{\partial}{\partial x}\left(e_x\frac{\partial C}{\partial x}\right) + \frac{\partial}{\partial y}\left(e_y\frac{\partial C}{\partial y}\right) + \frac{\partial}{\partial z}\left(e_z\frac{\partial C}{\partial z}\right) + E - G \quad (3.10)$$

in which C is sediment concentration, t time, u the along-channel velocity, v the across-channel velocity, e_i eddy diffusivity in the i direction, z height above bed, w the vertical velocity, W_s the sediment settling velocity, E represents erosion of the sea bed, and G deposition to the sea bed. The rate of change in sediment concentration – shown here as $\frac{\partial C}{\partial t}$ – is controlled by several factors: the settling of the sediment – represented by $(w - W_s)\frac{\partial C}{\partial z}$, advection – represented by $u\frac{\partial C}{\partial x} + v\frac{\partial C}{\partial y}$ and causing translation of the sediment in the water column with the flow velocity, dispersion – represented by $\frac{\partial}{\partial x}\left(e_x\frac{\partial C}{\partial x}\right) + \frac{\partial}{\partial y}\left(e_y\frac{\partial C}{\partial y}\right) + \frac{\partial}{\partial z}\left(e_z\frac{\partial C}{\partial z}\right)$ and causing the "spreading" of sediment within the water column, and E and G, the difference between which indicates whether sediment is being added to, or removed from, the system. The rate of change in the mass of sediment over time is equal to the rate of change in mass due to advection by the flow plus the rate of change in mass due to dispersion and diffusion, plus erosion, minus deposition. It is implicit within this equation

that material in suspension is advected in the x and y directions at the u and v water velocity components – a reasonable assumption for suspended sediment.

3.2.7 Sinks

The primary sinks of SPM are burial and re-mineralisation. Re-mineralisation principally affects organic matter, with bacterial colonies growing on particles and breaking them into smaller pieces (Jones, et al., 1998). This can occur to such an extent that particles join the background element of SPM (Jago & Jones, 1998), becoming so small, with settling velocities so low, that they are considered in permanent suspension.

Burial of material occurs through settling to the sea bed, with further settling on top resulting in compaction and the formation of a new sediment layer, as discussed previously in Section 3.2.4.

The advection of material away from the area of interest may not be a sink in the truest sense, since material may remain suspended in the water column. However, it may be considered a sink in the context of moving sediment away from a region of interest.

3.3 Flocculation

3.3.1 Definition of a floc

The Oxford English Dictionary defines a floc as “a loosely clumped mass of fine particles.” More specifically, a floc can be defined as “an aggregate with a complex random structure with low average density” (Meakin, 1989), which has resulted from flocculation within an aquatic medium (Droppo, 2000). Flocs are naturally cohesive and adhesive collections of mineral, and usually but not always, organic, matter, in a loosely bonded, porous state (Jago, et al., 2006). Flocs vary from small, quasi-spherical, compact structures to large, complex, multi-cored, loosely connected structures (Graham & Nimmo-Smith, 2010) in which up to 90-95% of the floc may be composed of water-filled pores (Manning & Bass, 2006). Flocs are held together by van der Waals forces and chemical ionic bonding (Manning, et al., 2006), but are susceptible to the impacts of biological substances such as polysaccharides, which may increase the bond strength of flocs (Eisma, 1986). Flocs are

prone to change over short time-scales (Gibbs, et al., 1989) as they can be affected by small hydrodynamic or biological fluctuations due to their fragile nature.

3.3.2 Floc formation

Clay mineral particles are naturally negatively charged due to cation substitutions within the particle lattice, wherein for example an Al^{3+} is substituted by an Mg^{2+}, leaving a -1 net negative charge across the clay particle in a process known as isomorphous substitution. Numerous cation substitutions may occur to a single clay particle, resulting in a strongly negative charge across the particle. As non-saline water is low in cations, this negative charge causes particles to repel each other whilst in fresh water, preventing flocculation (Dyer, 1986; Lintern, 2003), as illustrated in Fig. 3.2. The first panel shows clay particles in freshwater, with the negative charge illustrated by the surrounding circle. Particles repel due to their net negative charge. When the particles reach the saline environment of the estuary, mixing of the water masses (shown in panel two) results in the removal of the negative charge (panel three) due to the presence of abundant cations in the saline environment. After the removal of the negative charge, the particles flocculate under low-turbulence conditions (panel four – low turbulence conditions are indicated by the few white spirals) due to van der Waals forces in addition to the processes of both cohesion and adhesion (Edzwald & O'Melia, 1975). Flocs may also contain organic matter (green dots) if it is present in the system. Complete removal of the negative charge can occur in salinities as low as 5 PSU. For this reason, the upper reaches of estuaries tend to be regions of high flocculation. This process is reversible, and under high turbulence conditions (panel five – high turbulence is indicated by the abundant white spirals), flocs may be broken up. Flocculation may occur in freshwater regions if the biological component of the flocs is sufficiently adhesive to overcome the electrostatic repulsion of the particles, or flocs may be entirely biological in origin.

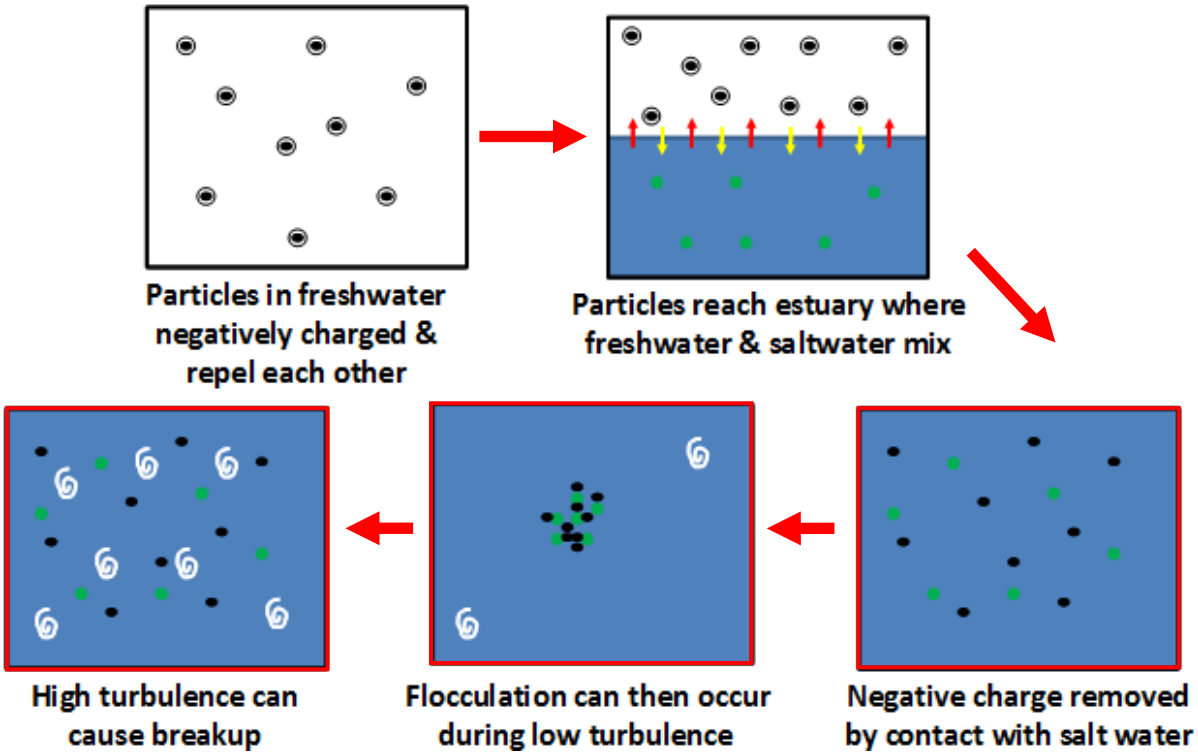

Fig. 3.2 – The process of flocculation in an estuary through the removal of the negative charge on the clay lattice

Benthic Fluff

Plankton, organic detritus, river-borne and marine sediments may combine in estuary regions to form a low density, high carbon, fluff-like deposit on the seabed (Jago, et al., 2002). This layer forms a major pathway for the flux of carbon from pelagic to benthic habitats, and can play a key role in the biogeochemical reactions that take place on the sea bed (Jago, et al., 1993). The low shear strength of benthic fluff means it is easily resuspended from the sea bed by tidal currents in shallow sea regions (Jago & Jones, 1998). It is believed that much of the SPM encountered in the Dee Estuary will be the product of this benthic fluff layer rather than erosion of the sea bed substrate.

Towards the estuary mouth, where the tidal variations in salinity are lower, turbulence and biogeochemical processes become the controlling factors on flocculation (Kranck & Milligan, 1988; Winterwerp, 1998; Manning, 2004; Verney, et al., 2009). Low levels of turbulence bring particles together, forming flocs, while higher levels result in rupture and breakup.

These processes are mediated by biological activity. It is in this region (indicated by the red boxes in Fig. 3.2) that the present study is primarily centred.

Flocs grow as more material is added to them. In addition to larger, more "obvious" particles, particles so small they were considered in permanent suspension may be scavenged and added to flocs (Krivtsov, et al., 2001). The effective density (bulk density minus density of contained water) reduces as flocs grow (Tambo & Watanabe, 1979), while the settling velocity increases, as shown in Fig. 3.3. Floc strength also generally decreases with increasing size, as less particle contacts are present (Dyer & Manning, 1999).

3.3.3 Floc classification

Flocs are commonly split into two classes based upon their diameter: microflocs (< 160 μm) and macroflocs (> 160 μm), based on Dyer and Manning (1999), and endorsed by Winterwerp et al. (2006), although the irregular shapes of flocs often makes an accurate diameter difficult to quantify. Although a value of 160 μm is used as the boundary between micro and macrofloc populations, in reality the transition occurs as a gradual change in floc characteristics. Primary floc forming particles are considered to be order 0 flocs, while each floc of order 1 or above is constructed of lower order flocs (Winterwerp, 1998), with microflocs defined as order 1, and macroflocs as unstable flocs of order 2 or higher (van Leussen, 1994).

Microflocs are small, quasi-spherical, dense and strong, being able to withstand turbulent eddies up to the size of the Kolmogorov length scale (van Leussen, 1997; Bowers, et al., 2007; van der Lee, et al., 2009; Verney, et al., 2011; Braithwaite, et al., 2012), and possibly beyond (Cross, et al., 2013). By contrast, macroflocs are larger, less dense, weaker, come in a wide variety of shapes and rupture under high turbulence conditions into constituent microflocs and individual particles (Dyer & Manning, 1999). Despite their fragile nature, the settling of macroflocs is the principal way through which very fine-grained particles reach the sea bed (Mikkelsen, et al., 2005). The maximum attainable floc size within a system is related to the Kolmogorov length scale (Eq. (2.24) – Kolmogorov (1991)), as at sizes greater than the size of the smallest turbulent eddies shear across the velocity gradient breaks the floc apart. However, recent data shows that flocs may, under certain conditions, exceed the

Kolmogorov lengthscale (Cross, et al., 2013). Macroflocs, due to their weak nature may break up before reaching the size of the Kolmogorov lengthscale. Dependent upon the conditions experienced at a site, the breakdown of macroflocs may result in two differing microfloc species: A species of higher density and higher settling velocity with a lower organic content, and a second species of lower density, lower settling velocity, and a higher organic content (Dyer & Manning, 1999).

The fragile nature of flocs makes physical sampling difficult (Baugh & Manning, 2007), and therefore non-intrusive measurement methods must be used. This often involves utilizing instruments such as the LISST which is considered within the present study.

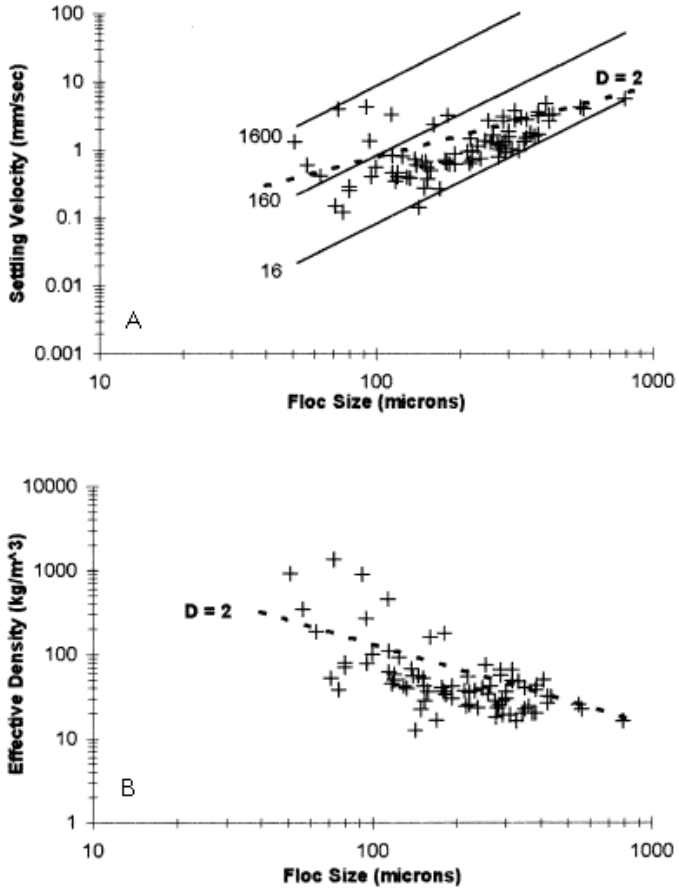

Fig. 3.3 – As floc size increases, settling velocity also increases (A), despite effective density decreasing (B). Solid lines in the top graph indicate effective density, dashed line indicates a fractal dimension of 2 (Dyer & Manning, 1999)

3.3.4 Flocculation mechanisms

There are three principal methods through which flocculation occurs within the water column:

i) Brownian motion (Perikinetic flocculation)

Moving water molecules resulting from small variations in thermal energy within a flow (Einstein, 1905) cause fluid shear, making SPM move in an apparently random manner (Kac, 1947), which results in collisions between suspended particles (Lick, et al., 1993). If these collisions have sufficient energy or particles have a sticky coating, flocculation occurs. This form of flocculation is almost entirely absent in estuaries, except for during short periods at slack water, due to the high current speeds and shear effects present in these regions (Maggi, et al., 2007).

ii) Differential settling

Large, low density flocs may settle faster than smaller, denser, individual particles, resulting in collisions (Winterwerp, 2002). Collisions of this nature should occur mainly around the pycnocline since SPM concentrations are elevated in this region (Fugate & Friedrichs, 2003). However, Stolzenbach and Elimelich (1994) showed that large, low-density, rapidly falling particles do not often collide with smaller particles as the small particle trajectory is deflected around that of the larger particle. The space between particles reduces upon approach, as the intermediate fluid is removed. This sideways fluid movement causes approaching particles to rotate relative to one another, resulting in non-linear curvilinear collisions (Thomas, et al., 1999). As such, differential settling collisions occur most frequently when particles are the same size (Adler, 1981). As the Dee Estuary is a well-mixed, high turbulence environment for most of the tidal cycle, the effects of differential settling in this region are negligible.

iii) Shear effects (Orthokinetic flocculation)

Turbulence and velocity gradients enhance particle collisions and flocculation rates by bringing particles together in an energetic fashion, up to the point at which flocculation transitions to floc rupture and breakup. Shear induced flocculation rates are therefore

primarily controlled by particle concentration and turbulent shear (Ives, 1977). This tends to result in relatively strong, quasi-spherical flocs, particularly in estuarine environments (Edzwald & O'Melia, 1975). Although a large amount of particle collisions occur, only a small percentage result in flocculation (Dyer & Manning, 1999), and as such, shear-induced flocculation within the water column is a highly inefficient process.

Aggregates

Aggregates of particles may also enter the water column through the erosion and suspension of partially consolidated pieces of the sea bed (Mehta & Partheniades, 1982), or though the excretion of silt and clay particles combined with organic material in the form of the fecal pellets of biological organisms (Edelvang & Austen, 1997). Although not flocs, they often share characteristics as both are formed from collections of particles.

3.3.5 Controls on flocculation

Biological Controls

Biological activity, such as the production of polysaccharide substances, has been strongly linked to a wide range of marine processes including the formation of flocs (Eisma, 1986). These substances play a key role in both enhancing flocculation during the spring and autumn bloom periods (Riemann, 1989), and their impact on flocs are, by some, believed to be the most important enhancer of flocculation (Dyer, 1986). Diatoms (Verney, et al., 2009; Manning, et al., 2010; Spearman, et al., 2011), dinoflagellates and other forms of plankton may contribute to floc formation at the end of their growth phase (Jones, et al., 1998; Jago & Jones, 2002) as diatoms secrete sticky polysaccharide substances, causing small particles to stick to them through adhesion, while dinoflagellates, which do not produce polysaccharides, attach themselves to flocs by means of their ejectosomes, through fibrillar bridging or by means of their flagella (Jones, et al., 1998).

Concentrations of plankton such as diatoms and dinoflagellates, as well as the polysaccharides that some forms of plankton, bacteria and plants produce tend to follow a seasonal signal, with concentrations lowest during winter and highest during the spring and

autumn bloom periods (Eisma, 1986; Eisma, et al., 1991). This seasonal variation impacts the flocculation process as the production of polysaccharides may increase the collision efficiency (Gratiot & Manning, 2007), particle strength and size and therefore SPM flux to the seabed (Manning & Dyer, 2002) as settling velocity is proportional to floc size (Dyer & Manning, 1999). As faster settling sediment is less likely to be transported out of the estuary, this may increase the rate of infill of the estuary during times of abundant polysaccharide production.

Diatoms and other forms of plankton, as well as bacteria and plants may also act to stabilize the sediment of mudflats and other regions of estuaries in which they grow (Paterson, 1989; Winterwerp, 2011) through the production of polysaccharides and other chemicals. This process can have important consequences for flocculation within estuaries by reducing the amount of material available for resuspension, and, subsequently, impacting upon the horizontal concentration gradient.

Fluorescence may be used as a proxy for chlorophyll (Lorenzen, 1966), which is representative of photosynthetic activity and therefore the presence of plankton and other photosynthetic organisms. These forms of organism generally produce polysaccharides, and it therefore follows therefore that fluorescence may be used to infer the presence of polysaccharides. This is not a simple relationship since polysaccharides are secreted by plankton predominantly toward the end of their growth phase, but these particles will always produce a fluorescence response (Jones, et al., 1998; Jago & Jones, 2002). However, in the context of this study, it is assumed that an increase in fluorescence response, and therefore chlorophyll, should represent an increase in levels of polysaccharides between the pre- and post-spring bloom periods.

Effects of temperature

Small-scale fluctuations in temperature may result in flocculation through Brownian motion; however, in high shear regions such as the Dee Estuary, this flocculation method is almost entirely absent (see Section 3.3.4). In addition, experiments have shown that flocculation occurs slower and the equilibrium floc size reached is lower, under low temperature conditions. This is due to the effects of temperature on flocculation kinetics (Hanson & Cleasby, 1990; Lim-Seok & Cleasby, 1995) as temperature is able to affect both the viscosity

of the water and the rate of reaction within a system. In addition, Fitzpatrick, et al., (2004) reported that water temperature is able to impact upon floc size, strength and the ability to re-form following shear breakup, with higher temperatures generally producing larger, more easily ruptured flocs. Flocs should therefore be larger, weaker and more easily ruptured during the summer months.

Causes of floc breakup

Turbulence is a major control on floc breakup, acting to either bring particles together, forming flocs, or to break existing flocs apart (Winterwerp, 2002), as demonstrated in Fig. 3.4 which shows how floc diameter decreases as the turbulent shear rate increases. The level of turbulence required for this process is dependent upon floc strength, which is related to floc density and biological effects, with higher density flocs, or those made stronger through biological strengthening, requiring more energy to break up (Yeung & Pelton, 1996).

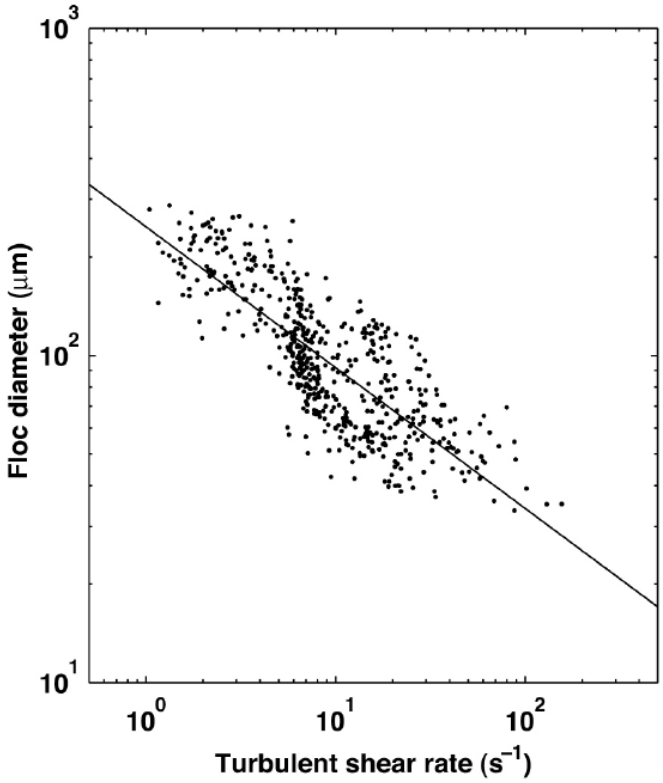

Fig. 3.4 – Floc diameter plotted against turbulent shear rate in the Dee Estuary showing how floc diameter decreases as the turbulent shear rate increases (Amoudry & Souza, 2011)

The processes of flocculation and breakup can affect the data gathered by both optical and acoustic instruments as instrument response can vary depending upon particle size, particle density and composition (Bunt, et al., 1999; Traykovski, et al., 2000). As an example, it was believed that advection under an asymmetrical tide created a unique signal in the SPM mass concentration (Fig. 3.5), termed the "twin peaks" signal by Jago and Jones (1998)), with stronger resuspension on either flood or ebb, in conjunction with a semi-diurnal advection signal, creating unequal slack water concentrations. However, more recent analysis has shown that this signal may also be caused by the breakup of flocs during high current velocities (Fig. 3.5) and that the transmissometer may overestimate the de-flocculated SPM concentrations due to its sensitivity to particle size (Bunt, et al., 1999). The asymmetric tide causes asymmetry in the turbulent shear and therefore greater floc breakup during one phase of the tide. Once current velocities decrease, turbulence reduces and flocculation occurs. The time available for flocculation is finite, and therefore flocs may be larger during one slack water due to less floc breakup occurring on one phase of the tide (due to tidal asymmetry). This asymmetry in floc breakup, and finite time available for floc formation results in uneven slack water particle sizes and contributes to the characteristic "twin peak" signal over the course of a full tidal cycle (Jago, et al., 2006). Using instruments such as the LISST can overcome this mis-identification as the LISST is able to provide a measure of particle size as well as volume concentration.

3.4 Settling

3.4.1 The Stokes settling velocity equation

Particles in still water eventually sink to the bottom under gravity provided that their density is greater than that of the water. For single, spherical particles, the settling velocity in still water is dependent upon the grain diameter, the viscosity of the fluid, gravity, and the difference in density between the fluid medium and the grain (Stokes, 1844; Hallermeier, 1981). The settling velocity of a particle (Eq. (3.11) in which D is the particle diameter, C_e an empirically derived coefficient and ρ_s particle density) is therefore calculated from the ratio of the immersed particle weight to the drag forces.

$$w_s = \frac{D^2}{18}\left(\frac{\rho_s - \rho_w}{\mu}\right) g \ (\equiv C_e D^2) \qquad (3.11)$$

This formula can be applied with small errors to quasi-spherical particles such as quartz grains, however, the settling velocities of cohesive sediments are more difficult to determine: particles are not uniform in shape or density, and tend to flocculate, which may change the size, shape, density (Hill, et al., 1998) and composition of the particles (Agrawal & Pottsmith, 2000). However, Stokes' law, or a modification thereof, has been used many times to determine the density, or settling velocity, of flocs (Yasumoto & Nambi, 1976; Tambo & Watanabe, 1979; Gibbs, 1985; Li & Ganczarczyk, 1987; Droppo, et al., 1997; Dyer & Manning, 1999; Sternberg, et al., 1999; Agrawal & Pottsmith, 2000; van der Lee, 2000; Mikkelsen & Perjup, 2001).

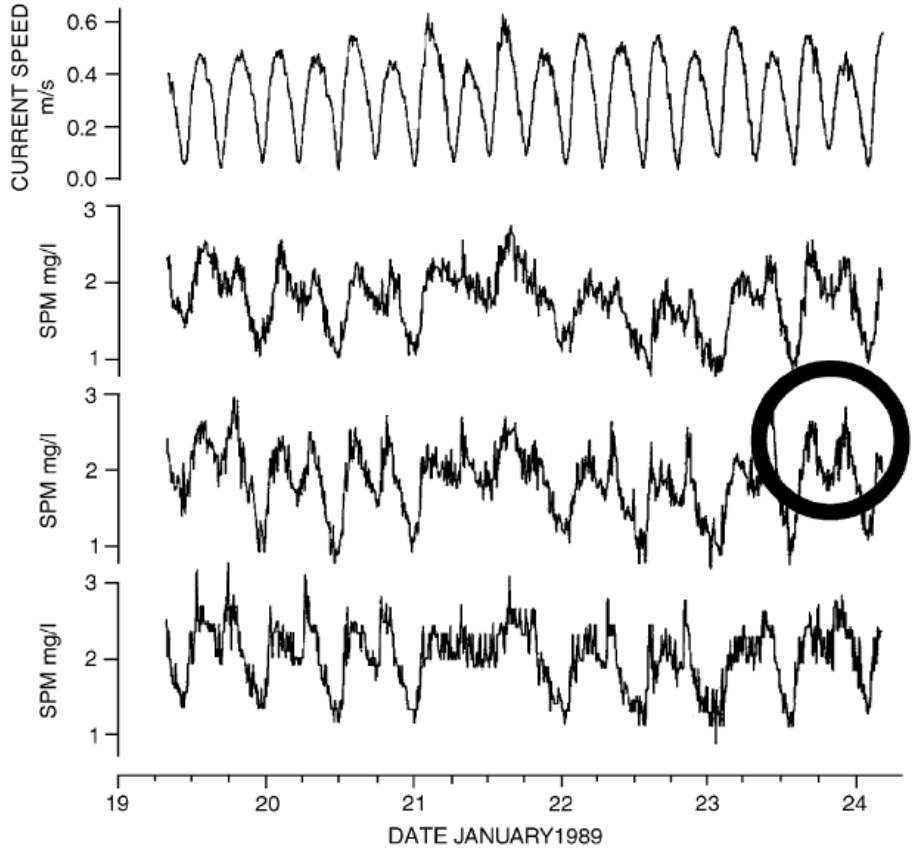

Fig. 3.5 – Time series showing current speed and transmissometer-derived SPM mass concentration at three heights above the seabed. The unequal mass concentration minima at successive slack waters display a "twin peak" signature. Black circle highlights the higher concentrations found during one slack water period. Reproduced from Jago & Jones, (1998)

3.4.2 Use of the Stokes equation

The use of the Stokes' settling velocity (Eq. (3.11)) as an approximation for the settling velocities of flocs reveals discrepancies in the published literature. Chase, (1977; 1979) showed that the Stokes' equation underestimates the settling velocities of flocs < 500 μm by up to an order of magnitude, while Kajihara, (1971) showed that the Stokes' equation underestimates the settling velocity for flocs of 100 – 1000 μm, though the results of both experiments showed that the difference between measurements and the Stokes' approximation decrease with increasing floc size.

The Stokes' settling velocity formulation was derived for a single, spherical particle settling in still water with a particle Reynolds number (Eq. (3.12)) << 1.

$$Re_p = \frac{DW_s}{\nu} \tag{3.12}$$

Settling velocity formulations for particles with a higher Re_p (i.e. that are not perfect spheres), including flocs, require a correction factor (Agrawal & Pottsmith, 2000). Two of the most commonly applied correction factors are those from Oseen (1927):

$$D_c = \frac{24}{Re_p}\left(1 + \frac{3}{16}Re_p\right) \tag{3.13}$$

which is valid for $0.5 < Re_p < 5$ (Graf, 1971), and Schiller-Naumann (1933):

$$D_c = \frac{24}{Re_p}\left(1 + 0.15{Re_p}^{0.687}\right) \tag{3.14}$$

which is valid for $Re_p < 800$.

The Stokes' formulation modified with the Schiller-Naumann drag coefficient is used in the flocculation models of Winterwerp, (1998; 2002). Applying these drag corrections allow the Stokes' settling velocity formulation to be used as an approximation for floc settling velocity (Ten Brinke, 1994; Fennessy, et al., 1994). However, Re_p cannot be used within the calculations since the calculation of Re_p includes the settling velocity. Re_{u*} is a modified version of Re_p (Eq. (3.12)) in which:

$$Re_{u*} = \frac{Du_*}{\nu} \tag{3.15}$$

u_* is defined in Eq. (2.30)). Re_{u*} is used within the flocculation models of Winterwerp, (1998; 2002).

3.4.3 Calculating settling velocities from fractal theory

The fractal dimension

It has been suggested that flocs are better represented as fractal entities (Kranenberg, 1994), D^{nf-1}, where D is the floc diameter and nf the fractal dimension (a function of water and sediment properties) as their shape reflects those of fractal objects (Winterwerp, 1998). This fractal nature is caused by the flocculation process, in which collisions increase the floc size and the resultant larger floc has a higher collision profile than a volume-equivalent spherical particle, enhancing collision rates. Due to the porosity of flocs fluid may penetrate the floc surface and this reduces the sideways fluid motion as particles approach each other (Kusters, et al., 1997), further increasing the size and settling velocity, and decreasing the effective density (Flesch, et al., 1999).

The floc fractal dimension usually varies between values of 1 and 3 dependent upon the nature of the floc (Kranenberg, 1994). The fractal dimension provides information about the floc, as it impacts upon the floc density (Kranenberg, 1994) and collision profile (Kusters, et al., 1997).

Calculating settling velocity using the fractal dimension

In a flocculating system flocs should display fractal growth and therefore it is possible to calculate settling velocities of flocs using measures of mass concentration (C_m), volume concentration (C_v), and particle size (D_{50}) based upon fractal theory (Kranenberg, 1994; Winterwerp, 1998), in which C_m, C_v, and D_{50} are related through:

$$C_m = \rho_s C_v \left(\frac{D_p}{D_{50}}\right)^{3-n_f} \tag{3.16}$$

in which ρ_s is the sediment density, D_p the primary particle diameter, and n_f the fractal dimension. Rearranging this equation provides a linear relationship:

$$C_m = \rho_s {D_p}^{3-n_f} \left(\frac{C_v}{{D_{50}}^{3-n_f}}\right) \tag{3.17}$$

which may be used in a least-squares regression to estimate n_f, assuming that it remains constant over the study period. Following this, the effective density of the suspension (ρ_e) can be calculated as:

$$\rho_e = (\rho_s - \rho_w)\left(\frac{D_p}{D_{50}}\right)^{3-n_f} \tag{3.18}$$

which rearranges into:

$$\frac{\rho_e}{{D_{50}}^{n_f-3}} = (\rho_s - \rho_w){D_p}^{3-n_f} = H \tag{3.19}$$

the left-side of which can be calculated using known values of C_m, C_v, D_{50} and n_f as:

$$\rho_e = \frac{C_m}{C_v} \tag{3.20}$$

Values of $\frac{\rho_e}{{D_{50}}^{n_f-3}}$ can be averaged for the dataset in question and used with the formulation of Winterwerp (1998) which includes the Stokes' settling velocity formulation modified with the Schiller-Naumann drag coefficient:

$$W_s = (\rho_s - \rho_w){D_p}^{3-n_f}{D_{50}}^{n_f-1}\left[\frac{g}{18\mu\left(1+0.15{Re_{u*}}^{0.687}\right)}\right] \tag{3.21}$$

which, after substitution with H (Eq. (3.19), becomes:

$$W_s = H{D_{50}}^{n_f-1}\left[\frac{g}{18\mu\left(1+0.15{Re_{u*}}^{0.687}\right)}\right] \tag{3.22}$$

3.4.4 Impacts of floc permeability on settling velocity

There is ongoing debate as to the impact of floc permeability on settling velocity. Highly porous flocs have been shown by Johnson, et al., (1996) to have significantly increased settling velocities. However, flocs with a fractal dimension greater than 2 (such as inorganic marine flocs) are not highly permeable (Gregory, 1997), and may therefore be treated as impermeable to the extent that the effects of flow through the floc structure can be ignored (Winterwerp & van Kesteren, 2004).

3.4.5 Use of settling columns

The use of settling columns is popular for determining particle settling velocity, with systems such as LabSFLOC (Manning, 2006) and PICS (Smith & Friedrichs, 2011) in use by different institutions as the fragile nature of flocs means non-intrusive settling velocity measurement methods are required. However, the reliability of measurements from settling columns varies with settling column type (Dyer, et al., 1996). Turbulence may be created around the ends of the settling column while open (Ten Brinke, 1994), within the settling column immediately after the closing of the ends, and during rotation of the settling column (Dearnaley, 1996; Smith & Friedrichs, 2011). When retrieving a sample for insertion into a settling column, or retrieving the settling column itself onto a boat or land, the sample may be affected by the motion of moving through the water column, or material may settle, and when the column is turned to the vertical form a density current which causes mixing, affecting the floc size distribution in suspension (Berlamont, et al., 1993; Dearnaley, 1996). Further disturbance can be caused by the pipetting of a sample into a settling column (Eisma, et al., 1991), return flows (Berlamont, et al., 1993), or differences in temperature between the air and water in the settling column (Dyer, et al., 1996), which can cause viscosity changes and set up convection currents (Dearnaley, 1996). Systems may be subject to one or more of these potential sources of error (Dyer, et al., 1996). In addition, flocs, unlike non-cohesive sediments, respond to environmental changes, and therefore flocs may begin to change immediately after removal from the natural environment, with the sample becoming progressively less representative of the environment from which it was extracted

over time (Dearnaley, 1996). Therefore, in-situ, none-intrusive methods of determining floc settling velocity are preferable.

3.4.6 Factors affecting settling velocities

Settling velocities are affected by floc growth, with large flocs settling up to an order of magnitude or more faster than individual grains (Syvitski & Murray, 1981), trapping sediment within estuaries (Geyer, et al., 2004) as particles fall out of suspension too fast to be transported out of the estuary during the ebb tide before being transported higher up the estuary on the flood tide and by the residual estuarine circulation. For this reason, SPM tends to have a high residence time in tidal estuaries, allowing extensive modification of the particles (Heip, et al., 1995).

Settling velocities can be modified through ingestion by organisms and conversion to fecal matter. Consumption by zooplankton is the primary source of this, as very fine organic and inorganic particles are ingested and repackaged into denser, faster sinking aggregates (Krivtsov, et al., 2001).

The major process preventing the settling of material to the sea bed is the upward component of turbulence, which can result not only in the prevention of settling, but in the resuspension of further particles. There are two further principal mechanisms which may affect particle settling velocities:

i) Wake Formation

Most falling particles, with the exception of spherical particles in low (<<1) Reynolds number conditions, create a wake. This wake interacts with particles in close proximity, affecting settling velocities, and decreasing the settling velocity of the suspension overall (Winterwerp, 2002).

ii) Viscosity

The effective viscosity of a suspension depends upon the salinity, temperature (Thomas, et al., 1999) and particle concentration (Winterwerp, 2002). Variations in concentration over depth may cover several orders of magnitude (Ross & Mehta,

1989) in the near-bottom layers of water bodies with a high supply of fine sediment that are subject to periods of low flow, such as estuaries or lakes (McAnally, et al., 2007). In high concentration suspensions (of the order of a few kgm^{-3} (Mehta, 1986)), particles begin to interfere with each other, reducing the effective settling velocity of the suspension (Dankers & Winterwerp, 2007) as particles come into close contact. This results in the formation of a network of electrostatic bonds that create a particle framework, suppressing turbulence and altering the flow to become firstly hyper concentrated (Wan & Wang, 1994), and then non-Newtonian (Wang & Larsen, 1994). The bonds formed are strong enough to form a particle-supported matrix, but not strong enough to eliminate the potential for mobility (McAnally, et al., 2007). Consolidation begins at the point of transition from a water to particle-support matrix, as water is squeezed out (Dankers & Winterwerp, 2007).

3.5 Disentangling SPM signals

Whether a signal is regarded as being one of resuspension or advection depends upon the area of interest, and therefore distinguishing between resuspension and advection can be complex. Material that is resuspended within the area of study is regarded as resuspension, while that which is resuspended outside, but passes through, the area of interest, is regarded as advection.

In an estuary in which the SPM is composed of both a resuspension and an advection component, observations of SPM concentration over time at any height above the bed can be thought of as a combination of a resuspension component that is proportional to the current speed, and an advection component that forms a horizontal concentration gradient and is therefore proportional, at the point of measurement, to the tidal displacement (Jago & Jones, 1998) as demonstrated in Fig. 3.6, in which local tidal resuspension (a) creates a quarter-diurnal in SPM concentration (c), while the advection signal (b) creates a semi-diurnal peak in SPM concentration (d). The combination of these signals (e) creates the characteristic twin peak signal. This is because the advection of a horizontal concentration gradient operates on a semi-diurnal timescale (Weekes, et al., 1993; Williams, et al., 1998; Souza, et al., 2007), with the concentration gradient either advecting into the estuary from

offshore on the flood, or down the estuary during the ebb. Conversely, resuspension of material tends to take place during both the flood and ebb tide (dependent upon the degree of tidal asymmetry), and therefore operates on a quarter-diurnal frequency (Weekes, et al., 1993; Williams, et al., 1998; Souza, et al., 2007). Distinguishing between resuspension and advection using these principals is therefore possible through the fitting of quarter-diurnal and semi-diurnal signals to an SPM time series, as shown in Weekes et al. (1993). The phase of this signal is of key importance: the quarter-diurnal resuspension signal should be in phase with the current speeds, indicating resuspension, while the semi-diurnal signal should be out of phase with the current speeds, indicating that the semi-diurnal concentrations are not controlled by the current speeds. Where a semi-diurnal signal is in phase with one of the quarter-diurnal peaks, this is indicative of asymmetry in resuspension, with both peaks being composed of a quarter-diurnal signal, but one peak having greater amplitude, which results in a semi-diurnal signal.

Jago and Bull (2000) used this principal to show that the turbid plume of the Humber Estuary was advecting past their site of interest as the SPM concentration peaked at the end of the ebb tide, after the peak ebb current speeds had been reached. Salinity was used to show that the peak in concentration occurred during a period of lower salinity – indicating the presence of the fresher water from the Humber Estuary. In this instance, a horizontally advected concentration gradient was present that was larger than the vertical resuspension gradient, demonstrating that advection may be the dominant process of SPM transport with coastal and estuarine regions.

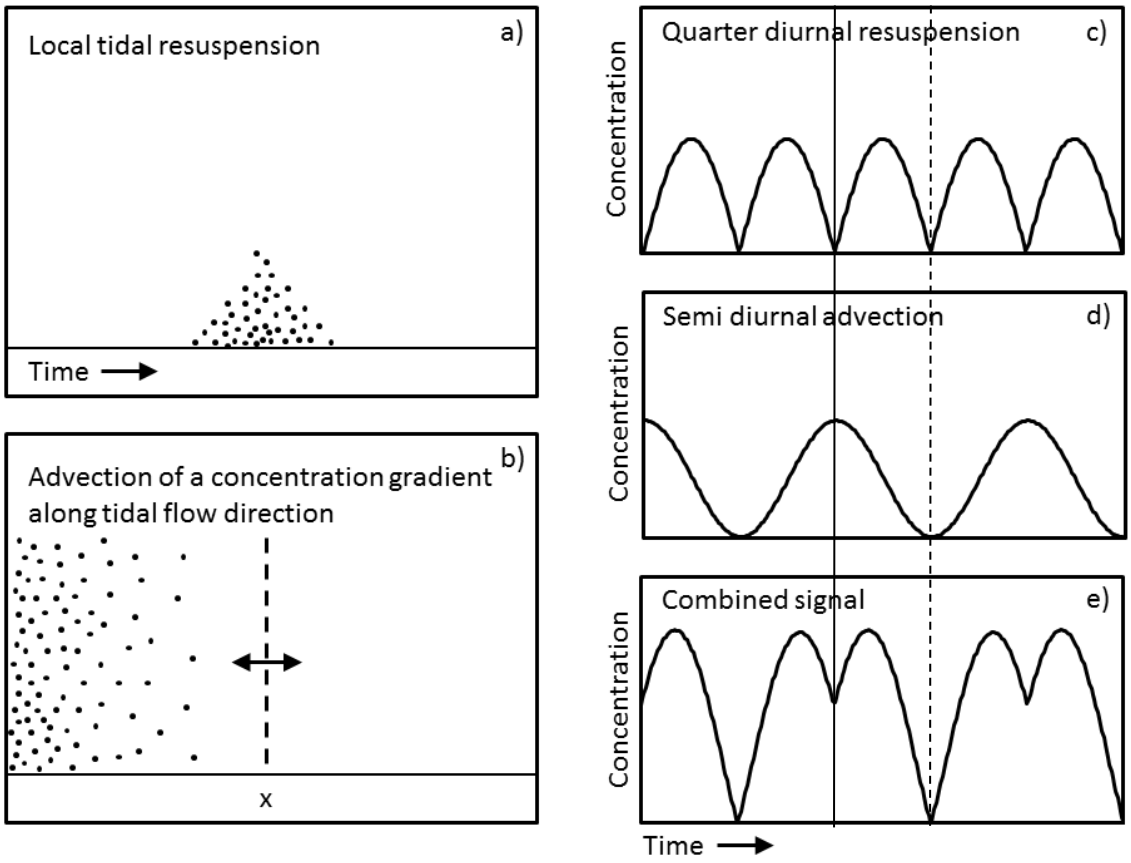

Fig. 3.6 – The twin peak signature (e) resulting from a quarter-diurnal resuspension signal (a) & (c) and a semi-diurnal advection signal (b) & (d). Reproduced and modified from Weekes et al, (1993). Solid line in (c), (d), (e) indicates high water, and dashed line low water. Dashed line (x) in (b) indicates the observation point

Chapter 4

The Dee Estuary

4.1 Introduction

The data presented herein was collected in the Hilbre Channel of the Dee Estuary. This region was chosen due to its high tidal range, near rectilinear currents, abundant amounts of cohesive sediment and abundant salt marsh and mud flat regions high up the estuary. In addition, the Hilbre Channel side of the Dee Estuary is subject to the strongest influence of the Coriolis effect (see Section 2.2.2), and therefore river influence, with riverine material and material originating from higher up the estuary found in greater concentrations on this side of the estuary. The combination of these factors makes the Hilbre Channel of the Dee Estuary a strongly turbulent environment with seasonally varying biological input and abundant cohesive sediment. This makes the Dee Estuary an ideal "natural laboratory" in which to study the interactions and effects of turbulence and biological material on flocculation.

This chapter provides background information to the area of study. 4.2 provides an introduction to the study area – its geographical setting, changes over time, and wildlife status, 4.3 gives an introduction to the tidal dynamics of the estuary and 4.4 introduces the estuary sediment, while 4.5 considers the effects of the Earth's rotation on the region.

4.2 Study area

The River Dee and Dee Estuary

The River Dee rises on the slopes of Dduallt above Llanuwchllyn in the Snowdonia mountain range and meanders through the Welsh countryside before forming the England-Wales border, eventually opening into an estuary to the north-west of Chester. The 110 km (68 mi) length of the River Dee drains from a catchment area of ~1817 km^2 (Fig. 4.1). The river is subject to an Environment Agency Regulation Scheme, set up to prevent the river from drying up during the summer months. Water is stored in reservoirs along the length of the

river, above the limit of saline intrusion, and released during dry periods. Monitoring stations are maintained by the Environment Agency, with the locations of three of these monitoring stations indicated in Fig. 4.1. River discharge recorded by these monitoring stations is considered further in Section 6.3.1.

The Dee Estuary was formed by the flooding of the river valley cut by the River Dee during the last major glaciation approximately 18000 years ago (Fairbanks, 1989) to create a funnel-shaped estuary 20 km long and 8.5 km wide at the mouth. It is located on the eastern side of the Irish Sea (Fig. 4.2) at 53.3°N, 3.2°W, and forms the junction of north-east Wales and north-west England.

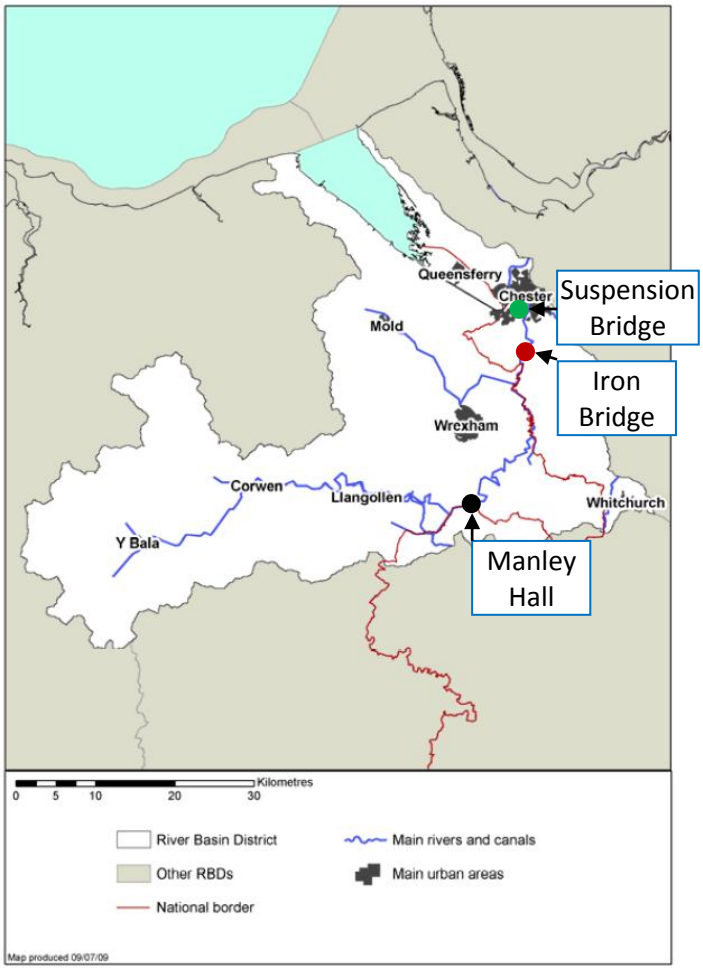

Fig. 4.1 – The River Dee catchment area, including the main rivers, canals and the national border between England and Wales (Environment Agency, 2009) with three monitoring stations at Manley Hall, Iron Bridge and Suspension Bridge indicated

Anthropogenic changes to the River Dee and Dee Estuary

The upper Dee Estuary and River Dee have been anthropogenically changed from their natural state. Between 1732 and 1736, a 10 km long, 100 m wide, 4 m deep artificial channel was excavated to the west of Chester to improve shipping navigation. Once completed, the river was diverted into this canalised section, which resulted in an increase in siltation such that the depth of the channel decreased to ~2 m or less (Simpson, et al., 2004) and became unnavigable (Pye, 1996). Land reclamation was also undertaken, with the towns of Sealand and Shotton both reclaimed from the estuary. Due to these changes, the main channel shifted, and began favouring the western side of the estuary, with this favouritism increasing after the banks of the artificial channel were extended in 1819.

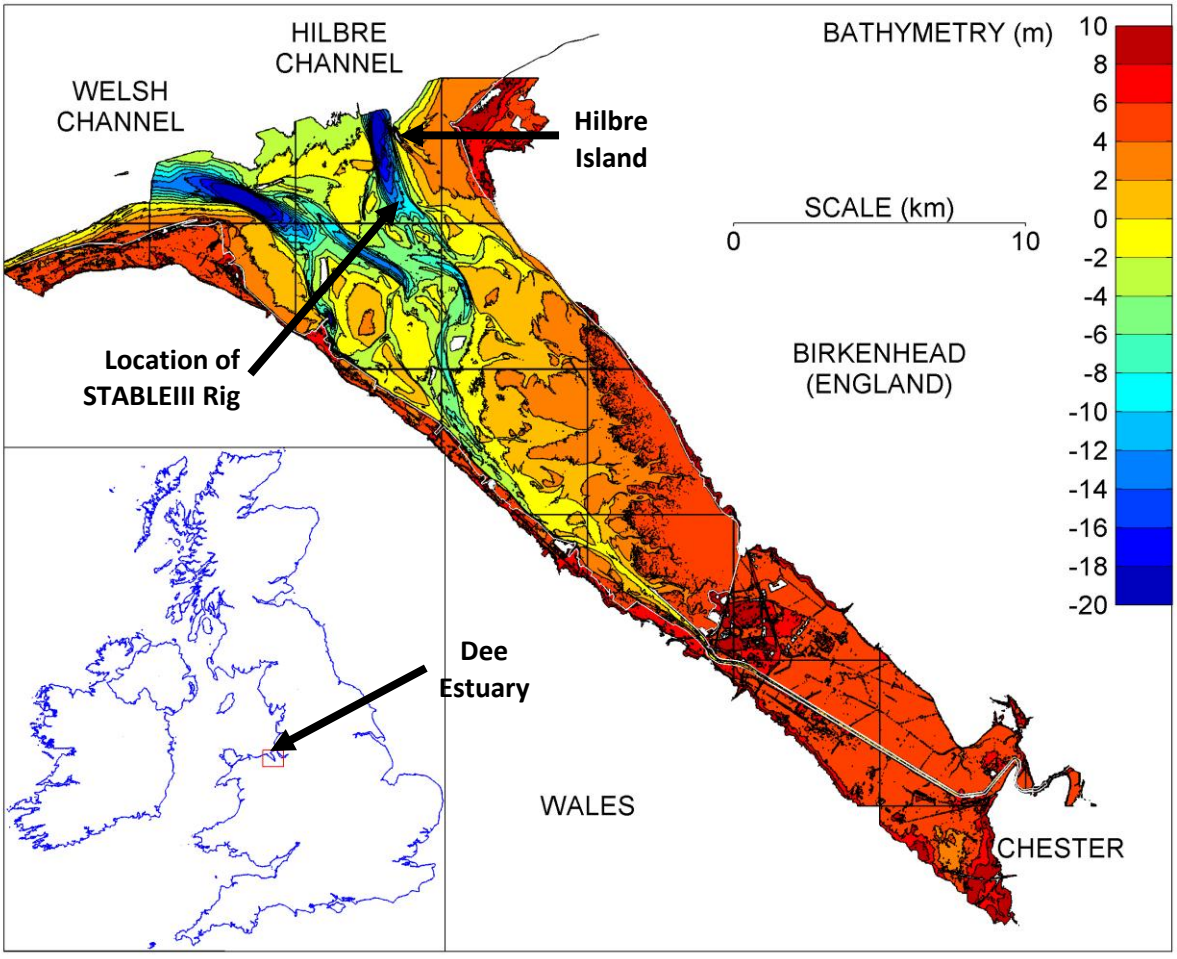

Fig. 4.2 – Location of the Dee Estuary and the STABLEIII benthic tripod deployment in the Hilbre Channel

Present-day land use of the Dee Estuary catchment

The catchment of the Dee Estuary is used for a variety of purposes, as indicated in Table 4.1, with data taken from Greenwood, et al., (2011). The majority of the catchment consists of grassland and other non-urbanised use, with only 1.7 % consisting of urban extent. Within the majority grassland fraction (62.9 %), most of the land area is used for farming purposes; the upper catchment region is used primarily for rough grazing, while farming in the lower reaches is more mixed.

Table 4.1 – Present-day land use of the catchment of the Dee Estuary

Dee Estuary land use					
	Woodland	***Arable / horticultural***	***Grassland***	***Mountain/heath/bog***	***Urban extent***
Use (%)	13.6	8.8	62.9	9.5	1.7

Dee Estuary wildlife

The Dee Estuary is regarded as important from both an industrial and wildlife perspective (Brown, et al., 2014). It is a highly regarded wildlife area within both Britain and Europe due to its populations of wildfowl and waders. The differing characteristics of the shorelines, with the industrialised Welsh coast and residential and recreational English coast (Bolanos & Souza, 2010), in combination with the vast areas of intertidal sand flats, mud flats and salt marsh, provide swathes of differing habitats for wildlife (Hutchinson, 1994).

4.3 The tidal dynamics of the Dee Estuary

The Dee Estuary is a hypertidal (Dyer, 2001; Archer, 2013), funnel-shaped, coastal plain estuary. The main discharge channel bifuricates approximately 12 km after the canalised section into two main channels – the Welsh channel to the western side, and the Hilbre channel to the east – both of which extend into Liverpool Bay, and are approximately 1 km wide, 4 km long and 20 m deep (Fig. 4.2).

With a tidal range varying from ~4 m during neaps (Brown, et al., 2014) to in excess of 10 m during large spring tides, the Dee Estuary has an average tidal prism of 4×10^8 m^3 and is one of three major estuaries emptying into Liverpool Bay along with the Ribble and Mersey. An

increase in tidal prism of greater than 80% occurs between mean low and mean high water during spring tides (Moore, et al., 2009), resulting in tidal currents in excess of 1.4 ms^{-1} (Brown, et al., 2014). The high tidal range, fast currents, large spring-neap variations and vast quantities of water transported during each tidal cycle result in approximately 130 km^2 (70% of the Dee Estuary surface area) being exposed at low water on spring tides (Hutchinson & Prandle, 1994).

The boundary layer of the Hilbre Channel of the Dee Estuary is turbulent, as can be shown from the use of Eq. (2.37) and Eq. (2.38), taken from Liu, (2001), and reasonable values for the mouth of the Dee Estuary of u = 1ms^{-1}, h = 20m and ν = 1 x 10^{-6}. Using these values, x has a value of 4204m and subsequently, Re_x has a value of 4.20 x 10^9. This value of Re_x is greater than the turbulent boundary layer threshold of 5 x 10^5, indicating that the Hilbre Channel of the Dee Estuary has a turbulent boundary layer.

The circulation pattern of the Dee Estuary differs between the Hilbre and Welsh channels, being vertically sheared in the Hilbre Channel, and laterally sheared in the Welsh Channel (Bolanos, et al., 2013). Weak influence of waves and wind within the Dee Estuary means that the long-term residual circulation is controlled mainly by baroclinic and tidal processes (Brown, et al., 2014).

The Stokes number (Souza, (2013) – shown in Eq. (2.42)), which represents the ratio of the boundary depth to the total depth, has a value of ~100 for the Dee Estuary indicating that the boundary layer will fill the whole water column during peak flow (Brown, et al., 2013). The horizontal Richardson number (Eq. (2.41)), which has an average value of 0.58 (Bolanos, et al., 2013), indicates that tidal straining occurs within the estuary despite the river flow being far weaker than the tidal flow (Brown, et al., 2013). Indeed, stratification occurs in both channels near low water; in the baroclinic Hilbre Channel stratification persists before being broken down mid-way through the flood tide, while stratification is established shortly after low water in the barotropic Welsh Channel and broken down quickly during the flood (Brown, et al., 2013). Storms appear to have little influence on these circulation patterns, with the two-layer vertically sheared system having been shown to persist in the Hilbre Channel even during a period of wind-wave influence. Waves within the Dee Estuary

may reach heights of up to 2.3 m, but generally remain below 1 m during calm or south-easterly (fetch limited) conditions (Brown, et al., 2014).

River influence

Average discharge at the Environment Agency's monitoring site at Manley Hall (shown in Fig. 4.1), located ~137 km from the estuary mouth, was 31 m^3s^{-1} between 1937 and 2011 (Brown, et al., 2013). Elsewhere, average discharge has been reported as being in the range of 31-40 m^3s^{-1} (Lambert, 1988; Simpson, et al., 2004; Bolanos & Souza, 2010), equating to roughly 0.4% of the tidal prism over an entire tidal cycle (Moore, et al., 2009). This shows that the river flow is small in comparison to the effects of the tide, and therefore the river would be expected to exert little influence, with the Dee Estuary being a tidally dominated system. The river influence however is important with regard to salinity stratification which occurs during low water. Peak discharge during extreme events may reach 300 m^3s^{-1} (Bolanos & Souza, 2010; Amoudry, et al., 2014).

4.4 The sediments of the Dee Estuary

The bed of the Dee Estuary is covered by a thick (up to 18 m) sediment layer, deposited after the last Ice Age, consisting of primarily mixed sediment composed of fine-grained sands and muds with some gravel beds (Steers, 1967). The sediment map of the Dee Estuary produced by DEFRA (Fig. 4.3) indicates that much of the estuary is predominantly sand, with mud and sandy mud towards the top (south-east) of the estuary. However, cohesive material of varying quantities is found in the surface sediments throughout the estuary and therefore the predominant sediment type is one of mixed sand and mud. Infilling of the estuary over time has led to the gradual accretion of the sand and mudbanks, and an increase in the area occupied by saltmarsh (Marker, 1967). The source of this material appears to be marine with only 0.5 % of the accreted sediment within the estuary attributed a riverine origin (Turner, et al., 1994) indicating that river sediment supply may be negligible. The mixture of cohesive and non-cohesive sediments within regions of the Dee Estuary modifies the threshold of motion, making predictions of resuspension within the estuary difficult (Bolanos & Souza, 2010).

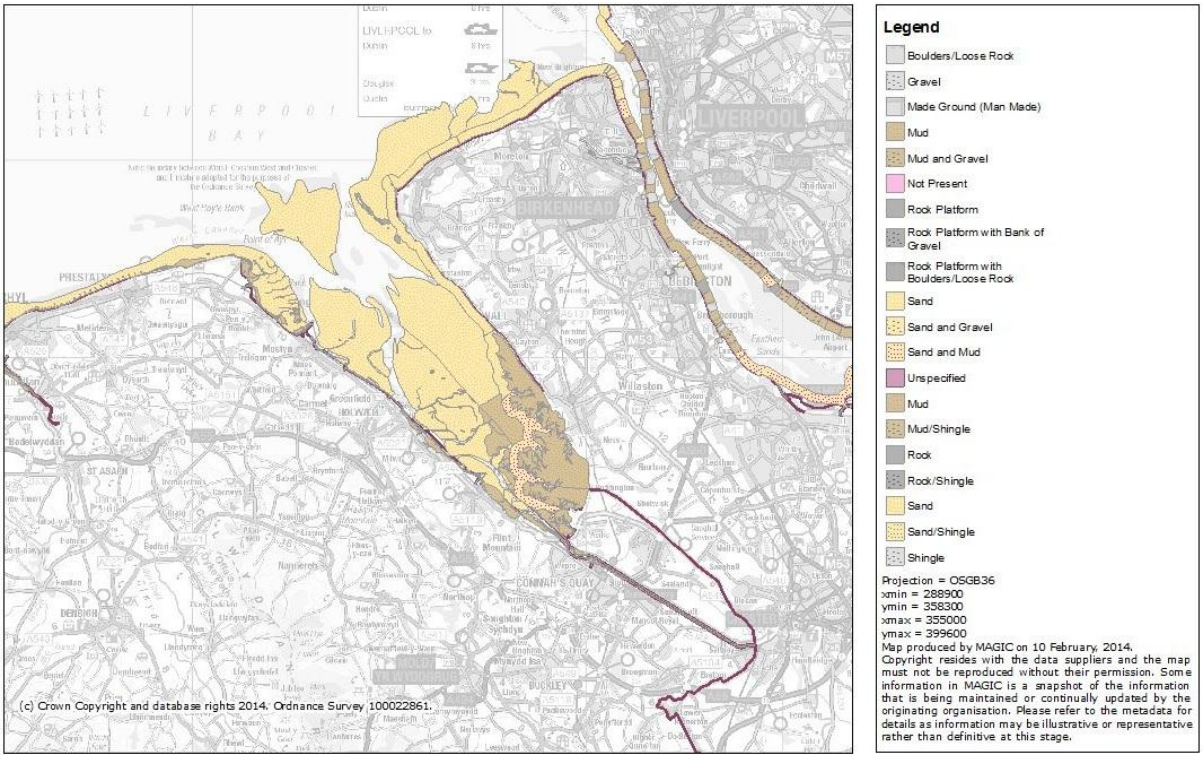

Fig. 4.3 – Sediment map of the Dee Estuary (Source: defra.gov.uk)

Large quantities of fine grained, cohesive material in the Dee give rise to SPM concentrations of up to 120 mgl^{-1} at the surface in the mouth of the estuary (Turner, et al., 1994; Thurston, 2009) due to tidal, current-induced resuspension (Bolanos, et al., 2009), with higher concentrations found at the sea bed. Concentrations at the bed of the neighbouring Mersey Estuary reach 600 mgl^{-1} (Martino, et al., 2002), providing an indication of the likely levels of SPM that may be found toward the bed of the estuary. An investigation of the particle dynamics of the Welsh Channel using data from February 2008 by Ramirez-Mendoza, et al., (2014) found SPM concentrations varying between 18.5 and 138 mgl^{-1}. Abundant evidence of flocculation during both high and low slack waters, with breakup during peak flood and ebb, was found, with flocculation at low water following the advection of fine particles during ebb. Advection of SPM from high up the estuary has been shown to be important for sediment transport, though the impact of river sediment has been shown to be negligible, with the advection of fine particles likely to be the result of spatial gradients in bed composition (Amoudry, et al., 2014). Flocs in the Dee Estuary have been shown to have an average fractal dimension of 2.4 during winter, with D_{50}

distributions of between 50 and 200 μm, and effective densities varying between 46 and 67 kgm^{-3}, with settling velocities between 0.1 and 2.1 mms^{-1} (Ramirez-Mendoza, et al., 2014). In addition, it is believed that the Dee Estuary is currently importing sediment, but that the estuary may be close to reaching a morphological equilibrium, which would result in a decrease in the rate of accretion (Moore, 2009).

4.5 The effects of the Earth's rotation on the Dee Estuary

The Ekman number (Eq. (2.6)), a measure of the impact of the earth's rotation, based upon the ratio of the planetary boundary depth to the total depth, ranges from 0.0138 to 1.15 in the Dee Estuary, with an average value of 0.14 within the Hilbre Channel and 0.19 within the Welsh Channel (Bolanos, et al., 2013). Both channels therefore fall within the transition zone between moderate (< 0.1) and high friction (> 1) conditions (Valle-Levison, 2008), indicating that the effects of the Earth's rotation may have an impact upon the estuary, with sediment sourced from the river and upper estuary reaches likely to be found in higher concentrations on the right side of the estuary, and therefore in the Hilbre Channel (Huijts, et al., 2006).

The Kelvin number (Thomson, 1879); shown in Eq. (2.2), is a measure of the effect of the Earth's rotation based upon the ratio between the width of the estuary basin and the internal Rossby radius. The Kelvin number had a value of 0.45 within the Hilbre channel and 0.32 within the Welsh Channel during the study period of Bolanos, et al., (2013). Rotational effects are important when the Kelvin number is > 1 (Bolanos, et al., 2013; Valle-Levison, 2008), and therefore the Kelvin number indicated that rotational effects were negligible for the Dee Estuary during the study period of Bolanos, et al., (2013). Brown, et al., (2013) however calculated an average Kelvin number of 0.97 using the mean density in the channels at the estuary mouth, indicating a moderate influence of Coriolis at the mouth of the estuary. The combination of the Kelvin number and Ekman number indicate that the Coriolis effect will be minor, but will act to make river influence, and therefore sediment sourced from the river and the upper estuary regions, greater in the Hilbre channel than the Welsh channel.

Chapter 5

Methodology

5.1 Introduction

This chapter outlines the methods used for data collection and processing within the present study. 5.2 discusses the instruments used for data collection deployed on a benthic tripod including the LISST and ADCP. 5.3 discusses the instruments used for data collection deployed on a profiling CTD frame including a transmissometer, CTD and fluorometer. The strategy and schedule for instrument deployment are presented in 5.4, while 5.5 details the instrument calibration procedures.

5.2 Sediment Transport and Boundary Layer Equipment (STABLEIII)

In addition to a Microcat CTD, the following instruments were deployed on the "STABLEIII" (Sediment Transport and Boundary Layer Equipment Mark III) platform, a 2.5 m high, 3500 kg benthic tripod (Fig. 5.1) in the Hilbre Channel (Fig. 4.2).

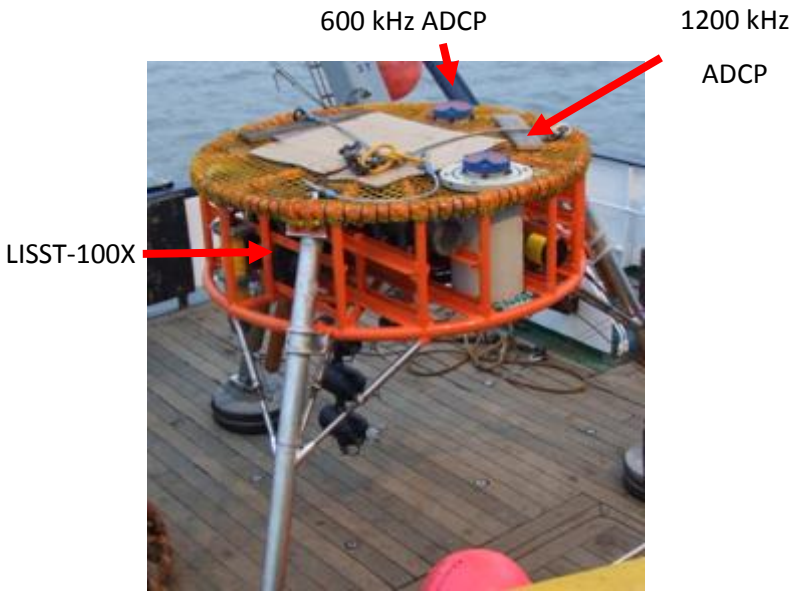

Fig. 5.1: The STABLEIII Platform pre-deployment with the locations of the LISST and ADCPs shown

5.2.1 The Laser In-Situ Scattering Transmissometer (LISST)

The LISST (Fig. 5.2, schematic of workings in Fig. 5.3) is an optical instrument providing size-correlated total volume concentration and an optical measure of water clarity (beam transmission), giving a unique view of SPM as the LISST takes size distribution into account when estimating volume concentration (Agrawal & Pottsmith, 1994; Gartner, et al., 2001).

Fig. 5.2 – The LISST 100X-Type C

The logarithmically spaced rings of the LISST for measuring volume concentration

The LISST measures laser light intensity over a distance of 10 cm at different scattered angles using 32 logarithmically spaced, concentric ring detectors (Fugate & Friedrichs, 2002; Meral, 2008). Particles in the water reflect, absorb (organics), or scatter the transmitted light onto the ring detectors (Meral, 2008), while the centre ring measures light that is neither absorbed nor scattered. The light intensity received by each ring detector is inverted, providing an estimate of particle area concentration, with each ring detector representing a different size range of particles. These size estimates, coupled with an empirically determined volume calibration constant, provide a spectrum of volume concentration over the size range (Fugate & Friedrichs, 2002). The LISST type used in the present study (LISST-100X type C) is able to measure particles in the size range of 2.5 – 500 µm (Mikkelsen, et al., 2005).

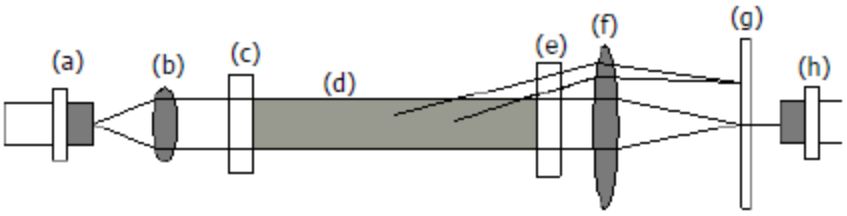

Fig. 5.3 – The LISST device: (a) laser diode source, (b) companion focusing optics, (c) and (e) pressure windows, (d) sample volume, (f) receiving lens, (g) concentric photodetector rings, (h) transmission detector (Meral, 2008)

Potential problems with the use of the LISST for size distributions

The LISST instrument provides in-situ measurements of particles within the water column, however, care must be taken to use the instrument correctly, and its limitations should be noted to allow for correct interpretation of results. The LISST is a large unit, and therefore deployment of the LISST instrument should be done perpendicular to the flow as the LISST unit may cause flow obstruction. Further, although the size spectrum of the LISST covers more than an order of magnitude, its range is smaller than the size spectrum of SPM, which incorporates sub-micrometer single particles to mm-sized flocs, making measurement of the entire SPM size range with a single instrument extremely difficult – an instrument would need to sample large enough volumes to view large, rare flocs, while resolving small individual particles, in situ, without disturbing fragile flocs (Mikkelsen, et al., 2005). Particles in suspension finer or coarser than the size range of the LISST may affect distribution estimates (Mikkelsen & Pejrup, 2000), resulting in an increase in the apparent volume concentration of the smallest particle size bins, and non-existent peaks at sizes between 250 and 400 µm (Davies, et al., 2012). This is generally shown within the data as a "rising tail" within the smallest size classes, and, where this is present, data should be discarded (Mikkelsen, et al., 2005).

The LISST does not require routine calibration in order to provide measurements of volume concentration, provided the laser optics are correctly aligned (Bolanos, et al., 2009), making the instrument useful in rapidly changing environments such as estuaries. It does, however, rely on inversion, making the calculated size distribution an approximation (Fugate &

Friedrichs, 2002). Further, particle sizes are grouped into classes, meaning single peaks may produce non-existent aliases, and multiple peaks may be blurred together due to a lack of resolution – particularly in the higher size classes where size ranges are largest.

The LISST is calibrated to measure spherical particles. Most natural particles are not perfect spheres, and even "natural spheres" do not give the same scattering response as "true" spheres. Therefore, scattering from non-spherical natural particles may be different from that of natural spheres. Because of this, it is recommended that LISST data be used to ascertain relative changes in concentration and size distribution, rather than relying on the absolute values of change provided by the instrument (Fugate & Friedrichs, 2002).

Optical instruments are influenced by particle shape and mineralogy; platy-shaped particles with high volume to cross-sectional area are up to 10 times more optically active than spherical particles (Bunt, et al., 1999), while sub-micron particles may be even more efficient at light scattering and diffusion (Stramski, et al., 2004). Flocculated particles may therefore have optical properties which vary from comparably sized, spherical mineral grains due to variations in the shape and mineral composition of flocs (a cylindrical floc may be viewed from the end as a small particle or from the side as much larger depending upon its orientation when viewed by the LISST).

Despite these potential problems, the LISST has had success when used in studies of flocculation (Fugate & Friedrichs, 2002; Fugate & Friedrichs, 2003; Voulgaris & Meyers, 2004; Jago, et al., 2006; Cartwright, et al., 2011; Smith & Friedrichs, 2011; Ramirez-Mendoza, et al., 2014; Amoudry, et al., 2014). A decrease in optical transmittance was traditionally interpreted as an increase in mass concentration, caused by resuspension, but the use of the LISST has shown that this may, in part, be caused by a decrease in particle size due to floc breakup (Jago, et al., 2006). In situations where flocculation may be present, the LISST is the best available instrument for in-situ measurements of size distribution as it is able to provide measures of size distribution and both mass (through calibration) and volume concentration in a stand-alone unit which can be left for prolonged periods and requires minimal post-processing to despike and filter the resultant data. Holocams and floc cameras may provide more detailed information on the flocs in suspension, but the extensive "hands-on" post-processing required currently makes the collection of large

datasets prohibitively expensive with regard to the time required to quality control and process the data.

The central ring of the LISST

The central ring of the LISST is a transmissometer (Agrawal & Pottsmith, 2000) and can therefore be used to derive sediment mass concentration through calibration with in-situ SPM samples. Transmissometers work through the use of a narrow, collated beam (laser) of light with a wavelength of 660 nm. The light beam is sent along the path between transmitter and receiver and the received light converted into a beam attenuation coefficient using the formula:

$$A_c = \ln(T)/L_z \tag{5.1}$$

Where A_c is the attenuation coefficient, T the fraction of transmitted light, and L_z the optical path length of the instrument. When calibrated against in-situ SPM samples, A_c is able to provide a measure of mass concentration.

Potential problems with the use of the transmissometer

Use of a transmissometer or any optical instrument in a non-dark environment can result in ambient and scattered light being received and contaminating the signal, giving a disproportionately low value of A_c. This is a particular issue in multiple-scattering systems, where limiting the acceptance angle is not sufficient to prevent contamination.

Examples of LISST usage

Despite the problems associated with its use, the LISST has been shown to be a useful instrument for measuring flocs in-situ:

- Jago et al. (2006) used the LISST to show that SPM concentrations in the Irish Sea change over time due to a combination of spatially-varying turbulence advection and time-varying turbulence at the measurement site. Tidal asymmetry in turbulence produced a quarter-diurnal signal due to floc breakup and resuspension during peak turbulence. The LISST showed flocculation during high and low water, with greater

flocculation at low water generating a semi-diurnal signal in the properties of the SPM;

- The LISST was used in a tidal creek by Voulgaris and Meyers (2004) to show that the background floc population was being enriched with larger flocs and individual grains during spring tides, and therefore that erosion of the tidal creek occurs during the ebb phase of spring tides. Conversely, accretion occurs during the flood tides. With no significant variation in settling velocity over the spring-neap cycle, it was concluded that the spring-neap cycle controlled salt marsh sedimentation through sediment availability and salt marsh inundation time with more sediment and more time available during spring tides;
- Working in the York River estuary in the USA, Cartwright et al. (2011) used the LISST to show that both fecal pellets and muddy flocs were occurring in the lower 1 m of the water column. Fecal pellets, being dense and fast sinking, were shown to be in phase with both current speeds and stress, consistent with resuspension and rapid sinking. Conversely, peaks in particle size occurring after the peaks in stress and current speed showed the formation of low density, fragile flocs;
- Fugate and Friedrichs (2002) used the LISST to show the presence of multiple particle populations in the bottom boundary layer of Chesapeake Bay, USA including a slowly settling background particle population and two rapidly settling populations.

Examples of transmissometer use

Transmissometers have been used in the marine environment for over 25 years. Examples of their application include:

- Jago & Jones (1998) used several transmissometers at differing heights above the bed to show the presence of a twin peak signature formed from a resuspension component in combination with a horizontal concentration gradient;
- Sanford (1993), Sanford (1994) and Sanford (2001) used a transmissometer calibrated against gravimetrically filtered water samples in investigations to quantify sediment resuspension and transport in the upper reaches of the Chesapeake Bay estuary;

- Gross and Dade (1991) used field observations collected with a transmissometer to validate their sediment transport model for storm-induced sediment resuspension;
- Edelvang and Austen (1997) used a transmissometer to measure trends in SPM concentration during their investigations into the abundance, size and settling velocities of single grains, flocculated and fecal material;
- Patchineelam and Kjerfve (2004) calibrated a transmissometer deployed on a CTD frame with gravimetrically filtered SPM samples to provide mass concentration during investigations of the Winyah Bay estuary;
- Souza et al. (2001) used a transmissometer calibrated with in-situ gravimetrically filtered SPM samples to provide a measure of mass concentration while investigating water column structure and SPM on a continental shelf.

Use of the LISST and transmissometer within the present study

In the present study, LISST measurements were taken in 40 s bursts at 1 Hz for 20 minutes per hour throughout the two month-long observation periods. Each 20 minute burst was subsequently averaged to provide one observation per hour.

The LISST central ring measurements were calibrated using Niskin bottle water samples taken during the CTD periods to provide a continuous time series of SPM mass concentration at one height above the bed for both mooring periods (details of the calibration are provided in Section 5.5.3). These measurements allow the investigation of how SPM mass and volume concentration changes over tidal, spring-neap, and seasonal timescales. Further, the LISST provides a measure of particle size at tidal, spring-neap and seasonal timescales. By comparing particle sizes and abundances between deployment periods it will be possible to ascertain seasonal changes in particle characteristics and behaviour. This is considered further in Chapter 6 and Chapter 8.

Resuspension and advection may both be occurring in the Dee Estuary. The time series recorded by the LISST, when coupled with measurements of current speeds and salinity make it possible to follow the methods outlined in Section 3.5 to differentiate between resuspension and advection signals based upon the phase and amplitude of the peak in SPM concentration relative to the peak current speed, and through the use of salinity to determine the presence of fresh water. This is considered further in Chapter 7.

As the LISST is able to provide a measure of mass concentration through calibration, in addition to measures of volume concentration and particle size, it will be possible to follow the methods outlined in Section 3.4 to determine both the effective density and bulk settling velocity of the suspension. This will provide an insight into how particle size, density and settling velocity vary over tidal, spring-neap and seasonal timescales.

5.2.2 The Acoustic Doppler Current Profiler (ADCP)

The Acoustic Doppler Current Profiler (ADCP) works through the transmission of a short (of the order of milliseconds but varies dependent upon frequency and bin size) pulse (or "ping") of high-frequency sound (300, 600, or 1200 kHz) from a transducer into the water column. A tiny amount of this sound is reflected back towards the transducer by particles suspended in the water (Thorne, et al., 1991). It is assumed that these scatterers are moving, on average, at the same velocity as the water, and the Doppler shift of the returned signal is then used to calculate the along-beam velocity of the water. The RDI ADCP is composed of 4 separate transducers, each inclined at 20° to the vertical in a Janus configuration (Fig. 5.4) a setup whereby opposite transducers are situated in the two horizontal planes at 90° to each other – yz and xz. An along beam velocity can be calculated for each ping for each transducer (termed u_1 to u_4), making it possible to calculate all three components of the water velocity (RDI, 1996) as the along beam velocities are found to be components of the vertical and horizontal velocities. For each beam therefore:

$$u_1 = v\sin\theta + w\cos\theta \quad (5.2) \quad \text{and} \quad u_2 = -v\sin\theta + w\cos\theta \quad (5.3)$$

$$u_3 = u\sin\theta + w\cos\theta \quad (5.4) \quad \text{and} \quad u_4 = -u\sin\theta + w\cos\theta \quad (5.5)$$

in which θ is the angle between the beam and the vertical (as shown in Fig. 5.4). Using these equations, it is possible to subtract the along beam pairs in order to resolve the horizontal velocities:

$$u = \frac{u_3 - u_4}{2\sin\theta} \quad (5.6) \quad \& \quad v = \frac{u_1 - u_2}{2\sin\theta} \quad (5.7)$$

The vertical velocity can be determined from each pair of transducers, providing two estimates, with the difference between these estimates being the "error velocity," which provides a measure of the homogeneity within the measured flow:

$$w_x = \frac{u_3+u_4}{2\cos\theta} \qquad (5.8) \qquad \& \qquad w_y = \frac{u_1+u_2}{2\cos\theta} \qquad (5.9)$$

The delay between signal transmission and receipt provides the distance to the particle, allowing the returned signal to be divided into depth bins, the size of which can be specified by the user. The value assigned to each bin is based on a triangular weighting function, with the maximum at the centre of the bin, and the value for each bin an average calculated over the entire bin, rather than at a single point. The weighting function applied means a correlation of ~15% exists between adjacent bins (RDI, 1996), and therefore adjacent bins should not be used in shear calculations.

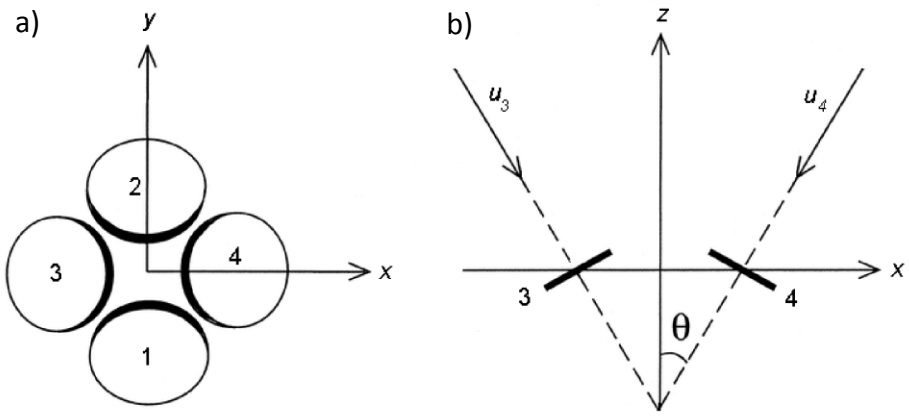

Fig. 5.4 – The head of an ADCP unit in plan (a) and profile (b) view showing the Janus configuration of the ADCP's 4 transducer heads (RDI, 1996)

Turbulence production

For the purposes of this study, the variance technique was selected to calculate turbulence production (see Section 2.3.8), since it provides reliable estimates and has been extensively tested in other scientific investigations (Lu & Lueck, 1999; Stacey, et al., 1999; Rippeth, et al., 2002; Souza, et al., 2004; Lorke & Wüest, 2005; Souza & Howarth, 2005; Thurston, 2009). Horizontal homogeneity of the observed flow is assumed, which is acceptable when

working within the confines of an estuary (Stacey, et al., 1999), since beam pairs angled at 20° will be measuring velocities separated by a horizontal distance of 7.3 m at 10 m from the ADCP.

The variance technique is used to calculate Reynolds stresses (see Section 2.3.2) in the xy-plane through the decomposition of each Cartesian and along-beam velocity into a mean and fluctuating quantity, giving an along-beam variance:

$$\overline{u_4'^2} = \overline{u'^2}\sin^2\theta + \overline{w'^2}cos^2\theta - 2\overline{u'w'}\sin\theta\cos\theta \quad (5.10)$$

$$\overline{u_3'^2} = \overline{u'^2}\sin^2\theta + \overline{w'^2}cos^2\theta + 2\overline{u'w'}\sin\theta\cos\theta \quad (5.11)$$

The RMS (root mean squared) value of the component of the Reynolds stress in the xz-plane can then be extracted through:

$$\tau_x = -\rho\overline{u'w'} = -\rho\frac{\overline{u_3'^2} - \overline{u_4'^2}}{4\sin\theta\cos\theta} \quad (5.12)$$

Following the same process, but subtracting U_2 from U_1 reveals the Reynolds stress in the yz-plane. These Reynolds stresses can then be used to retrieve TKE production:

$$P = \rho\left(\overline{u'w'}\frac{\partial u}{\partial z} + \overline{v'w'}\frac{\partial v}{\partial z}\right) \quad (5.13)$$

The averaging time over which turbulence is calculated is important. Too short a time and fluctuations may not be captured properly; too long, and the mean value will not be representative. Periods of between 10 (Rippeth, et al., 2002; Souza, et al., 2004; Souza & Howarth, 2005) and 20 minutes (Lu & Lueck, 1999; Lorke & Wüest, 2005; Thurston, 2009) are commonly used. Within this thesis, results were obtained using a 20 minute averaging period.

Problems with using ADCPs

While ADCPs provide information on the natural environment there are problems specific to them which can affect data quality. As ADCPs have not been used in the present study to measure suspended sediment concentration, the main potential source of error is the axial

tilt, which can cause errors in the calculation of turbulent stresses (Williams & Simpson, 2004).

Use of the ADCP in the present study

The ADCPs used in the present study were operated in Mode 12 which allows faster sampling (8 sub-pings per ensemble) than other modes of operation. This was used as it reduces instrument noise when the ADCP is to be used for Reynolds stress and turbulence production and dissipation estimates using the variance technique (Williams & Simpson, 2004; Giddings, et al., 2011). Due to the depth of the water column in the present study (which may exceed 20 m), the bin size of the ADCP was set to 0.5 m. The blanking distance above the ADCP unit before the first data bin is 0.44 m, making the centre of the first bin 0.69 m above the ADCP unit.

The ADCP was used to provide velocity fluctuations through the water column in 0.5 m intervals during the two month-long deployment periods. This is considered further in Chapter 6. The ADCP also provides a measure of water depth since it was equipped with a pressure transducer.

5.3 Instrumentation of the CTD

In addition to the use of the moored STABLEIII benthic tripod (see Section 5.2), vertical profiles through the water column from an anchored boat were made at the start and end of each deployment. Profiles were taken every 0.5 h for 25 h periods, with measurements taken of conductivity, temperature, depth, transmission, LISST and fluorescence. In addition, bottle samples were taken within 3 m of the sea surface and at the lowest point of each cast to be filtered for gravimetric analysis to determine SPM mass concentration. Additional gravimetrically filtered samples were collected during the May and June CTD stations for chlorophyll analysis. Details of the instruments attached to the CTD frame are given in Table 5.1.

The CTD frame did not profile through the entire water column, stopping instead a distance of some metres from the sea bed. This was intentional to avoid impacting the CTD frame

into the sea bed. Therefore, no data are available for the bottom few metres of the water column.

Table 5.1 – Details of the instruments deployed on the STABLE III frame during February-March and May-June 2009

Instrument	Height above bed (m)	Sampling frequency (Hz)	Minutes burst per hour	Bin Size (m)	No. of bins
LISST 100X-C	1.82	1	20	N/A	N/A
ADCP 600khz	2.3	1	20	0.5	49
ADCP 1200khz	2.3	1	20	0.5	49

5.3.1 The CTD transmissometer

A SeaTech T1000 transmissometer was deployed on the CTD frame during each CTD station. This instrument functions in the same way as the central ring of the LISST. Details are therefore provided in Section 5.2.1.

Use of the CTD transmissometer in the present study

Calibration of the CTD transmissometer with SPM samples taken during the CTD periods was undertaken to provide a measure of mass concentration and an insight into how SPM concentration varied through the water column during the CTD periods. Details of this calibration are provided in Section 5.5.2.

5.3.2 The fluorometer

Fluorometers use a type of electromagnetic spectroscopy to measure the intensity and wavelength of light given off by fluorescing material after excitation with a certain spectrum of light, usually in the ultraviolet range. Excitation causes certain molecular compounds to vibrate and collide with other molecules, losing energy. As energy is lost, the molecules emit light, usually in the visible range.

Fluorescence can be used as a proxy for the presence of chlorophyll, as chlorophyll responds well to light excitation (Lorenzen, 1966). This requires calibration with in-situ samples, and is a method which must be used carefully as differing concentrations of chlorophyll may give

the same response to excitation by a fluorometer dependent upon the physiology of the organism being sampled.

Use of the fluorometer within the present study

Within the present study, the fluorometer was used as a proxy for the presence of chlorophyll (Lorenzen, 1966), and therefore photosynthetic biological activity and substances such as polysaccharides. Chlorophyll samples were taken during the May and June CTD periods to calibrate the fluorometer, providing a measure of chlorophyll concentration through the water column over time. The impact of the presence of polysaccharides on the characteristics and behavior of the particles in the Dee Estuary is considered in Chapter 8.

5.4 Strategy of deployment

The observations presented in the following chapters were made during a 31-day period from 2nd February to 5th March 2009, and a 30-day period from 5th May to 4th June 2009 in the Hilbre Channel of the Dee Estuary. A deployment cruise was conducted between 2nd and 4th February, and a recovery cruise from 3rd to 5th March. A further deployment cruise occurred between 5th and 7th May, with the recovery cruise from 2nd to 4th June, all using the RV Prince Madog. Observations during February-March 2009 were recorded at 53° 22.525'N 3° 14.198'W, and during May-June at 53° 22.514'N 3° 14.156'W. These co-ordinates are within the central region of the Hilbre Channel (Fig. 4.2), and separated by a distance of approximately 50 m. The Hilbre Channel is approximately 1 km wide at this point, and for the purposes of this study the moorings are considered to be sufficiently close as to be co-located.

After deployment of the STABLEIII benthic tripod during both February and May a 25-hour CTD station was undertaken (details of instruments are presented in Section 5.3). During the recovery cruises, 25-hour CTD stations were undertaken prior to recovery of the platform, however, during the June recovery cruise the platform was recovered prior to the CTD station being undertaken.

5.5 Instrument calibration

5.5.1 Calibration of the CTD conductivity sensor

The conductivity meter of the CTD was calibrated after each cast using a bottled water sample taken towards the bottom of the CTD cast. Using a sample from a known depth at which the conductivity meter had already made a measurement allowed any pressure bias or other offset to be determined and the data to be adjusted accordingly.

5.5.2 Calibration of the CTD transmissometer

Data from the CTD transmissometer were used in a multiple regression against the SPM mass concentration (obtained through the gravimetric filtering of water samples taken during each CTD cast), salinity and fluorescence to provide a measure of mass concentration throughout the CTD periods (Fig. 5.5). Salinity and fluorescence were included in the regression as salinity affects the optical properties of water (Werdell, et al., 2013) while estuarine SPM often contains fluorescing particles. The inclusion of these parameters increased the correlation between the regressed parameters and the A_c (m^{-1}) measurements from the transmissometer.

The regressions for February and March were combined, as were the regressions for May and June, to provide one regression for the surface, and one for the bottom, for each deployment period (Fig. 5.5). The regressions have R^2 values of between 0.6 and 0.89. When the surface and bottom data were combined, the R^2 values were lower.

5.5.3 Calibration of the central ring of the moored LISST

Data from the central ring of the LISST were used in a multiple regression against the SPM mass concentration (obtained through the gravimetric filtering of water samples taken during each CTD cast), salinity and fluorescence to provide a measure of mass concentration throughout the mooring periods.

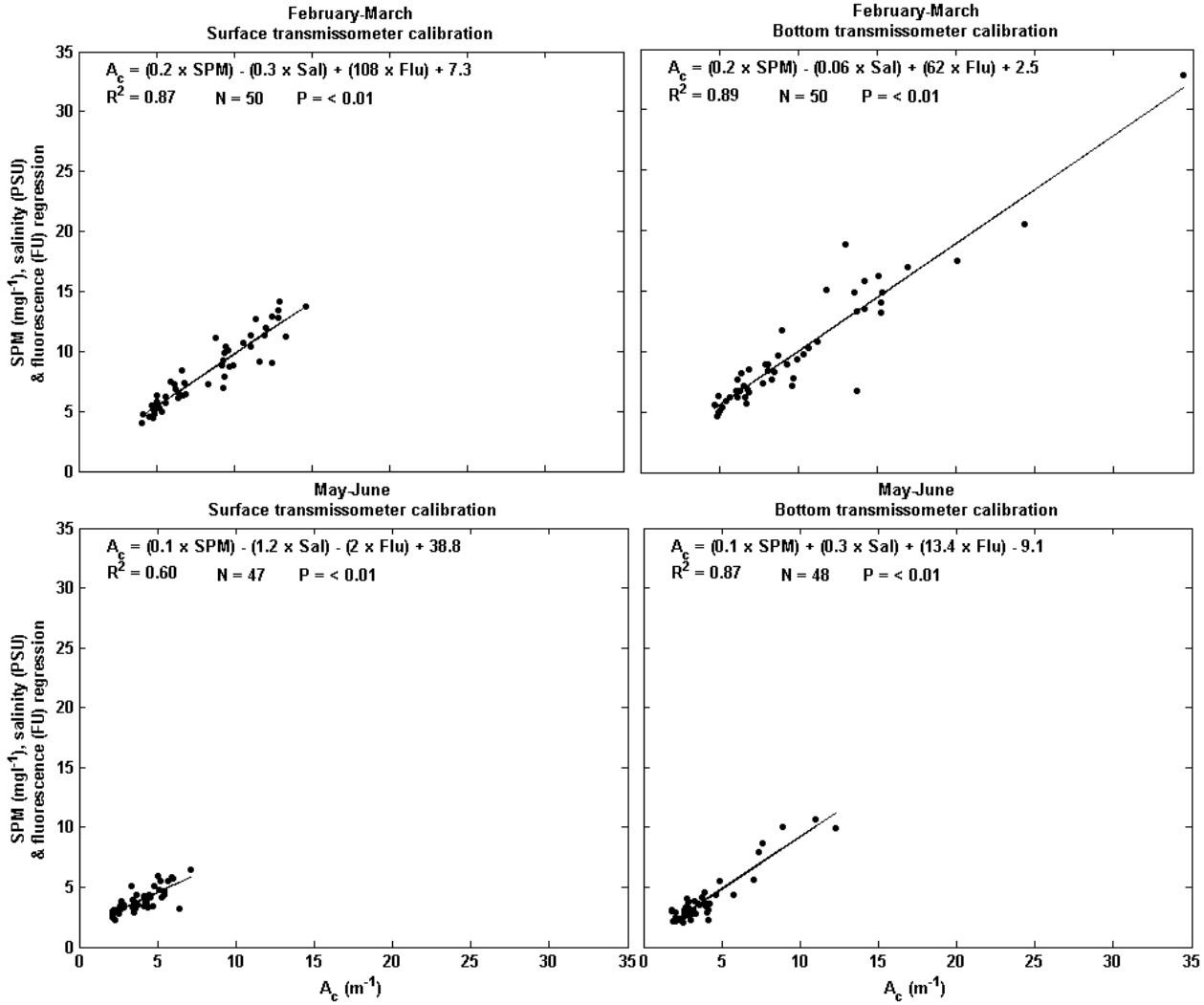

Fig. 5.5 – Calibration of the CTD transmissometer for February-March surface (top left) and bottom (top right) & May-June surface (top left) and bottom (top right). Regression is against SPM, salinity and fluorescence values

The regressions for February and March were combined. No data were available for June as all CTD casts during this period took place after the recovery of the STABLEIII tripod, and in addition, the LISST data were subject to biofouling and therefore only the first 250 hours of LISST data were available for use. In light of this, only the values derived from the CTD casts during May were used in the calibration of the central ring of the LISST for the May-June deployment. The resulting regressions, shown in Fig. 5.6, have R^2 values of 0.63 and 0.66. These calibrations were applied to the February-March dataset and the first 250 hours of the May-June data set.

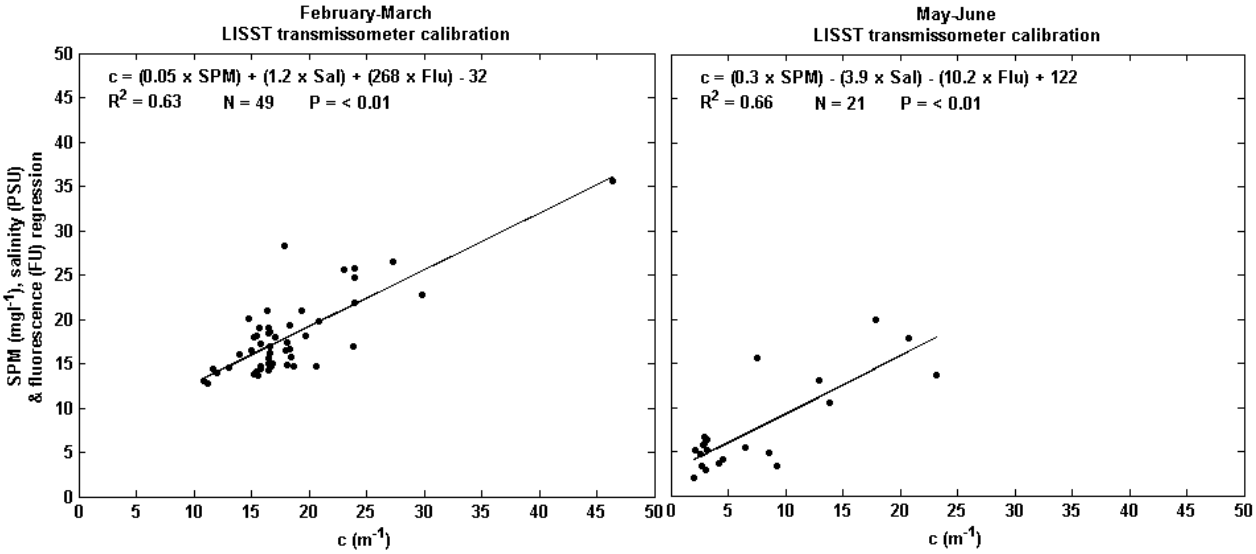

Fig. 5.6 – Calibration fits for the central ring of the moored LISST for February-March (left) and May-June (right). Regression is against SPM, salinity and fluorescence values

5.5.4 Calibration of the fluorometer

Additional gravimetrically filtered water samples taken during the May and June CTD stations were frozen immediately after filtering, and, after thawing, chlorophyll was extracted through the addition of 90% acetone. The chlorophyll concentration within the solution was then determined through spectrophotometry. Calibration of the CTD fluorometer with the chlorophyll samples (Fig. 5.7) showed concentrations in excess of 20 μgl^{-1} during the May CTD station, while concentrations peaked at ~15 μgl^{-1} during the June CTD station. The data indicated little difference between the surface and bottom chlorophyll samples. It is standard practice to exclude points from a dataset that are considered outliers. An outlier is typically classed as one that falls greater than 3 standard deviations from the mean. Two points (highlighted as filled red squares) from the May fluorescence readings were deemed outliers on this basis and were therefore not included in the regression calculation. These points may be the result of several factors: measurement errors by the instrument, water sample handling, or occasional events at the time of measurement.

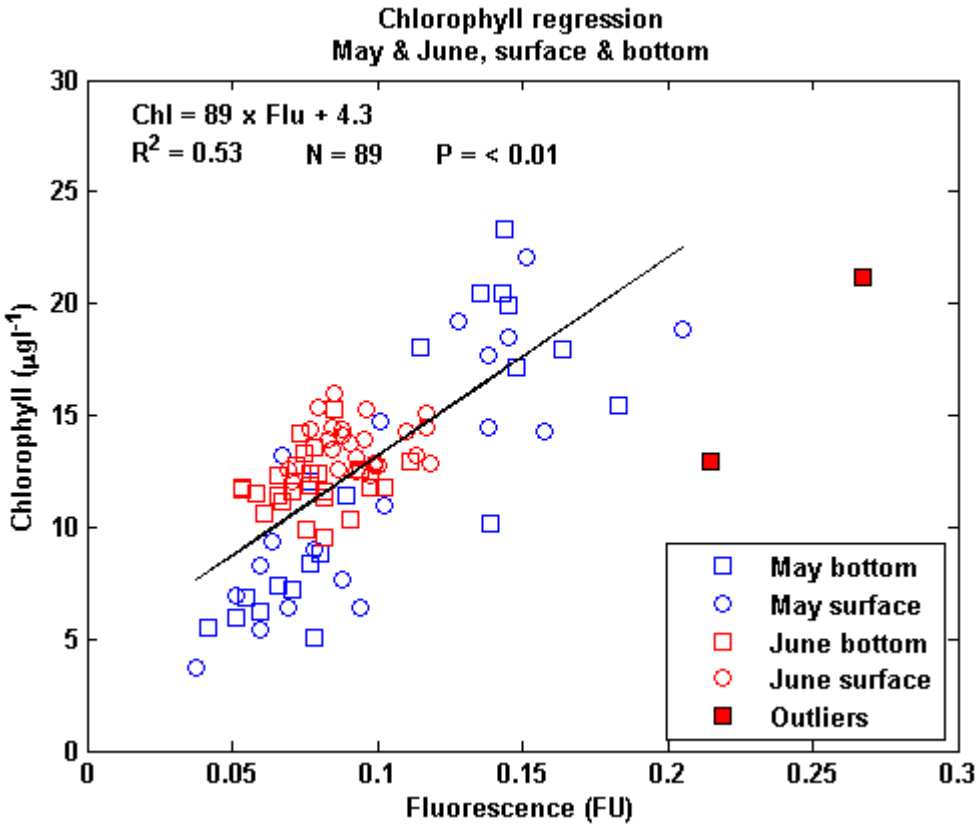

Fig. 5.7 – Chlorophyll calibration from fluorescence including outlying data points

Chapter 6

Hydrodynamics and sediment dynamics of the Dee Estuary

6.1 Introduction

The following investigations will enable the quantification of changes in the hydrodynamic and sedimentological conditions within the Dee Estuary during the study periods. Observations including tidal height, river discharge and atmospheric processes will be investigated over the duration of the deployment periods, while current speeds and the turbulence regime will be investigated over tidal and spring-neap timescales and SPM, including concentrations and particle sizes, will be investigated over tidal, spring-neap and seasonal timescales. This will enable some quantification of the processes occurring within the water column of the Dee Estuary, and the data will feed into further analysis of SPM variations in Chapter 7, and investigations of the particle characteristics and behavior presented in Chapter 8.

In the remainder of this chapter, data availability and possible data contamination is discussed in 6.2. 6.3 presents the river discharge, atmospheric and hydrodynamic conditions during the study periods, while 6.4 presents a harmonic analysis of the tidal elevations and current velocities recorded by the ADCP to establish the amplitudes of the controlling tidal harmonics. 6.5 provides an analysis of the water column structure including changes in velocity, turbulence, salinity, temperature, SPM and fluorescence over tidal, spring-neap and seasonal timescales (dependent upon data availability). 6.6 presents particle size and concentration data recorded by the LISST. Section 6.7 draws on the results of the preceding sections with discussion of the variations in water column structure and SPM characteristics, and finally 6.8 synthesises the previous sections and draws conclusions from the investigations presented.

6.2 Data contamination and availability

While all of the recorded data were available for the February-March deployment, only the first 250 hours of LISST data were available for the May-June deployment due to fouling of the LISST. This caused baseline concentrations to rise continuously, making data recorded after 250 hours unreliable. This data has therefore been discarded.

Temperature data were not available for the March CTD period due to a malfunction of the temperature probe on the CTD.

No rising tail was visible in any of the available LISST data (see Section 5.2.1), and therefore these data are deemed valid within the limitations of the LISST.

No significant tilting of the ADCP occurred during either deployment period as the ADCP was rigidly fixed to the deployed frame, and therefore the turbulence measurements made using the ADCP are deemed valid within the limitations of the ADCPs (see Section 5.2.2).

6.3 River discharge, atmospheric and hydrodynamic conditions during the study periods

6.3.1 River discharge into the Dee Estuary

The daily averaged discharge of the River Dee between July 2008 and July 2009 is shown in Fig. 6.1. The locations of the three monitoring sites shown in this figure are indicated in Fig. 4.1. The Suspension Bridge station is located ~78 km from the estuary mouth, the Iron Bridge station ~86 km from the estuary mouth, and the Manley Hall station ~137 km from the estuary mouth. A lag of approximately 1 day was seen between the peaks at Manley Hall and those at the other monitoring stations. Average discharge for the three monitoring stations during the time period shown was 33 m^3s^{-1} at the Suspension Bridge, 37 m^3s^{-1} at the Iron Bridge, and 31 m^3s^{-1} at Manley Hall – relating closely to the average discharge of 31-40 m^3s^{-1} given by Lambert, (1988), Simpson, et al., (2004), and Bolanos and Souza (2010). A peak discharge of ~175 m^3s^{-1} was recorded during September 2008, far short of the peak discharge of 300 m^3s^{-1} reported by Bolanos and Souza (2010).

Table 6.1 shows the average and peak river discharge recorded at the Manley Hall monitoring station (Fig. 4.1) during the February-March and May-June deployment periods, and the first 250 hours of the May-June deployment for which LISST data were available. The Suspension Bridge and Iron Bridge monitoring stations are located within the tidally influenced river, and therefore discharge rates from Manley Hall are presented as these figures represent a true measure of the freshwater river discharge.

Both peak and average discharge decreased between the deployment periods, with the average discharge during the first 250 hours of the May-June deployment 31% lower than the average discharge during the February-March deployment. Concurrently, peak discharge was decreased by 52%.

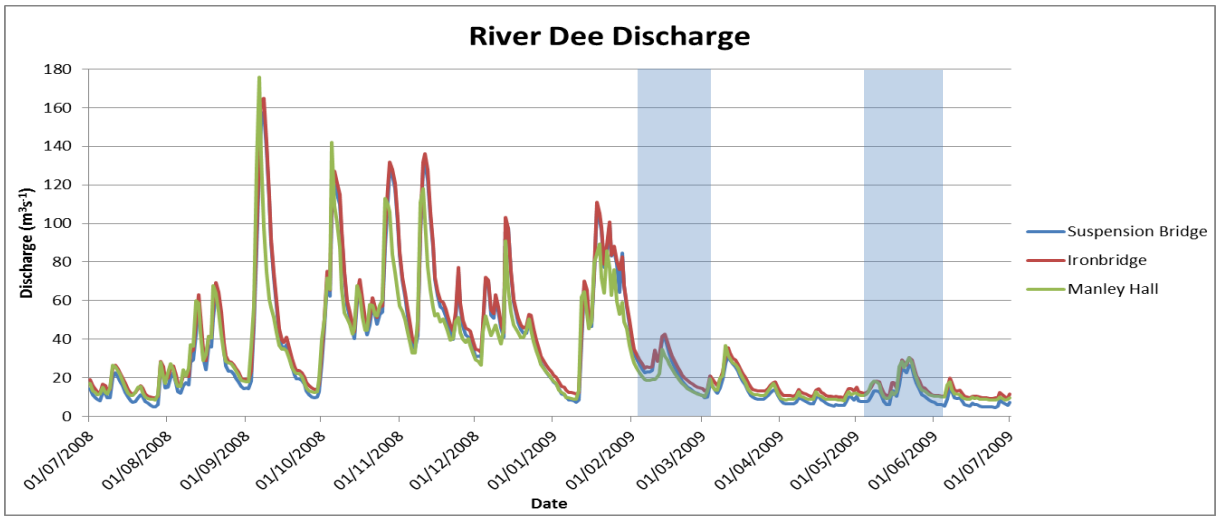

Fig. 6.1 – Daily averaged discharge of the Dee River between July 2008 and July 2009 measured at three Environment Agency monitoring stations with data collection times for the present study highlighted

6.3.2 Atmospheric conditions during the observation periods

The atmospheric conditions during both the February-March and May-June deployment periods were recorded by a permanent weather station on Hilbre Island (location shown in Fig. 4.2) which records atmospheric conditions at 10 minute intervals. Precipitation records were not available for either deployment period; however, measurements of wind speed, wind direction, temperature and solar radiation were available. Average values of the

atmospheric conditions across the deployment periods and during the first 250 hours of the May-June deployment are presented in Table 6.2. The hourly-averaged atmospheric conditions are presented in Fig. 6.2 for February-March and Fig. 6.3 for May-June.

Table 6.1 – Peak and average river discharge for the February-March and May-June deployment periods in 2009 recorded at the Environment Agency monitoring station at Manley Hall

Time period	Peak discharge (m^3s^{-1})	Average discharge (m^3s^{-1})
February-March	38.5	19.5
May-June (full month)	31.4	15.4
May-June (first 250 hours)	18.3	13.4

Average wind speed values were comparable between the two full deployment periods, however, the first 250 hours of the May-June deployment were subject to periods of high wind speed (Fig. 6.3), and therefore the average wind speed during this time was almost twice that recorded during the February-March deployment (Fig. 6.2). The high wind speed events during the first 250 hours of May-June originated from ~220°, and not from the 270-360° sector, which provides the largest fetch and therefore largest waves to the Dee Estuary. Overall, winds originated from the 270-360° sector during February-March for 186 hours, averaging 8.2 ms^{-1}, compared with just 13 hours at an average of 6.5 ms^{-1} during the May-June deployment. Therefore, the February-March deployment was subjected to a greater duration of higher-influence wind conditions.

Table 6.2 – Average values of atmospheric conditions during the February-March and May-June deployment periods

Time Period	Wind speed (ms^{-1})	Wind direction (°N)	Air temperature (°C)	Solar radiation (Wm^{-2})
February-March	6.5	214.2	4.7	47.3
May-June (full month)	6.7	178.3	12.0	184.7
May-June (first 250 hours)	12.5	236.0	11.9	92.3

Average air temperature was higher during May-June than February-March (Table 6.2), and generally increased during both deployment periods (Fig. 6.2c & Fig. 6.3c). Values of solar radiation (Fig. 6.2d & Fig. 6.3d) were almost 4 times higher on average during May-June than February-March. During the first 250 hours of the May-June deployment, this ratio was lower, but the average solar radiation value was still almost double that for the February-March period (Table 6.2).

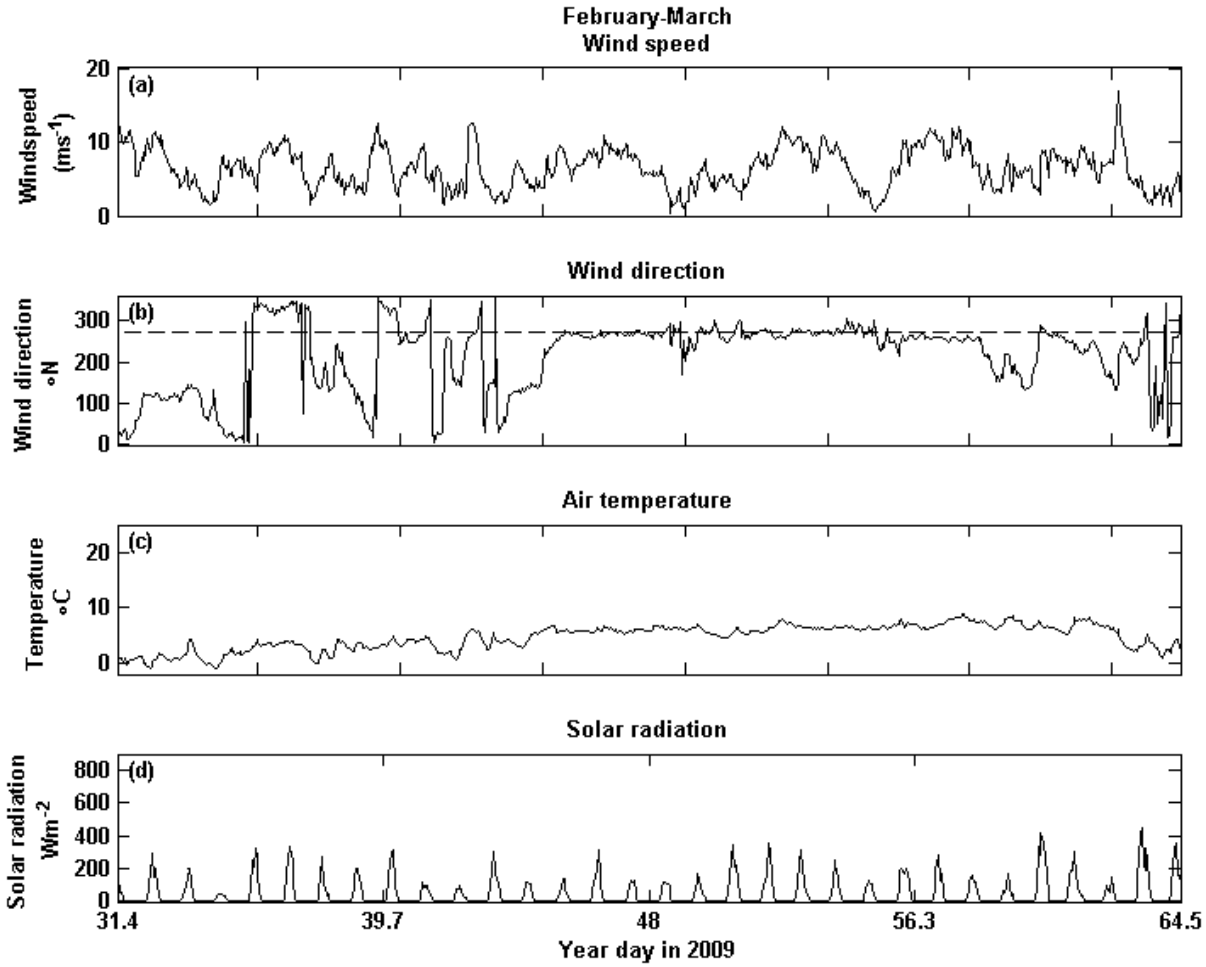

Fig. 6.2 – Hourly-averaged Hilbre Island weather station conditions during the February-March deployment including wind speed (a), wind direction (b), air temperature (c) and solar radiation (d). Wind direction (b) includes a line at 270° as wind directions between 270° and 360° have the greatest fetch distance

6.3.3 Tidal conditions during the observation periods

Velocities and tidal ranges

Fig. 6.4 shows the tidal conditions experienced during the two observation periods, with the CTD station periods highlighted with grey boxes. More than an entire spring-neap cycle of data was collected during both the February-March and May-June observations. The period of data recording for which LISST data is available during the May-June deployment is indicated in Fig. 6.4g, h & i.

The maximum positive and negative depth averaged velocities (Fig. 6.4a & d – positive velocity indicates flood) were similar during the deployment periods. Depth averaged velocities reached a maximum of 1.22 ms^{-1} during the flood and -1.26 ms^{-1} during the ebb in February-March, 1.24 ms^{-1} during the flood and -1.31 ms^{-1} during the ebb in May-June. Despite this perceived ebb dominance, averaging the tidal currents over the mooring periods gives an average flood current speed 0.1 ms^{-1} faster than the average ebb current speed during May-June and a concurrent flood dominance of 0.12 ms^{-1} during February-March. The maximum ADCP error velocities were 0.02 ms^{-1} during the February-March deployment and 0.009 ms^{-1} during May-June, giving confidence that the differences in average values between the flood and ebb tidal periods are a true representation that the velocities were flood dominant during both deployment periods. Water depth, measured using the pressure sensor of the ADCP displays a semi-diurnal tidal signal, with strong spring-neap modulation (Fig. 6.4c & f). The spring tidal range reached 9.4 m during February-March, 8.1 m during May-June and reduced during neaps to 2.9 m in February-March, 3.1 m in May-June.

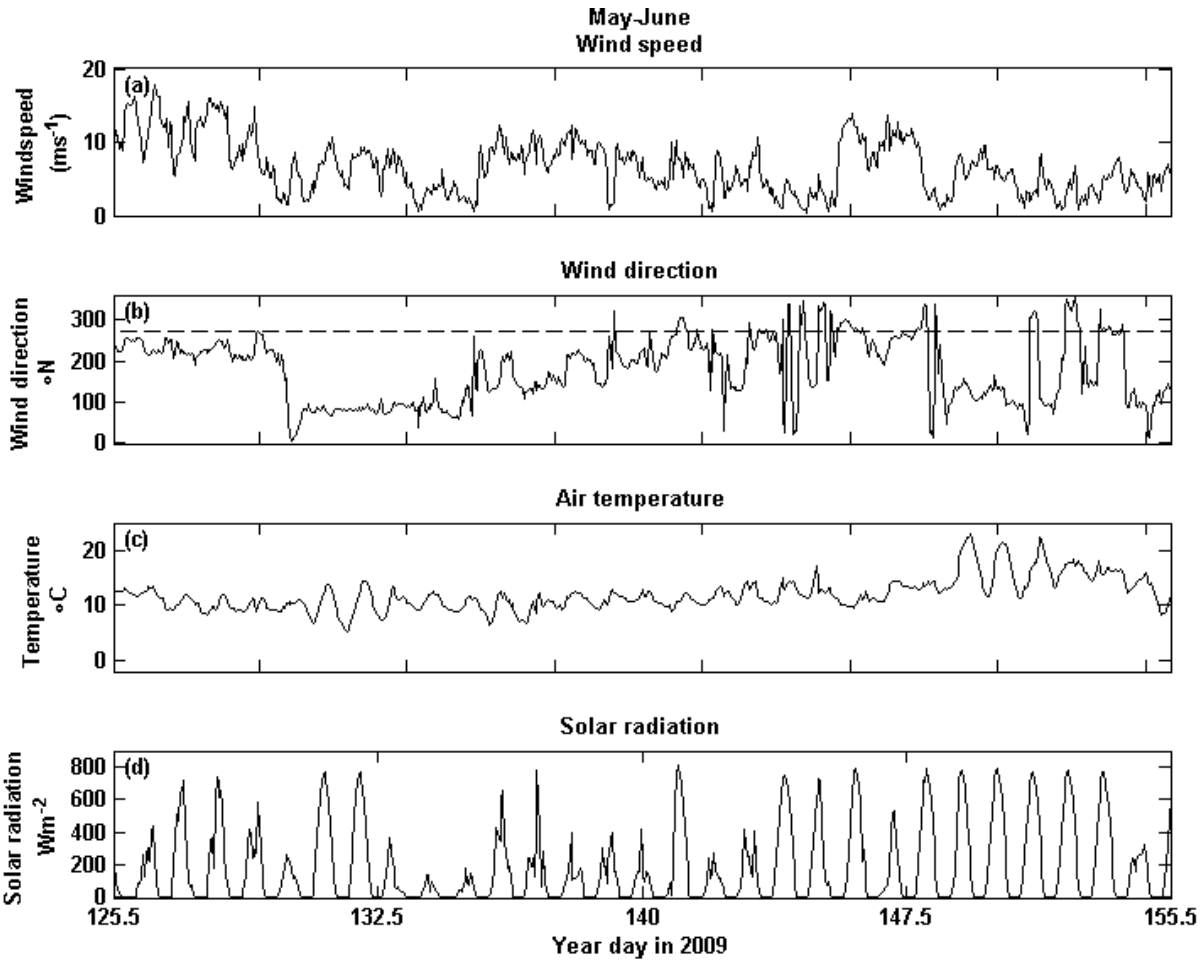

Fig. 6.3 – Hourly-averaged Hilbre Island weather station conditions during the May-June deployment including wind speed (a), wind direction (b), air temperature (c) and solar radiation (d). Wind direction (b) includes a line at 270° as wind directions between 270° and 360° have the greatest fetch distance

Tidal excursion

The tidal excursion (the distance water is transported during a flood or ebb tidal period) can be approximated by integrating the current speed over the time available. The tidal excursion changes over the spring-neap cycle as current speeds change due to changes in the tidal elevation. Tidal excursions for the present study were calculated using the hourly-averaged current speeds from the ADCP. During peak spring conditions, the tidal excursion in both February-March and May-June reached a maximum of 15.7 km. During neap

conditions, the tidal excursion in February-March fell to 6 km, with a minimum of 7 km reached during May-June.

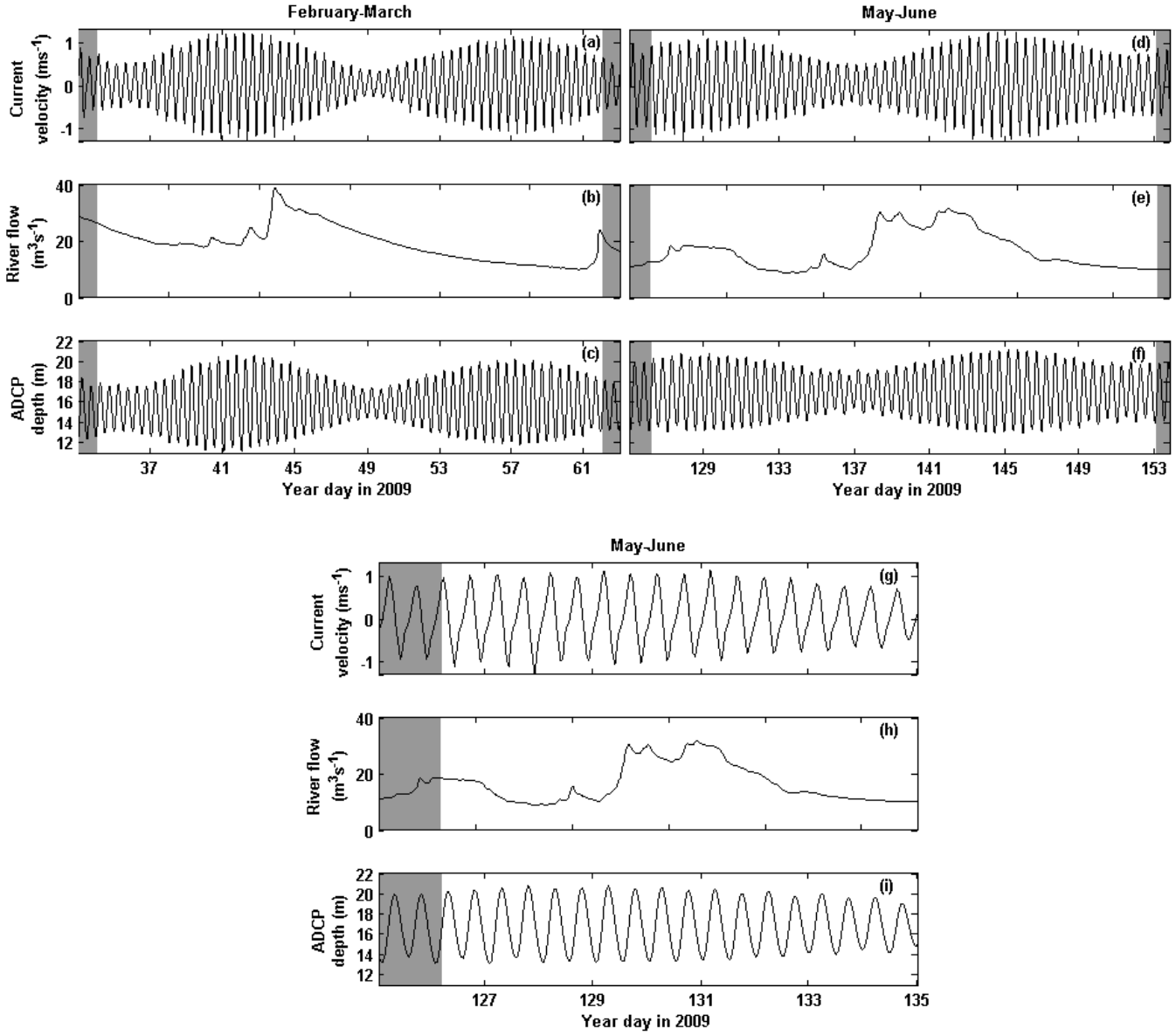

Fig. 6.4 – Conditions during the observation periods. (a), (d) & (g) are depth-averaged current velocity with positive values indicating flood velocities. (b), (e) & (h) are river flow from the Environment Agency monitoring station at Manley Hall, Chester, and (c), (f) & (i) are water depth recorded by the ADCP. (d), (e) & (f) indicate the entire May-June period, (g), (h) & (i) the first 250 hours only

6.3.4 Wave conditions during the observation periods

Impact of waves upon the Dee Estuary

The waves inside the Dee Estuary are modulated by the tidal forcing. During low water, waves are small as the majority of the wave energy is dissipated on the sand banks extending out from the estuary mouth, and therefore only small, locally generated wind waves occur in the estuary channels. Surface elevation is the main controlling factor on wave propagation into the Hilbre Channel of the Dee Estuary (Bolanos, et al., 2014); with high levels of wave propagation occurring only when water levels exceed the mean tidal level (Brown, et al., 2014). As the impact of waves tends to be greatest in a shallow water column and reduce as the water column depth increases, the impact of waves in the Hilbre Channel tends to be small. In addition, the NW-SE alignment of the estuary is perpendicular to, and therefore sheltered from, the SW-W wind direction that is associated with the most extreme surge events (Brown, et al., 2014).

Wave heights from Liverpool Bay during the deployment periods

The daily-averaged significant wave heights in Liverpool Bay, provided by the CEFAS WaveNet Buoy (http://www.cefas.co.uk/data/wavenet.aspx) remained below 2 m (Fig. 6.5) during both deployment periods, indicating that waves had a negligible impact upon the recorded data. Daily averaged significant wave heights ranged from 0.19 to 1.58 m during February-March, averaging 0.7 m, and 0.19 to 1.85 m during May-June, averaging 0.68 m. This indicates that the two time periods were comparable from the perspective of offshore wave forcing.

Wave heights from the STABLEIII ADCP during the deployment periods

The ADCP data from the STABLEIII benthic tripod was analysed using the Teledyne RDI WavesMon software (http://www.rdinstruments.com/waves.aspx) which provides measures of significant waveheight (H_s), wave period (T_p) and wave direction (dir). The data follows the general pattern of wave heights seen in the CEFAS WaveNet Buoy data (Fig. 6.5) and emphasises the low impact of waves during both deployment periods (Fig. 6.6). The largest significant wave heights during the May-June deployment occurred during high water at spring tides, while the largest waves during February-March were found shortly

after the first neap period, again during high water. Maximum H_s during February-March was 1.27 m, with a mean of 0.32 m by comparison with a maximum of 1.72 m and mean of 0.28 m during the May-June deployment.

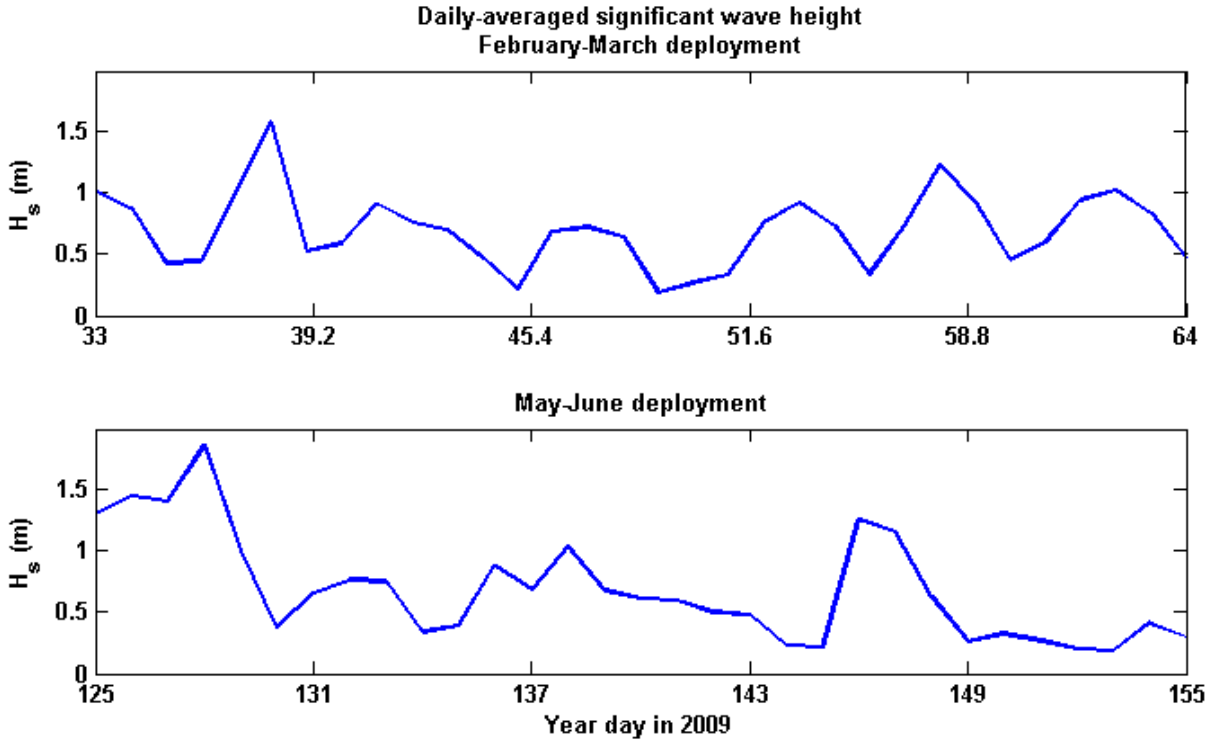

Fig. 6.5 – Daily averaged significant wave height from the Liverpool Bay CEFAS WaveNet Buoy (located at 53°32.01'N, 03°21.33'W) during the February-March (top) & May-June (bottom) deployment periods

The maximum observed wave heights during both deployment periods occurred close to high water (Fig. 6.6 & Fig. 6.7). Because of this, no waves larger than 1 m occurred in water shallower than 18.4 m. The ratio of water depth to significant wave height had a minimum value of 16:1 during February-March (H_s of 1.27m in water of depth 20.6m) and 13:1 during May-June (H_s of 1.72m in water of depth 23m).

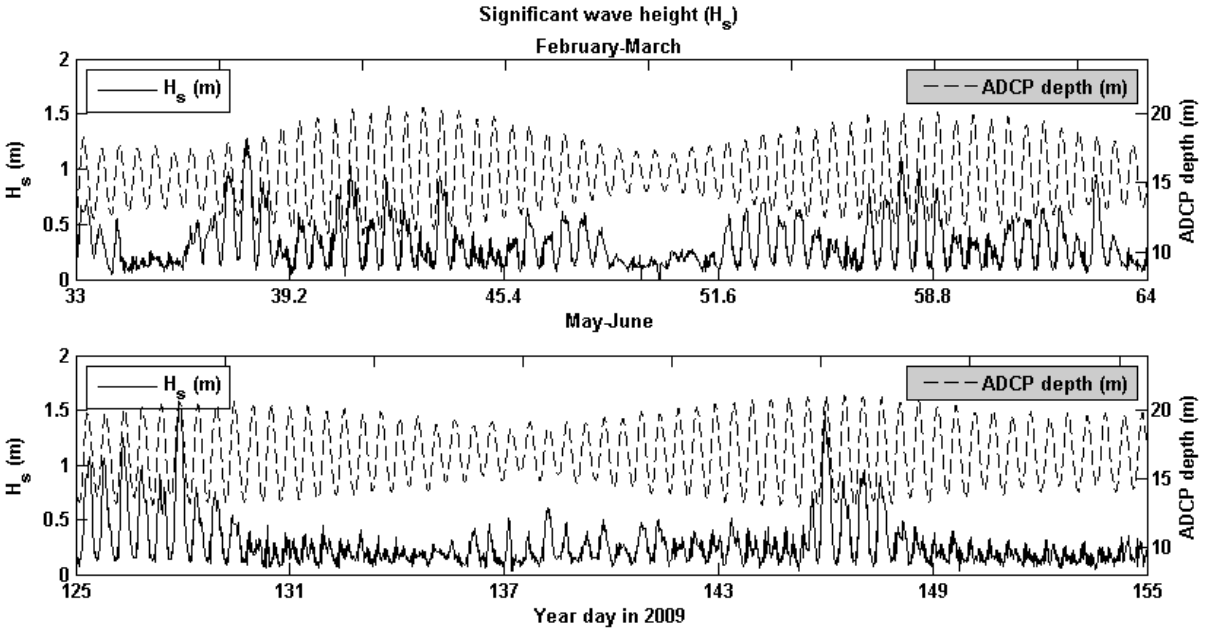

Fig. 6.6 – Time series of H_s during the February-March (top) and May-June (bottom) deployment periods

Values of u_w (Fig. 6.8), calculated using the method outlined in Section 3.2.4, were comparable between the deployment periods, with maxima of 0.06 ms^{-1} during February-March and 0.08 ms^{-1} during May-June. The mean u_w value during both deployment periods was 0.01ms^{-1}. Therefore, wave effects during both the February-March and May-June deployment periods were negligible.

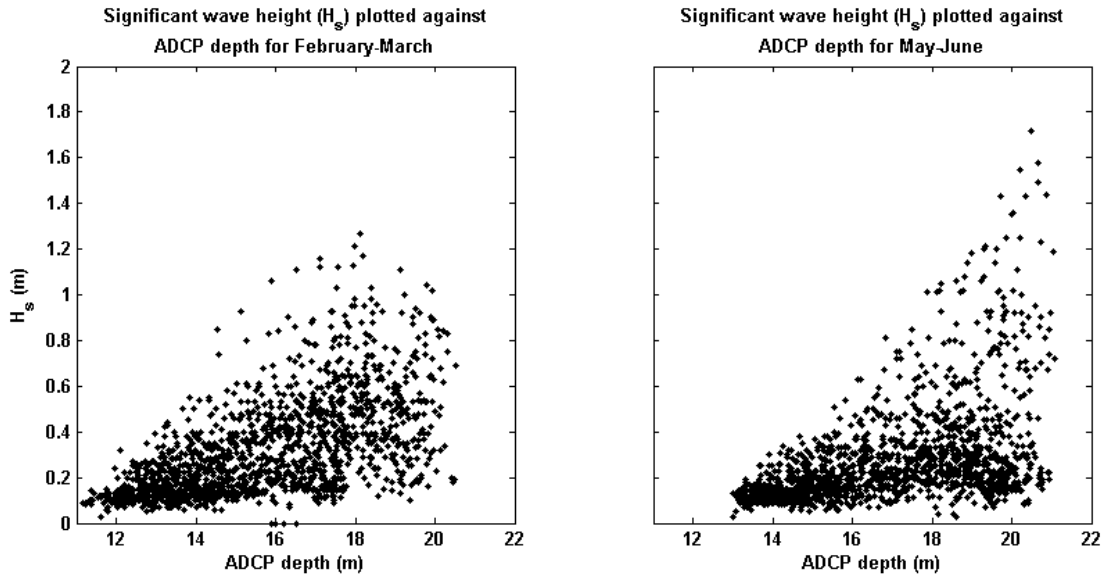

Fig. 6.7 – Significant wave height plotted against ADCP depth during the February-March (left) and May-June (right) deployment periods

6.4 Harmonic analysis of the tidal signal

Newton (1687) was the first to reason that oceanic tides were produced by the gravitational attraction of the sun and the moon upon the waters. This was furthered by Thomson (1881) who reasoned that variations in tidal amplitude could be expressed as a number of combined sine waves, and his initial work progressed by Doodson (1921), Proudman (1928), Godin (1972), and Pugh (1987), amongst others, who showed that by adjusting the amplitudes of these sine waves, it is possible to reproduce observed data. To determine the tidal constituents driving the changes in tidal elevation and velocities in the Hilbre Channel of the Dee Estuary, harmonic analyses were performed on the tidal elevation and velocity data by fitting harmonic constituents based upon astronomical frequencies to the data using the "least squares" method in t_tide – a MATLAB software package which analyses a time-series of data and establishes the relative strengths of the controlling tidal harmonics (Pawlowicz, et al., 2002). t_tide provides error levels using a bootstrap technique, signal-to-noise ratios, and the amplitudes of the harmonic constituents identified in the analysis.

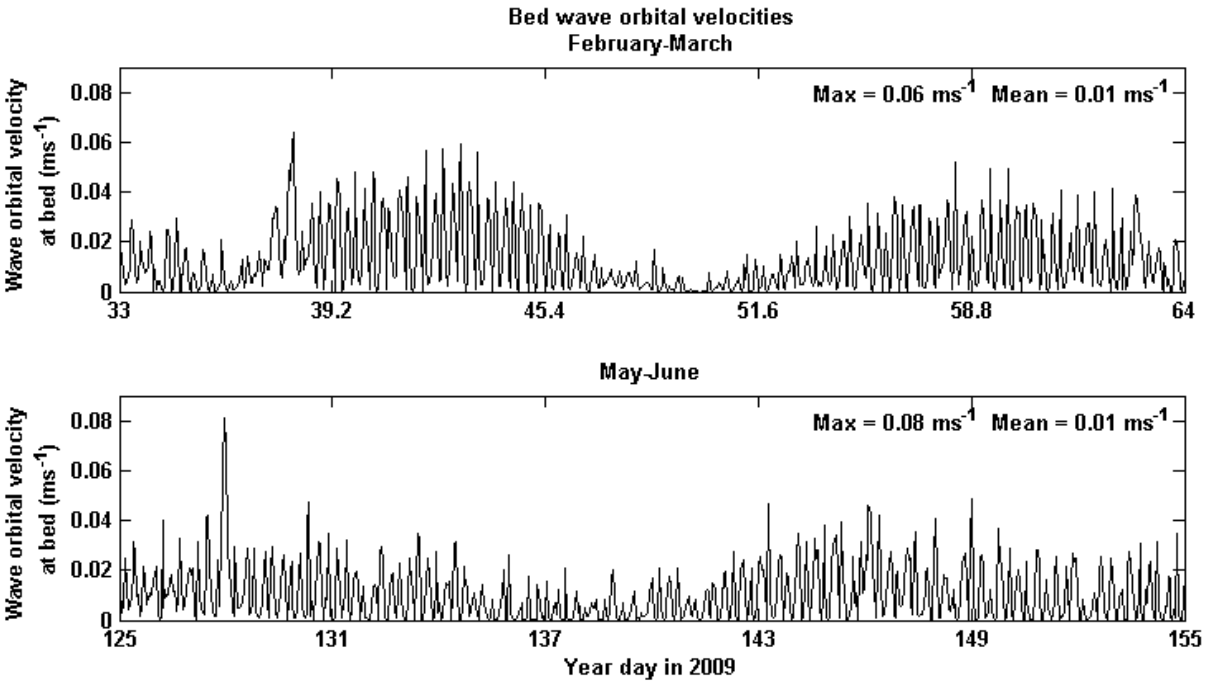

Fig. 6.8 – Approximation of bed wave orbital velocities for the February-March (top) and May-June (bottom) deployment periods

Table 6.3 shows the harmonic components (in m) resulting from the harmonic analysis of the ADCP pressure signal, with the error range and signal-to-noise ratio (S.N.R.). All of the tidal constituents presented have signal-to-noise ratios in excess of 6.5 (the strength of the signal power is 6.5 times that of the noise power), providing confidence that the figures presented are accurate within the error limits shown.

Most of the tidal harmonics presented in Table 6.3 show variations in amplitude of a few percent between the February-March and May-June deployment periods. Exceptions to this are the S_2 and K_1 tides. The M_2 constituent was the dominant tidal harmonic during both observation periods, accounting for a tidal elevation of greater than double that of the next most significant constituent (S_2).

Table 6.3: Tidal harmonics produced from analysis of the month-long pressure series from the STABLEIII ADCP's for February-March (left) & May-June (right)

	February-March		May-June	
Tide	**Elevation (m)**	**S.N.R.**	**Elevation (m)**	**S.N.R.**
M_2	3.0 +/- 0.15	3.9×10^2	3.1 +/- 0.14	4.7×10^2
S_2	1.3 +/- 0.15	72	0.74 +/- 0.11	44
N_2	0.57 +/- 0.15	13	0.61 +/- 0.13	21
M_4	0.20 +/- 0.031	40	0.19 +/- 0.021	83
MS_4	0.17 +/- 0.032	27	0.087 +/- 0.023	15
O_1	0.12 +/- 0.013	82	0.12 +/- 0.018	49
M_6	0.02 +/- 0.009	6.8	0.028 +/- 0.009	9.6
M_3	0.03 +/- 0.013	6.7	0.038 +/- 0.007	31
K_1	0.10 +/- 0.015	40	0.15 +/- 0.016	87

Table 6.4 is the result of a harmonic analysis performed using t_tide (Pawlowicz, et al., 2002) on the depth-averaged velocity time series from the ADCP for the February-March and May-June deployment periods, respectively. The tidal harmonics presented in Table 6.4 show variations in amplitude greater than those displayed in Table 6.3 between the February-March and May-June deployment periods. As with the tidal elevation (Table 6.3), the M_2 tidal harmonic was dominant, accounting for double the current speed of the next most significant harmonic, which was again the S_2 constituent.

6.5 Water column structure

The velocity and turbulence profiles presented in this section (Fig. 6.9 to Fig. 6.11) show conditions typical of those recorded during both the February-March and May-June deployments.

Table 6.4: **Velocity contributions produced from analysis of the month-long velocity series from the STABLEIII ADCPs for February-March (left) & May-June (right)**

	February-March			May-June		
	Major (ms^{-1})	**Minor (ms^{-1})**	**S.N.R**	**Major (ms^{-1})**	**Minor (ms^{-1})**	**S.N.R**
M_2	0.68 +/- 0.026	-0.016 +/- 0.01	7×10^2	0.74 +/- 0.018	-0.009 +/- 0.02	1.7×10^3
S_2	0.29 +/- 0.026	0.008 +/- 0.01	1.3×10^2	0.19 +/- 0.018	0 +/- 0.02	1.1×10^2
M_4	0.16 +/- 0.018	-0.004 +/- 0.01	83	0.18 +/- 0.013	0 +/- 0.01	2.1×10^2
MS_4	0.15 +/- 0.018	0.003 +/- 0.01	66	0.09 +/- 0.012	0.003 +/- 0.01	53
N_2	0.12 +/- 0.025	0.016 +/- 0.01	23	0.15 +/- 0.018	-0.006 +/- 0.02	66
$2MS_6$	0.032 +/- 0.009	0.005 +/- 0	11	0.024 +/- 0.006	0 +/- 0	14
M_6	0.026 +/- 0.01	0.001 +/- 0	7	0.033 +/- 0.006	-0.002 +/- 0	26

6.5.1 Changes in velocity over the tidal and spring-neap cycles

Velocity changes over the tidal cycle

The along-channel and vertical velocities, as recorded by the ADCP during peak spring conditions in February-March, are presented in Fig. 6.9. The along-channel velocities during spring tides (Fig. 6.9a) reached maxima in excess of 1.2 ms^{-1} during both flood and ebb. The highest velocities during the flood were found in the middle of the water column, while velocities during ebb were greatest in the middle and towards the upper parts of the water column. The lowest current speeds were found during high and low water. These slack water periods were not equal in length, with low water (defined for the purposes of this study as the time when the depth averaged current speed was < 0.2 ms^{-1}) lasting approximately 2.2 times longer than high water. During low water, a weak seaward (negative) flow was present in the upper water column.

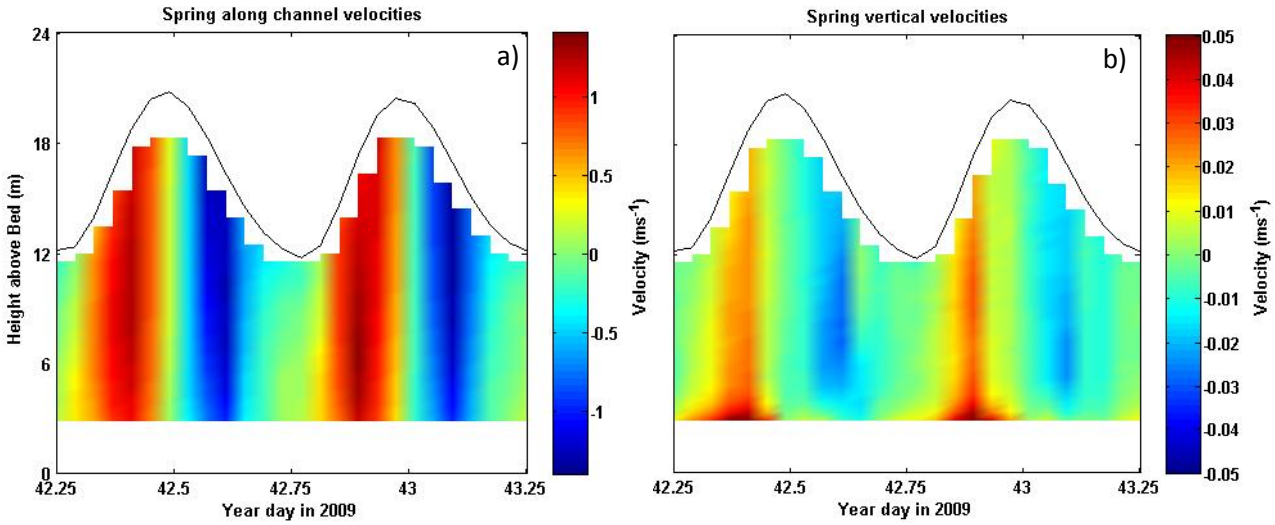

Fig. 6.9 – Typical along channel (a) and vertical (b) velocities during spring tides, from February-March deployment

The vertical velocities (Fig. 6.9b) showed a positive (upward) velocity during the flood tide, greatest in the lowest bins of the ADCP and decreasing towards the sea surface. Conversely, a negative (downward) velocity occurred during the ebb tide that was present at the sea surface, greatest in the middle of the water column, and disappeared almost entirely in the lowest bins of the ADCP. Little vertical shearing of velocity occurred.

Velocity changes over the spring-neap cycle

During neap tides, the along-channel velocities (Fig. 6.10a) displayed the same patterns as those during spring tides (Fig. 6.9a) but with key differences. The magnitude of the velocities was reduced, with current speeds rarely exceeding +/- 0.5 ms^{-1}. The highest velocities were again found in the middle of the water column during the flood and towards the surface during the ebb, as during spring conditions. Greater velocity shear was present during the early flood, with higher velocities (~0.3 ms^{-1}) found in the lowest bins of the ADCP while surface velocities were still low (~0 ms^{-1}). Low water again lasted for longer than high water. During low water, some velocity shear occurred, with a negative outward surface flow persisting over a positive inflow lower in the water column.

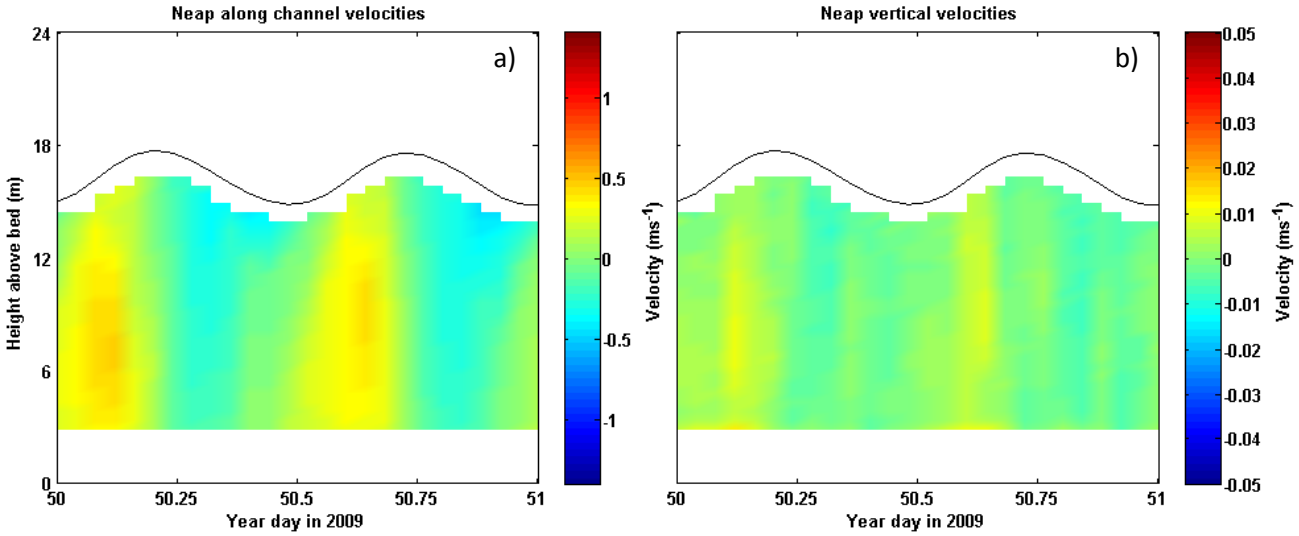

Fig. 6.10 – Typical along channel (a) and vertical (b) velocities during neap tides, from the February-March deployment

The vertical velocities (Fig. 6.10a) displayed similar patterns to those seen during spring tide conditions (Fig. 6.9a), but with a reduction in magnitude. Positive, upward flow occurred during the flood tide, with a negative, downward flow during ebb. The large upward flow seen in the lowest bins of the ADCP was no longer as prevalent, and the strong downward flow seen in the middle of the water column during the spring tidal conditions was also no longer present (Fig. 6.9b). Vertical velocities during neap tides were generally weak, reaching a maximum of +/- 0.01 ms^{-1}.

6.5.2 Changes in turbulence over the tidal and spring-neap cycle

Examples of turbulence production during spring and neap tides are presented in Fig. 6.11 (note that these figures are plotted on a log scale). During spring tides (Fig. 6.11a), turbulence production was asymmetric with higher production during the ebb by comparison with the flood tide. Production was greatest in the lowest bins of the ADCP, reducing in magnitude toward the sea surface. Turbulence production was low during both high and low water, though regions of high turbulence persisted in the surface regions of the water column during all stages of the tide. Elevated levels of production were present in much of the water column during the early flood.

Turbulence production during neap tides (Fig. 6.11b) displayed a similar pattern to that recorded during spring tides, but on a much reduced scale and with less ebb dominance of production. Peaks in production occurred in the lowest bins of the ADCP during the flood and ebb tides, while the estuary surface experienced elevated levels in the top metre of the water column. Elevated levels also occurred in the surface regions (top ~3 m) during low water.

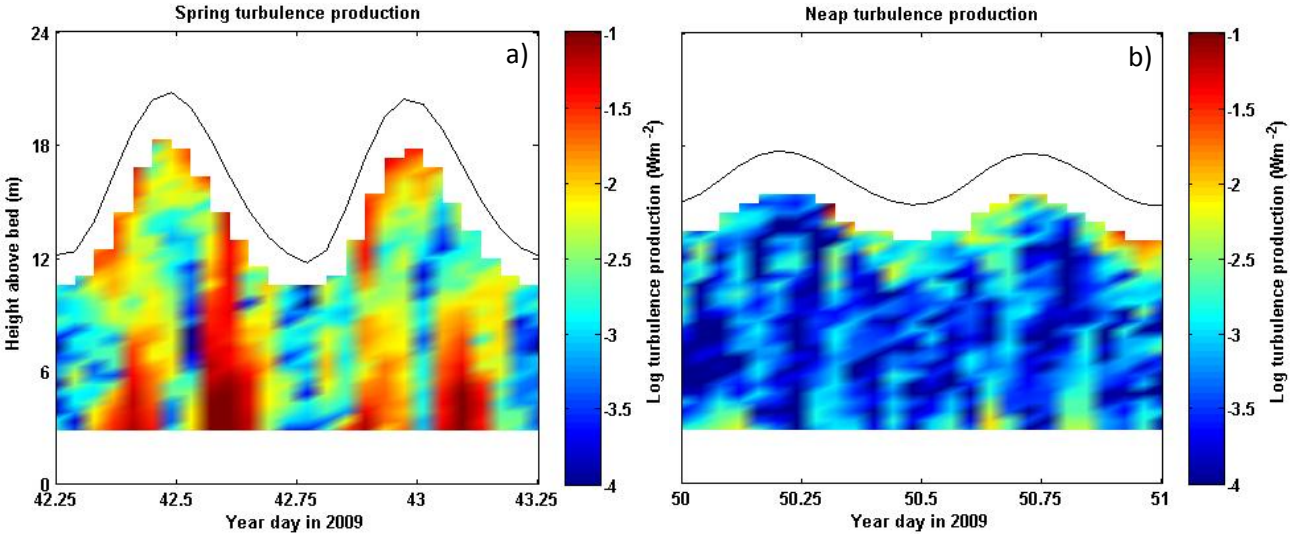

Fig. 6.11 – Typical log of turbulence production during spring (a) and neap (b) tides, taken from the February-March deployment

6.5.3 Changes in salinity over the tidal and seasonal cycle

The salinity of the water column varied almost continuously over the tidal cycle (Fig. 6.12) during all CTD periods. The water column was well-mixed and reached maximum salinity during high water (exceptions include the second high water during February (Fig. 6.12a) and March (Fig. 6.12b) during which some salinity stratification was present). Conversely, salinity reached a minimum and the water column experienced periodic vertical stratification near low water in all months. A gradual, vertically homogeneous reduction in salinity occurred between high water and low water. During low water, salinity stratification was established and persisted into the early flood before being broken down by the incoming tide.

The difference in surface salinity between high and low water (Fig. 6.12) varied from a maximum of 4.6 PSU (in February) and 1.43 PSU (in June), while the surface to bottom

salinity difference during low water varied from a maximum of 3.5 PSU (in February) and 1.6 PSU (in May).

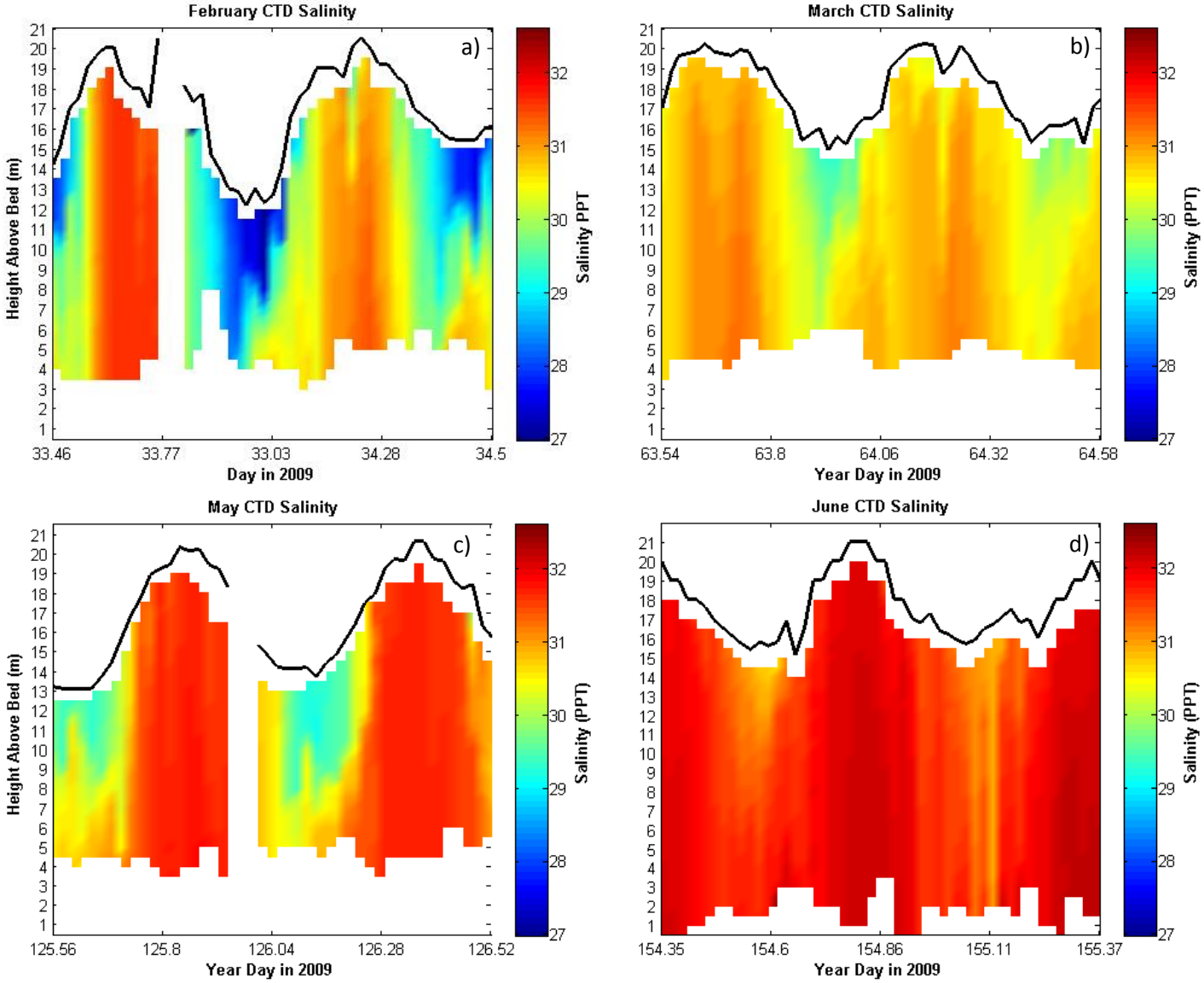

Fig. 6.12 – Salinity profiles from CTD casts during February (a), March (b), May (c), and June (d)

6.5.4 Changes in temperature over the tidal and seasonal cycles

Water temperature, recorded during the CTD stations, is presented in Fig. 6.13. Data were not available for the March CTD period due to a temperature probe malfunction. Overall,

temperatures increased between CTD observation periods from a minimum of 2.9 ˚C in February to a maximum of 17.9 ˚C in June.

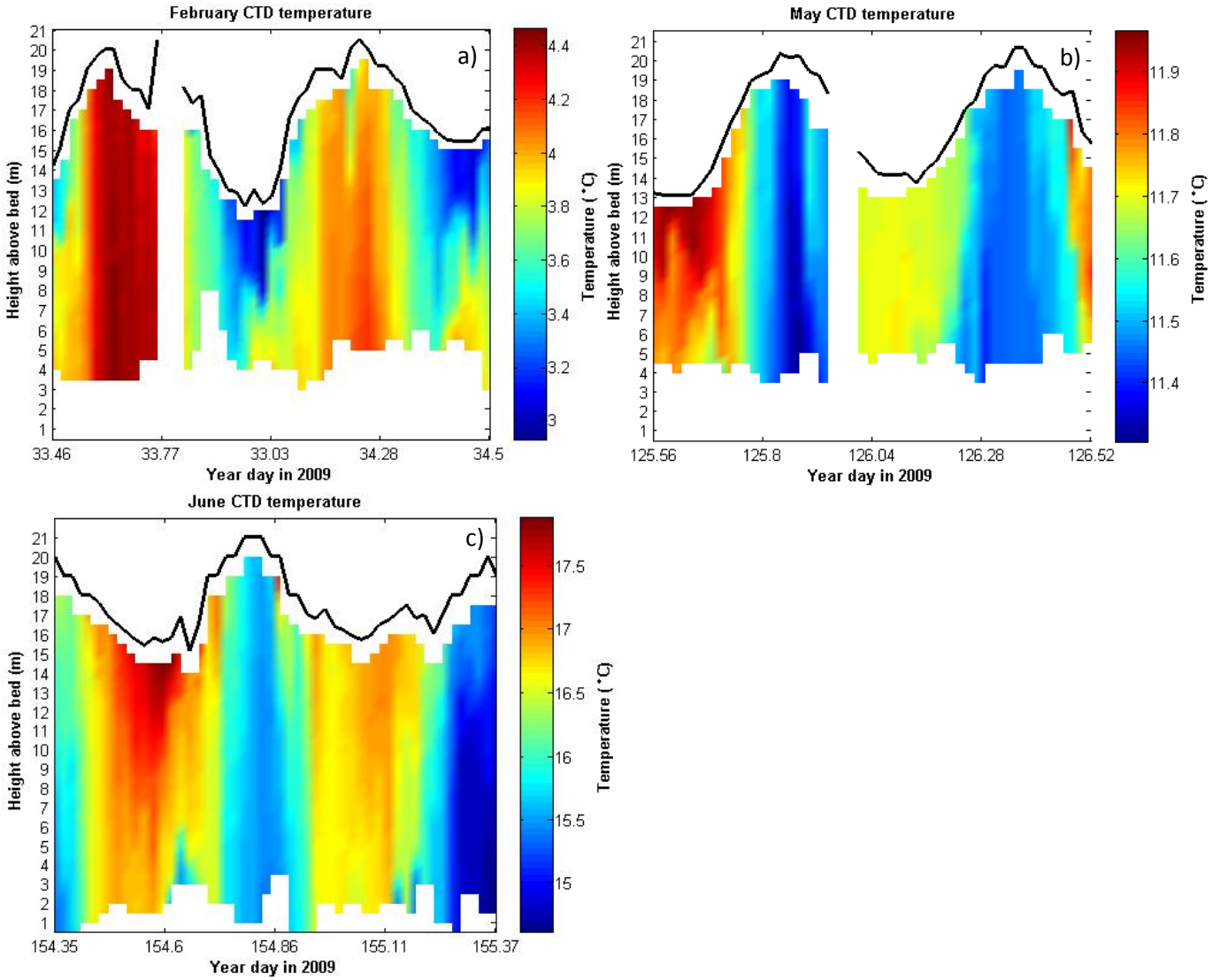

Fig. 6.13 – Temperature profiles from CTD casts during February (a), May (b) and June (c)

During the May and June CTD stations, the highest temperatures were recorded in the surface regions during low water, with the lowest values recorded during high water (Fig. 6.13b & c). However, during February (Fig. 6.13a), this pattern was reversed, with the lowest temperatures recorded during low water, and the highest temperatures during high water. The difference between the high and low water temperatures at the estuary surface varied from a maximum of 2.7 ˚C (in June) to 0.2 ˚C (in May), while the low water surface to bottom temperature gradient varied from a maximum of 2.3 ˚C (in June) to 0.1 ˚C (in May).

6.5.5 Changes in SPM mass concentration over the tidal and seasonal cycles

Calibrated SPM mass concentration from the CTD transmissometer is shown in Fig. 6.14. Because separate regressions between the transmissometer and SPM concentrations were calculated for the surface and bottom as the regression improved when salinity and fluorescence were included (see Section 5.5.2), in order to determine where to apply the surface and bottom regressions, the N^2 (buoyancy frequency) was calculated (Eq. (2.40)), providing the point of maximum density change on each cast.

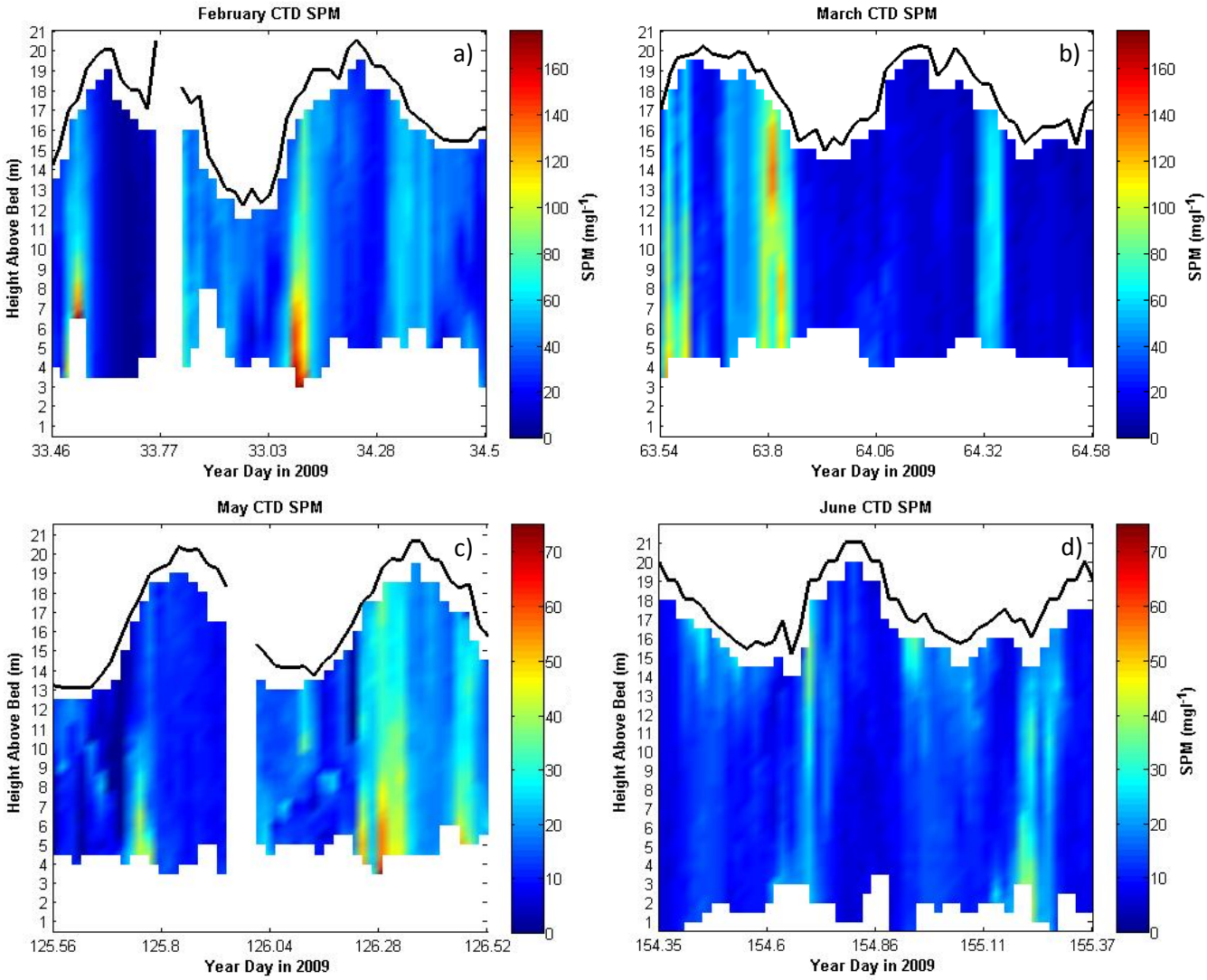

Fig. 6.14 – Calibrated SPM from the CTD transmissometer. Note that May (c) and June (d) are plotted on a different colour scale to February (a) and March (b) as without this no data are visible during the June CTD period

Where the N^2 value was significant (> 0.025 s (Mikkelsen, et al., 2008)), the surface calibration was applied to data above this depth, with the bottom calibration applied below. During periods where N^2 did not reach 0.025 s, the bottom calibration was applied throughout the water column, as this occurred during high water when the water column was fully mixed, and close to maximum salinity.

6.5.6 Changes in fluorescence over the tidal and seasonal cycles

Fluorescence response (used in Fig. 6.15 for all months for comparison as chlorophyll samples were not taken during the February or March CTD stations) during the February and March CTD stations peaked during the flood and ebb, with response decreasing with height above the bed. Response increased rapidly for a short period (2-3 hours) during the flood and ebb tides before falling to low values during both high and low water – decreasing slower during low water than high. By contrast, fluorescence response recorded during the May and June CTD stations increased during the late ebb and low water, with no obvious vertical gradient present. Fluorescence response during June had a higher overall average value than that during May despite the range of values encountered during May (0.03 to 0.31 by comparison with 0.05 to 0.14 during June) being higher. It should be noted that the scales on the fluorescence figures in Fig. 6.15 are not the same, as the fluorescence values during February and March were so low that no data are visible if the figures are scaled to the maximum value encountered during May.

6.6 Particle size and volume concentration data from the LISST instrument

6.6.1 Particle size and volume concentration time series

Month-long moored observations of SPM volume concentration and particle size were recorded by the LISST attached to the STABLEIII tripod during both February-March and May-June. In addition, LISST profiles were taken during the CTD stations at the beginning and end of each deployment period. Further details of the LISST are presented in Section 5.2.1. A time series of the measurements made during February-March is presented in Fig. 6.16, with Fig. 6.17 illustrating a period during peak spring tides with lines indicating the

high and low water periods to aid comparison between panels. Current speed from the lowest bin of the ADCP is presented as a reference to the state of the tide.

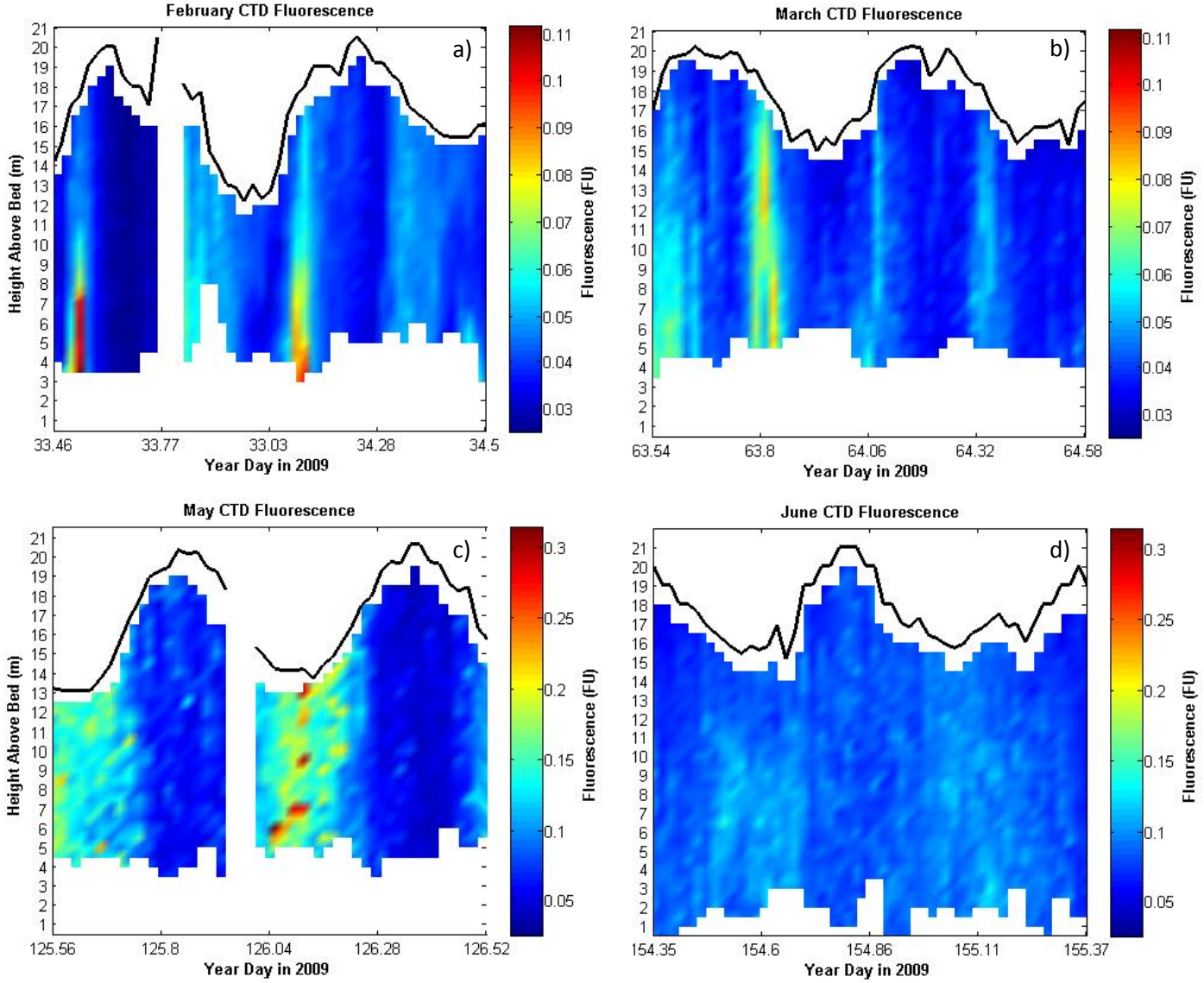

Fig. 6.15 – Fluorescence data from the CTD stations. Note that May (c) & June (d) are plotted on a different scale to February (a) & March (b) as without this, no data are visible in February & March

D_{50} during February-March decreased during the flood tide before increasing during high water, decreasing again during ebb, and increasing during low water (Fig. 6.16 bottom & Fig. 6.17 bottom), with the peak during low water consistently higher than that during high water. Volume concentration peaked before the high current speed conditions on the flood

tide before falling as current speeds declined (Fig. 6.16 top & Fig. 6.17 top). Concentrations reached a minimum shortly before high water, and remained low across the high water period. Concentrations increased again during the ebb tide, peaking late on the ebb after current speeds had already peaked, before falling across low water and the early stages of the flood. This pattern is reflected in the LISST volume concentration data recorded during the February CTD period (Fig. 6.18), with elevated concentrations during the flood and ebb, and concentrations falling slower after the ebb than following the flood.

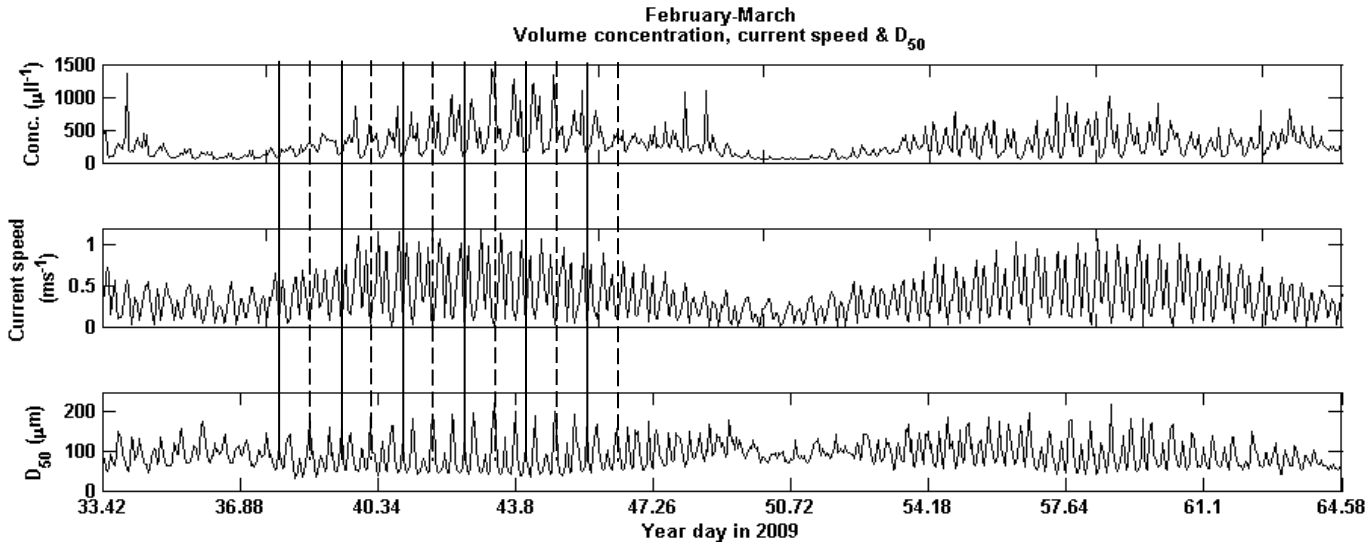

Fig. 6.16 – Volume concentration (top), current speed (middle) & D_{50} (bottom) for the February-March deployment. Solid and dashed lines indicate selected high and low waters respectively

The first 250 hours of LISST data for the May-June deployment are presented in Fig. 6.19. D_{50} demonstrated a more erratic pattern during May-June than that observed during February-March (Fig. 6.17). Particle size initially increased during the flood tide as current speeds increased before decreasing marginally during peak current speeds. As current speeds began to fall, particle size again increased before falling rapidly over high water. This pattern of increase during early ebb and flood, decrease during peak speeds, increase as current speeds fell, and decrease during slack waters is repeated; however, the pattern is at times inconsistent. As peak current speeds reduced toward neap tide conditions, the signal simplified, with D_{50} peaking in the early stages of the flood and late stages of the ebb as

current speeds reduced toward low water. Volume concentration during May-June increased during the flood and ebb periods, and decreased during high and low water, as shown for the May CTD period in Fig. 6.20. Some increase in concentration was also visible during the low water periods.

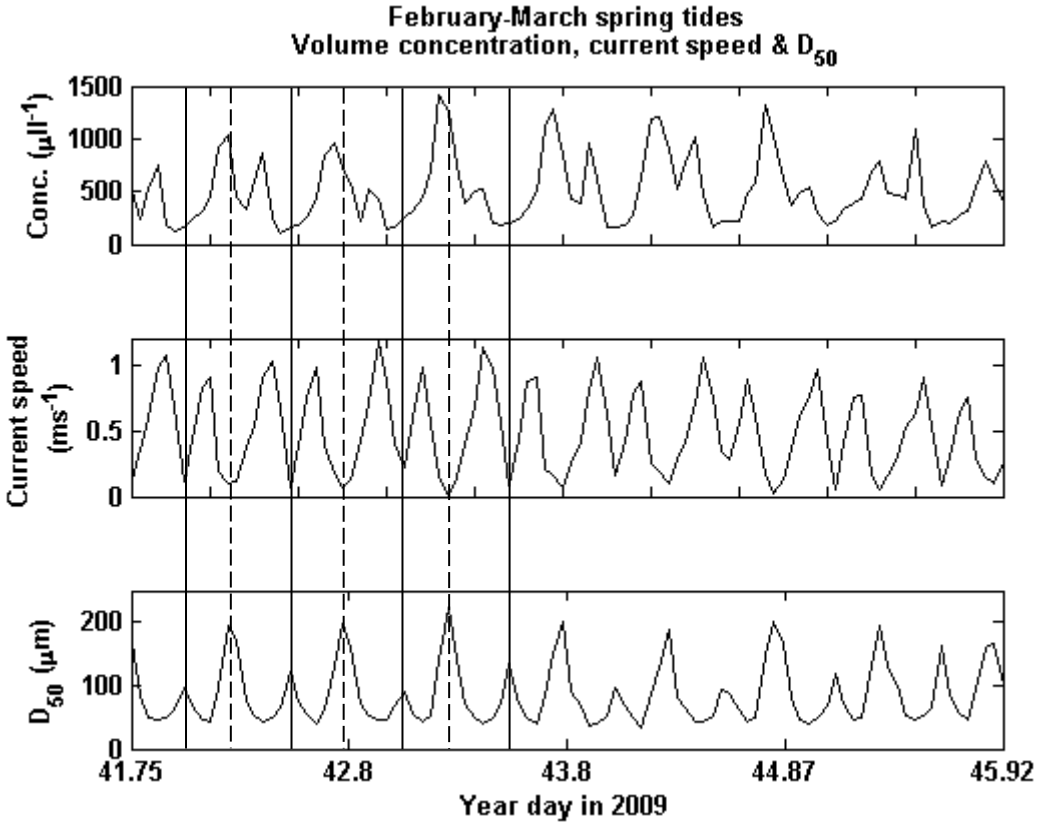

Fig. 6.17 – Volume concentration (top), current speed (middle) & D_{50} (bottom) for peak spring during the February-March deployment. Solid line indicates high water, dashed line indicates low water

6.6.2 Particle size distribution over the tidal cycle

The particle size distribution recorded by the moored LISST varied over the course of the tidal cycle. Examples of the recorded particle size distributions (PSD's) at hourly intervals during spring tides are presented in Fig. 6.21 for February-March and Fig. 6.22 for May-June. In the top left corner of each figure are two panels showing the tidal height and current speeds during the time period shown. On each of these panels, the extracted points from the time series are indicated with tick marks. The remaining 14 panels plot particle size

against volume concentration, indicating the concentration of particles of differing sizes in suspension at that time.

During the February-March deployment (Fig. 6.21), concentrations were initially low during high water, with similar concentrations of both small and large particles in suspension. Small particle concentrations remained similar between hours 1 and 2 while the concentrations of larger particles decreased. As current speeds increased during the ebb through to hour 4, concentrations of all size classes increased. Concentrations of larger particles then remained similar between hours 4 and 5 while concentrations of small particles increased further, despite a corresponding decrease in current speeds on the late ebb. Large particle concentrations increased over low water as small particle concentrations fell during hours 6 and 7, before concentrations of all sizes fell during hours 7 to 9. Small particle concentrations increased during hour 10 on the flood tide before falling as large particle concentrations increased marginally during hour 11, before falling to low levels during hours 12 to 13, with a marginal rise in concentration seen during hour 14.

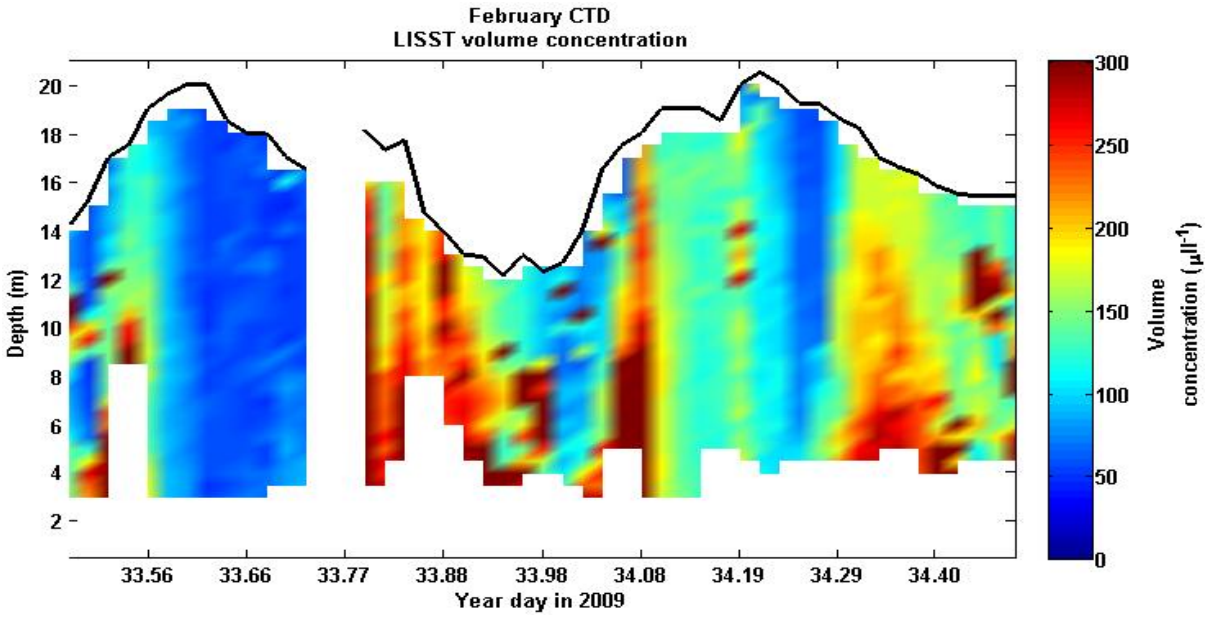

Fig. 6.18 – Volume concentration from the CTD LISST during the February CTD period

During the May-June deployment (Fig. 6.22), concentrations were again initially low during high water, however, concentrations of all particle sizes increased during the ebb to hour 4, with large particle concentrations increasing further during hour 5. As current speeds fell

across low water during hours 6 to 8 concentrations of all particle sizes also fell to low levels. Concentrations of all sizes increased during the flood in hours 9 and 10, falling slightly during hour 11, before falling to very low levels across hours 12 to 14.

6.7 Discussion

6.7.1 River discharge

A seasonal signal is visible in river discharge, with discharge highest during the period between September 2008 and January 2009. One elevated discharge event is visible during each deployment period. Data are available for this period during February-March; however, the event during May-June occurred after the biofouling of the LISST instrument (see Section 6.2), and therefore this event is not present in the LISST data for May-June.

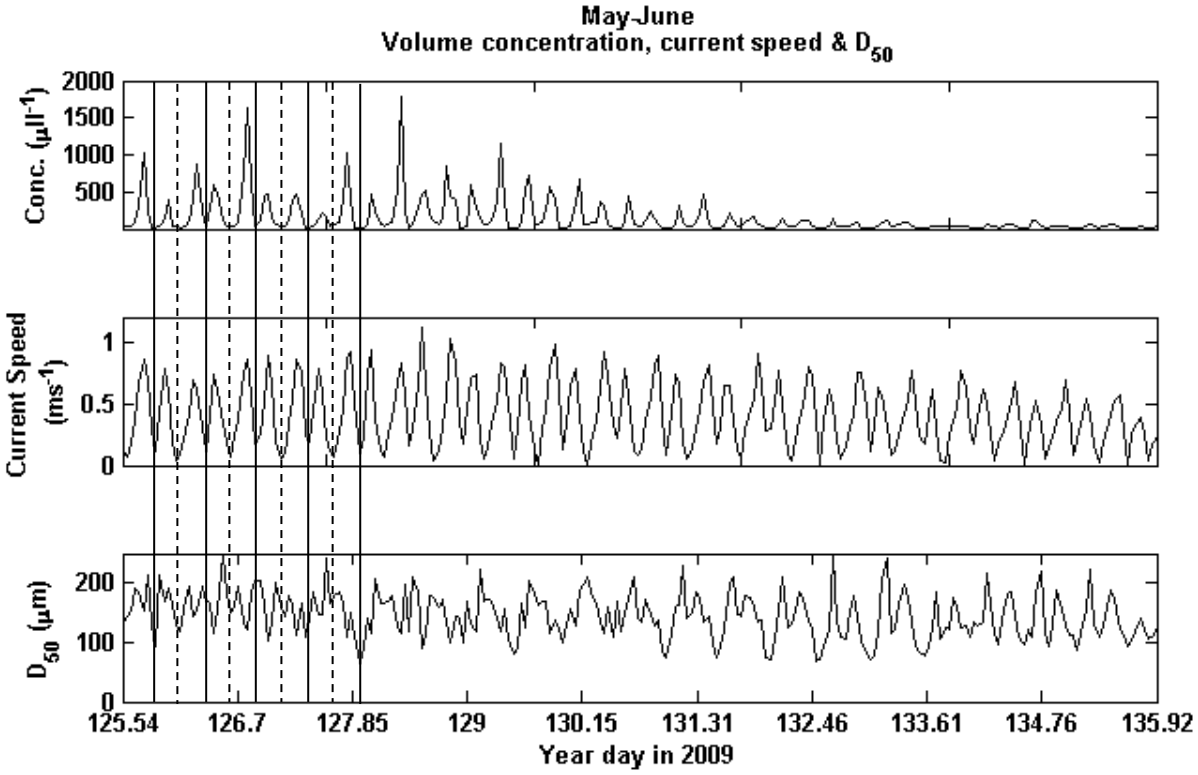

Fig. 6.19 – Volume concentration (top), current speed (middle) & D_{50} for the first 250 hours of the May-June deployment. Solid line indicates high water, dashed line indicates low water

6.7.2 Stratification of the water column

Stratification during the flood and ebb tides

The transition between high water and the ebb tide occurred simultaneously throughout the water column during both spring and neap tidal conditions, keeping velocities (Fig. 6.9a) and isopycnals (Fig. 6.12) seemingly vertically homogenous. However, some unstable stratification was present, as indicated by the Richardson number in Fig. 6.23 which shows areas of the water column below the critical Richardson number of 0.25 (Eq. (2.39)). It should be noted that the calculation of the Richardson number was done using current speeds from the ADCP combined with data from the CTD that was interpolated into 0.5m bins. These measurements were not co-located, and therefore the error levels in the calculations are unknown. The calculation does however provide an indication of the stability of the water column and indicates that most of the water column was stably stratified the majority of the time. The February CTD period was chosen as during this month the temperature of the fresher river water was lower than that of the sea water (Fig. 6.13a) making unstable stratification more likely.

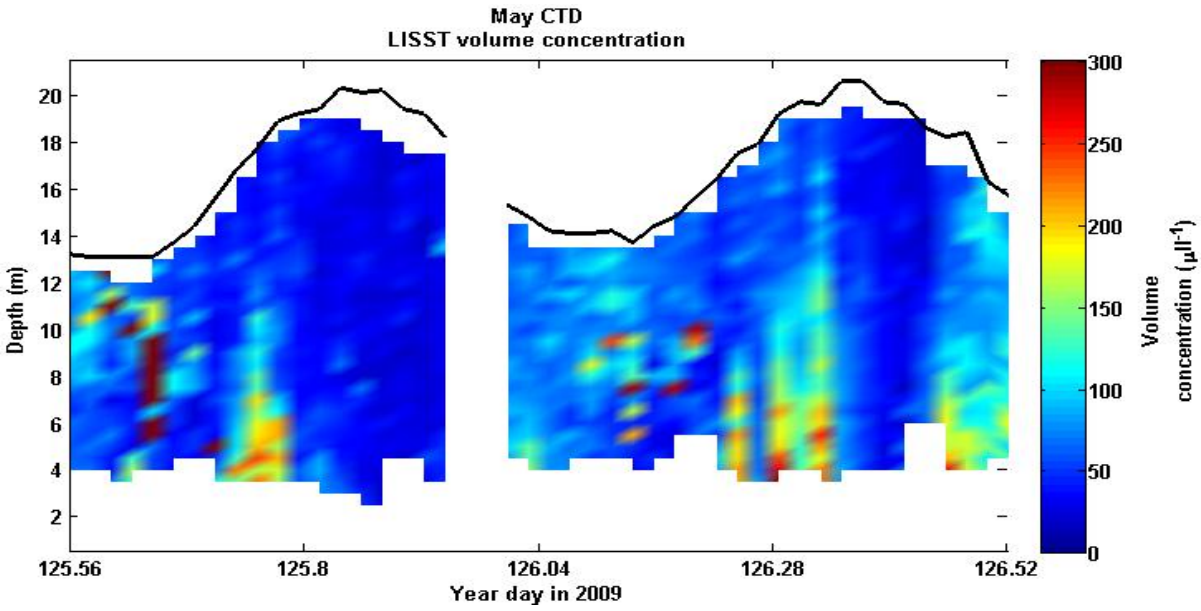

Fig. 6.20 – Volume concentration from the CTD LISST during the May CTD period

Rather than in the classical SIPS process (Simpson, et al., 1990) in which water begins to ebb at the surface over inflowing water at the sea bed, the ebb in the Dee Estuary occurred

simultaneously, with fresher water appearing throughout the water column as a “slug.” The temperature of the fresher water was time-dependent, being colder than the seawater during February, but warmer during the other CTD station periods (Fig. 6.13, no temperature data were available for the March CTD period); however, a change in water temperature was indicative of the presence of fresher water during the ebb tide. The water column gradually freshened until low water, at which point, under low velocity conditions, vertical stratification occurred.

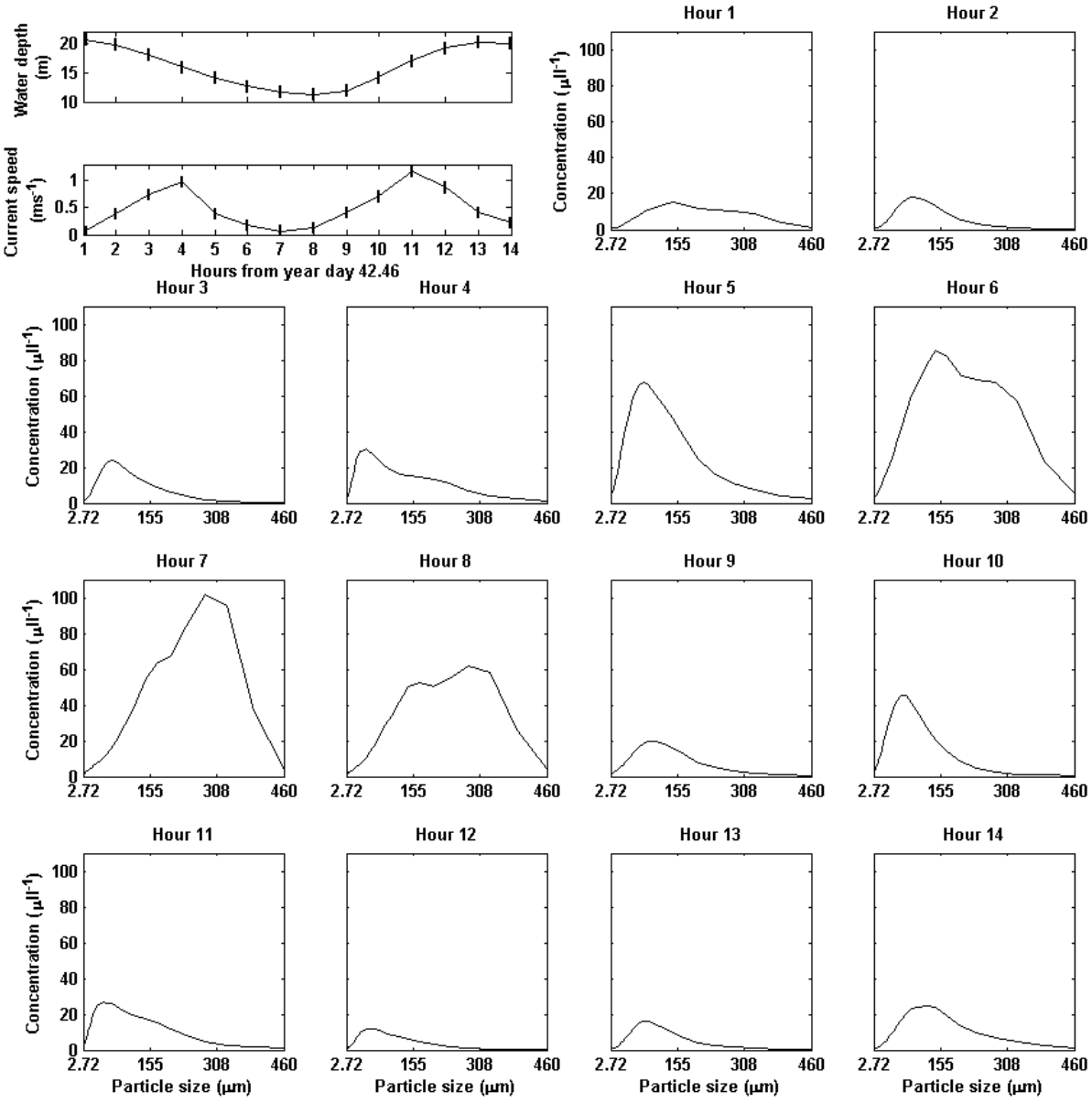

Fig. 6.21 – Water depth (top left), current speed (below top left) and particle size distributions at hourly intervals for peak spring tides during February-March from the LISST on the STABLEIII tripod

The transition from low water to flood during neap tides (Fig. 6.10a) began in the near-bed region whilst the surface waters were still ebbing, resulting in a salt wedge-type system with saltier water inflowing at the sea bed, reinforcing the vertical stratification in a similar manner to Giddings, et al., (2011). This caused vertical shear of the horizontal current, tilting the velocity contours and isopycnals as the incoming water was of higher salinity than that outflowing at the surface (Fig. 6.12). As current speeds and turbulence increased during the flood, this stratification was eroded by the incoming tide until a fully mixed water column was established midway through the flood. This process was also visible during the stages between the spring and neap tides, when the observed CTD surveys were undertaken, as salinity stratification was seen during the early flood (Fig. 6.12). During the early flood on spring tides, little evidence of vertical shear was present (Fig. 6.9a) by comparison with the neap tide conditions (Fig. 6.10a). The reduction in the visibility of shear is likely to have been caused by the rapid acceleration of the current velocities of the spring tides and the hourly-averaged resolution of the ADCP data (compared to the half-hourly resolution of the CTD profiles). The fast currents (Fig. 6.9a & Fig. 6.10a) and high turbulence (Fig. 6.11a) during spring tides, may have resulted in the breakdown of the stratification over a shorter period of time than is seen during neap tides (Fig. 6.10a). In addition, the coarse resolution of the ADCP data may have been insufficient to capture the full extent of the vertical shear. Stratification was salinity and temperature driven and therefore related to river discharge, being greatest during February and weakest during June (Fig. 6.12a & d), concurrent with the recorded river discharge (Fig. 6.4b & e).

Vertical velocities

The vertical velocities were tidally controlled during both spring and neap tidal conditions (Fig. 6.9b & Fig. 6.10b). The barotropic pressure gradient during the ebb resulted in fresher water outflowing at the estuary surface over more stationary water toward the estuary bed, resulting in negative vertical velocities. By contrast, the reverse occurred during the flood tide as the salt wedge, composed of saltier, denser water flowed into the estuary at the sea bed, resulting in upward vertical velocities.

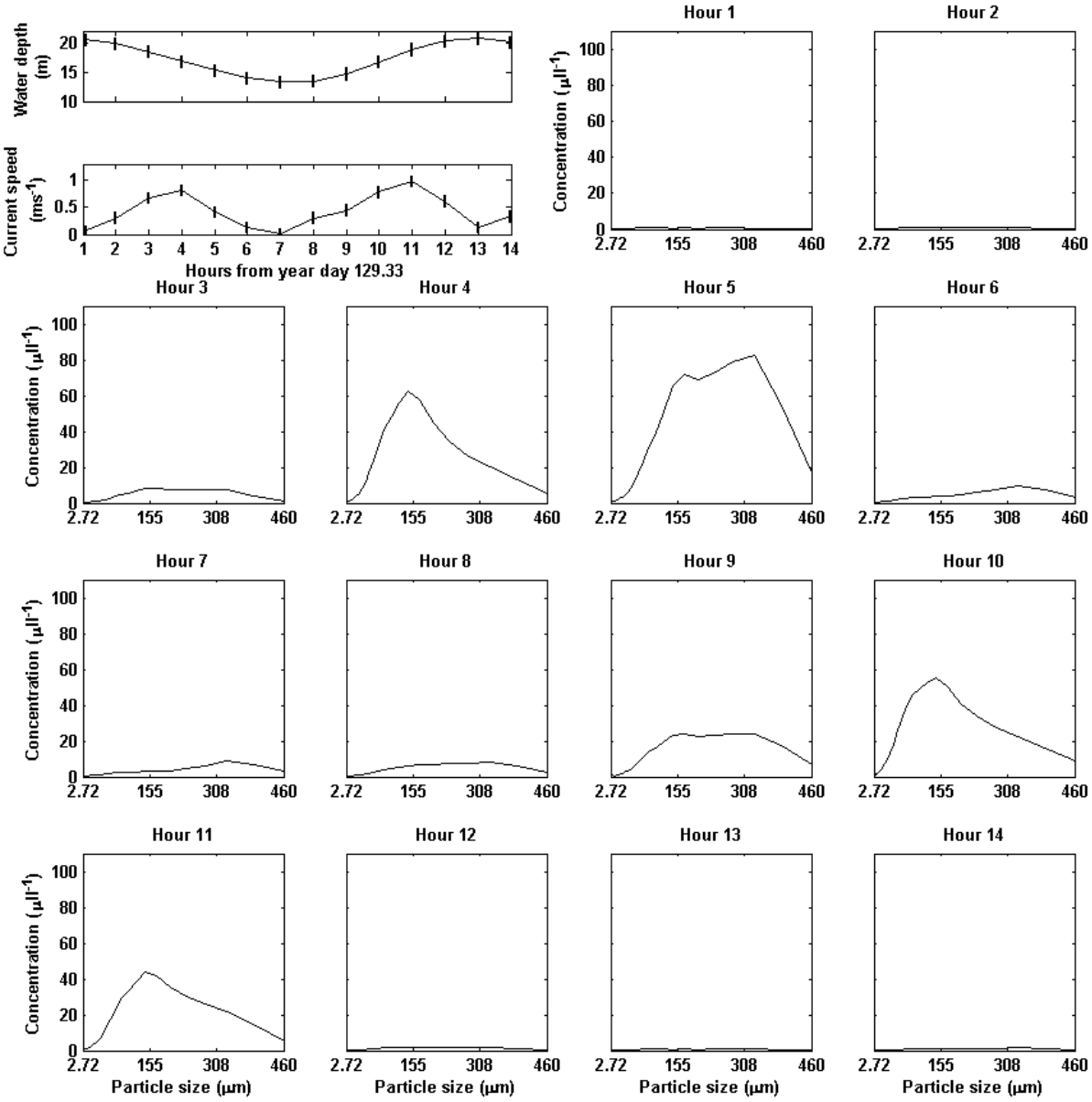

Fig. 6.22 – Water depth (top left), current speed (below top left) and particle size distributions at hourly intervals for peak spring tides during May-June from the LISST on the STABLEIII tripod

Low Water

The salinity structure of the water column, indicated by the CTD-derived salinity, suggests an axial salinity gradient (Fig. 6.12) brought about by the flux of freshwater from the Dee River in a similar manner to that explained by Simpson, et al., (1990) and Simpson & Souza, (1995). This created a horizontal density gradient, inducing outflow at the estuary surface,

and inflow in the lower water column. This regime persisted during low water, and is visible in Fig. 6.9a and Fig. 6.10a. The strength of this gradient was increased during the May and June CTD periods, partly due to the river water being warmer than the seawater (Fig. 6.13b & c – no temperature data were available for the March CTD period), impacting upon the density of the overlying freshwater. During the February CTD period, the river water was colder than the seawater (Fig. 6.13a), and this reduced the stratification by decreasing the density difference between the two water bodies.

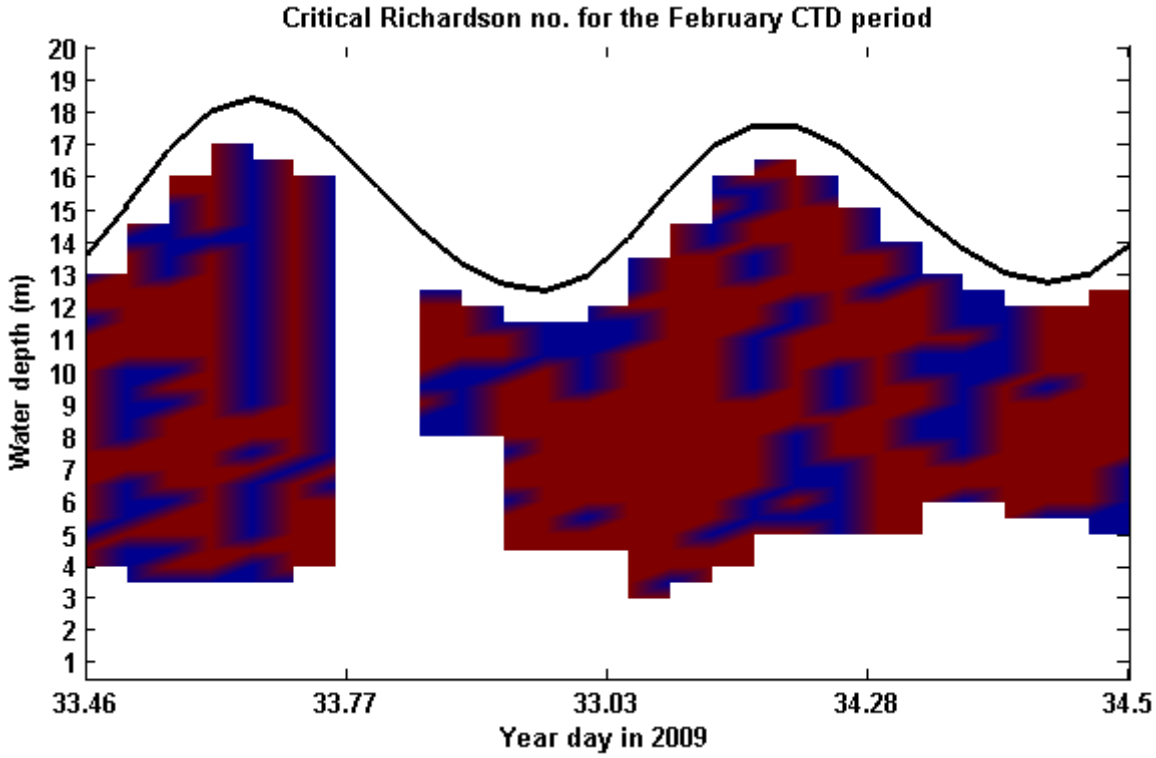

Fig. 6.23 – Areas of the water column above (blue) and below (red) the critical Richardson Number (0.25) for the February CTD period

6.7.3 Harmonic analysis of tidal heights and current velocities

The results of the harmonic analysis of the tidal heights and current velocities for the two moored observation periods, illustrated in Table 6.3 and Table 6.4, demonstrate the strength of the semi-diurnal tide during both the February-March and May-June deployment periods, with the M_2 and S_2 tidal constituents higher in amplitude than all other tidal harmonics. The spring-neap (M_2 - S_2 interaction) modulation was strong (Fig. 6.4c & d),

while the weakness of the O_1 and K_1 tides, the only significant diurnal constituents, indicates a lack of diurnal inequality, accounting for only 0.22 m of tidal height (Table 6.3) during February-March, and 0.27 m during May-June. Friction as the tidal wave propagates through shallow water caused the shallow-water overtides, (M_4 and MS_4) which were small, but greater in amplitude than the diurnal O_1 and K_1 constituents. The difference in the spring-neap tidal range observed between the February-March and May-June deployments occurred as a result of the S_2 amplitude, which changed between the two deployments. The tidal range was 6.5 m (9.4 during peak spring to 2.9 during neaps) during February-March, but reduced to only 5 m during May-June (8.1 m on peak springs to 3.1 m during neaps).

In keeping with the harmonic analysis of the pressure signal, the dominant tidal constituents impacting the current speeds (Table 6.4) were the M_2 and S_2 semi-diurnal tides. These were followed by the quarter-diurnal M_4 and MS_4, and the semi-diurnal N_2. No significant diurnal constituents were present, with the only other significant constituents being the high-order overtides M_6 and $2MS_6$. The low values of the minor-axis current speeds by comparison with the major-axis current speeds showed that the tidal currents in this region were almost rectilinear, and in fact, that the tidal ellipses were effectively straight lines.

6.7.4 SPM

Vertical distribution of SPM

The vertical distribution of SPM volume concentration, derived from profiles using the CTD LISST (Fig. 6.18 & Fig. 6.20) shows short, episodic increases in SPM during both the flood and ebb tides. These increases were consistently of the order of 2 to 3 hours in length. SPM volume concentration generally decreased with height above bed, but events were of sufficient strength to elevate SPM concentrations at the estuary surface, affecting the entire water column.

The water column was well mixed with regards to salinity (Fig. 6.12) and SPM (Fig. 6.18 & Fig. 6.20) at high water during all months, with SPM concentrations generally evenly distributed as concentrations fell. Conversely, during low water, SPM concentrations were higher in the surface regions of the estuary than lower in the water column during the May

CTD period (Fig. 6.20). This was linked to the low water stratification in salinity (Fig. 6.12), which resulted in a 2-layer system with fresher water containing elevated concentrations of SPM overlying higher salinity water with a pycnocline separating the two. During low water in the February CTD period, SPM concentrations were higher in the mid-water column regions of the estuary with lower concentrations towards the estuary surface (Fig. 6.18).

Time Evolution of SPM

SPM volume concentration varied greatly over the spring-neap cycle. Fig. 6.16 & Fig. 6.19 show how SPM concentration changed during both the February-March and May-June deployments. Concentrations varied from a minimum of 45 $\mu l l^{-1}$ at neaps to a maximum of 1400 $\mu l l^{-1}$ at springs during February-March (Fig. 6.16), and from a minimum of 13 $\mu l l^{-1}$ to a maximum of 1780 $\mu l l^{-1}$ during May-June (Fig. 6.19).

Volume concentration of all particle sizes increased during both the flood and ebb in May-June, (Fig. 6.22), concurrent with the increase in SPM mass concentration (Fig. 6.14). Volume concentrations were lower and more asymmetric during May-June (Fig. 6.20) by comparison with February-March (Fig. 6.18), with greater values reached during the flood tide, while higher volume concentrations were reached on the ebb during February-March despite the February CTD indicating a flood dominance of mass concentration (Fig. 6.14a). There is therefore a discrepancy between SPM mass concentration transport and SPM volume concentration transport during the February CTD period which may indicate a change in particle size, and this is confirmed in Fig. 6.21, which shows a transition between small and large particles during February-March through the ebb tide and across low water (Fig. 6.21 hours 4 to 8). This indicates possible flocculation at low water under low current speeds (Fig. 6.9) and therefore low turbulence conditions (Fig. 6.11) during February-March.

The March CTD station was taken close to neap tides (Fig. 6.16), which may explain the lack of flood dominance shown in the SPM mass concentration (Fig. 6.14b). However, this does not explain the lack of increase in SPM concentration during the second flood tide. This may have resulted from inaccurate measurements, or possibly from the boat swinging around its anchor into a region of lower concentration.

During the February-March deployment, the LISST-derived D_{50} followed an asymmetric pattern with larger particle sizes during high and, predominantly, low water (Fig. 6.16 & Fig. 6.17). Particle sizes reduced during the flood and ebb tides, as illustrated in Fig. 6.21, concurrent with times of high current speed (Fig. 6.9) and high turbulence production (Fig. 6.11). This was out of phase with the volume concentration signal recorded by the LISST (Fig. 6.16 & Fig. 6.17), with the minima in particle size occurring close to the maxima in volume concentration, and the maxima in particle size occurring close to the minima in volume concentration. This suggests the flocculation of small particles into large particles during times of low current speed (Fig. 6.9) and low turbulence production (Fig. 6.11) during high and, predominantly, low water.

During May-June, the variation in D_{50} was complex during spring tide conditions (Fig. 6.19), but generally displayed an increase during the flood and ebb and a decrease during high and low water. This signal simplified during neap tides to reflect the changes in both volume concentration and current speeds (Fig. 6.9, Fig. 6.19). The increase during the flood and ebb occurred over a range of particle sizes (Fig. 6.22) during times of high current speed (Fig. 6.9) and high turbulence production (Fig. 6.11) indicating resuspension, while concentrations of large particles decreased during high and low water (Fig. 6.22), indicating that particles were settling out of suspension.

6.7.5 Fluorescence

Fluorescence response (Fig. 6.15), a proxy for chlorophyll (Lorenzen, 1966) and therefore sticky polysaccharide substances (see Section 3.3.5), changed between deployments, being higher during May-June than February-March. This trend of higher chlorophyll concentrations during May-June was reflected in the NEODAAS satellite chlorophyll measurements (Fig. 6.24) which indicated concentrations in and around the entrance to the Dee Estuary of ~4-8 $\mu g l^{-1}$ during the first week (1^{st} – 7^{th}) of March, and ~4-50 $\mu g l^{-1}$ during the second / third week (10^{th} – 16^{th}) of May. Much satellite data of the Dee Estuary region during the deployment periods was unavailable due to cloud cover or data contamination caused by light reflections from snow on the ground.

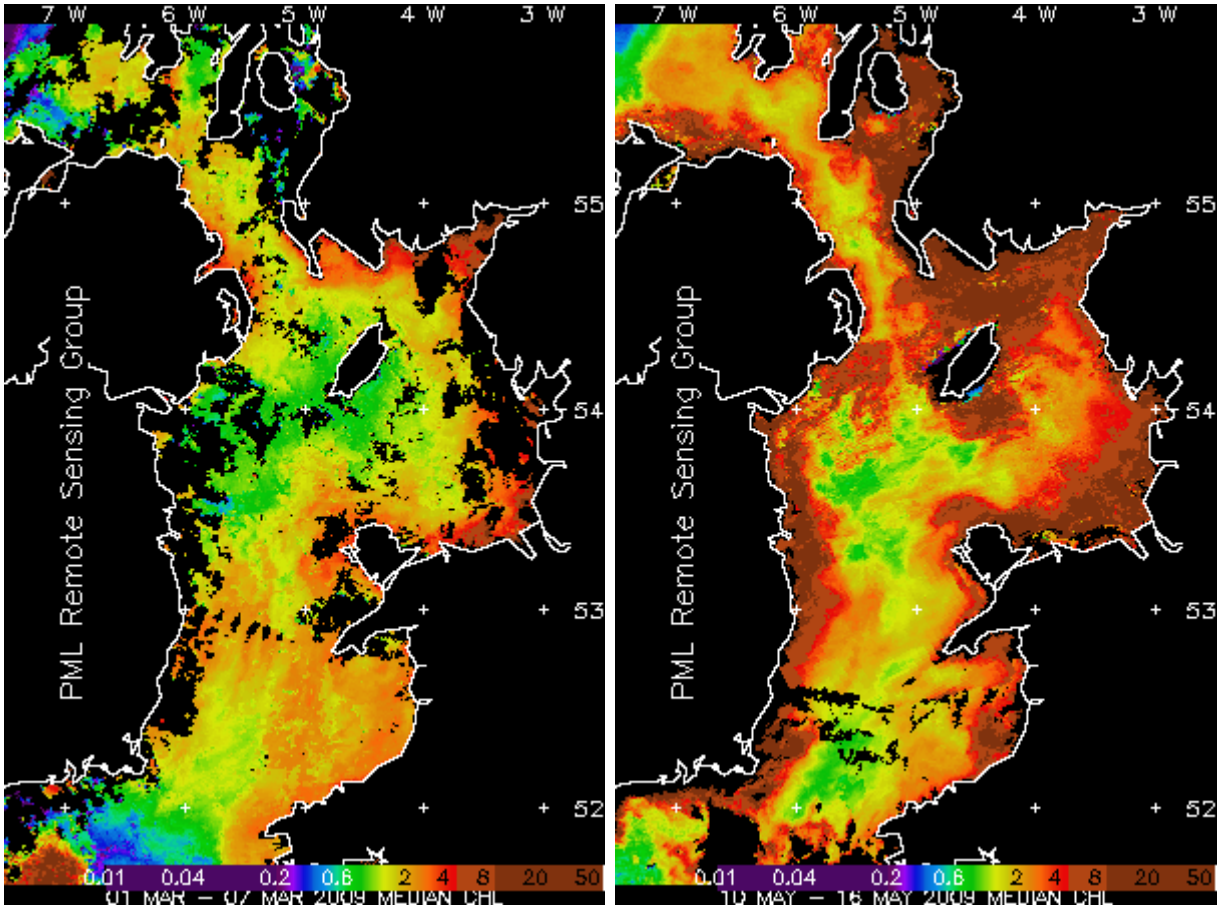

Fig. 6.24 – Chlorophyll concentrations (µgl^{-1}) during the first week of March (left) and second week of May (right) 2009 from the NEODAAS satellite

Fluorescence response during the February and March CTD stations (Fig. 6.15a & b) increased episodically for short durations during the flood and ebb tides, in a similar pattern to that shown by the SPM mass concentration (Fig. 6.14a & b), with concentrations elevated during times of high current speeds (Fig. 6.9) and high turbulence production (Fig. 6.11). During the February CTD in particular, higher fluorescence response persisted for longer during the ebb tide than during the flood, and response remained elevated through to low water (Fig. 6.15a). This elevated response was concurrent with the presence of the fresher water (Fig. 6.12a) which brought SPM down the estuary (Fig. 6.14a) toward the end of the ebb and over low water. This trend is emphasised by plotting SPM mass concentration from the calibrated CTD transmissometer (Fig. 6.14a) against the fluorescence response obtained from the CTD fluorometer (Fig. 6.15a). The resultant figure, Fig. 6.25, shows a strong relationship between SPM mass concentration and fluorescence response during the

February CTD period (R^2 = 0.91), indicating that fluorescence response varied with SPM concentration.

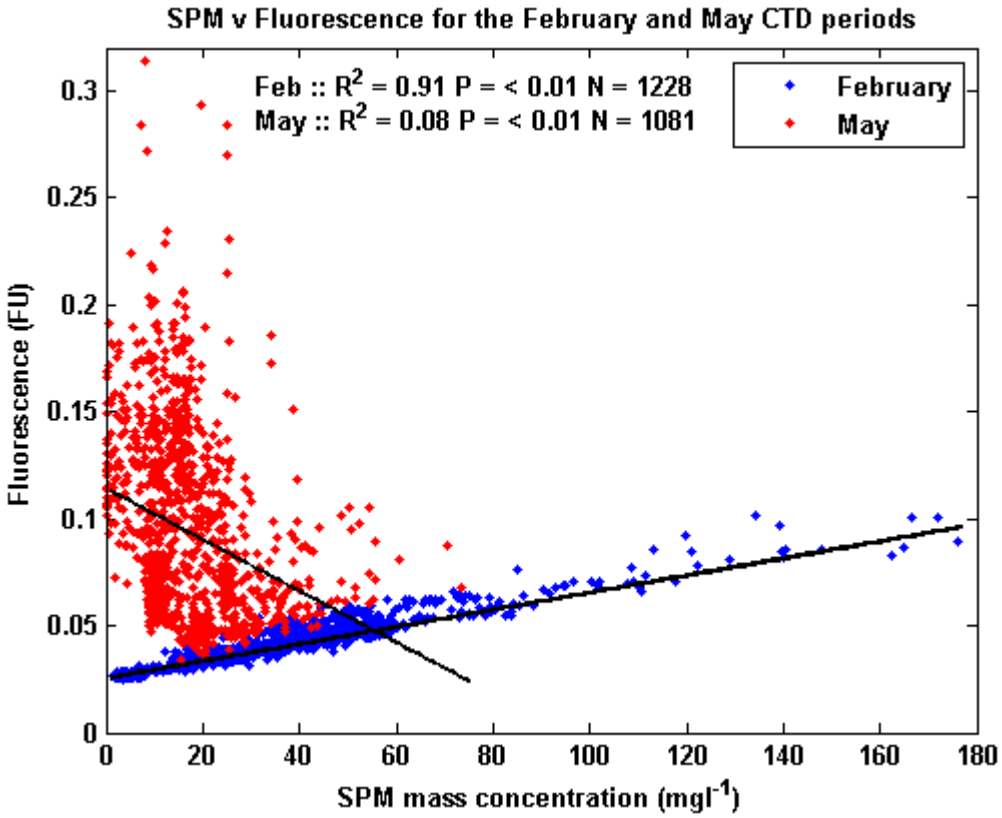

Fig. 6.25 – SPM mass concentration plotted against fluorescence for the February (blue) and May (red) CTD periods with associated trend lines

Values of fluorescence response recorded during the May and June CTD periods were up to three times higher than those recorded during the February and March CTD's (Fig. 6.15). The relationship between SPM mass concentration and fluorescence response during the May CTD period was weak (Fig. 6.25, R^2 = 0.08), showing that fluorescence response was not linked to SPM mass concentration during this period and highlighting a strong seasonal variation between the February-March and May-June periods.

The increase in fluorescence response between the February-March and May-June deployments indicates an increase in biological activity. This is confirmed by the chlorophyll-a concentrations from the SmartBuoy (location shown in Fig. 6.26) located offshore of the Dee Estuary in Liverpool Bay, approximately 19.5 km from the STABLEIII mooring location,

which showed daily averaged chlorophyll concentrations ranging from 0.4 to 1.3 μgl^{-1}, averaging 0.6 μgl^{-1}, during February-March, and from 1 to 10.6 μgl^{-1}, averaging 4.9 μgl^{-1}, during May-June (Fig. 6.27), concurrent with the cross-seasonal increase seen in the satellite observations (Fig. 6.24).

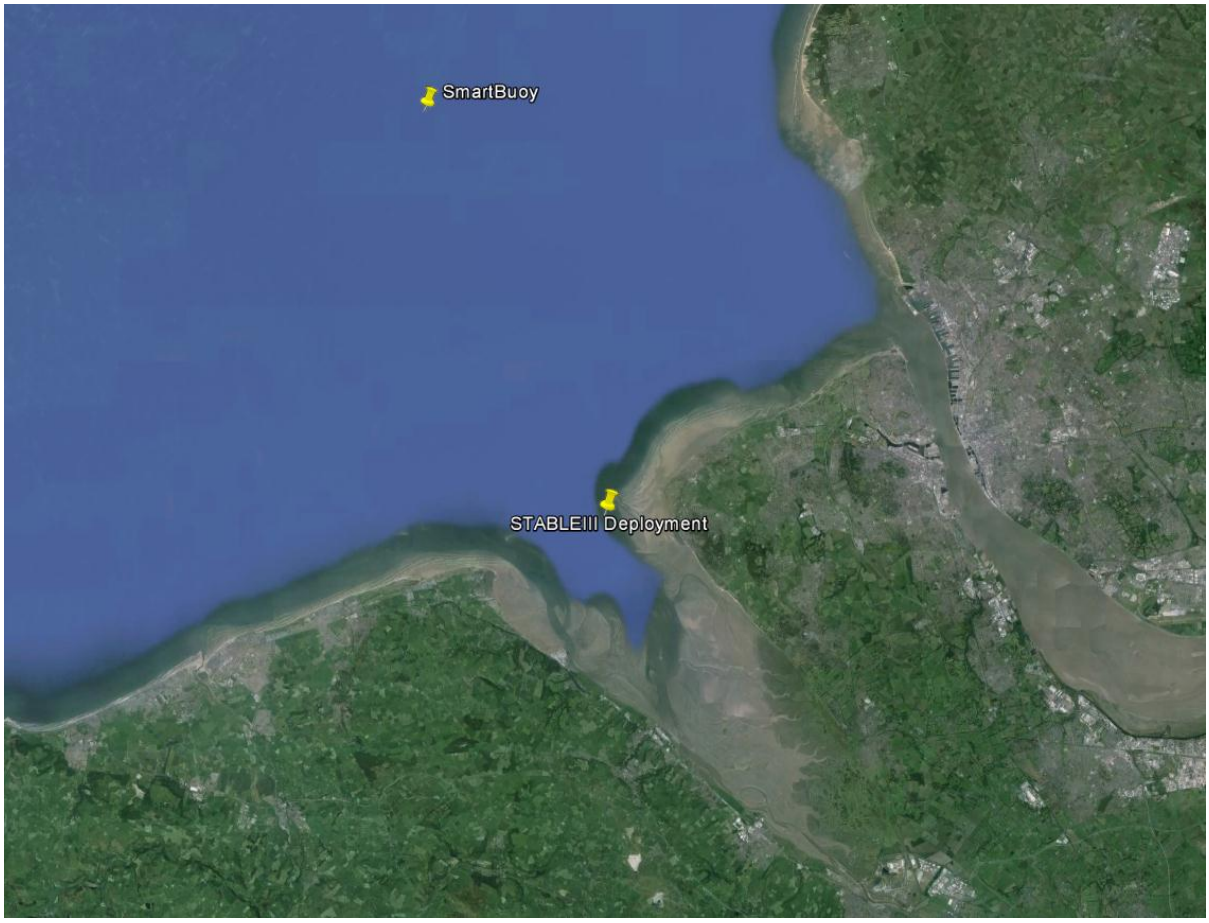

Fig. 6.26 – Location of the CEFAS SmartBuoy relative to the Dee Estuary and STABLEIII deployment site

Increased biological activity may indicate increased levels of polysaccharides and it would be anticipated therefore that any flocs occurring during the May-June deployment period were likely to have been larger and stronger than those observed during February-March (Gratiot & Manning, 2007). The range of the D_{50} values recorded during the February-March deployment was wider (29 – 222 µm with a mean of 93 µm) than that recorded during the first 250 hours of May-June (66 – 249 µm with a mean of 146 µm). Particles were therefore larger on average during the May-June deployment, as anticipated. In addition, it is likely

that the elevated levels of polysaccharides, coupled with the strengthening of the sediment due to changes in atmospheric conditions between the deployment periods (see Section 3.2.4) resulted in an increase in the threshold for erosion, reducing the sediment available for resuspension during May-June by comparison with February-March as indicated in Fig. 6.14, Fig. 6.18 and Fig. 6.20.

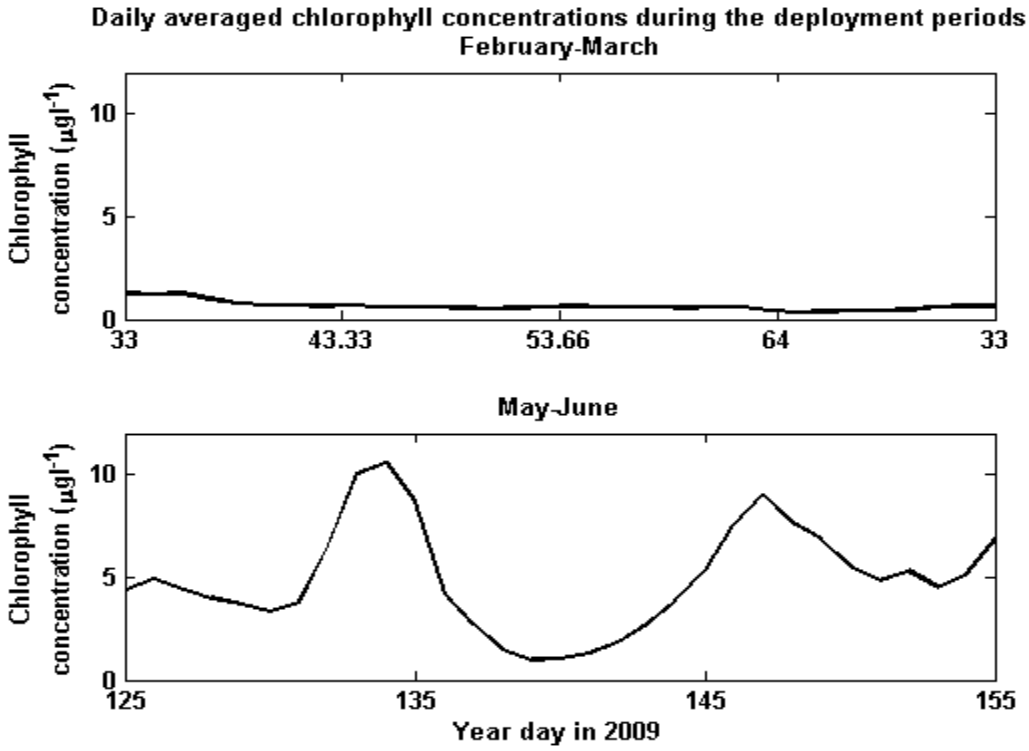

Fig. 6.27 – Chlorophyll concentrations from the CEFAS SmartBuoy during the February-March (top) and May-June (bottom) deployment periods

The increase in fluorescence response during the late ebb and over low water observed during the May, and to a lesser degree June, CTD stations (Fig. 6.15c & d), concurrent with the observed reduction in salinity (Fig. 6.12), may be explained by the inundation of the intertidal areas of the estuary. The maximum tidal excursion during both February-March and May-June was 15.7 km, which, as illustrated in Fig. 6.28, resulted in the inundation of the salt marsh and mud flat areas. In addition, the shortest distance from the STABLEIII mooring location to the edge of the salt marsh area was 9 km. Fig. 6.29 (bottom panel) shows the maximum tidal excursion during the May CTD period. The point at which the excursion exceeds 9 km is indicated by the magenta line. During the first ebb period, a lack

of data means it is not possible to infer anything about the source of the fluorescing material, however, during the second ebb period, fluorescence response (top panel) began to increase after the tidal excursion exceeded 9 km, indicating that water from the salt marsh region was responsible for the increase in fluorescence response observed.

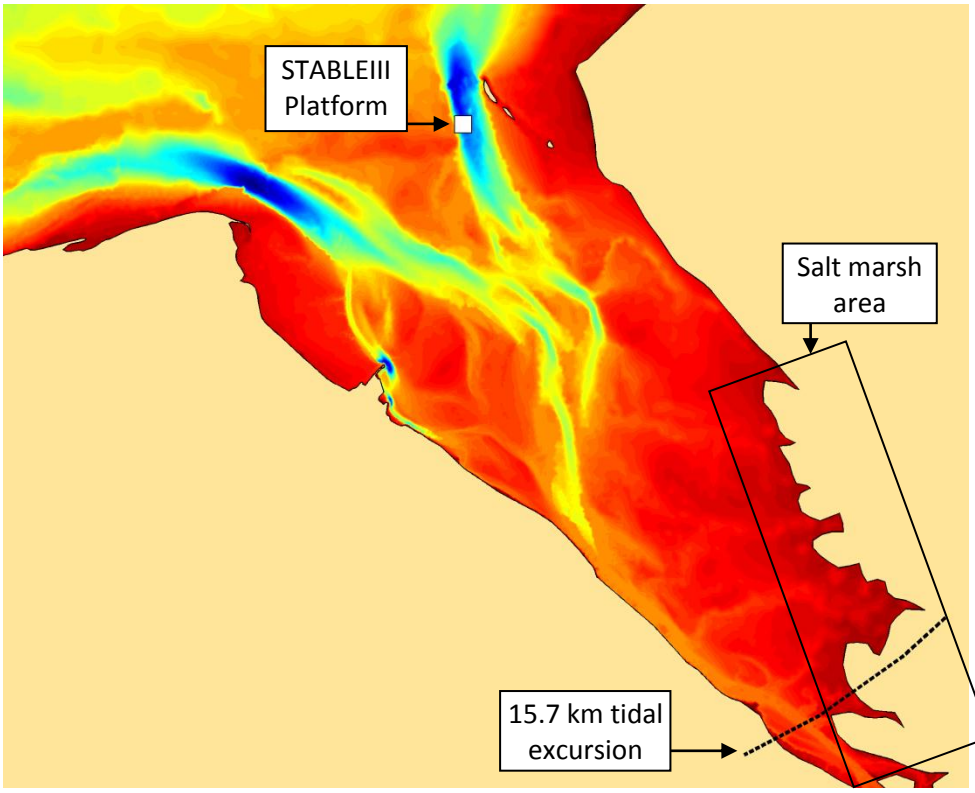

Fig. 6.28 – The Dee Estuary with the location of the STABLEIII rig in the Hilbre Channel indicated. The dashed line indicates the 15.7 km maximum spring tidal range excursion

The May CTD station was undertaken on the run up to spring tides, while June was undertaken around neap tides. June demonstrates the same signal as that displayed by the May fluorescence response, but with the variation between high and low water lower than during May. This is significant, as during the May CTD the increasing tidal range will have inundated salt marsh and mudflat areas on each tide that had not been previously covered by the tide for at least a few days. During this time, abundant biological productivity was occurring on the salt marshes and mudflats, resulting in the delivery of a “pulse” of organic material into the estuary on the ebb with each increasing tide.

The June CTD station was undertaken around neap tides, and therefore this pulse of organic material was far smaller as the salt marsh and mud flat regions had had less time to develop organic material as they were inundated during each successive tide. These combined factors explain the differences in fluorescence response seen between the May and June CTD periods. The lower productivity occurring during February and March explains why this same pulse was not seen in the data during these CTD stations. Although speculative, this hypothesis fits well with the recorded observations and emphasises the importance of the salt marshes and mud flats in this region in providing biological material to the estuary system.

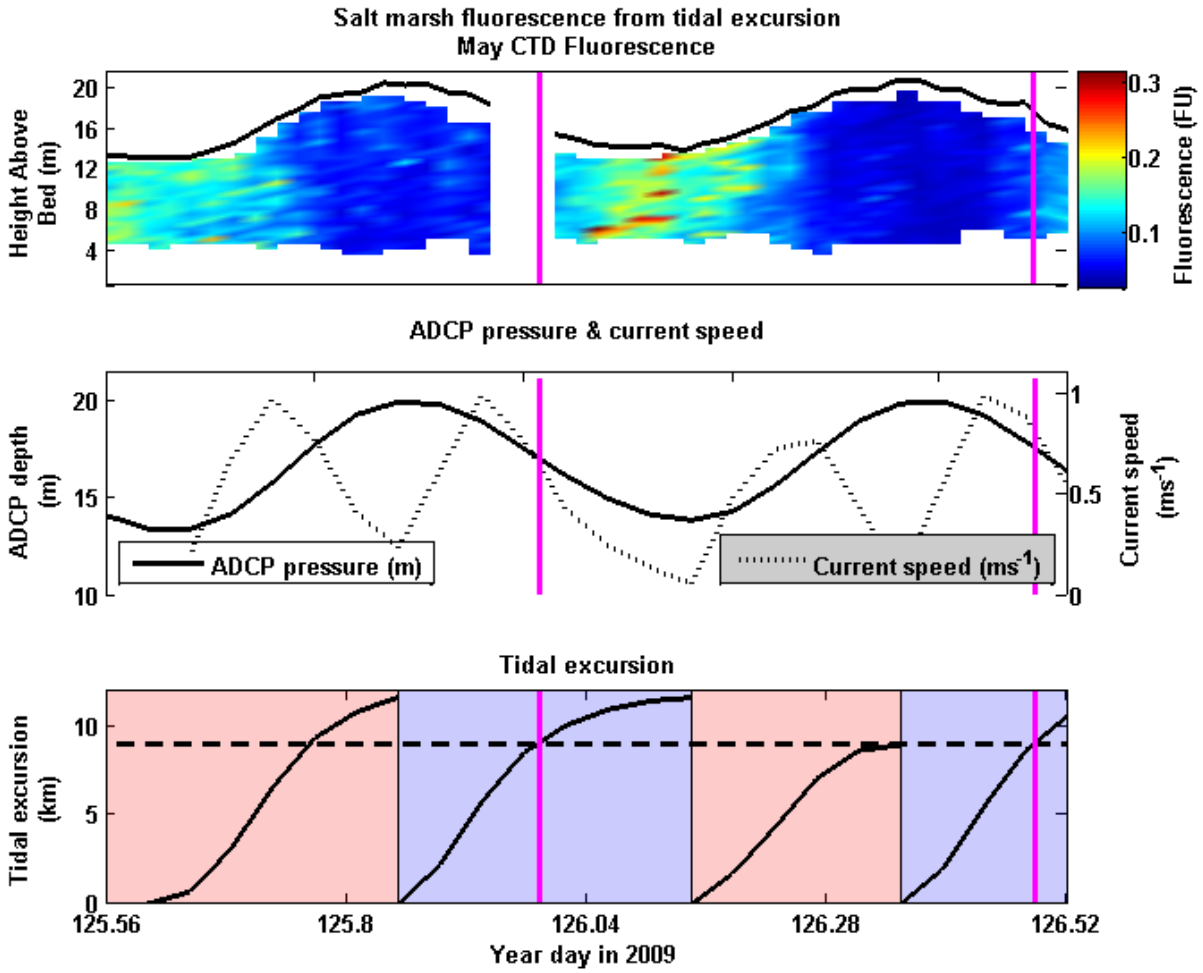

Fig. 6.29 – Fluorescence response during the May CTD station (top), pressure and current speed from the ADCP (middle), tidal excursion for both flood (red) and ebb (blue) tidal periods (bottom). Magenta line indicates the point at which tidal excursion exceeds 9 km

6.8 Conclusions

- Wave effects were negligible during both deployment periods;
- The water column of the Hilbre Channel experienced periodic stratification during low water and the early stages of the flood tide. This stratification was related to the horizontal density (salinity) gradients, and was therefore greater during February-March than May-June. Stratification was broken down by the incoming flood tide;
- Vertical shear at low water created by outward flow at the estuary surface with a deeper return flow beneath;
- Both the large tidal range and high tidal current velocities of the Hilbre Channel of the Dee Estuary were dominated by the M_2 & S_2 tides;
- Periodic increases in SPM concentration occurred during both the flood and ebb tides in all CTD stations, with concentrations decreasing with height above bed;
- During low water, the fresher water coming down the estuary contained a higher mass of SPM than the more saline water below;
- SPM volume concentration increased during the flood and ebb tides in February-March, concurrent with the increase in mass concentration. However, a transition between small and large particles towards the end of the ebb tide and over low water produced a discrepancy between the mass and volume concentrations and may indicate the flocculation of suspended sediment. A similar transition occurred during high water but on a much reduced scale;
- During May-June, volume concentration increased during both the flood and ebb tides, decreasing during high and low water;
- Fluorescence response was up to three times higher during May-June than February-March. Fluorescing material correlated well with SPM mass concentration during February-March, but not during May-June;
- In May-June, fluorescing material was transported down the estuary, probably from the salt marshes and mud flats at the end of the ebb tide and during low water.

The investigations in this chapter have allowed the quantification of changes in the meteorological conditions within the Dee Estuary during the periods studied, including investigations of the driving tidal harmonics behind the observed tidal heights and current speeds. Further, the impact of river discharge on salinity, temperature and

stratification has been investigated. Changes to the turbulence regime and SPM, including both mass and volume concentration and particle size have been investigated over tidal, spring-neap and seasonal timescales. Preliminary evidence for the presence of flocculation during low waters in February-March has been identified, and this will be further investigated in Chapter 8. In addition, tidal and seasonal changes in fluorescence response have been assessed and the likely source of the fluorescence response observed during May-June has been identified as the salt marsh and mud flat regions higher up the estuary.

Chapter 7

Harmonic analysis of SPM

7.1 Introduction

Terrestrial material is supplied to an estuary system by the river, while marine material is supplied by the sea. Whether the estuary acts as a trap or a bypass zone for SPM depends upon the properties and dynamics of both the estuary, including the tidal and residual behavior of the currents, and the SPM, including particle sizes and settling velocities, which together control the dynamics, such as the trapping efficiency, of the estuary.

Fig. 7.1 shows the first low water period during the February and May CTD stations (indicated by the grey boxes in Fig. 6.4). Stratification in salinity, temperature and SPM concentration occurred toward the end of low water during these observation periods, as shown in Chapter 6, with concentrations in the fresher, upper water column higher than those in the more saline water below. SPM concentrations during low water in May averaged 57 % less than those during low water in February. Elevated SPM concentrations in the fresher water on the late ebb and over low water may indicate the presence of a horizontal concentration gradient with SPM being advected down the estuary in the lower salinity water. The reduction in SPM concentration between the late ebb and low water in February, and the late ebb and low water in May may be indicative of a reduction in this horizontal concentration gradient.

The presence of a horizontal concentration gradient can be inferred through the use of harmonic analysis and will be discussed in this chapter. The presence of a horizontal concentration gradient should also show a relationship between the minimum SPM concentration and salinity at high and low water, with higher concentrations over high water potentially indicative of a horizontal concentration gradient bringing material into the estuary, and likewise, higher concentrations at low water indicative of a horizontal concentration gradient bringing SPM down the estuary. Plotting SPM against salinity for the February and May CTD periods (Fig. 7.2) shows that during the February CTD period, SPM concentrations were low under the high salinity conditions of high water, but had a minimum concentration up to 35 mgl^{-1} higher in the low salinity water of low water during

the February CTD period (Fig. 7.2 top). This gradient in the minimum SPM concentration between high and low water indicates the potential presence of a horizontal concentration gradient with concentrations higher at the top of the estuary. By contrast, during the May CTD period (Fig. 7.2 bottom), much more scatter was present in the data and no discernable change or minimum SPM concentration gradient can be seen.

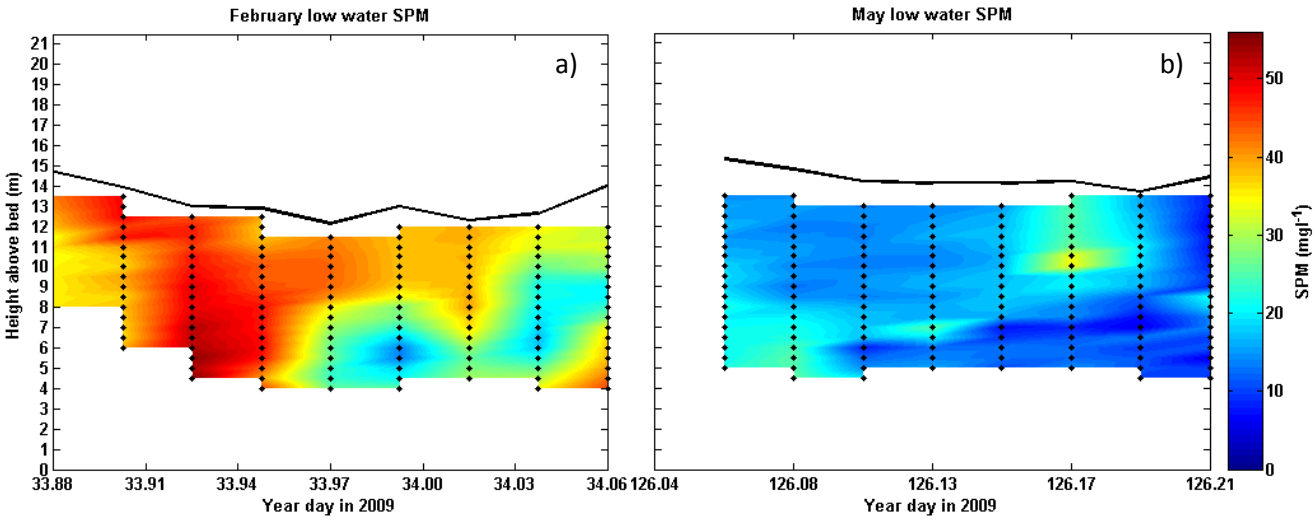

Fig. 7.1 – Low water SPM mass concentration for the February (a) & May (b) CTD stations with data points shown

Previous work has shown that in tidally stirred regions, local SPM concentrations vary at semi-diurnal and quarter-diurnal frequencies (Sternberg, et al., 1985). The semi-diurnal signal results from the advection of a horizontal concentration gradient, while the quarter-diurnal signal is the product of local resuspension due to excess shear stress at the seabed (Jago, et al., 1993; Sanford & Halka, 1993; Weekes, et al., 1993; Souza, et al., 2004). The combination of these two signals generates a time series of SPM concentration with maxima close to the peak flood and ebb currents and minima at high and low slack waters but, because of the horizontal concentration gradient, the slack water minima are unequal. This produces the characteristic 'twin peaks' time series (Jago, et al., 1993). Where a twin peak signal is present in a data timeseries, it is possible, using harmonic analysis, to reverse-engineer the signal to obtain the relative amplitudes and phases of the quarter-diurnal resuspension and semi-diurnal advection signals within the concentration time series.

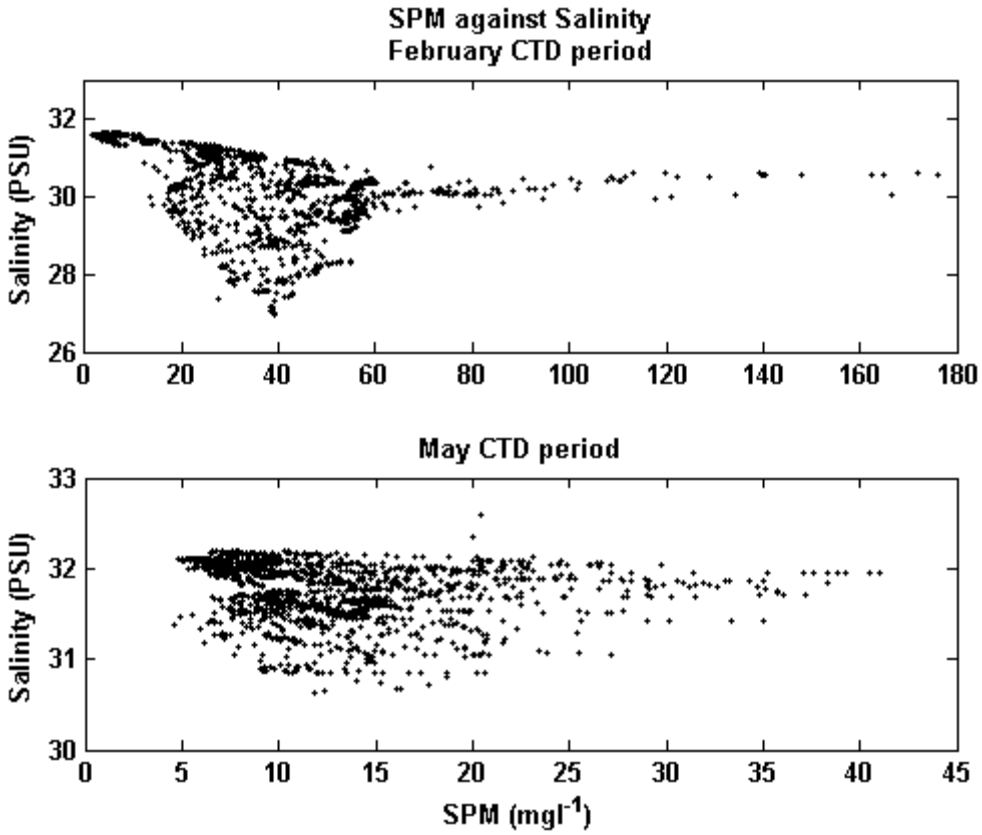

Fig. 7.2 – SPM mass concentration plotted against salinity for the February (top) and May (bottom) CTD periods

In this chapter, tidal, spring-neap and seasonal changes in SPM volume concentration recorded by the LISST during both the February-March and May-June deployments are investigated through the use of harmonic analysis. Harmonic analysis allows the separation of the recorded volume concentration fluctuations into advection and resuspension components through investigation of the phase and coherence of the harmonic frequencies relative to the ADCP-derived current speeds. A quarter-diurnal signal in phase with the ADCP-derived current speeds can be considered a resuspension signal, while a semi-diurnal signal out of phase with the ADCP-derived current speeds can be considered an advection signal. Basic harmonic analysis of LISST data has been undertaken before (Jago, et al., 2006); however, this technique has not previously been used to estimate SPM flux by particle size.

In the remainder of this chapter, a harmonic analysis is performed in Section 7.2 to determine the timescales over which SPM concentrations varied. This is further analysed in

7.3 to split the data into resuspension and advection signals, the variation of which is investigated in 7.4. Based upon these investigations, the mass and volume flux of SPM is calculated in 7.5 for both deployment periods. These results are discussed in 7.6, and finally, 7.7 brings together the results and discussion to present a series of conclusions.

7.2 Harmonic analysis of SPM

A harmonic analysis of the volume concentration recorded by the LISST, performed using the "t_tide" software (Pawlowicz, et al., 2002), as used previously in Section 6.4, provides the signal amplitude of each harmonic constituent. The time series of each particle size class from the LISST was analysed using t_tide for the entire February-March deployment and first 250 hours of the May-June deployment. The resulting amplitudes of the controlling harmonic frequencies (quarter-, semi-, and sixth diurnal) are shown in Fig. 7.3.

The results of the harmonic analysis show that during the May-June deployment period, concentrations of all particle sizes fluctuated on a quarter-diurnal timescale (Fig. 7.3 bottom), with the semi-diurnal signal having approximately half of the amplitude of the quarter-diurnal. By contrast, concentrations during the February-March deployment fluctuated on a quarter-diurnal timescale up to the 104 μm size class of the LISST, with the larger size classes fluctuating predominantly on a semi-diurnal timescale, though for the larger particle sizes (those larger than ~270 μm), the amplitudes of the quarter- and semi-diurnal signals were similar. Two quarter-diurnal modes were present within the February-March data (Fig. 7.3 top), with a transition between the two occurring at ~122 μm. Subsequently, particle sizes are divided into two modes – small and large particles – with small particles defined as those < 122 μm, and large particles as those > 122 μm.

The values shown for the sixth diurnal tides in Fig. 7.3 are not presented with confidence. For all of the size classes analysed, the signal to noise ratio for the sixth diurnal tides was less than 2:1, and for the majority of size classes less than 1:1. Therefore, for many particle sizes, the amplitude of the noise was greater than that of the signal itself, making the sixth diurnal signal difficult to determine accurately. Due to the small amplitude of the sixth diurnal signal (Fig. 7.3), and the lack of confidence in the calculated amplitudes, the sixth diurnal has been excluded from further analysis in the remainder of this chapter.

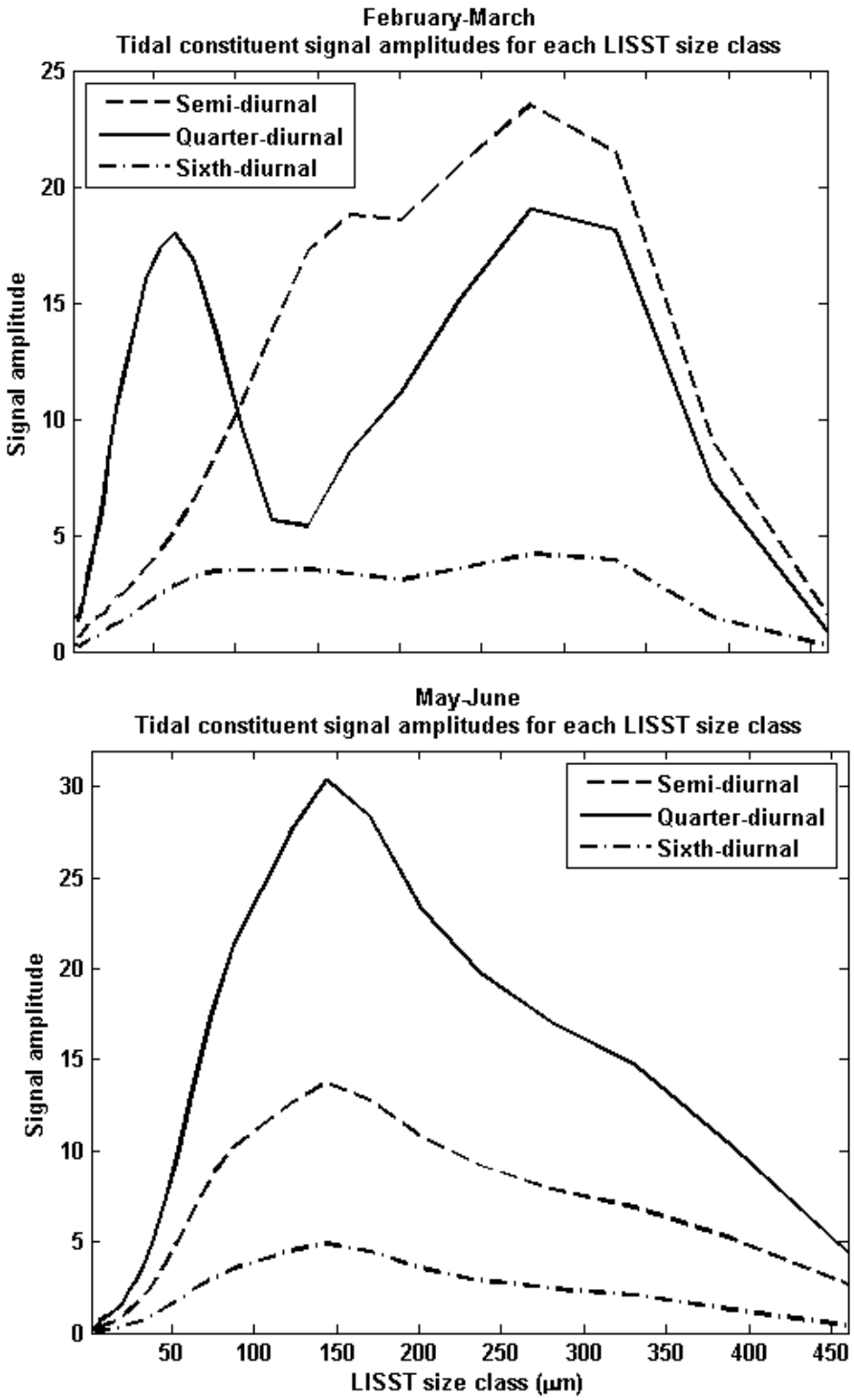

Fig. 7.3 – Amplitudes of the quarter-, semi- and sixth-diurnal harmonic constituents for the February-March (top) & May-June (bottom) deployments extracted through harmonic analysis of the different size classes of the LISST

7.3 Distinguishing between resuspension and advection signals

7.3.1 Identifying the twin peak signal

In an estuary in which both resuspension and advection occur, observations of SPM concentrations over time at any height above the bed are a combination of the resuspension component, that is proportional to a high power of the current speed, in combination with the advection component, created by a horizontal concentration gradient, if present, which is proportional to the tidal displacement (Jago & Jones, 1998), as discussed in Section 3.5.

Peak small particle concentrations during February-March occurred late on the ebb tide, after the peak ebb current speeds had been reached, and early on the flood tide, before the peak flood current speeds had been reached (Fig. 7.4 top). The peaks in SPM concentration were therefore shifted towards low water – concurrent with the twin peak signature shown in Fig. 3.6. In addition, asymmetric concentrations were present during the slack water periods, with concentrations higher during low water than high water (Fig. 7.4 top), a feature of a twin peak signal (Fig. 3.6) indicating advection bringing material down the estuary. By contrast, small particle concentrations during the May-June deployment displayed a stronger relationship with the peak current speeds (Fig. 7.4 bottom). Particle concentrations still peaked early on the flood and late on the ebb by comparison with the peak current speeds (Fig. 7.4 bottom), but the offset was less than during February-March (Fig. 7.4 top). Asymmetry was present in the low and high water minima, but this asymmetry was much lower than that seen during February-March. A twin peak signal was therefore present during the May-June deployment, but at a much reduced level.

The strongly twin peak nature of the February-March concentrations, in which the low water concentration was higher than that which occurred during high water corresponds well with Fig. 7.2 and may indicate the presence of a horizontally advected concentration gradient. This signal is much reduced in May-June, indicating that the horizontal concentration gradient was seasonally varying.

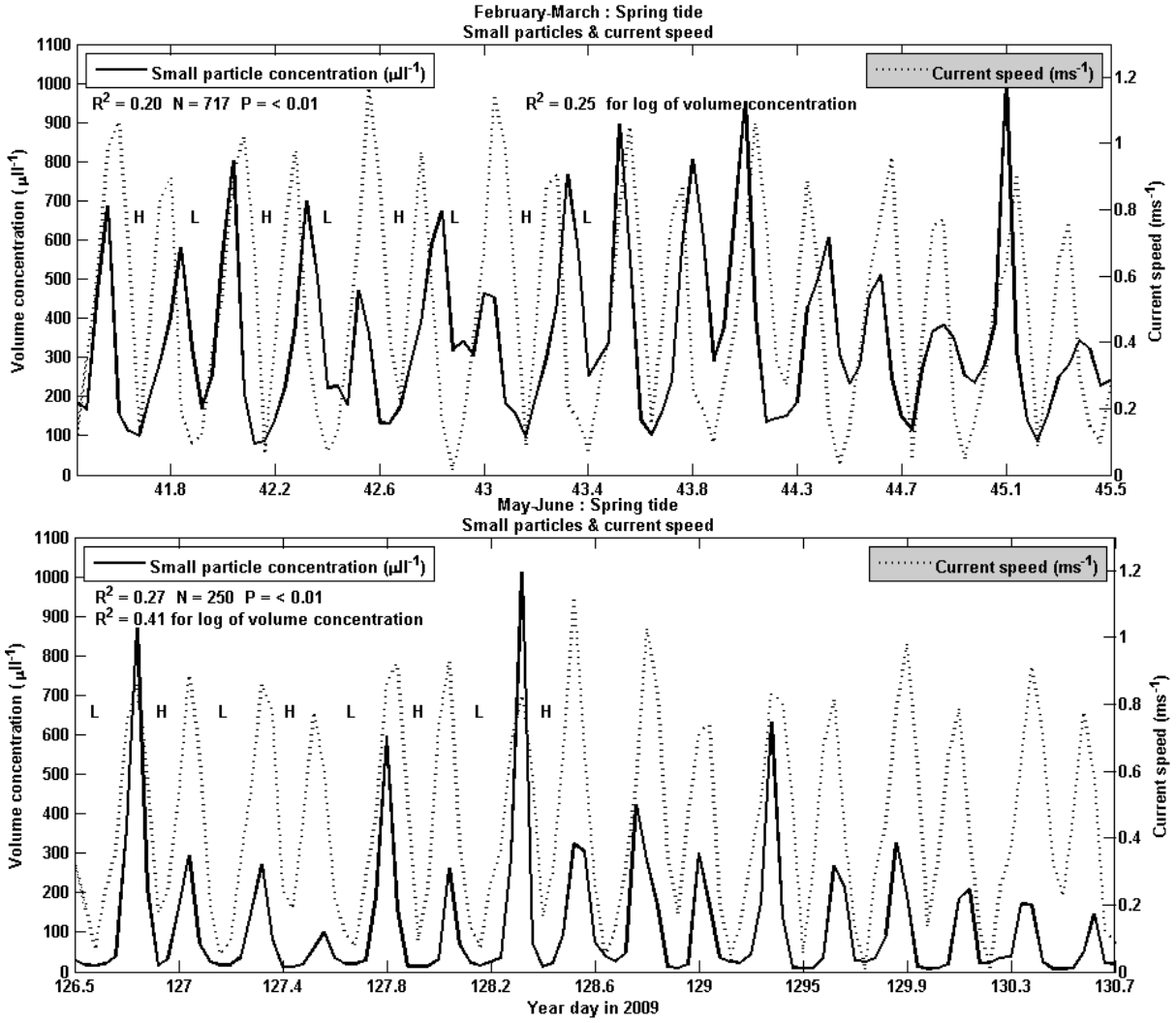

Fig. 7.4 – Small particle (< 122 µm) concentrations and current speeds during peak spring conditions in February-March (top) and May-June (bottom). H & L indicate high and low water periods

7.3.2 Coherence and phases between particle classes and current speeds

Having established the presence of a twin peak signal within the LISST-derived SPM concentration data during February-March, and to a much reduced extent during May-June, the phase and coherence of the harmonic frequencies present in the data can be used to distinguish the presence of a quarter-diurnal resuspension signal and a semi-diurnal horizontally advected concentration gradient when they are calculated relative to the ADCP-derived velocities.

To establish the strength of the relationship between particle concentration and current speed, a spectral analysis, shown in Fig. 7.5 and Fig. 7.6, was run for both the February-March and May-June data to determine the magnitude squared coherence (MSC) and phase relationship between the small (< 122 µm) and large (> 122 µm) particle classes, as established in Section 7.2, and the current speeds. The phases shown in Fig. 7.5 and Fig. 7.6 are relative to the current speed fluctuations.

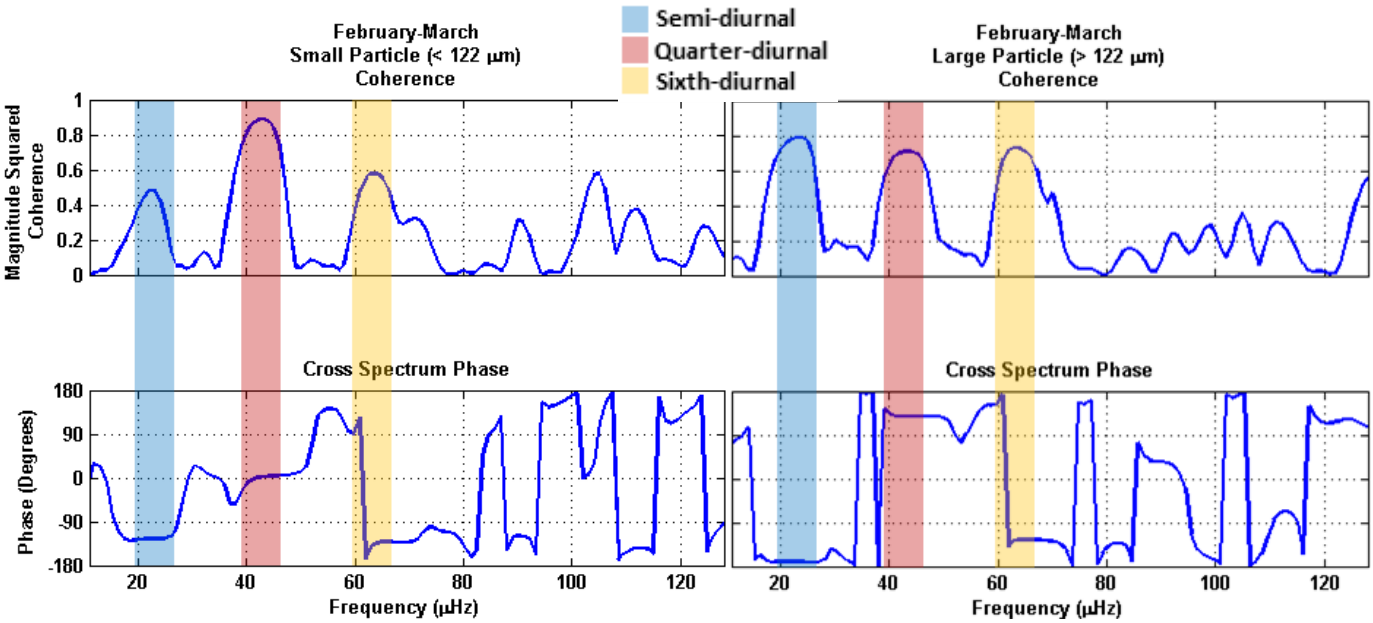

Fig. 7.5 – Spectral analysis of small (left) and large (right) particle concentrations during February-March. Top panel shows coherence, bottom panel shows phase, both are relative to the current speeds from the bottom bin of the ADCP. Semi-, quarter- and sixth-diurnal tidal harmonic frequencies are highlighted

During February-March, small particle concentrations fluctuated on a predominantly quarter-diurnal frequency (Fig. 7.3) with an MSC in excess of 0.8 and a zero phase relative to the ADCP-derived current speeds. This demonstrates that this signal was predominantly a resuspension signal associated with the high current speeds during the flood and ebb tides. The semi-diurnal signal displayed lower coherence between the current speeds and concentrations of small particles during February-March, with a phase of -130° indicating that these concentrations were not predominantly controlled by the current speeds, and instead represented the advection of a horizontal concentration gradient of small particles. A phase of -180° would indicate a semi-diurnal advection signal peaking during low water,

and therefore the phase of -130° indicates a semi-diurnal advection signal with its peak during the late ebb. This corresponds well with the SPM mass concentration seen during the late ebb in Fig. 6.14a.

The large particles present during February-March did not display a zero phase with the current speeds at either the quarter- or semi-diurnal frequency. This indicates that the large particles were not resuspended, but were the result of flocculation and / or advection. The highest coherence for large particles during February-March was displayed by the semi-diurnal signal, with a phase close to -180° indicating an increase in concentrations of large particles during low water. Coupled with the advection of small particle concentrations during the late ebb, this probably indicates that small particles, arriving on the late ebb, flocculated into large particles over low water. This will be considered further in Chapter 8. The quarter-diurnal signal of the large particle time series during February-March had a lower MSC at ~0.7 and a phase of 135° relative to the current speeds, indicating the presence of flocculation approximately 2 hours after peak current speeds at the start of high and low water.

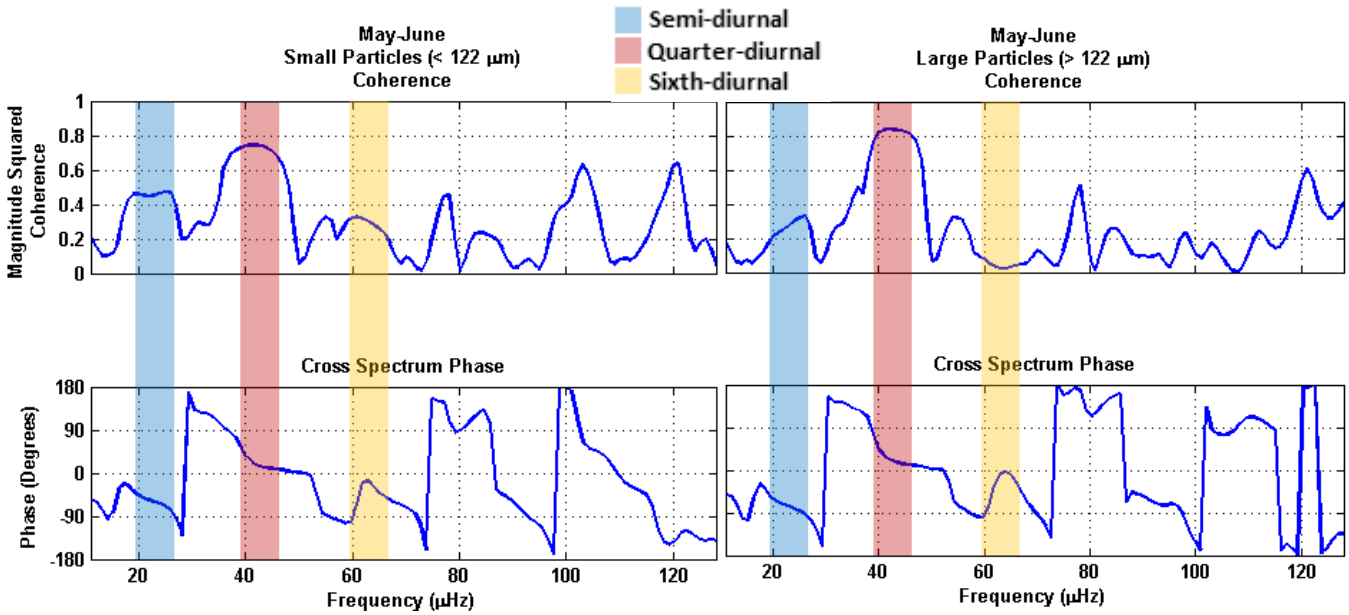

Fig. 7.6 – Spectral analysis of small (left) and large (right) particle concentrations during the first 250 hours of the May-June deployment. Top panel shows coherence, bottom panel shows phase, both are relative to the current speeds from the bottom bin of the ADCP. Semi-, quarter- and sixth-diurnal tidal harmonic frequencies are highlighted

Coherence at a sixth diurnal frequency was shown in both the small and large particle classes with a phase of roughly -135° during February-March, however, the signal amplitude of the sixth diurnal tides was small (Fig. 7.3), and the signal to noise ratio predominantly low, as discussed in Section 7.2. Therefore, despite the coherence, the sixth diurnal tides are considered unimportant in this context. The small and large particles were both dominated by the quarter-diurnal frequency during the May-June deployment. Both had phases of less than 10° relative to the current speeds, indicating that small and large particle concentrations during the May-June deployment were primarily the result of resuspension from the sea bed with little semi-diurnal advection present.

Small particle concentrations during February-March were the result of resuspension from the sea bed in combination with the advection of a horizontal concentration gradient during the late ebb tide. The horizontal concentration gradient resulted in large offsets between the particle concentration maxima and the maxima of the current speeds. This gave rise to high concentrations of small particles (up to 300 $\mu l l^{-1}$ – Fig. 7.4 top) during low water, which were consistently greater than twice the concentration encountered during high water (~100 $\mu l l^{-1}$), despite asymmetry in velocity resulting in higher average currents speeds during the flood (see Section 6.3.3). Large particle concentrations increased primarily during low water on a semi-diurnal frequency, probably due to the flocculation of small particles advected from high up the estuary. Some increase in the concentration of large particles occurred during high water, and therefore some correlation was present with the quarter-diurnal frequency. By contrast, both small and large particle concentrations had phases of less than 10^{o} during the May-June deployment and were therefore the product of quarter-diurnal resuspension from the sea bed. A semi-diurnal horizontal concentration gradient was present, but at a much reduced level, which resulted in lower slack water concentrations of around 25$\mu l l^{-1}$ during low water and 15 $\mu l l^{-1}$ during high water (Fig. 7.4 bottom).

Changes to the harmonic frequencies controlling the various particle classes (Fig. 7.3) were brought about by a decrease in the horizontal concentration gradient between the deployment periods (Fig. 7.5 and Fig. 7.6), resulting in an improved correlation between current speeds and small particle concentrations during May-June by comparison with February-March (Fig. 7.4). A large variation therefore existed in the control of small particles

between the deployment periods: during February-March small particle concentrations varied over both quarter- and semi-diurnal frequencies due to the presence of both resuspension and a strong horizontal concentration gradient, while during May-June, the quarter-diurnal resuspension signal was much stronger than the semi-diurnal advection.

7.4 Variations in the strengths of advection and resuspension across the spring-neap cycle

7.4.1 Reconstruction of the full spring-neap cycle

Having demonstrated that the variations in small particle SPM concentration during February-March and May-June were driven primarily by a quarter-diurnal resuspension signal in combination with a seasonally-varying semi-diurnal advection signal, the amplitude of which decreased between the deployment periods, it is necessary to investigate the changes in the quarter- and semi-diurnal signals across the spring-neap cycle. With the semi-diurnal advection signal during February-March peaking late on the ebb tide and the advected material originating from high up the estuary, the decrease in tidal range encountered during the transition from spring to neap conditions may decrease the importance of this horizontal concentration gradient to the SPM concentrations. However, concurrent with the decrease in the tidal excursion and therefore influence of the semi-diurnal advection signal is a decrease in the bed shear stress since as the tidal excursion decreases, current speeds also decrease and therefore bed shear stress and the associated quarter-diurnal resuspension of bed material decreases. It is hypothesised therefore that the semi-diurnal advection signal will dominate small particle SPM concentrations during spring tides in February-March (Fig. 7.4 top), with the amplitude of this advection signal and importance relative to the quarter-diurnal resuspension signal decreasing between spring and neap tidal conditions. During spring tides in May-June, the quarter-diurnal resuspension signal will dominate due to the minor twin peak inequality displayed by the data (Fig. 7.4 bottom).

7.4.2 Reconstruction of separate neap and spring periods

Semi-diurnal and quarter-diurnal harmonic frequencies were fitted to the data series' of small particle concentrations across the first spring-neap cycle of the February-March deployment (Fig. 7.7 top) and first 250 hours of May-June (Fig. 7.7 bottom). As can be seen from the figures, the reconstruction does not accurately recreate either the lowest concentrations during neap tide conditions or the highest concentrations during the peak spring periods for either of the deployment periods. This offset is the result of applying a single harmonic reconstruction to the entire period, resulting in an offset, Z_0, which is the time-averaged mean concentration. This mean concentration changes between the spring and neap periods during both February-March and May-June, resulting in the offset shown. This indicates that the amplitudes and phases of the harmonic constituents driving the small particle concentrations changed between the spring and neap periods (e.g. a decrease in the amplitude of the quarter-diurnal resuspension brought about by a decrease in the tidal range). To investigate these changes, the peak spring and lowest neap periods were isolated (only the spring period was isolated for the May-June deployment since the lowest neap was not recorded by the LISST), and the harmonic analysis re-run using quarter-diurnal and semi-diurnal constituents to determine the changes in the relative strengths of the quarter- and semi-diurnal signals over the spring-neap cycle.

The resulting reconstructions (Fig. 7.8, Fig. 7.9 & Fig. 7.10) show that small particle concentrations during spring tide conditions in May-June (Fig. 7.8) operated mainly on a quarter-diurnal frequency, corresponding well with the results shown in Fig. 7.6. The quarter-diurnal resuspension signal had twice the amplitude of the semi-diurnal advection signal, indicating that this time period was resuspension dominated. The quarter-diurnal resuspension was flood dominant, as indicated by the semi-diurnal peak being close to the flood peak of the quarter-diurnal resuspension. The residual concentration (Fig. 7.8 bottom), showed one clear spike during peak current speeds on the second flood tide. Concentrations at this time increased to 1000 $\mu l l^{-1}$, and this spike was not well represented by the reconstruction.

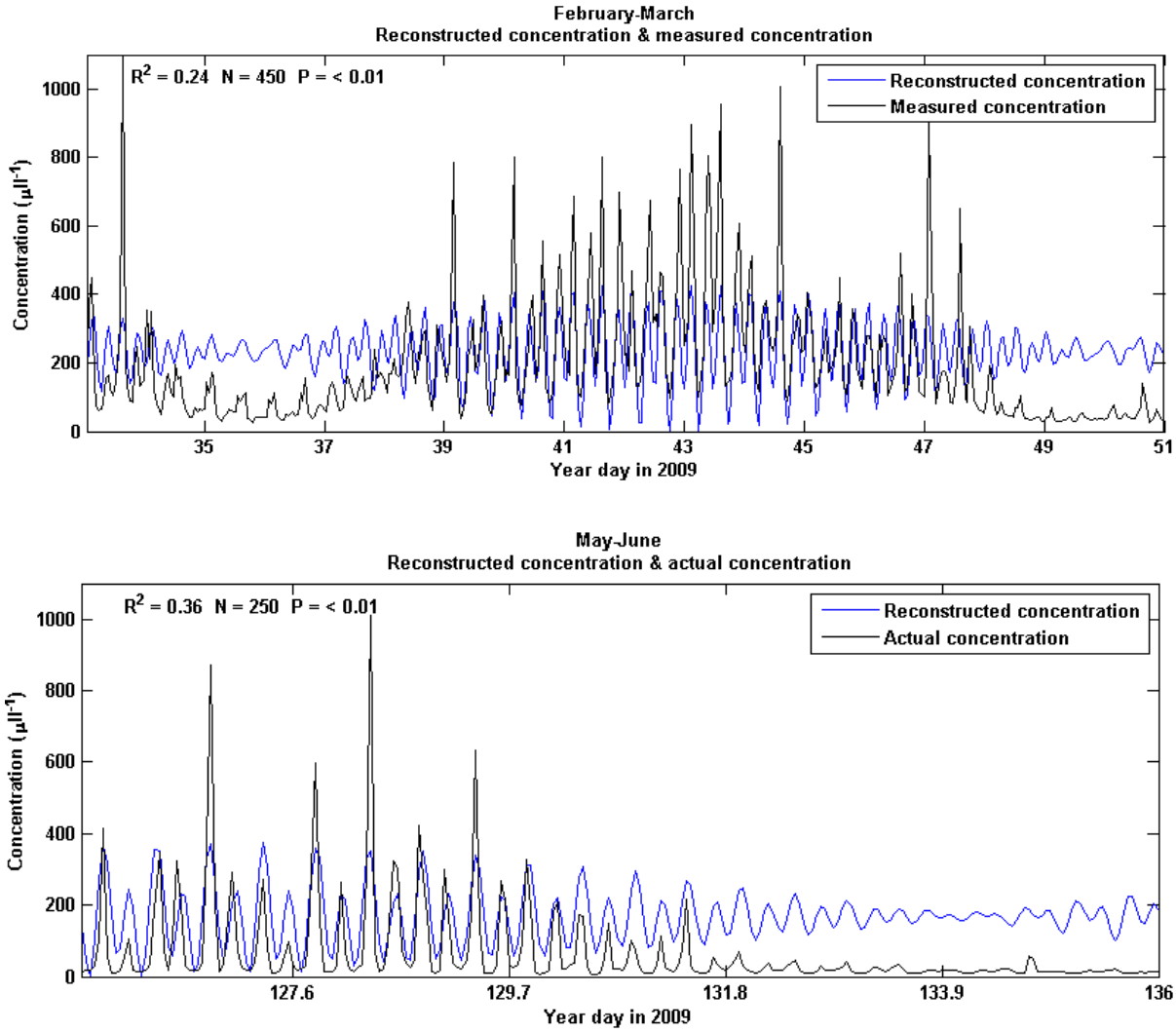

Fig. 7.7 – Small particle (< 122 µm) concentrations recorded by the LISST and reconstructed using the quarter- and semi-diurnal signals for spring-neap periods during February-March (top) & May-June (bottom)

Analysis of the February-March spring and neap reconstructions (Fig. 7.9 & Fig. 7.10) shows that the semi- and quarter-diurnal components changed in phase relative to each other between the spring and neap periods. During spring tides (Fig. 7.9), the semi- and quarter-diurnal components were approximately equal in amplitude, however under neap conditions, although both the semi- and quarter-diurnal signals had reduced in amplitude, the semi-diurnal advection component was dominant, with the semi-diurnal amplitude approximately 25% greater than that of the quarter-diurnal component. The residual

differences (bottom panel in both Fig. 7.9 and Fig. 7.10) indicate that the harmonic frequencies provided a good fit to the data during both the spring and neap periods.

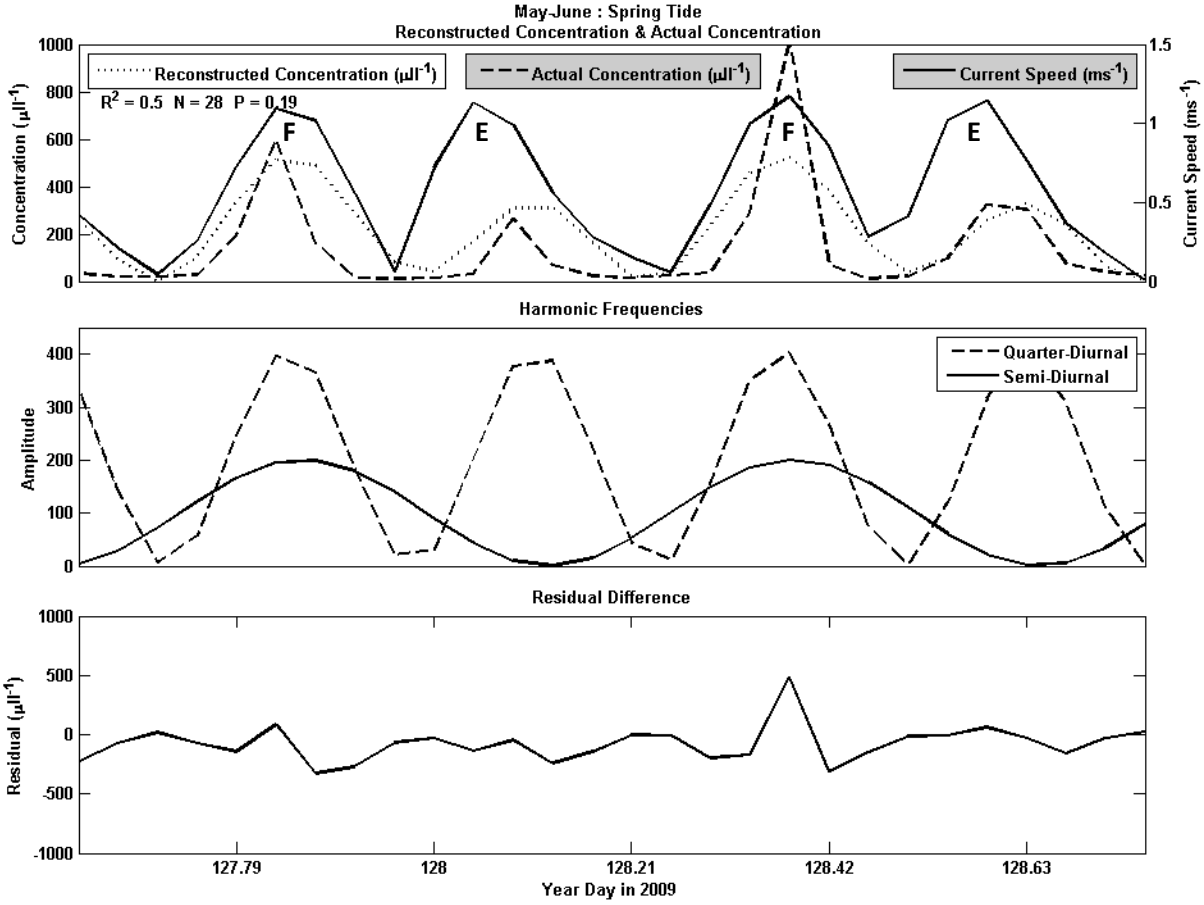

Fig. 7.8 – Upper panel: May-June spring tide small particle concentrations (dashed) with reconstruction (dotted) & current speed (solid line). F and E indicate the flood and ebb tides. Middle panel: Semi- and quarter-diurnal harmonic frequencies used to generate the reconstructed concentrations. Lower panel: Residual concentrations after subtracting the recorded concentration from the reconstructed concentration

Between the spring and neap tidal conditions in February-March, the decrease in tidal range resulted in a decrease in current speeds, and therefore a decrease in the quarter-diurnal resuspension signal. The reduction in tidal range also reduced the tidal excursion, and therefore decreased the concentration change brought about by the semi-diurnal advection observed on the late ebb and over low water. This reduction in the amplitudes of both the quarter-diurnal resuspension signal and the semi-diurnal advection signal seen during spring

tide conditions resulted in a minor increase in concentration during the early flood tide in what may be indicative of a semi-diurnal advection signal with material entering the estuary from offshore (Fig. 7.10).

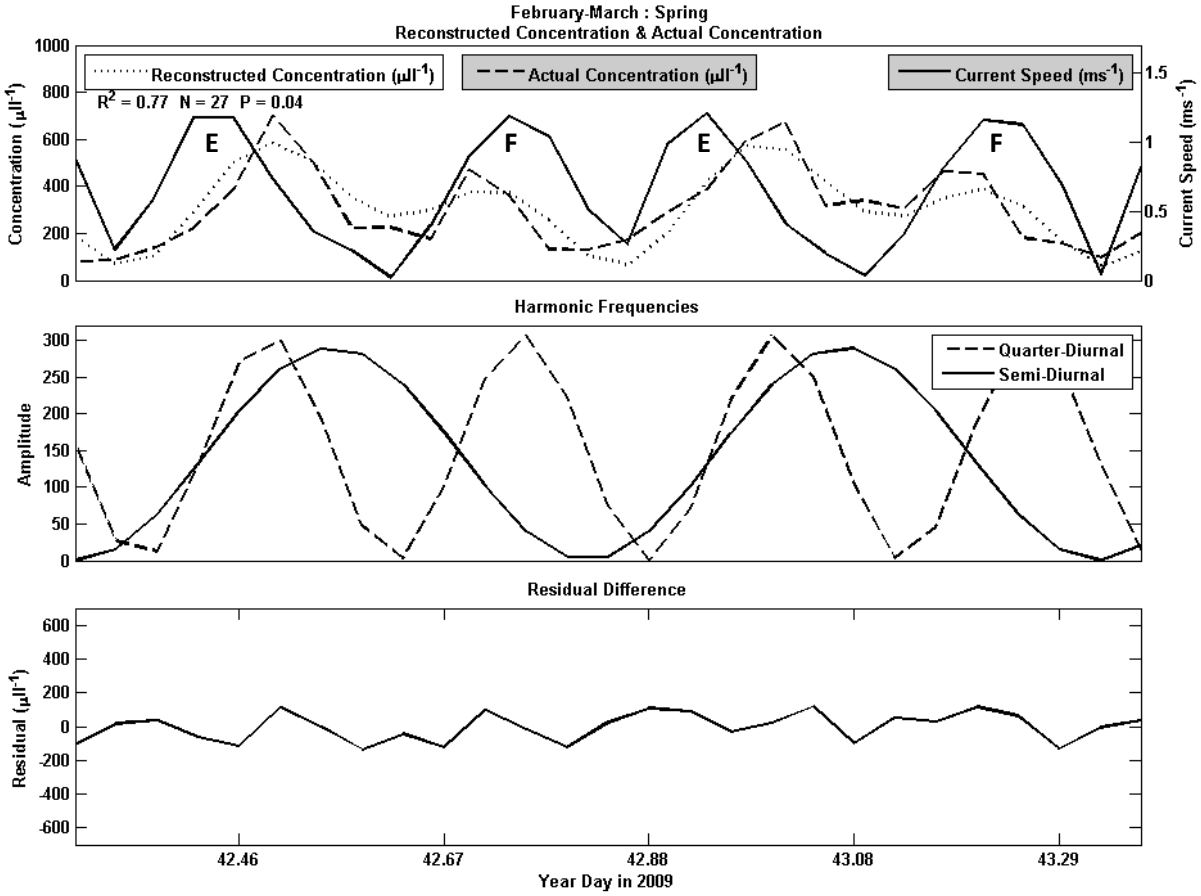

Fig. 7.9 – Upper panel: February-March spring tide small particle concentrations (dashed) with reconstruction (dotted) & current speed (solid line). F and E indicate the flood and ebb tides. Middle panel: harmonic frequencies used to generate the reconstructed concentrations. Lower panel: Residual concentrations after subtracting the recorded concentration from the reconstructed concentration

The interactions between the quarter- and semi-diurnal components are shown over repeated tidal cycles for both small and large particles in Fig. 7.11 for February-March and Fig. 7.12 for May-June. In this figure, time is shown along the x-axis, with particle size on the y-axis, and colour (blue to red) representative of the log of the volume concentration of SPM in suspension. The white line shows D_{50}, while the bottom panel shows current speed.

Concentrations during February-March (Fig. 7.11) showed concentrations of small particles increasing during peak current speed, with concentrations of large particles increasing at high and, predominantly, low water. Higher concentrations of small particles were present on the transition between ebb and low water than between the flood and high water, showing that small particles were advected down the estuary during this time. The May-June deployment (Fig. 7.12) showed concentrations across all particle sizes increasing during flood and ebb, and falling during high and low water, indicating resuspension during peak current speeds. However, low concentrations of very large particles remained during low water.

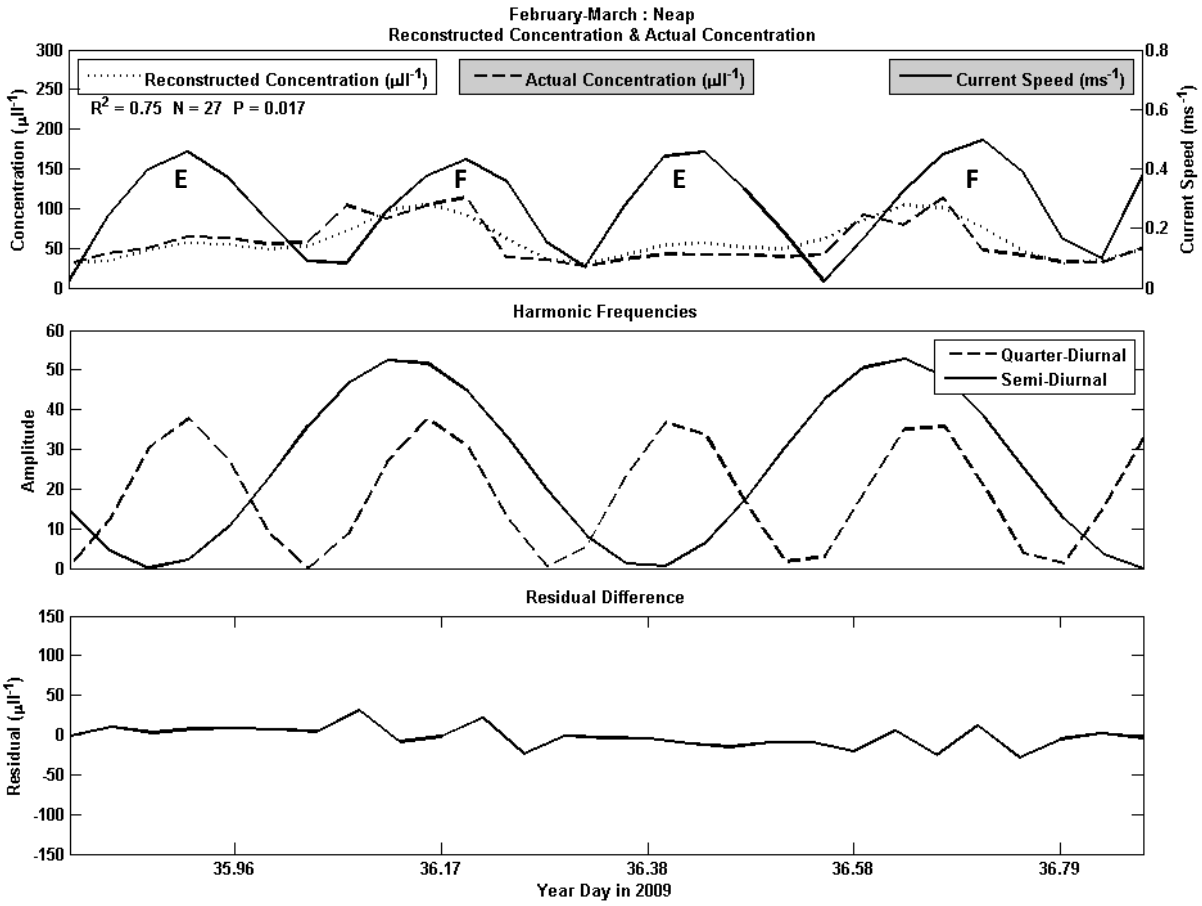

Fig. 7.10 – Upper panel: February-March neap tide small particle concentrations (dashed) with reconstruction (dotted) & current speed (solid line). F and E indicate the flood and ebb tides. Middle panel: harmonic frequencies used to generate the reconstructed concentrations. Lower panel: Residual concentrations after subtracting the recorded concentration from the reconstructed concentration

7.4.3 Asymmetry in SPM concentrations

In an idealised scenario (Fig. 7.13a & b) in which the maxima of the semi-diurnal advection signal occurs concurrently with the minima of the quarter-diurnal resuspension signal, the impact of the semi-diurnal advection signal on both SPM concentrations and the timing of the concentration maxima (resulting in the twin peak signal) increases in line with the amplitude of the semi-diurnal signal. In this instance, a semi-diurnal advection signal with an amplitude double that of the quarter-diurnal signal is able to shift the peak SPM concentrations by one hour (Fig. 7.13b). In a scenario such as this, the semi-diurnal signal impacts equally on the quarter-diurnal maxima, resulting in symmetrical maximum concentrations on each tidal phase.

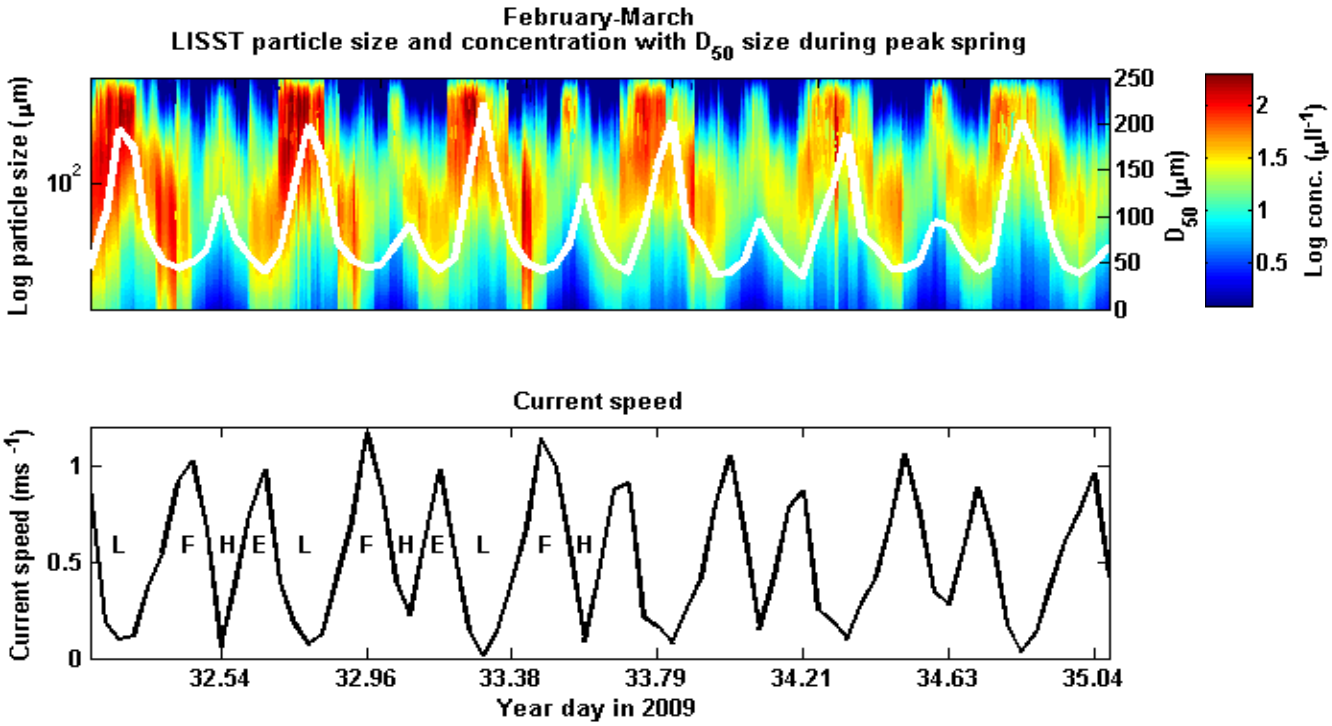

Fig. 7.11 – LISST volume concentration with D_{50} (top) and current speeds (bottom) for February-March. For the top panel, x axis shows time, y axis shows log of particle size, colour represents the particle concentration and the white line shows the D_{50} particle size. L F H E indicate the times of low water, flood tide, high water, and ebb tide respectively

The magnitude of the time shift increases as the amplitude of the semi-diurnal signal increases – i.e. as the horizontal concentration gradient increases (Fig. 6.17b). During May-June, the horizontal concentration gradient was small (Fig. 7.8), and therefore the time shift

seen in the SPM concentration peaks was small (Fig. 7.4 bottom). During February-March, the time shift was larger (Fig. 7.4 top) as the concentration gradient was larger relative to the quarter-diurnal resuspension signal (Fig. 7.9).

When the semi-diurnal advection signal maxima do not coincide with one of the quarter-diurnal resuspension minima, particle concentrations become asymmetric (Fig. 7.13 c & d) due to the phase shift between the minima of the quarter- and semi-diurnal signals. In a situation in which a semi-diurnal advection signal is phase shifted relative to the quarter-diurnal signal (the semi-diurnal maxima does not coincide with one of the quarter-diurnal minima), the direction of the phase shift is important: a shift toward the ebb indicates higher concentrations on the ebb, which may result in the estuary flushing SPM onto the shelf, or may indicate that the estuary is eroding. Conversely, a phase shift toward the flood indicates higher concentrations during the flood, and may indicate that the estuary is infilling.

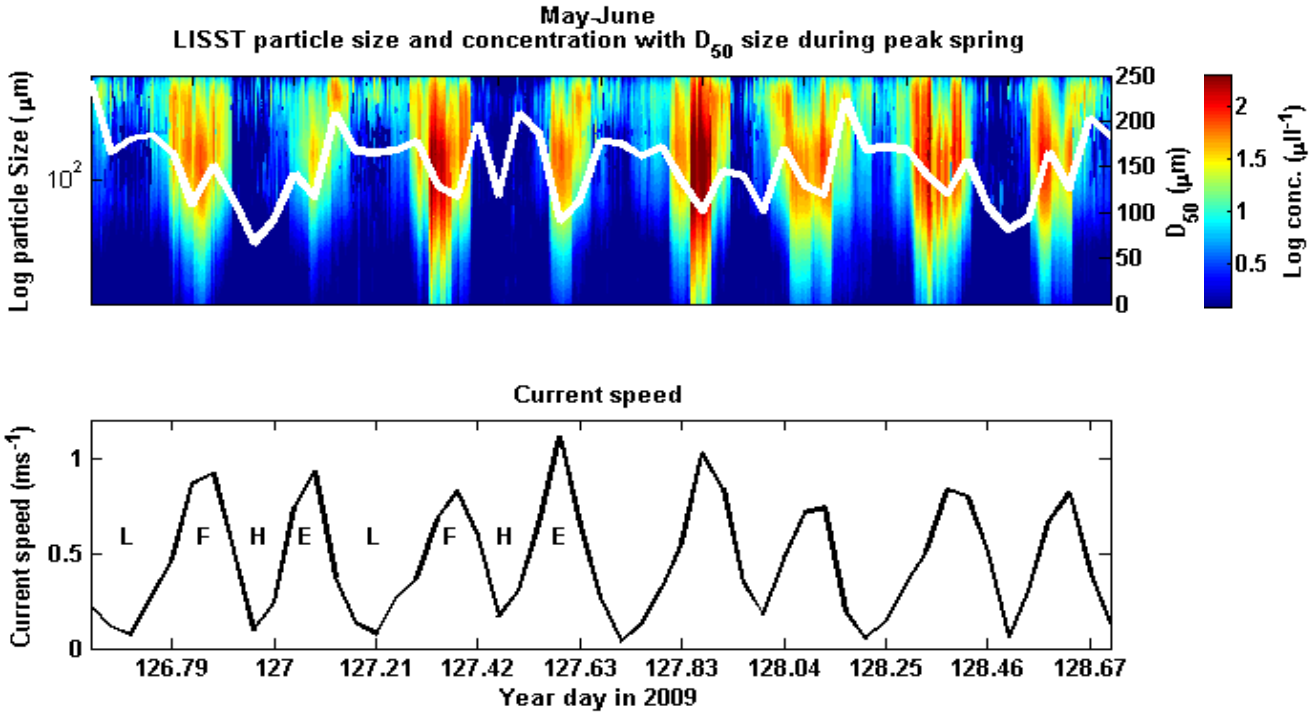

Fig. 7.12 – LISST volume concentration with D_{50} and (top) current speeds (bottom) for May-June. For the top panel, x axis shows time, y axis shows log of particle size, colour represents the particle concentration and the white line shows the D_{50} particle size. L F H E indicate the times of low water, flood tide, high water, and ebb tide respectively

A semi-diurnal phase shift also alters the timing of the concentration peak, with the greatest change in timing occurring during the steepest gradient of the semi-diurnal signal – as evidenced in Fig. 7.13d where the peak in concentration of the combined signal is altered by approximately half an hour for the first peak and an hour for the second.

7.5 Calculations of sediment flux

7.5.1 Ebb dominant sediment flux under flood dominant velocity conditions

Measurements of concentration alone are insufficient to demonstrate whether an estuary is importing or exporting material. However, multiplying the volume concentration by velocity and integrating over time provides a measure of particle volume flux over time.

Flood dominance of velocity is often indicative of flood dominance in bedload transport (dependent upon the duration of the different tidal phases) since bedload transport is proportional to u^3 (Meyer-Peter & Mueller, 1948; Bagnold, 1966) However, in suspended sediment transport, the presence of a strong horizontal concentration gradient, for example in an estuarine region, in which the highest SPM concentrations are found toward the top of the estuary, could theoretically result in an ebb dominance in SPM volume flux, even with flood dominant velocities, as shown in Fig. 7.14. In this figure, asymmetrical flood-dominant current speeds (u) are shown in the top panel. These current speeds are used to generate an idealised quarter-diurnal resuspension signal (Fig. 7.14 middle panel red line). Sediment flux is often proportional to a high power of u, such as u^3-u^5 (van Rijn, 1984; Hoitink, et al., 2003; Abdel-Fattah, et al., 2004; Ralston & Geyer, 2009). u^3 is used here as a conservative estimate. A semi-diurnal advection signal is presented (Fig. 7.14 middle panel green line), making the total concentration at any point in time (Fig. 7.14 middle panel black line) equal to the concentration provided by the resuspension signal (R), plus the concentration provided by the advection signal (A). The suspended sediment flux (Qs) can then be calculated as the integral over time (t) of current speed (u) multiplied by the sum of the concentration provided by the resuspension signal (R) and the concentration provided by the advection signal (A):

$$Q_s = \int_0^t u \times (R + A) \tag{7.1}$$

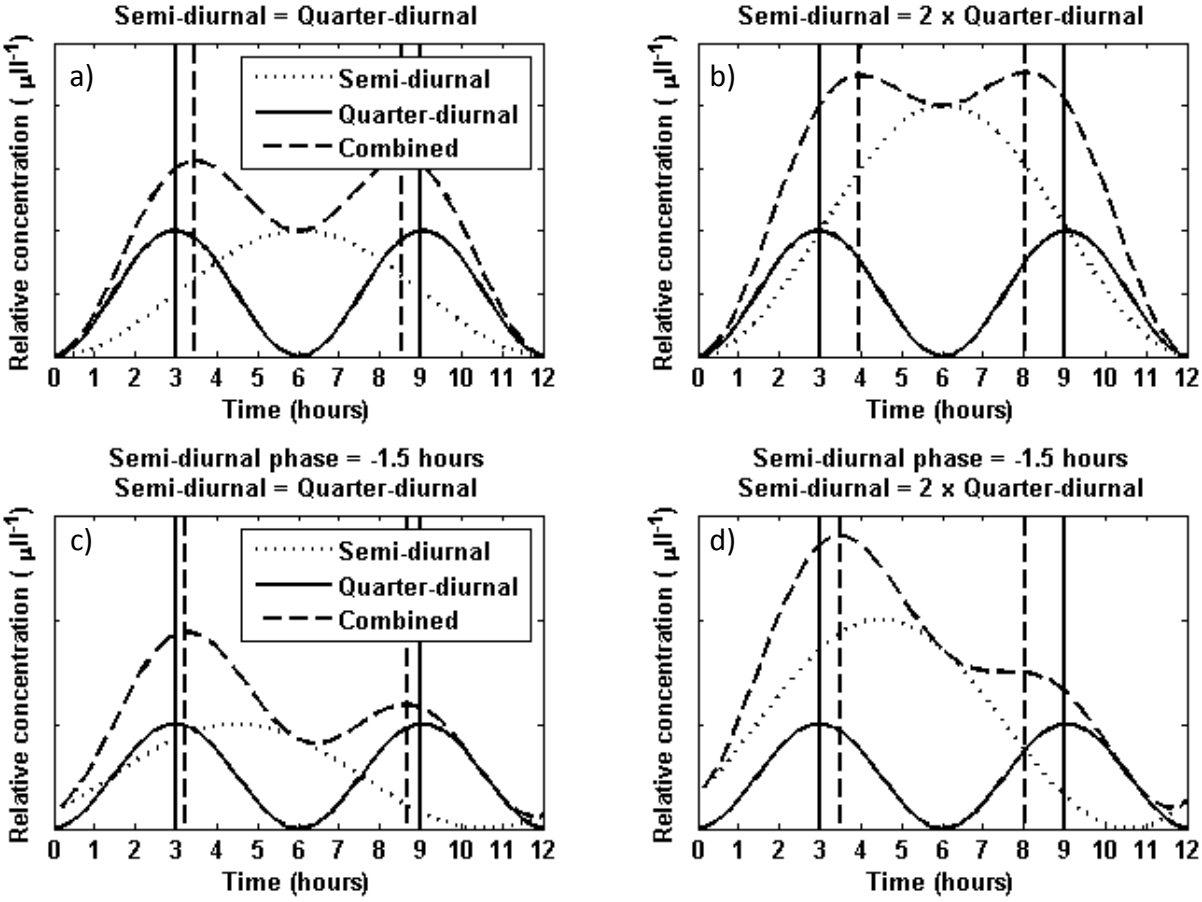

Fig. 7.13 – a & b: Idealised representations of a semi-diurnal signal (dotted) with maxima during the quarter-diurnal signal (solid line) minima and resultant combined twin peak signal (dashed). c & d: Idealised representations of a semi-diurnal signal (dotted) and quarter-diurnal signal (solid) with a phase shift in the semi-diurnal signal of -1.5 hours relative to low water, and their resultant combined asymmetric twin peak signal (dashed)

In Fig. 7.14, the peak flood current speed is 10% higher than the peak ebb speed, and the advection signal has a phase of -1 hours relative to low water with the maximum semi-diurnal concentration equal to the peak quarter-diurnal concentration encountered during the ebb tide. These parameters result in an ebb dominant flux of 3 %. The suspended sediment flux is therefore dependent on three parameters:

- Velocity dominance;
- Advection phase relative to low water;
- Peak advection concentration relative to peak resuspension concentration.

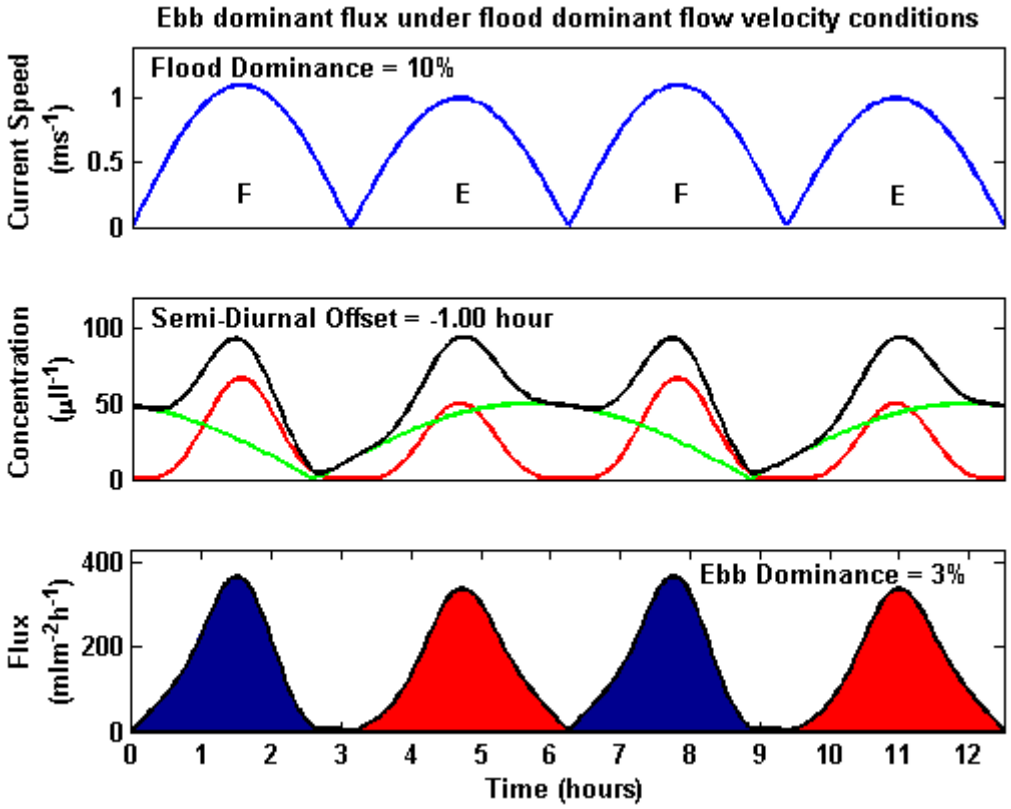

Fig. 7.14 – 3% ebb sediment flux dominance as a function of 10% flood velocity dominance and a phase offset of -1 hour of the semi-diurnal advection signal relative to low water. Top panel shows current speed; middle panel shows the resulting quarter diurnal resuspension concentration (red), semi-diurnal advection concentration (green) and combined total concentration (black). Bottom panel shows the resulting flood (blue) and ebb (red) fluxes

Keeping the peak advection concentration constant (and equal to the peak resuspended concentration encountered on the ebb tide) and varying the flood velocity dominance and phase of the advection signal relative to low water produces Fig. 7.15. The 0 % dominance level is highlighted on the figure, indicating the point at which the estuary changes flux from flood to ebb dominant. This figure demonstrates that ebb dominant SPM flux under flood dominant velocity asymmetry is possible for a range of advection phases relative to the flow velocities, and a range of velocity asymmetries. This figure assumes a constant peak advection concentration relative to the peak resuspension concentration, and varying this

parameter can either increase or decrease the area of the surface that corresponds to an ebb dominant sediment flux.

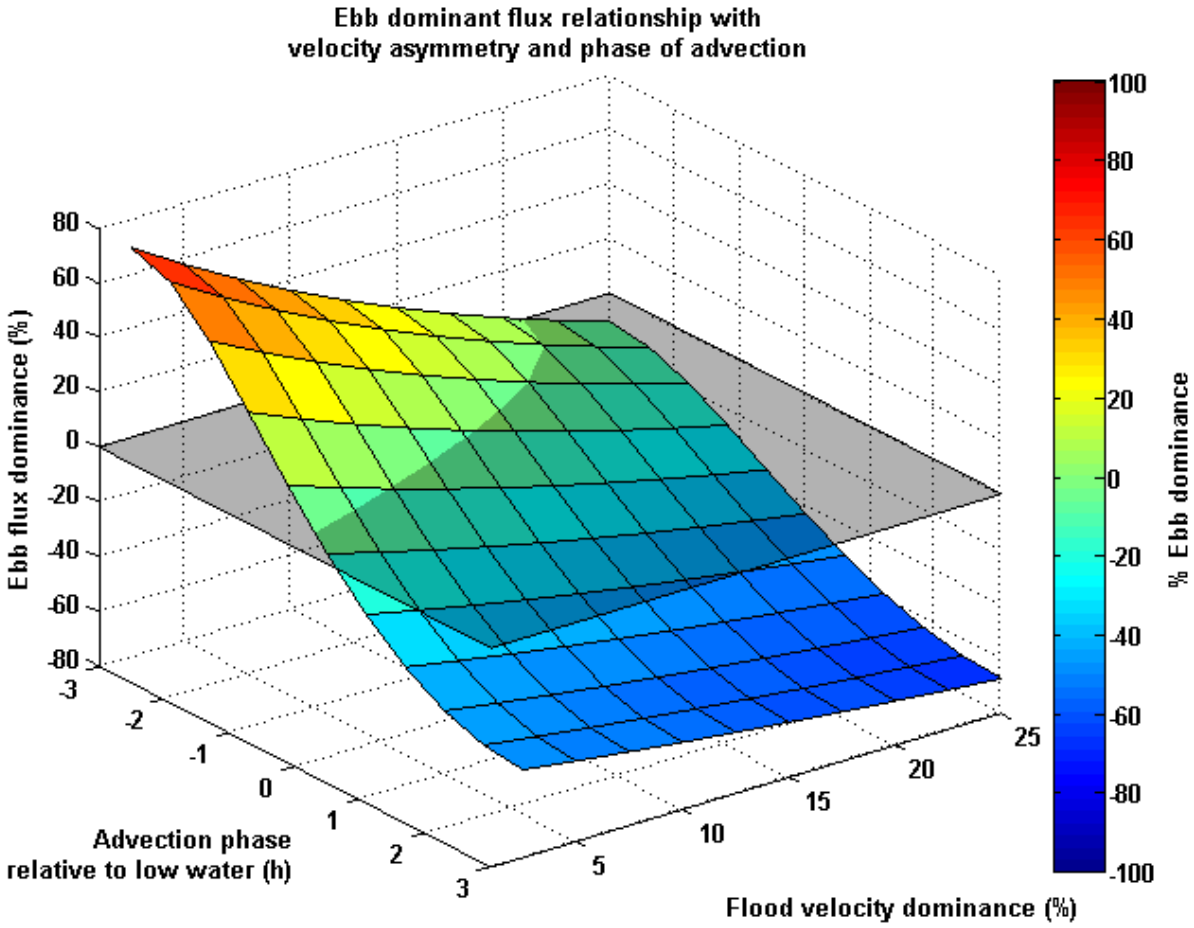

Fig. 7.15 – Flux dominance as a function of flood velocity dominance and the phase of the semi-diurnal advection signal. x axis shows flood velocity dominance as a %, y axis shows the phase of the advection signal in hours relative to low water, and z axis the resulting ebb dominance of flux as a %. Ebb flux dominance is also indicated by the colour of the surface

7.5.2 Sediment flux in the Dee Estuary

Using the LISST-derived volume concentration provides the possibility to investigate the point flux of sediment by particle size. The volume flux calculations have been split into small and large particle classes with a transition at 122 µm, concurrent with the rest of the analysis in this chapter. Mass concentration provides no indication of particle size, and therefore cannot be split in this way.

The LISST-derived SPM volume concentrations averaged 170 $\mu l l^{-1}$ during flood, 124 $\mu l l^{-1}$ during ebb during the May-June deployment period (Fig. 6.19), and 280 $\mu l l^{-1}$ during flood, 310 $\mu l l^{-1}$ during ebb during the February-March deployment period (Fig. 6.17). The point flux of SPM, calculated at hourly intervals for the first 250 hours of the May-June deployment at a single point ~2.5m above the bed is presented in Fig. 7.16. Overall, both the small and large particle sediment fluxes were flood-dominant: small particle flux was 75 % flood dominant, large particle flux 56 % flood dominant, mass flux 39 % flood dominant (Fig. 7.16), showing that material was entering the estuary from offshore. After combining the small and large particle fluxes, the net sediment volume flux for the first 250 hours of the May-June deployment was 63 % flood dominant. The net sediment flux direction at this height above the bed was therefore into the estuary from offshore.

During the February-March deployment, the sediment volume flux was also flood dominant for small particles, but this dominance was reduced to 24 % (Fig. 7.17). For the large particles, the flood dominance was not only reduced, but the flux direction reversed, with the sediment volume flux for large particles during February-March 11 % ebb dominant (Fig. 7.17). The net SPM mass flux flood dominance had also reduced by 46 % from 39 % during May-June to 21 % during February-March. After combining the small and large particle fluxes, the net SPM flux for the February-March deployment was 16 % flood dominant – a reduction of 75 % (63 % during May-June to 16 % during February-March) in the net sediment volume flux flood dominance between deployments.

The difference in particle volume flux between the deployment periods is summarised in Table 7.1. The biggest difference in particle transport between these time periods was the decrease in the horizontal concentration gradient between February-March and May-June, shown through the earlier harmonic analysis (Fig. 7.8 & Fig. 7.9) and indicated by the change in twin peak signature shown in Fig. 7.4. This reduction in the horizontal concentration gradient was insufficient to change the dominant flux direction of the estuary; however, the flood dominance was reduced by 75 % (Fig. 7.17).

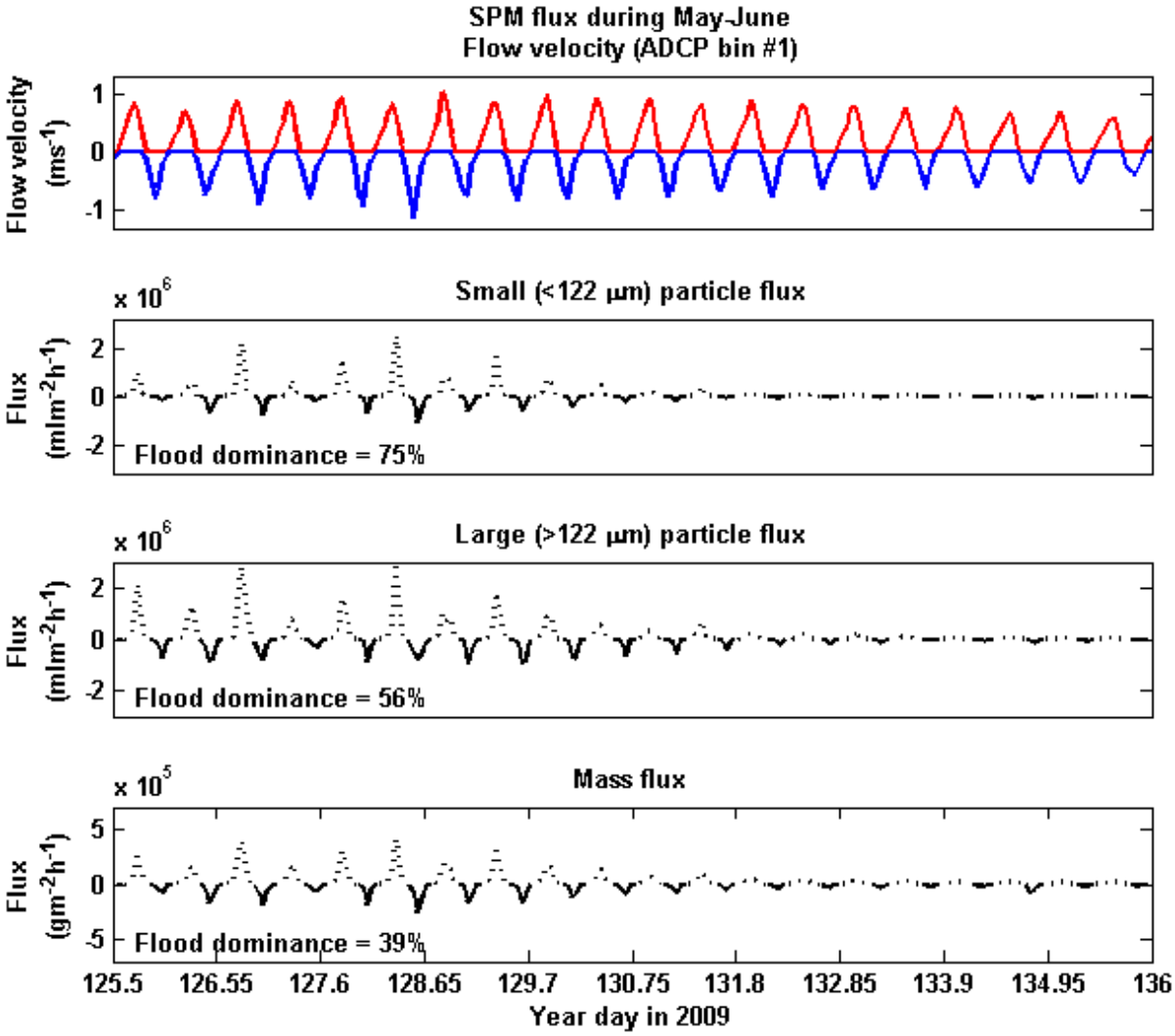

Fig. 7.16 – SPM flux during May-June for small and large particles. Flow velocity (positive indicates flood, negative indicates ebb) from the bottom bin of the ADCP (top panel), small particle flux (second panel – positive indicates flood, negative indicates ebb), large particle flux (third panel – positive indicates flood, negative indicates ebb) and mass flux (bottom panel – positive indicates flood, negative indicates ebb) are shown

7.6 Discussion

At the mouth of the Dee Estuary a quarter-diurnal resuspension signal and a semi-diurnal advection signal have been shown to be the primary controls on SPM flux (Fig. 7.3, Fig. 7.5 & Fig. 7.6). Flood dominant velocity asymmetry occurred during both February-March and May-June (see Section 6.3.3), resulting in flood dominant SPM concentrations during the May-June period (Fig. 6.19), however, the large horizontal concentration gradient present

during February-March, manifested as a semi-diurnal advection signal, was sufficient to make SPM concentrations ebb dominant during February-March (Fig. 6.17).

SPM concentrations varied over tidal, spring-neap and seasonal timescales. Variations in current speed and tidal excursion (Fig. 6.16 & Fig. 6.19) across the spring-neap cycle affected both the amplitude of the quarter-diurnal resuspension signal, and the amplitude and phase of the semi-diurnal advection signal (Fig. 7.8, Fig. 7.9 & Fig. 7.10).

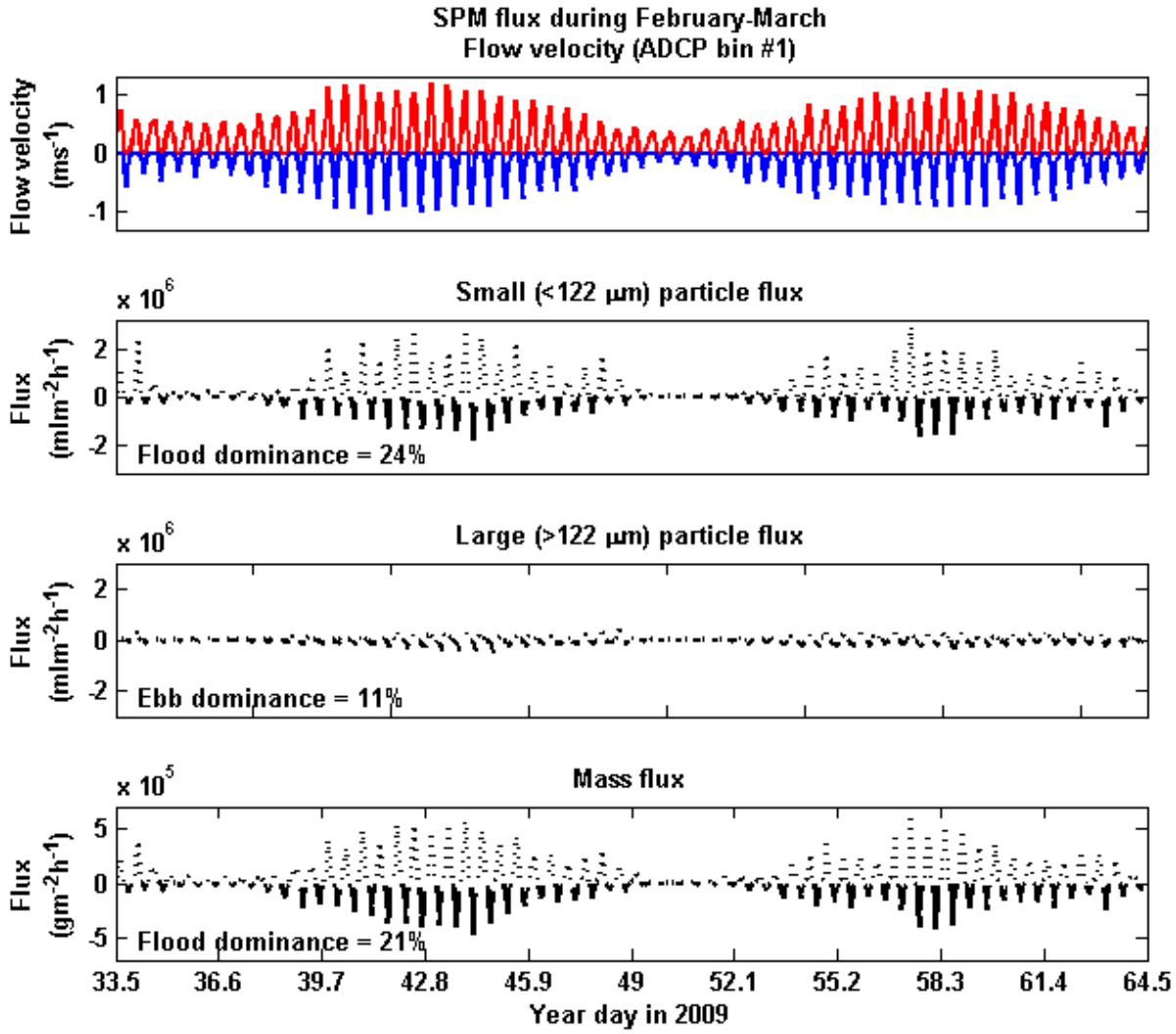

Fig. 7.17 – SPM flux during February-March for small and large particles. Flow velocity (positive indicates flood, negative indicates ebb) from the bottom bin of the ADCP (top panel), small particle flux (second panel – positive indicates flood, negative indicates ebb), large particle flux (third panel – positive indicates flood, negative indicates ebb) and mass flux (bottom panel – positive indicates flood, negative indicates ebb) are shown

During February-March, small particle (< 122 μm) concentrations were the product of a quarter-diurnal resuspension signal and a semi-diurnal advection signal of approximately equal amplitude during spring tides (Fig. 7.9), resulting in a characteristic twin peak signal (Fig. 7.4 top). The reduction in tidal excursion and current speeds between spring and neap meant that during the neap tides small particle concentration variations operated over a predominantly semi-diurnal frequency (Fig. 7.10). Flood dominant velocity asymmetry in combination with ebb dominant SPM concentrations (Fig. 6.16) resulted in a flood dominant SPM flux (Fig. 7.17), with the ebb dominance of SPM concentration insufficient to change the net flux direction of the estuary during this time.

During the May-June period, the horizontal concentration gradient was vastly reduced, and the twin peak signature not present to the same extent as during February-March (Fig. 7.4). Both small and large particle concentrations were predominantly the result of quarter-diurnal resuspension (Fig. 7.8). In the presence of flood dominant velocities, and flood dominant SPM concentrations, the SPM net flux direction was into the estuary (Fig. 7.16). The flux of SPM varied seasonally, with the average flood flux reducing by 11 % by volume between February-March and May-June, and the average ebb flux reducing by 37 % by volume (Table 7.1) due to the reduction in the horizontal concentration gradient between the deployment periods. This is illustrated diagrammatically in Fig. 7.18.

The ebb dominant flux of large particles and flood dominant flux of small particles during February-March indicates that the estuary is exporting large particles and importing small particles during this time. However, if the large particles are the result of flocculation during February-March, as indicated by the coherence and phase analysis in Section 7.3.2, this process may result in the estuary infilling faster than would occur in a system without flocculation. Small particles were transported up and down the estuary during the flood and ebb tides, with flocculation occurring during high and, predominantly, during the late ebb and low water (Fig. 7.11). Flocculated particles tend to have settling velocities that increase with particle size (Kranenberg, 1994), and therefore the large particles that were present during the late ebb and over low water had higher settling velocities than the large particles that occurred during high water. Due to this, the large particles during the late ebb and over low water settled faster, and therefore were transported less distance, than those which occurred during high water. This trend would be augmented if an up-estuary residual

circulation exists near the estuary bed, which has been shown to exist (Brown, et al., 2014) though for the present study no data are available in this region. This asymmetry in settling velocities would result in a net tidal pumping mechanism which transports SPM further during the flood than ebb and therefore increases the rate of infill of the estuary than would otherwise be found in the presence of flood dominant velocities and the strong horizontal concentration gradient. It may therefore be that the flux of the estuary is not ebb dominant during this period due to the pumping effects of the asymmetrical flocculation. This is illustrated diagrammatically in Fig. 7.19.

Table 7.1: Average and seasonal change in sediment volume flux during the February-March and May-June deployment periods

Tidal state	February-March	May-June	Change
Flood avg. ($mlm^{-2}h^{-1}$)	454790	404590	-11%
Ebb avg. ($mlm^{-2}h^{-1}$)	393020	248430	-37%
Dominance	16% Flood	63% Flood	

These results have shown that in an estuarine region with flood dominant currents and a strong horizontal concentration gradient, the ratio and phase offset between the semi- and quarter-diurnal signals affects both the timing of peak particle concentrations and the net flux of sediment (which is also dependent upon the velocity asymmetry of the tide). In the case of the Dee Estuary, the horizontal concentration gradient was insufficient to reverse the net flux direction, but in a system with larger gradients, such as during a storm period, the horizontal concentration gradient may be sufficient to reverse the direction of the net flux of the estuary, as shown in Fig. 7.15, and the estuary may begin exporting material.

Reasons for the seasonal variation in strength of the horizontal concentration gradient

River flow decreased by an average of 31% between the February-March and first 250 hours of the May-June deployment periods (Table 6.1), while concurrently, low water SPM concentrations (Fig. 7.1) decreased by 57 %, and ebb sediment flux decreased by 37 % (see Table 7.1) indicating that the sediment loading of the river may have been responsible for the observed changes in the horizontal concentration gradient and therefore the variations

in SPM flux since river sediment load tends to be proportional to river flow (Nagano, et al., 2003; Geyer, et al., 2004; Bianchi, et al., 2014). However, concentrations in the Hilbre channel were in excess of 40 mgl^{-1} across low water during the February-March deployment (Fig. 7.1), and to achieve this, concentrations within the river would need to be in excess of several grams per litre as the measurements were made at the estuary mouth, which is 8.5 km wide, much deeper than the River Dee, and therefore the riverine material had been subject to dilution on its progression down the estuary. Even with the effects of the Earth's rotation turning SPM from the river toward the Hilbre Channel side of the estuary, it is unlikely that the sediment loading of the river was solely responsible for the observed change in SPM flux, though the material supplied by the river will have been a contributing factor. This is supported by the work of Amoudry, et al., (2014) which demonstrated that river input to the Dee Estuary is negligible with regard to the horizontal concentration gradient.

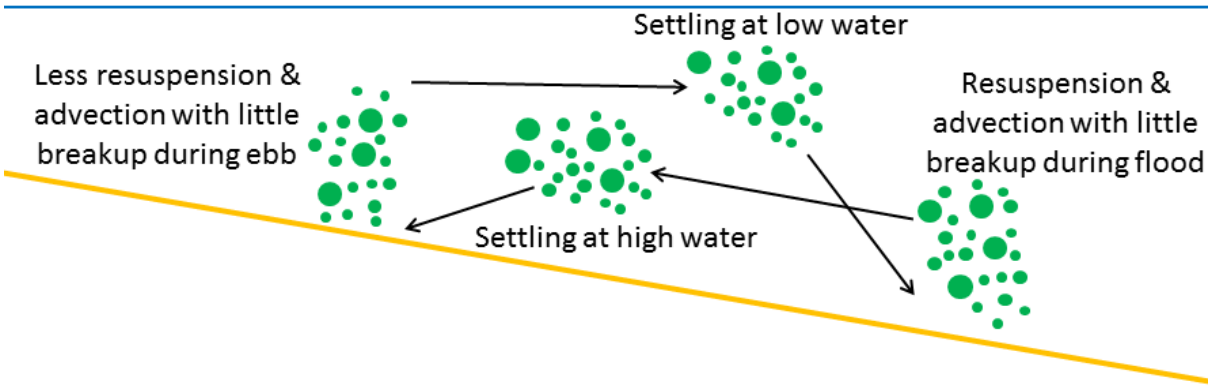

Fig. 7.18 – Schematic illustration of particle transport during May-June. Yellow line indicates estuary bed, blue line the estuary surface. Resuspension and advection with limited breakup occurs during the flood, settling at high water, less resuspension and advection with limited breakup during the ebb, and settling during over low water, leading to a net flood dominant SPM flux

Another change between the February-March and May-June deployment periods was an increase in biological activity, indicated by the increase in fluorescence response (Fig. 6.15) between sample periods (Gitelson, et al., 1999). The presence of benthic diatoms and algal mats on salt marsh and mudflat regions, in addition to the growth of salt marsh plants

during the summer months can have a binding effect on sediment, making it harder to erode than during the winter months when these binding agents are not present (Wright, et al., 1997; Sanford, 2008) (see Section 3.2.4). During February-March therefore, low biological activity meant that the fine sediments of the mudflats and salt marshes high up the estuary were more exposed to resuspension induced by tidal currents, wind and wave stresses, potentially resulting in transport down the estuary. By contrast, during May-June, the growth of biological entities such as algal mats and benthic diatoms which secrete sticky polysaccharide substances and bind particles together will have increased the erosion threshold, and may have resulted in the observed reduction in resuspension and particle transport down the estuary.

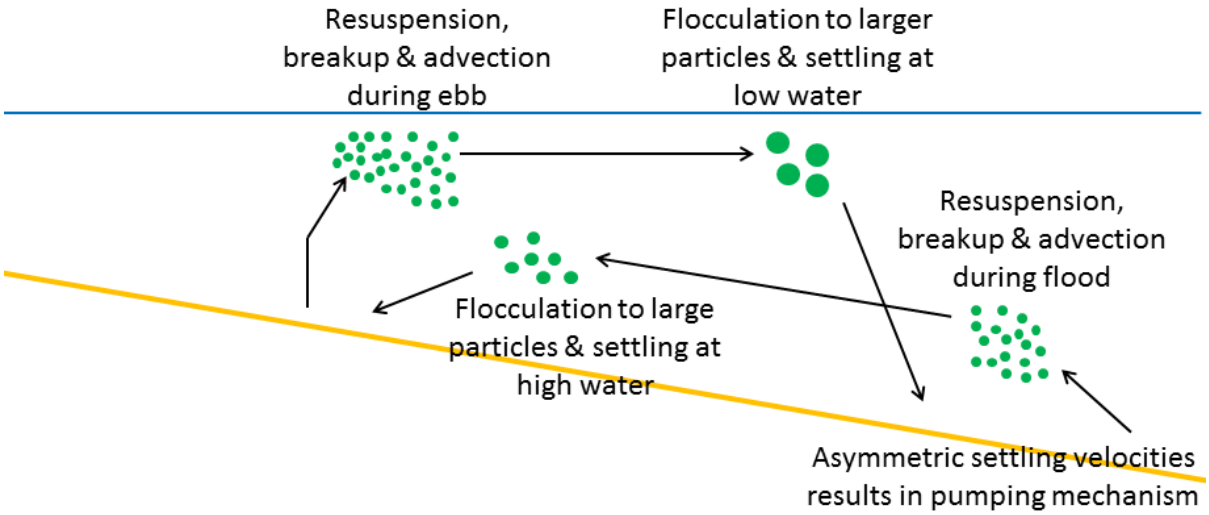

Fig. 7.19 – Schematic illustration of particle transport during February-March. Yellow line indicates estuary bed, blue line the estuary surface. Resuspension, breakup and advection occurs during the flood, flocculation and settling at high water, resuspension, breakup and advection during the ebb and flocculation to larger particle sizes and settling over low water

The change in biological activity between the February-March and May-June deployment periods was the result of changes in temperature and solar radiation (shown in Fig. 6.2 & Fig. 6.3), which have themselves been shown to increase the shear strength of intertidal sediment (Amos, et al., 1988) and therefore have the potential to reduce the horizontal concentration gradient (see Section 3.2.4). The horizontal concentration gradient may

therefore have been generated by a combination of the physical and biological characteristics of the estuary: during the February-March deployment, low biological activity combined with high river flow and low solar radiation may have resulted in the erosion, resuspension and advection of fine-grained material past the point of observation, while during the May-June deployment, reduced river flow in combination with the growth of algal crusts, diatom mats and salt marsh plants, and increased solar radiation, may have increased the erosion threshold, leading to the observed reduction in the horizontal concentration gradient.

It is likely that a combination of the increase in the erosion threshold of the intertidal sediment, combined with the reduction in river flow, resulted in the observed reduction in the horizontal concentration gradient between February-March and May-June, while the observed change in sediment flux was due to a combination of the change in the horizontal concentration gradient and the changing flocculation characteristics of the particles, which will be considered further in Chapter 8.

7.7 Conclusions

- A twin peak signal was present in both the February-March and May-June LISST data;
- The amplitudes and phases of the semi- and quarter-diurnal signals present in the LISST time series changed between the deployment periods;
- The low signal-to-noise ratio of the sixth diurnal tide signal made the analysis of this constituent unreliable;
- Small particle (< 122 μm) concentrations during February-March varied on a quarter-diurnal frequency in phase with current speeds and were therefore the product of resuspension;
- Small particle (< 122 μm) concentrations during February-March also varied on a semi-diurnal frequency with phase of -135° relative to current speeds indicating the advection of small particles down the estuary during the late ebb;
- Large particle (> 122 μm) concentrations during February-March varied on a semi-diurnal frequency with a phase -180° indicating that concentrations of large particles increased during low water due to flocculation;

- Small (< 122 μm) and large (> 122 μm) particle concentrations varied on a quarter-diurnal frequency and were in phase with the current speeds during May-June indicating resuspension of all particle sizes dominated;
- It is possible for an estuary to experience flood dominant velocity asymmetry but still have an ebb dominant SPM flux;
- Small particle (< 122 μm) volume flux was 75 % flood dominant during May-June, while large particle (> 122 μm) volume flux was 56 % flood dominant during the same period;
- Small particle (< 122 μm) volume flux was 24 % flood dominant during February-March, while the large particle (> 122 μm) volume flux had changed direction, being 11 % ebb dominant during the same period;
- Net SPM volume flux flood dominance reduced by 75 % between May-June and February-March, from 63 % flood dominant during May-June, to just 16 % during February-March;
- Net SPM mass flux flood dominance reduced by 46 % between May-June and February-March, from 39 % flood dominant during May-June, to just 21 % during February-March;
- Asymmetric flocculation, suggested by the presence of large particles during high and, predominantly, low water may result in a tidal pumping mechanism which increased estuary infill due to the asymmetry in particle settling velocities brought about by the asymmetry in particle size;
- The change in the magnitude of the horizontal concentration gradient between February-March and May-June was likely due to changes in biological activity and atmospheric forcing between these periods;
- The change in the net flux of the estuary was due to the changes in the horizontal concentration gradient and the presence of asymmetric, low water dominant flocculation during February-March.

In this chapter, the changes in SPM concentration and flux across tidal, spring-neap and seasonal timescales have been investigated. The presence of resuspension and the advection of a horizontal concentration gradient that is highest towards the top of the estuary have been established through a harmonic analysis. The combination of these

signals produces the characteristic twin peak signal. Quantification of the flux of SPM indicated strong flood dominance during the May-June period due to the flood dominant velocity asymmetry and flood dominant SPM concentrations. The February-March period still displays a flood-dominant net flux, but at a much reduced level due to the strength of the horizontal concentration gradient which acted to make SPM concentrations ebb dominant. This ebb dominance was not sufficient to overcome the flood dominance of velocities and reverse the flux direction, but under a stronger horizontal concentration gradient (i.e. during storm periods) SPM flux may become ebb dominant.

The ebb-dominant concentrations brought about by the horizontal concentration gradient were opposed by a possible asymmetrical flocculation signal with asymmetrically larger particles occurring during low water than high water leading to faster settling particles at low water and therefore, over time, a tidal pumping mechanism which transports material up the estuary.

The presence of a flood dominant small particle flux in combination with an ebb dominant large particle flux may be important for engineers using 2D models such as TELEMAC or MIKE21 which use a total flux formulation, or single size class models, as these models may not take account of the differing particle transport directions for different particle size classes. In addition, this research has shown the requirement to include flocculation models in models of sediment transport as without this the tidal pumping mechanism, which appears to show flocculation, would not be represented in the model and therefore predictions of estuary infill rates could be highly inaccurate.

Chapter 8

Flocculation and particle dynamics

8.1 Introduction

Previous studies on the continental shelf have shown that resuspension and advection, combined with the flocculation and breakup of SPM, are the major controls on SPM concentration (e.g. Jago et al. (2006)). The previous chapter (Chapter 7) has shown the importance of resuspension and advection in the Dee Estuary, while this chapter will show how the processes of flocculation and breakup contribute to the SPM dynamics in this high energy, hypertidal environment.

This chapter focuses on the characteristics and behavior of SPM within the Dee Estuary, including confirming the presence of flocculation. The properties of the SPM will be investigated, including the sizes, densities, strengths and settling velocities of flocculating material, and an attempt will be made to determine if flocculating material during both the February-March and May-June deployment periods originated from the same primary particle type, and what this particle type was. Particles with similar characteristics during both deployment periods will be investigated to determine if the same type of material occurred during both February-March and May-June.

In the remainder of this chapter, 8.2 looks at evidence for the presence of flocculation during the two deployment periods, 8.3 investigates the effective densities of the SPM, while 8.4 presents calculations of floc strength. Settling velocities are calculated using two different methods in 8.5, and an anomalous particle population is analysed in 8.6. 8.7 synthesizes the previous sections in a discussion section, and presents an investigation into whether flocs during both deployment periods originated from the same primary particle type and finally 8.8 draws the chapter together and presents conclusions.

The principal research objectives for this chapter are to establish the controls on SPM size, settling velocity and effective density at the mouth of the Dee Estuary. Since both resuspension and flocculation are turbulence and biologically-mediated processes, it is

anticipated that the physical controls on SPM will be most important during spring tides in February-March, while the influence of biological substances such as polysaccharides will have the greatest influence during the May-June deployment.

8.2 Evidence for the presence of flocculation

8.2.1 The fractal dimension of particles

Previous research has shown that the Dee Estuary is a system in which flocculation occurs (Thurston, 2009; Ramirez-Mendoza, et al., 2014). It is possible to confirm this for the 2009 deployment periods through examining the relationship between SPM mass concentration, volume concentration and particle size. According to Kranenberg (1994), if SPM is undergoing flocculation and de-flocculation, so that a floc is composed of collections of primary particles, the flocculated SPM should display fractal growth, shown in Eq. (3.16). This can be rearranged into a linear relationship (Eq. (3.17)) which can be used to estimate the values of n_f and ${\rho_p D_p}^{3-n_f}$ for each deployment period, assuming that the fractal dimension remains constant through each deployment period, through linear regression. The best relationships (Fig. 8.1) were found for fractal dimensions of 2.46 during February-March (R^2 of 0.98) and 2.74 during May-June (R^2 of 0.97). The strength of these relationships indicates that the Dee Estuary was a flocculating system during both deployment periods. The mean value of ${\rho_p D_p}^{3-n_f}$ to convert $\frac{C_v}{D^{3-nf}}$ into an approximation of mass concentration was 1.94 during the February-March deployment and 0.86 during the May-June deployment. These values differ due to the difference in fractal dimension between deployment periods, but may also indicate that the primary particles from which the flocs were composed varied between February-March and May-June, potentially indicating a different particle source, or the presence of biological material during one, or both, periods (i.e. the particles were not entirely mineralic). The determined fractal dimensions (2.46 during February-March and 2.74 during May-June) fall within the anticipated range of 1-3 (Kranenberg, 1994), while the February-March value is similar to the value of 2.4 determined by Ramirez-Mendoza, et al., (2014) for the Welsh channel of the Dee Estuary during February 2008.

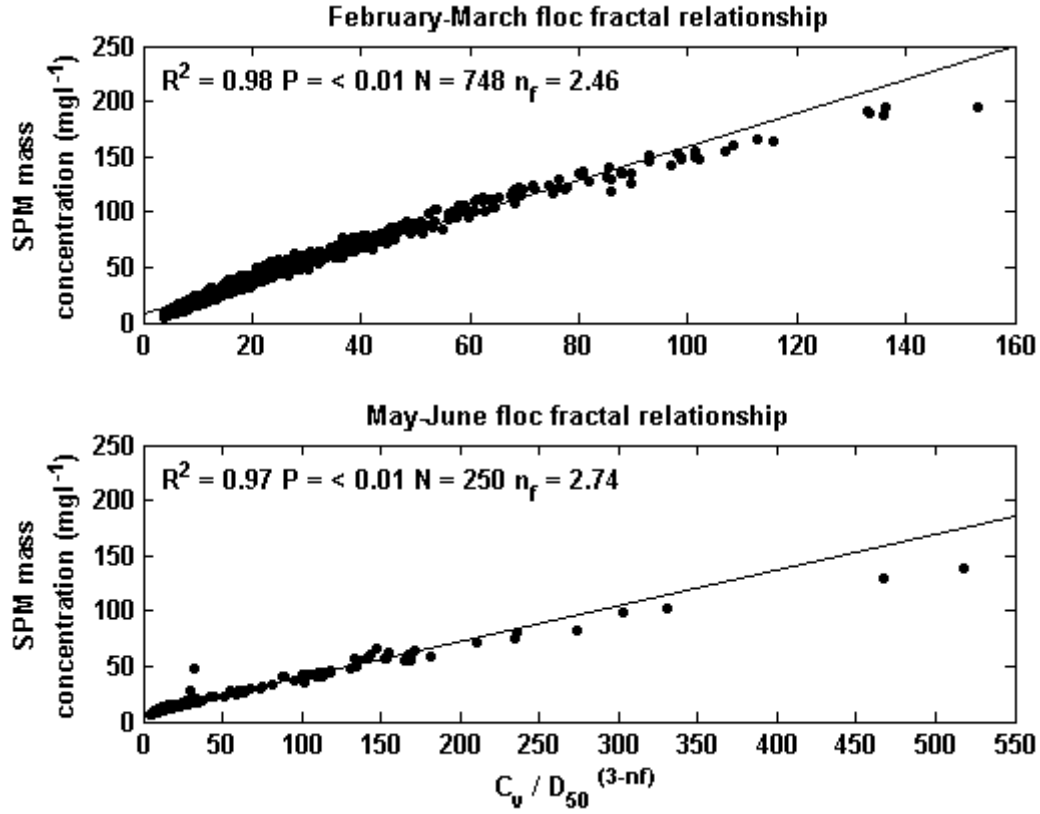

Fig. 8.1 – SPM mass concentration plotted against C_v / $D_{50}^{(3-nf)}$ for both the February-March and May-June deployment periods. C_v is measured in $\mu l l^{-1}$ and D_{50} in µm

8.2.2 Relationship between volume concentration and current speed

The relationship between SPM volume concentration and current speed varied between deployment periods, as shown in Fig. 8.2. During May-June, volume concentration displayed a positive relationship with current speed for both small (< 122 µm) and large (> 122 µm) particles (Fig. 8.2c & d), suggesting that particles resuspended during peak current speeds and settled under low flow conditions, consistent with the harmonic analysis of the resuspension and advection signals discussed in Chapter 7. During February-March, concentrations of small particles displayed a weak positive relationship with current speed (Fig. 8.2a), while large particles showed a weak inverse relationship (Fig. 8.2b), with large particle concentrations highest during periods where current speeds were low (< ~0.2 ms^{-1}), indicating the occurrence of flocculation during periods of low current speeds. This relationship shows that the large particles present during February-March were flocs rather than sand particles, as in a sand environment the concentrations of large particles in

suspension would generally be higher under higher shear stress conditions, while in a flocculating system, concentrations of large particles increase under low current speed, and therefore low shear stress, conditions.

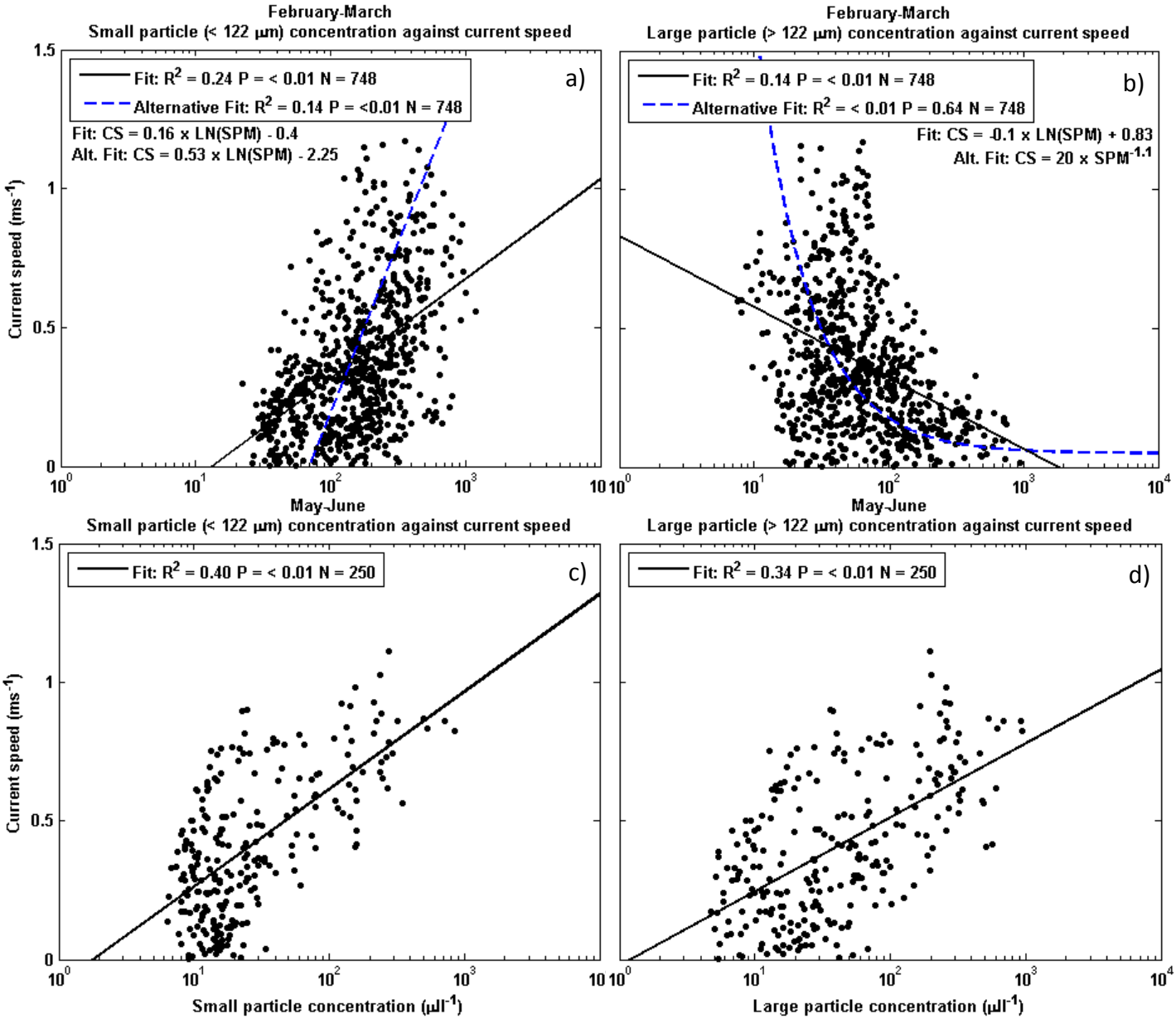

Fig. 8.2 – LISST volume concentration plotted against current speed from the first bin of the ADCP for small (a and c) and large (b and d) particles for both February-March (top) and May-June (bottom)

Fig. 8.2a & b are shown with two trend lines – a black line produced through a regression analysis, while the blue line, with associated statistics, represents what is believed to be

occurring within the system as it has been shown that the Dee Estuary was a flocculating system during the February-March deployment (Fig. 8.1 top). The differences between the black and blue lines are produced by the high levels of scatter and high density of data recorded under low current speed conditions. This difference may have been caused, in part, by the horizontal concentration gradient (Chapter 7) which resulted in high concentrations of small particles under low current speed conditions. Without this, small particles during February-March would be expected to be related to current speed, due to higher current speeds resulting in resuspension and floc breakup, increasing the concentrations of small particles. Conversely, in a turbulence-mediated flocculating system, at some level of turbulence floc breakup changes to flocculation, and therefore concentrations of large particles increase once current speeds fall below a certain level. This indicates that the February-March deployment period may have been a turbulence-mediated flocculating system, while the May-June deployment shows evidence of resuspension without breakup (Fig. 8.2c & d).

The previously discussed LISST size spectrum showed strong low water dominance of large particles during spring tides in February-March (Fig. 7.11). Small particles resuspended at high current speeds and flocculated to large particles under the low current speed conditions of low and, to a lesser extent, high water. This asymmetric, low water dominated flocculating system was enhanced by:

- The advection of the horizontal concentration gradient (Chapter 7) which brought small particles down the estuary during the ebb tide;
- Tidal asymmetry, which causes low water (defined here as the period in which current speeds are < 0.2 ms^{-1}) to last on average ~2.2 times longer than high water (Fig. 7.11), giving more time during low current speed conditions for flocs to form, and;
- The dilution effect, which makes particle collisions less likely during high water.

This combination of factors resulted in a flocculation and breakup system during February-March (Fig. 8.1 top) with large particle concentrations peaking during the low current speed conditions of low water, with a small increase also seen during high water (Fig. 7.11). By contrast, the entire size spectrum of particles resuspended during periods of high current

speeds on both the flood and ebb tides during May-June (Fig. 7.12, Fig. 8.2c & d), without evidence of significant breakup, before settling under low current speeds at high and low water. This indicates that flocs during the May-June deployment period may have been stronger than those during February-March.

8.3 Effective density

8.3.1 Effective density calculation using the LISST

The central ring of the LISST measures transmittance (see Section 5.2.1), which can be calibrated using gravimetrically filtered SPM samples to provide a measure of mass concentration. This was done for both the February-March and first 250 hours of the May-June deployment using samples taken during the CTD casts (see Section 5.3). The calibrated mass concentration from the LISST was divided by the volume concentration to provide a measure of the bulk effective density of the particles in suspension (ρ_e – Eq. (3.20)).

8.3.2 Relationship between effective density and D_{50}

Plotting the bulk effective density of the particles in suspension (see Section 8.3.1) against the D_{50} for both the February-March and May-June deployment periods (Fig. 8.3) shows that the particle characteristics varied between deployment periods. For both periods, effective density generally decreased as particle size inceased, with particles of equivalent size generally having a higher effective density during the May-June deployment than during February-March. However, some particles during May-June that had an effective density < 200 kgm^{-3} did not follow this relationship, instead displaying an almost constant density despite changing particle size. Further, this data overlapped with some of the larger particles in the February-March data. This group of particles from the May-June data with an effective density of < 200 kgm^{-3} will henceforth be referred to as “population X,” as distinct from the February-March data and the remainder of the May-June data (referred to as “population B”).

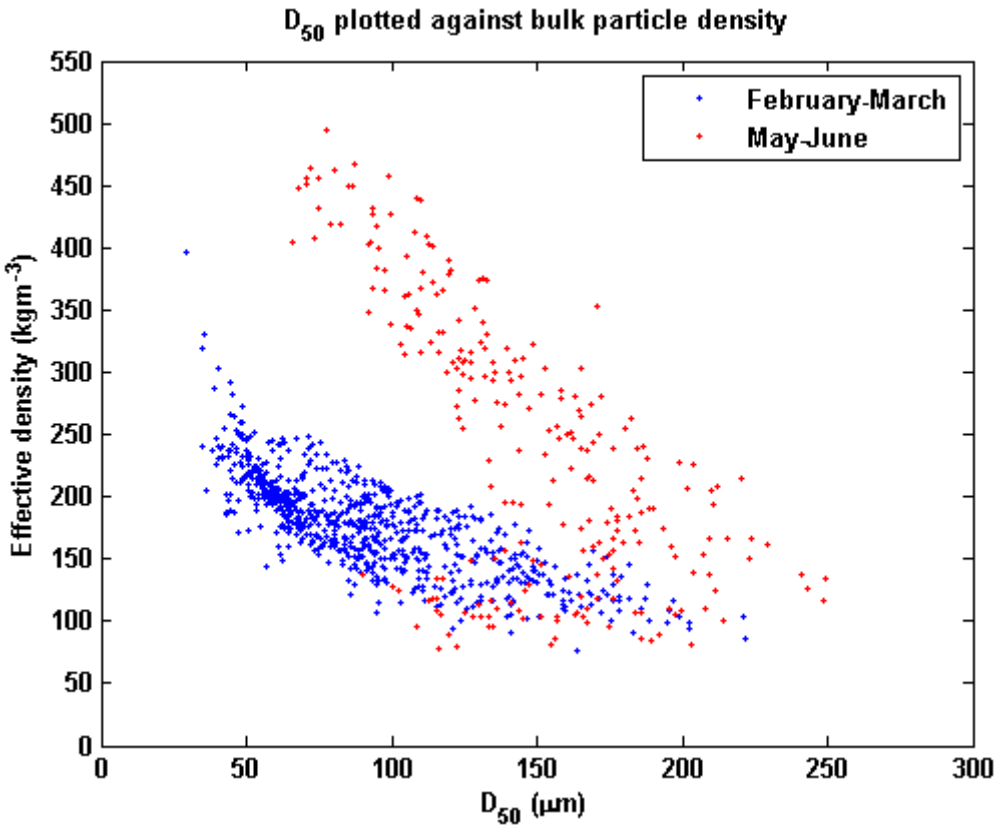

Fig. 8.3 - D_{50} plotted against the effective particle density for both the February-March (blue) and May-June (red) deployment periods

8.3.3 Relationship between effective density and current speed

Plotting the effective particle density against current speed (u) for the February-March (Fig. 8.4) and May-June (Fig. 8.5) deployments showed a strong positive relationship during spring tide conditions in February-March (Fig. 8.4 bottom left, R^2 = 0.89), while a weaker positive relationship was also present during neap conditions (Fig. 8.4 bottom left, R^2 = 0.41). This relationship was the result of the resuspension and floc breakup during peak current speeds resulting in smaller, denser microflocs being in suspension, as shown previously in Fig. 7.11 and Fig. 8.2a & b, while flocculation during high and, to a greater extent, low water, caused the effective density of the particles in suspension to reduce.

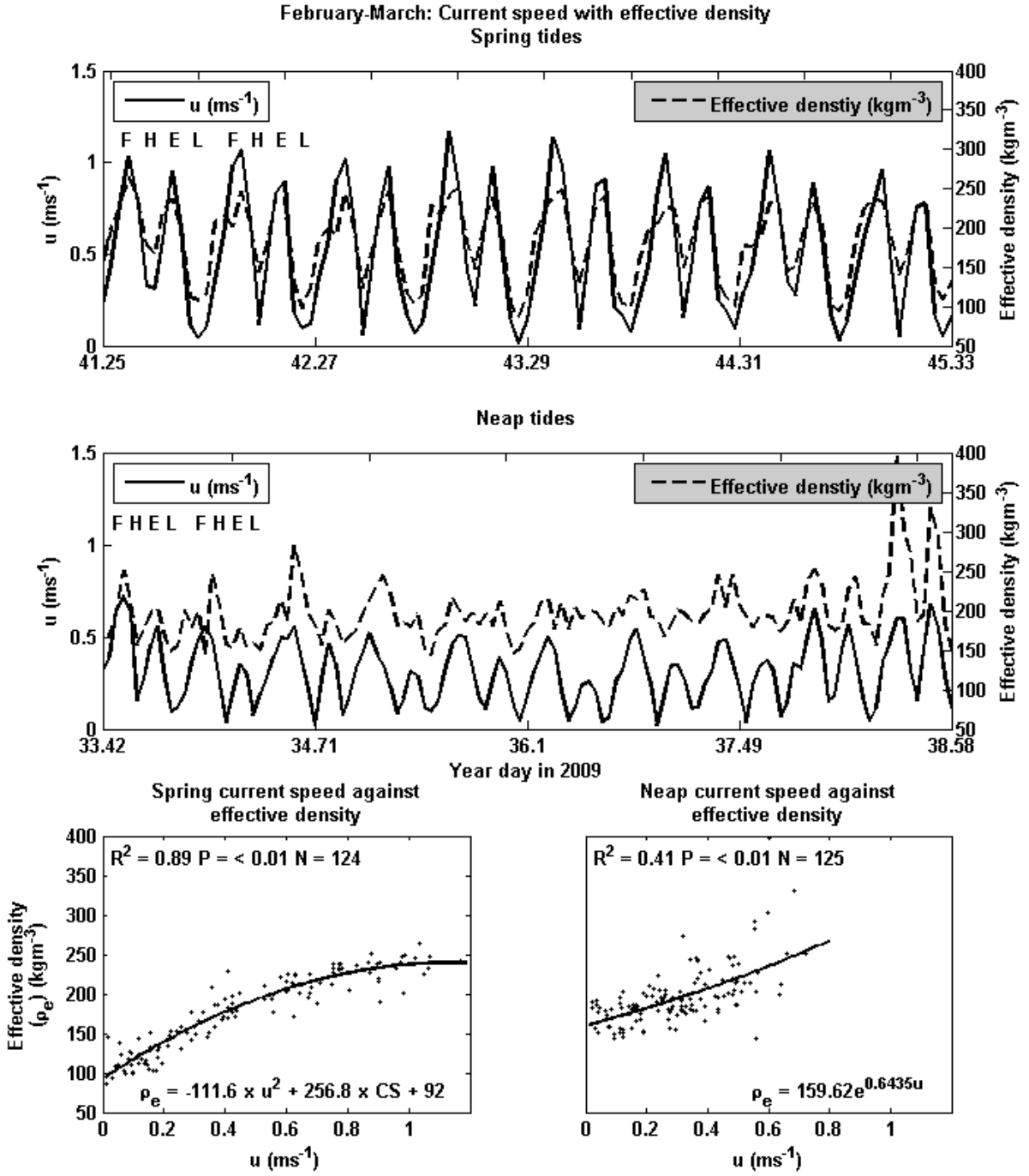

Fig. 8.4 - Current speed plotted with effective particle density (top & middle) in which FHEL indicates flood, high, ebb and low water, and plotted as scatter plots for the spring (bottom left) and neap (bottom right) periods of the February-March deployment

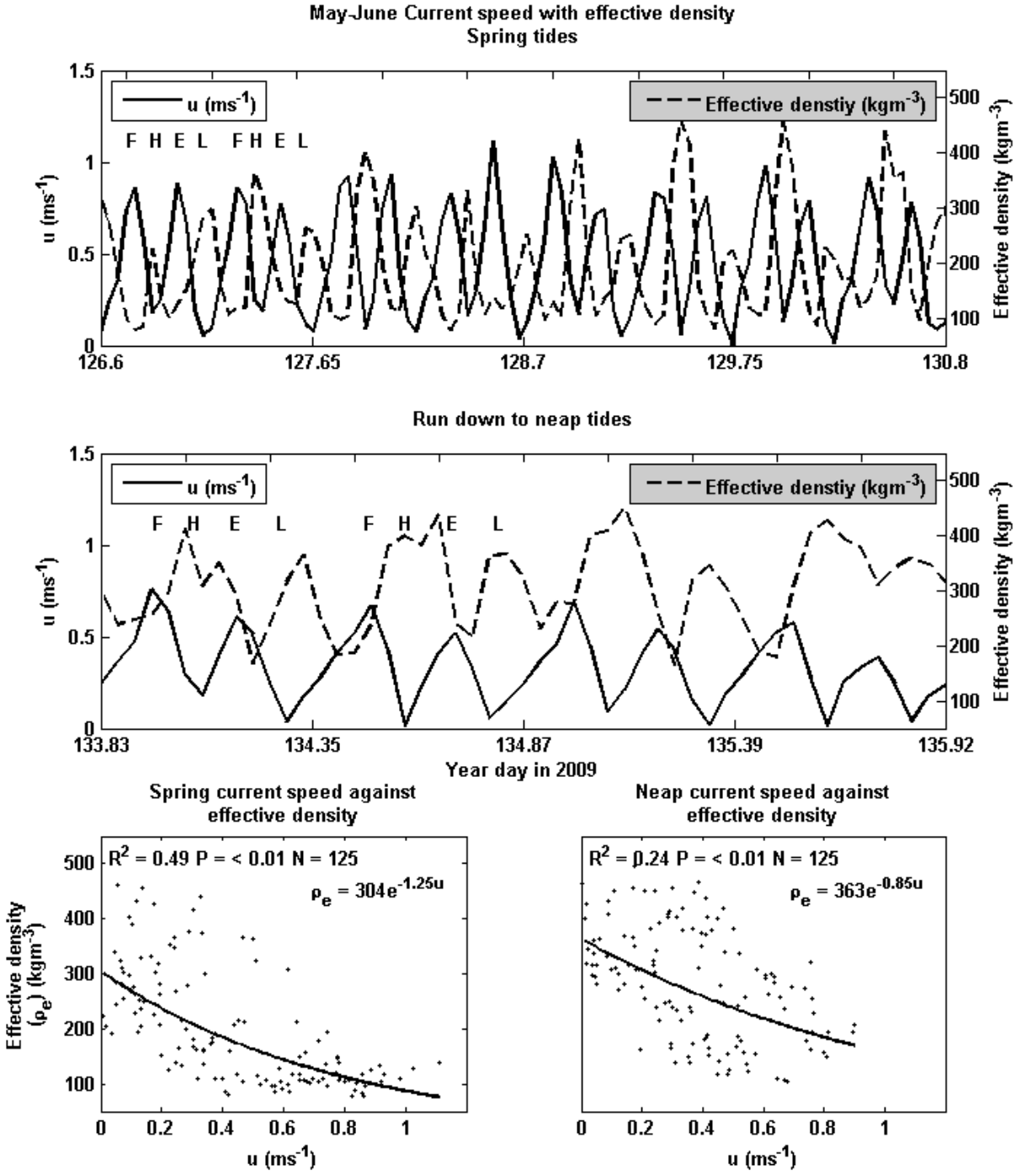

Fig. 8.5 - Current speed plotted with effective particle density (top(top & middle) in which FHEL indicates flood, high, ebb and low water, and plotted as scatter plots for the spring (bottom left) and neap (bottom right) periods of the May-June deployment

During the May-June deployment (Fig. 8.5), effective density generally increased during high and low water and fell during flood and ebb. This inverse relationship was in direct contrast

to that seen during February-March (Fig. 8.4). The presence of an inverse relationship may be indicative of the presence of stronger flocs, with large, low density macroflocs being resuspended on the flood and ebb tides. During high and low water, the larger, lower density flocs, which have higher settling velocities, would settle faster than the smaller, denser particles, increasing the effective density of the suspension.

8.4 Floc strength

8.4.1 Turbulence and particle size for determining floc strength

The C strength parameter

The strength of flocs in suspension can be determined through the use of the "C" parameter (Parker, et al., 1972; Jago, et al., 2007) which provides an estimate of the strength of flocs both larger and smaller than the Kolmogorov lengthscale (Eq. (2.24)) on the assumption that floc size is in equilibrium with the fluid shear:

$$Floc\ size = C\varepsilon^{-\gamma} \tag{8.1}$$

in which Ɛ is turbulent dissipation in Wkg^{-1} and γ takes the value of 1 when flocs are larger than the Kolmogorov lengthscale, and 0.5 when they are smaller, with higher values of C indicative of stronger flocs.

Water density and dynamic viscosity (Fig. 8.6 top & middle) were derived from the continuous water temperature and salinity record recorded by the Microcat CTD deployed on the STABLEIII platform during both the February-March and May-June deployment periods and these values were used to calculate the kinematic viscosity (μ/ρ, shown in Fig. 8.6 bottom), which was used to calculate the Kolmogorov lengthscale (Eq. (2.24)).

Plotting the Kolmogorov lengthscale with the D_{50} particle size (Fig. 8.7) it can be seen that the D_{50} did not exceed the Kolmogorov lengthscale size during either the February-March or May-June deployment periods and therefore, γ in Eq. (8.1) takes the value of 0.5.

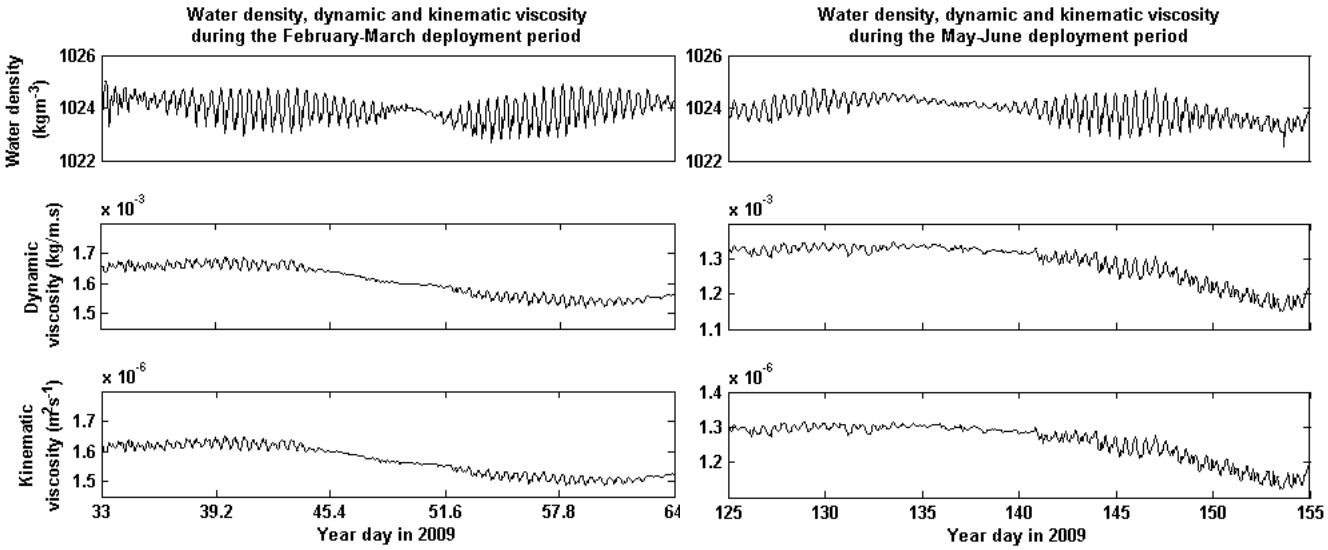

Fig. 8.6 – Water density (top), dynamic (middle) and kinematic viscosity (bottom) for the February-March (left) and May-June (right) deployment periods

The C parameter (Eq. (8.1)), in which higher values of C indicate stronger flocs, was calculated for the entire February-March deployment and the first 250 hours of the May-June deployment. Values ranged from 0.01 to 0.85, averaging 0.26, during February-March, and from 0.02 to 2.1, averaging 0.52, during May-June, indicating that flocs were stronger during May-June. These values are of similar magnitude to those reported by Jago, et al., (2007) for the Irish Sea (0.003 to 0.5).

Using the relationship between D_{50} and the Kolmogorov lengthscale to determine floc strength

The relationship between particle size and turbulence can be seen by plotting the Kolmogorov lengthscale (Eq. (2.24)) against the D_{50} particle size (Fig. 8.8) for the two deployment periods. The values of D_{50} attained under low and moderate turbulence conditions were comparable during February-March and May-June; however, those recorded during high turbulence conditions, indicated by low values of the Kolmogorov lengthscale, were higher during May-June than those recorded under similar values of turbulence during February-March. This indicates that flocs were stronger during the May-June deployment, concurrent with the higher average value of the C strength parameter

attained during May-June, as a higher strength is required to resist higher levels of turbulence.

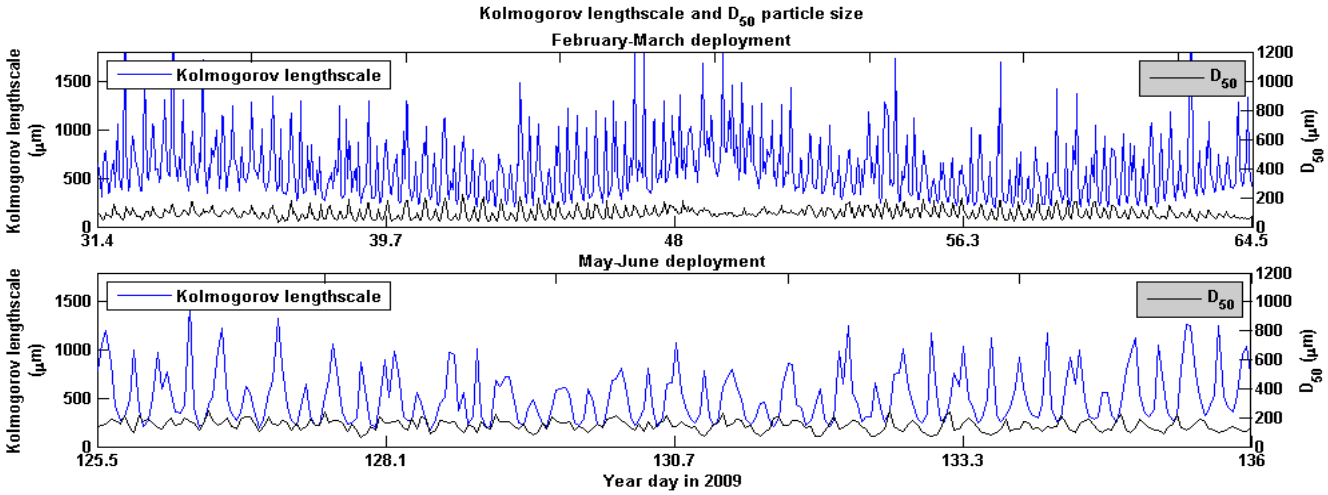

Fig. 8.7 – Kolmogorov lengthscale plotted with D_{50} showing that the D_{50} never exceeds the size of the Kolmogorov lengthscale

The positive correlation for the February-March deployment (Fig. 8.8) suggests that particle size during this time was controlled by turbulence, with larger particles occurring during times of lower turbulence, as shown in Fig. 7.11 and Fig. 8.2a & b. While the R^2 of the relationship is only 0.37, it is speculated that this relationship may have been adversely impacted by the advection of small particles due to the horizontal concentration gradient discussed in Chapter 7, and also by the lack of variation in particle size during low turbulence conditions at neap tides shown in Fig. 8.7. By contrast, the weakness of the relationship and high P value for the May-June deployment (Fig. 8.8) indicates that particle size during May-June was not turbulence controlled, even under high turbulence conditions, as indicated in Fig. 7.12 and Fig. 8.2c & d in which large particles were found during peak current speed conditions.

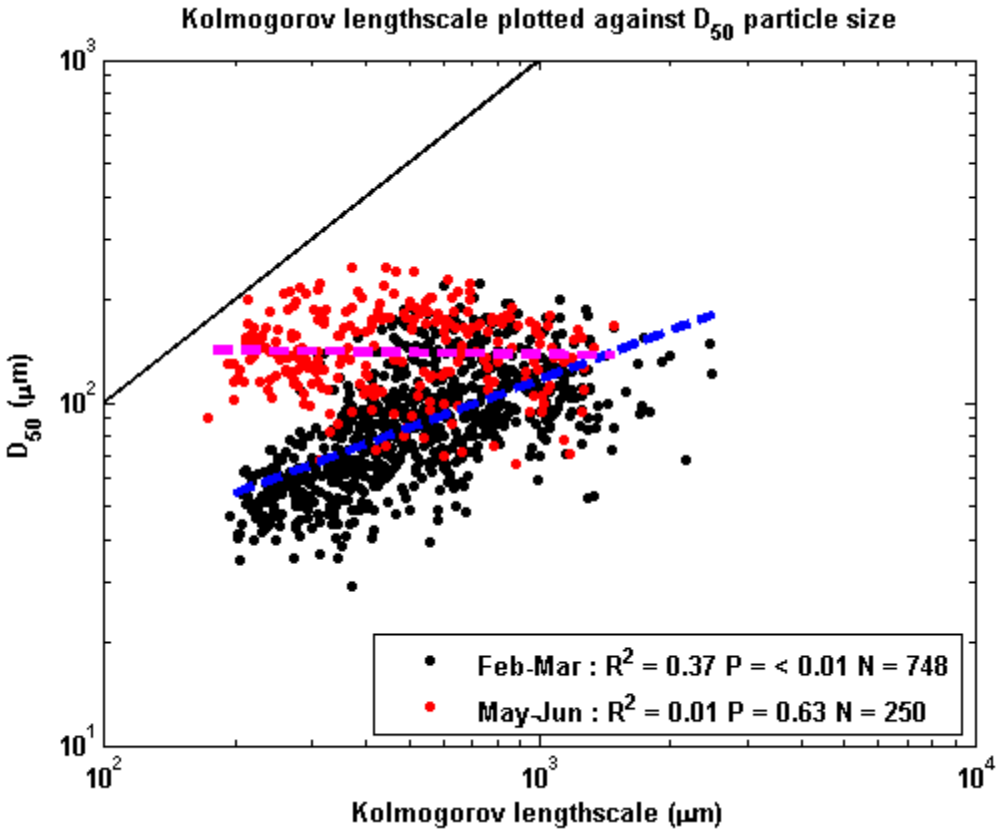

Fig. 8.8 - D_{50} plotted against the Kolmogorov lengthscale (Eq. (2.24)) for February-March (black dots) and May-June (red dots) with best fit lines for February-March (blue) and May-June (pink). Also included is a 1:1 line (black) between the Kolmogorov lengthscale and the D_{50} showing that D_{50} never exceeds the Kolmogorov lengthscale. Particles during May-June get closer to the Kolmogorov lengthscale than those during February-March

8.4.2 Determining floc strength from the fractal dimension

Flocs commonly have fractal dimensions in the range of 1-3 (Kranenberg, 1994). The complex fractal structure of a floc impacts both its density and yield strength (Ramirez-Mendoza, et al., 2014), with a fractal dimension of 1 indicative of loosely connected, low density, weak flocs, while a fractal dimension of 3 is indicative of compact, higher density, strong flocs (Kranenberg, 1994; Winterwerp, 1998). The fractal dimension calculated for the February-March deployment period (see Section 8.2.1) was 2.46, compared with 2.74 for the May-June deployment. This indicates that flocs were stronger during the May-June deployment, supporting the evidence of Section 8.4.1.

8.5 Settling velocity

8.5.1 Stokes' settling velocity formula calculations

Using the bulk effective density of the particles in suspension (see Section 8.3.1) and the D_{50} particle size, it is possible to calculate an approximation for the settling velocity of the suspension using the Stokes' settling velocity formulation (Eq. (3.11)). Settling velocity was calculated at hourly intervals for the entire February-March deployment and the first 250 hours of the May-June deployment using the time-varying dynamic viscosity calculated in Section 8.4.1. In addition, a separate calculation using a constant dynamic viscosity of 1.45 x 10^{-3} $kgm^{-1}s^{-1}$ – the average value of the dynamic viscosity across both deployment periods – was used as a sensitivity test to investigate the importance of using a time-varying dynamic viscosity.

The resulting settling velocities show that the use of a constant viscosity overpredicted the settling velocity during February-March (Fig. 8.9) by up to 17 %, with the error directly proportional to the derived settling velocity. During May-June, the use of a constant viscosity under predicted the settling velocity (Fig. 8.10) by up to 11 %. This shows that the use of a time-varying dynamic viscosity can improve settling velocity calculations using the Stokes' method by up to 17 %.

Settling velocities during February-March increased during high and, to a greater extent, low water, reducing during the flood and ebb tides (Fig. 8.9 right). This pattern was also seen during the May-June deployment (Fig. 8.10 right) but with the inequality observed between the settling velocities at high and low water during February-March (Fig. 8.9 right) greatly reduced. Settling velocities were, on average, higher during the May-June deployment, with those calculated using the time-varying dynamic viscosity averaging 0.52 mms^{-1} during February-March with a range of 0.09 to 1.8 mms^{-1} by comparison with an average of 1.9 mms^{-1} – almost four times higher than the February-March average – during May-June, with a range of 0.43 to 4.3 mms^{-1}.

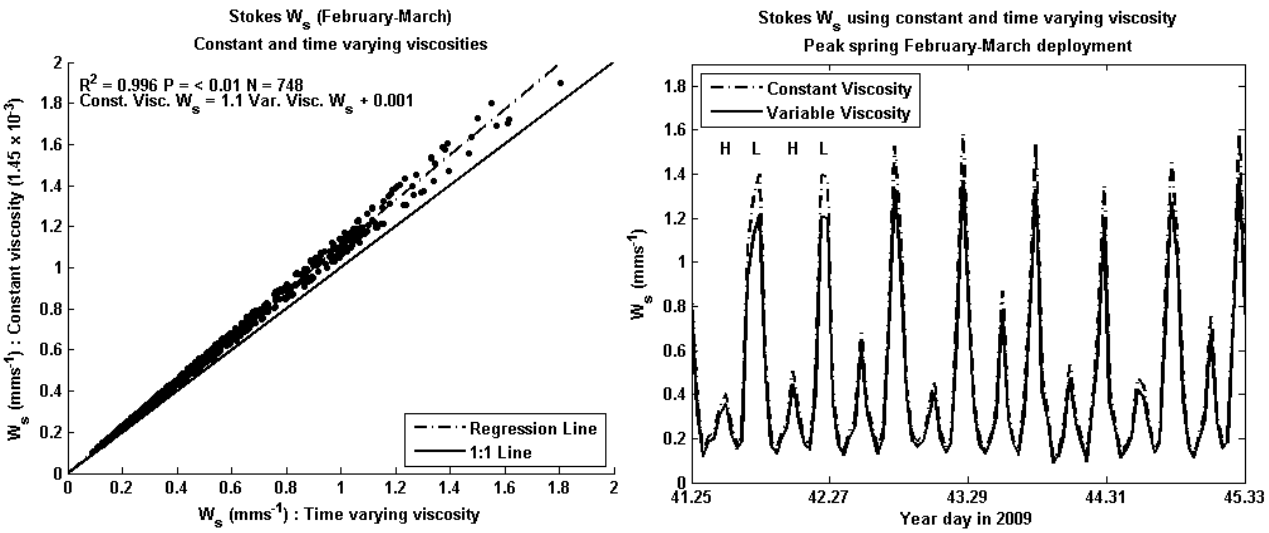

Fig. 8.9 – Stokes' W_s for February-March derived using a time varying viscosity plotted against derivation using a constant viscosity with a regression line (dotted and dashed) and a 1:1 line (solid) (left) and both derivations plotted for the first spring period (right). H & L indicate high and low water periods

The Stokes' settling velocities, calculated using the time-varying dynamic viscosity, are plotted against D_{50} in Fig. 8.11, with lines of equal density shown. The February-March (red) and May-June (blue) datasets both follow the general trend of positive correlation between particle size and settling velocity, with settling velocities, on average, higher during May-June than February-March. In general, the effective density of the suspension reduced as both size and settling velocity increased. An exception to this trend is found during the May-June deployment as some data is shown to overlap data from the February-March deployment and these particles, unlike the majority of those found during May-June, do not appear to change density with increasing particle size and settling velocity. This overlap, shown previously in Fig. 8.3 and identified in Section 8.3.2 as population X, will be considered further later. Two distinct groups of particles appear to be present within the May-June data – population B in which particles change density with changing particle size, and population X in which effective density remains constant despite changes in particle size.

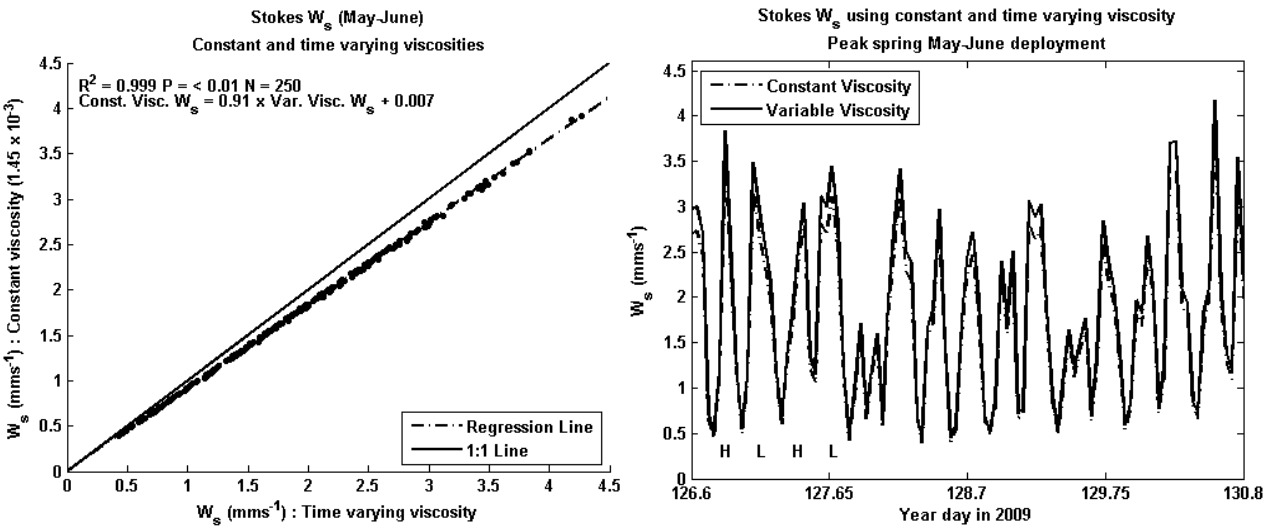

Fig. 8.10 – Stokes' W_s for May-June derived using a time varying viscosity plotted against derivation using a constant viscosity with a regression line (dotted and dashed) and a 1:1 line (solid) (left) and both derivations plotted for the first spring period (right). H & L indicate high and low water periods

8.5.2 Winterwerp (1998) settling velocity formula calculations

The Stokes' settling velocity formulation is intended to calculate the settling velocity of a single, spherical particle falling in still water, and is therefore potentially inaccurate for non-spherical particles, as discussed in Section 3.4.2. However, it is possible to modify the Stokes' formulation using the Schiller-Naumann (1933) drag coefficient (Winterwerp, 1998) as outlined in Section 3.4.3 making it applicable to a wider range of particles. Using this approach, the left hand side of Eq. (3.19), averaged over all samples for the respective deployment periods, gives values of H of 1.12 for February-March and 23.7 for the May-June deployment respectively, indicating that the relationship between effective density, D_{50} and the fractal dimension varied between the deployment periods.

Settling velocities were calculated using this method (termed the Winterwerp (1998) method as distinct from the Stokes' method) at hourly intervals for the entire February-March deployment and the first 250 hours of the May-June deployment. Settling velocities were, consistent with the Stokes' settling velocities calculated in Section 8.5.1, higher on average during the May-June deployment, averaging 0.46 mms^{-1} during February-March

with a range of 0.08 to 1.5 mms^{-1} by comparison with an average of 1.7 mms^{-1} during May-June with a range of 0.46 to 4.3 mms^{-1}.

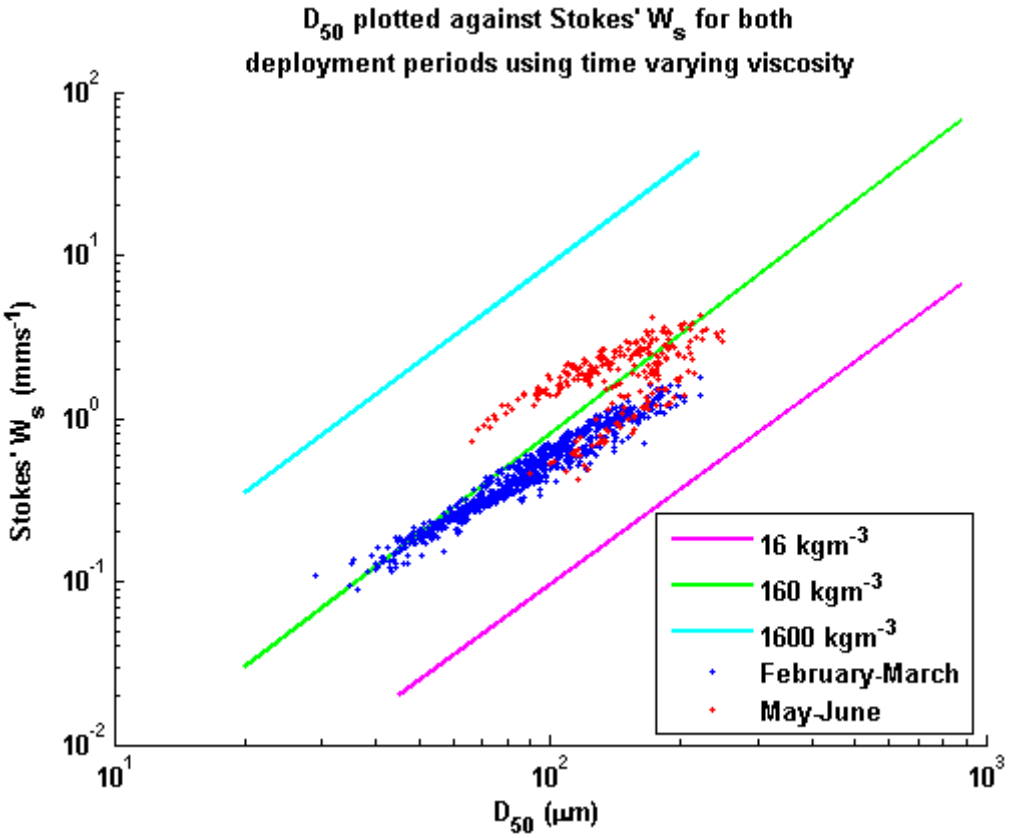

Fig. 8.11 – D_{50} plotted against the Stokes' W_s derived using a time varying viscosity for both the February-March deployment (red dots) and the first 250 hours of the May-June deployment (blue dots) with lines of equal effective density. The pink line indicates an effective density of 16 kgm^{-3}, green is 160 kgm^{-3} and light blue 1600 kgm^{-3}

8.5.3 Comparison between Stokes' and Winterwerp (1998) settling velocities

A comparison between the time-varying dynamic viscosity Stokes' settling velocity calculations and those utilising the Winterwerp (1998) method is presented in Table 8.1 and Fig. 8.12. The Stokes' settling velocities generally overpredicted the settling velocity by comparison with the Winterwerp (1998) method. Some scatter was present in the February-March calculations (Fig. 8.12 left) while the May-June calculations (Fig. 8.12 right) showed large amounts of scatter.

Table 8.1: Differences between the time-varying dynamic viscosity Stokes' and Winterwerp (1998) derived settling velocities

	Min W_s (mms^{-1})		Mean W_s (mms^{-1})		Max W_s (mms^{-1})	
Method	**Feb-Mar**	**May-Jun**	**Feb-Mar**	**May-Jun**	**Feb-Mar**	**May-Jun**
Stokes'	0.09	0.43	0.52	1.9	1.8	4.3
Winterwerp (1998)	0.08	0.46	0.46	1.7	1.5	4.3
Difference (%)	-11 %	7 %	-12 %	-11 %	-17 %	0 %

The difference between the Stokes' and Winterwerp (1998) settling velocity calculations was generally proportional to the calculated settling velocity value during February-March (Fig. 8.12 left), with greater differences found for higher settling velocities, and, while this trend continued during May-June (Fig. 8.12 right), the relationship was weaker. Calculating the difference between the Stokes' and Winterwerp (1998) methods for each data point across both deployment periods shows that the Stokes' method overpredicted the settling velocity by an average of 13 % during February-March and 20 % during May-June.

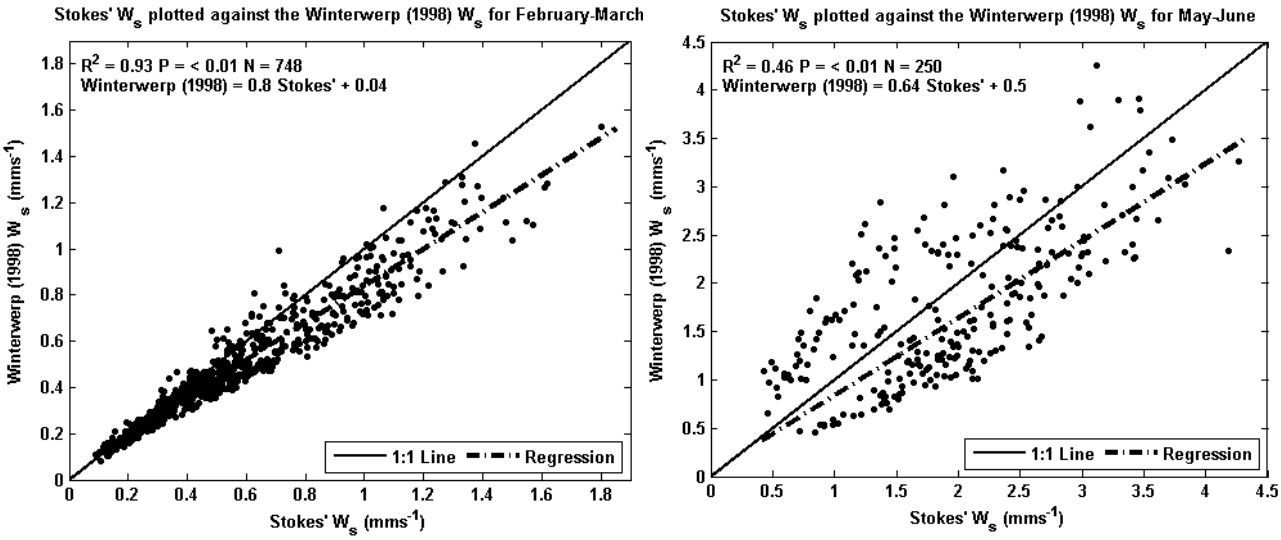

Fig. 8.12 – Stokes' W_s calculated using a time-varying viscosity plotted against W_s calculated using Winterwerp (1998) for the February-March (left) and May-June (right) deployment periods. Dotted-and-dashed lines indicate the regression analysis, while the solid black lines indicate the 1:1 relationship

The settling velocities derived using the Winterwerp (1998) method are plotted against D_{50} in Fig. 8.13. In a similar manner to the trends exhibited by the Stokes' settling velocity calculations in Fig. 8.11, size and settling velocity are positively correlated during both the February-March and May-June deployment periods (Fig. 8.13). However, the population X data from May-June which overlapped with data from the February-March deployment that was present in Fig. 8.11 does not show this overlap in Fig. 8.13. This is due to the Winterwerp (1998) method using an effective particle density that is based upon the sediment density and fractal dimension (Eq. (3.18)) which is calculated in Eq. (3.19) as an average for the entire dataset. This average removes any variations in the relationship shown in Eq. (3.19) and the slope is therefore based primarily upon the fractal dimension of the data rather than the measurements of the bulk effective density of the particles as with the Stokes' formula (Eq. (3.11)). This results in the population X data from the May-June deployment, discussed previously in Section 8.3.2 and Section 8.5.1, being integrated into the rest of the May-June data despite having different particle characteristics (Fig. 8.3). Potentially therefore, the May-June particles may be composed of two particle populations with differing fractal dimensions. In order to accurately parameterize the May-June data, it is necessary to identify the population X data and re-examine the May-June data as two separate particle populations (populations B and X) with unique particle characteristics.

8.6 Anomalous particles in May-June: Population X

8.6.1 Identification of the population X data

To isolate the population X particles, Fig. 8.3 was redrawn for only those particles with an effective density > 200 kgm^{-3} and a linear trend line fitted (Fig. 8.14 top left). Similarly, the Winterwerp (1998) settling velocities were plotted against effective density for particles with an effective density > 200 kgm^{-3} and a linear trend line fitted (Fig. 8.14 top right). These trend lines were extrapolated assuming that this relationship, and therefore these trend lines, applied to the remainder of the dataset. The standard deviation of the regression was calculated (17.2 μm for D_{50} against effective density, 0.4 mms^{-1} for W_s against effective density), and data points were deemed part of the population X data if they fell outside of +/- 3 standard deviations in ***both*** the D_{50} against effective density and W_s against effective

density data series. The extrapolated trend lines and the +/- 3 standard deviation lines are indicated in Fig. 8.14 bottom left and bottom right. Data highlighted in red indicates data that fell outside of +/- 3 standard deviations in both data sets and is therefore identified as being part of population X, as the properties of these particles do not match those of the remainder of the May-June data. The remaining data is identified as population B.

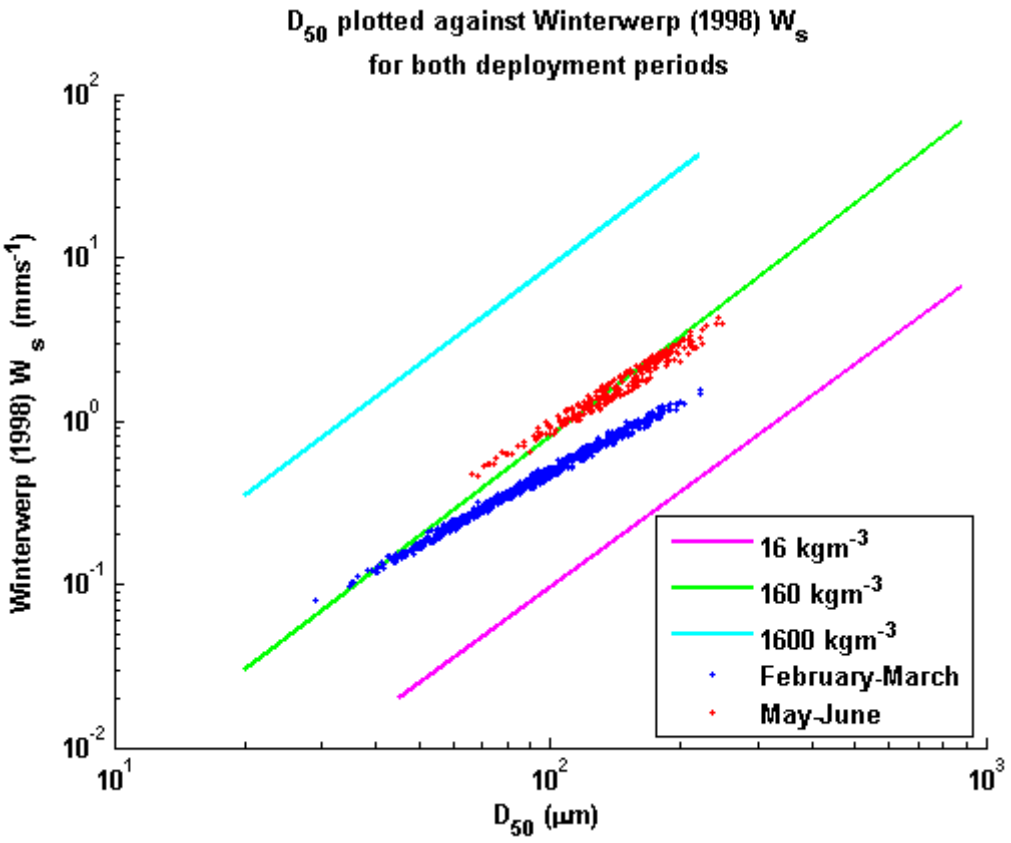

Fig. 8.13 – D_{50} plotted against the Winterwerp (1998) W_s for both the February-March deployment (red dots) and the first 250 hours of the May-June deployment (blue dots) with lines of equal effective density shown. The pink line indicates an effective density of 16 kgm^{-3}, green is 160 kgm^{-3} and light blue 1600 kgm^{-3}

8.6.2 Properties of population X

Fractal dimension

Re-analysing the May-June data as population X and population B (see Section 8.3.2 & Section 8.6.1) in the same manner as outlined in Section 8.2.1, the best relationship was

found for a fractal dimension of 2.33 for the population X particles (R^2 of 0.99 – Fig. 8.15 top) and 2.62 for the population B particles (R^2 of 0.9 – Fig. 8.15 bottom). These values differ from the original value of 2.74 established in Section 8.2.1 for the entire May-June dataset.

Strength of population X: the C strength parameter

The May-June particles have been shown to be stronger than the February-March particles (Section 8.4). Calculating the C strength parameter (Eq. (8.1)) for populations B and X separately, the population X particles were of comparable strength to the population B particles, with a maximum strength of 1.78 for population X compared to a maximum of 2.06 for population B, and therefore both particle species (B & X) that occurred during the May-June deployment were stronger than those of the February-March deployment, which had a maximum strength parameter value of 0.85 (Section 8.4).

Strength of population X: the fractal dimension

The fractal dimensions of the population B and X particles (2.62 and 2.33) suggest that the population X particles should be weaker than both the population B particles and those from the February-March deployment, which had a fractal dimension of 2.46, as higher fractal dimensions tend to indicate higher yield strengths (Kranenberg, 1994; Winterwerp, 1998). This indicates therefore that the bonds within the population X particles were stronger and more shear resistant than those in the February-March and May-June population B particles in order for the low density, low fractal dimension population X particles to have a high maximum C strength parameter value as indicated in the previous section.

Relationship with turbulence

Plotting the Kolmogorov lengthscale (Eq. (2.24)) against the D_{50} particle size for the three particle populations (February-March, B & X) shows that the values of D_{50} under high turbulence conditions were comparable between populations B and X and larger than those recorded during February-March (Fig. 8.16). This indicates that the flocs of population X were of similar strength to those of population B, and stronger than the flocs of the February-March deployment, concurrent with the higher values of the C strength parameter (see previous section), as a higher strength is required to resist higher levels of turbulence.

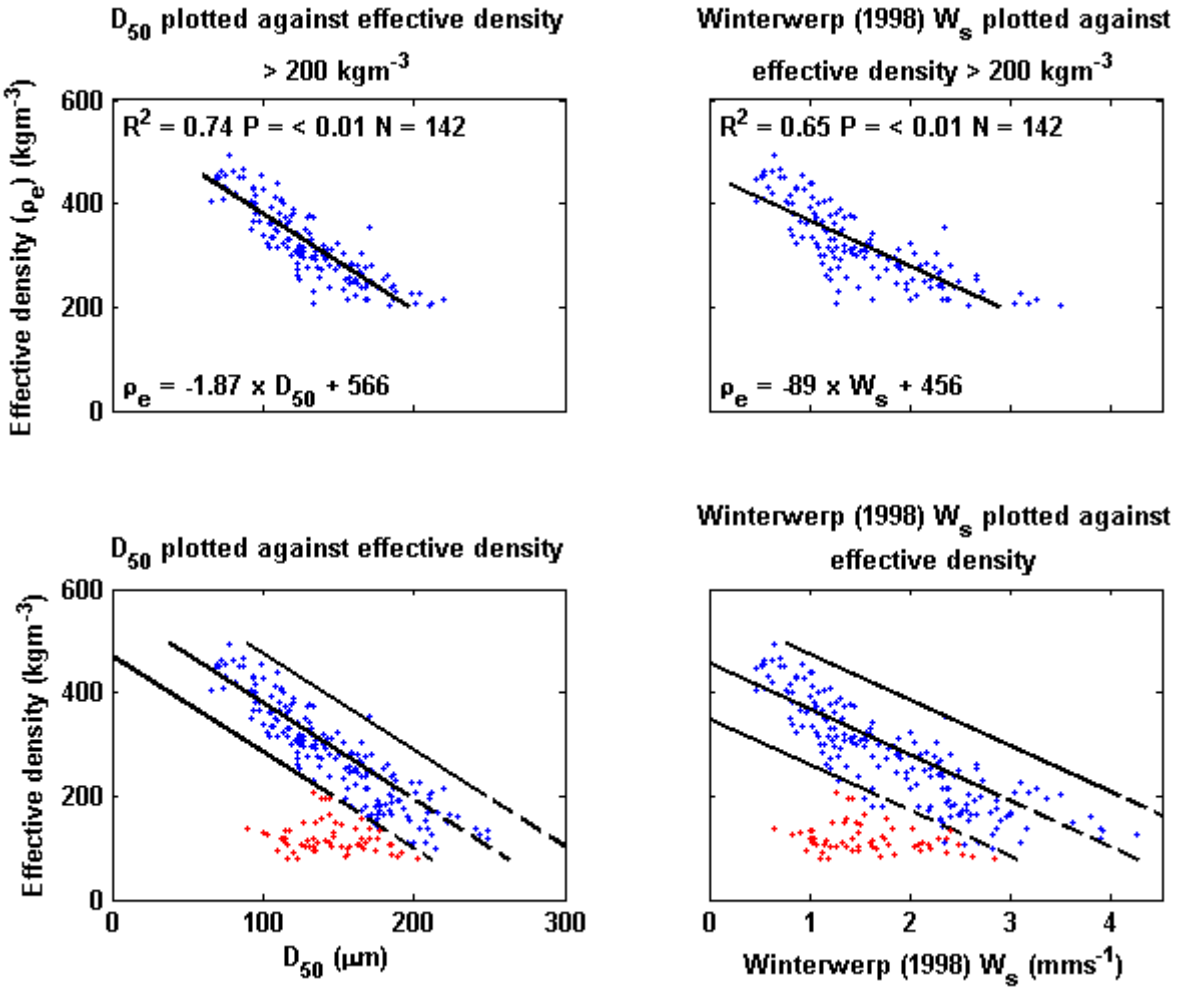

Fig. 8.14 – D_{50} (top left) and Winterwerp (1998) W_s (top right) plotted against effective density where effective density is > 200 kgm^{-3}, with linear trend lines shown. Bottom left: D_{50} plotted against effective density with linear trend line (as top left) and additional trend lines indicating + / – 3 standard deviations. Dashed extensions to the trend lines indicate extrapolation. Bottom right: Winterwerp (1998) W_s plotted against effective density with linear trend line (as top right) and additional trend lines indicating + / – 3 standard deviations. Dashed extensions to the trend lines indicate extrapolation. Red dots in bottom left and bottom right indicate data which falls outside of + / - 3 standard deviations in both the bottom left and bottom right figures

Settling velocity

The mean values of H (see Section 8.5.2) to convert $\frac{C_v}{D^{3-nf}}$ into an approximation of mass concentration were 22 for the population X data and 17.33 for the population B data. These values are different from the original value for the whole May-June dataset of 23.7 due to the difference in fractal dimension between the two particle populations, but this difference may also indicate that the primary particles from which populations B and X were composed may not have been the same. Both of the determined fractal dimensions (2.33 for population X and 2.62 for population B) fall within the anticipated range of 1-3 (Kranenberg, 1994).

The Winterwerp (1998) settling velocities were recalculated for the population B and population X particles. Fig. 8.17 shows D_{50} plotted against the Winterwerp (1998) settling velocities for the February-March and original May-June data in addition to the re-analysed population B and X data. Density lines are not presented on the plot since the gradients of the relationship between D_{50} and W_s are determined primarily by the fractal dimensions of the data. The population B data closely tracks the original May-June data; however, the population X data overlaps with the February-March data in a similar manner to that shown in the Stokes' settling velocities (Fig. 8.11).

The recalculated Winterwerp (1998) settling velocities for particle populations B & X were combined into a single time series and plotted along with the original Stokes' time varying viscosity settling velocities, with the February-March Stokes' and Winterwerp (1998) settling velocities included separately for comparison (Fig. 8.18). The Stokes' and Winterwerp (1998) settling velocities followed the same pattern during peak spring conditions in February-March with increases during high and, predominantly, low water (Fig. 8.18 top), with good agreement between the two methods. The highest settling velocities were found during low water, and this was also the time of the largest differences between methods. During peak spring conditions in May-June (Fig. 8.18 bottom), the recalculated Winterwerp (1998) settling velocities for particle populations B & X increased around high and low water, though the pattern was more erratic and the differences between the two methods larger, with differences often visible at high and low water.

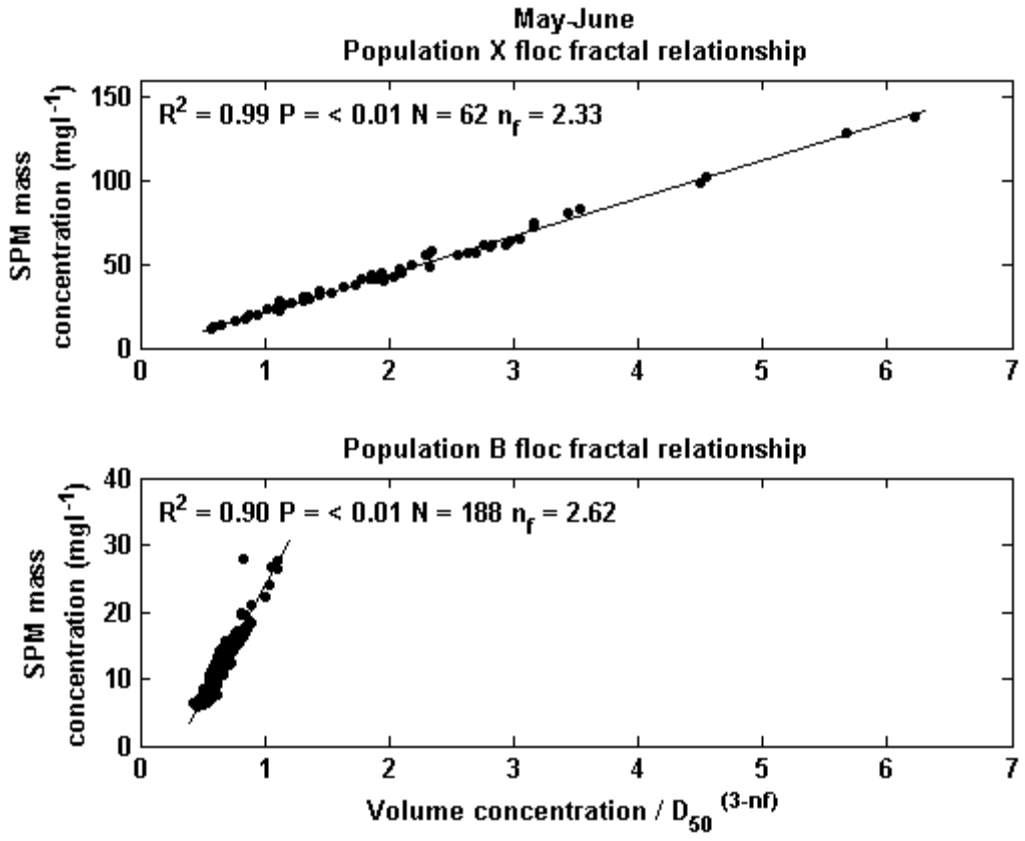

Fig. 8.15 – Re-determination of the fractal dimension of the May-June data for population X (top) and population B (bottom)

During neap tide conditions (Fig. 8.19), both the Stokes' and Winterwerp (1998) settling velocities follow the same pattern during February-March (Fig. 8.19 top), with increases at high and, predominantly, low water, though the inequality between the two was lower than during spring tides (Fig. 8.18 top), and the values of the Winterwerp (1998) method were at times much lower than those calculated using Stokes'. During the May-June deployment however, settling velocities increased during the flood and ebb tide and were lowest during high and low water (Fig. 8.19 bottom), in direct contrast to those recorded during peak spring conditions (Fig. 8.18 bottom).

A change occurred in particle behavior between the spring and neap periods during May-June (Fig. 8.19). During spring tides, settling velocities increased at high and low water, and fell during peak current speeds. During neap tides, settling velocities increased during the flood and ebb periods, and fell during high and low water (Fig. 8.19 bottom).

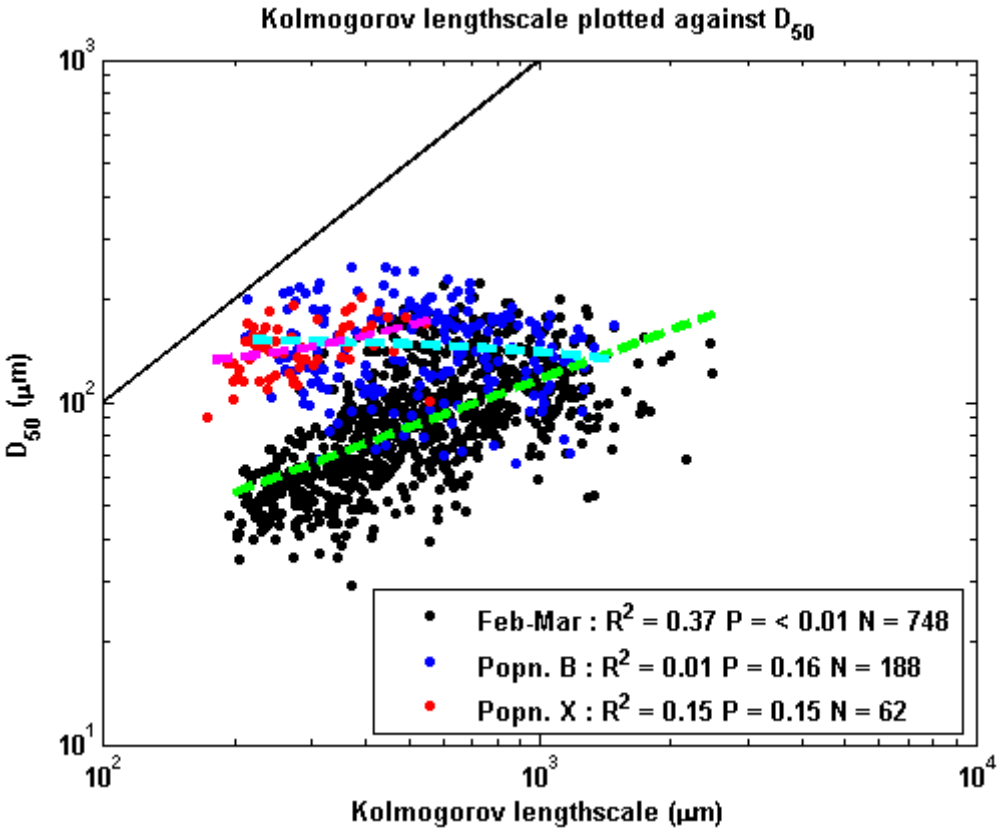

Fig. 8.16 - D_{50} plotted against the Kolmogorov lengthscale (Eq. (2.24)) for February-March (black dots) and May-June population B (blue dots) and population X (red dots) with best fit lines for February-March (green), population B (cyan) and population X (pink). Also included is a 1:1 line (black) between the Kolmogorov lengthscale and D_{50}

8.7 Discussion

8.7.1 Possible causes of population X

Population X did not change density with size (Fig. 8.14 bottom left), as flocs have been shown to do (Tambo & Watanabe, 1979; Flesch, et al., 1999), despite displaying a fractal relationship (Fig. 8.15 top) and therefore the population X particles are unlikely to have been flocs. Further, the lack of variation in density with size suggests a homogeneous composition, while the densities of the particles were too low to be entirely mineralic (e.g. quartz sand which has an effective density of ~1650 kgm^{-3}). There are several possibilities for the cause of population X, and these will be considered below.

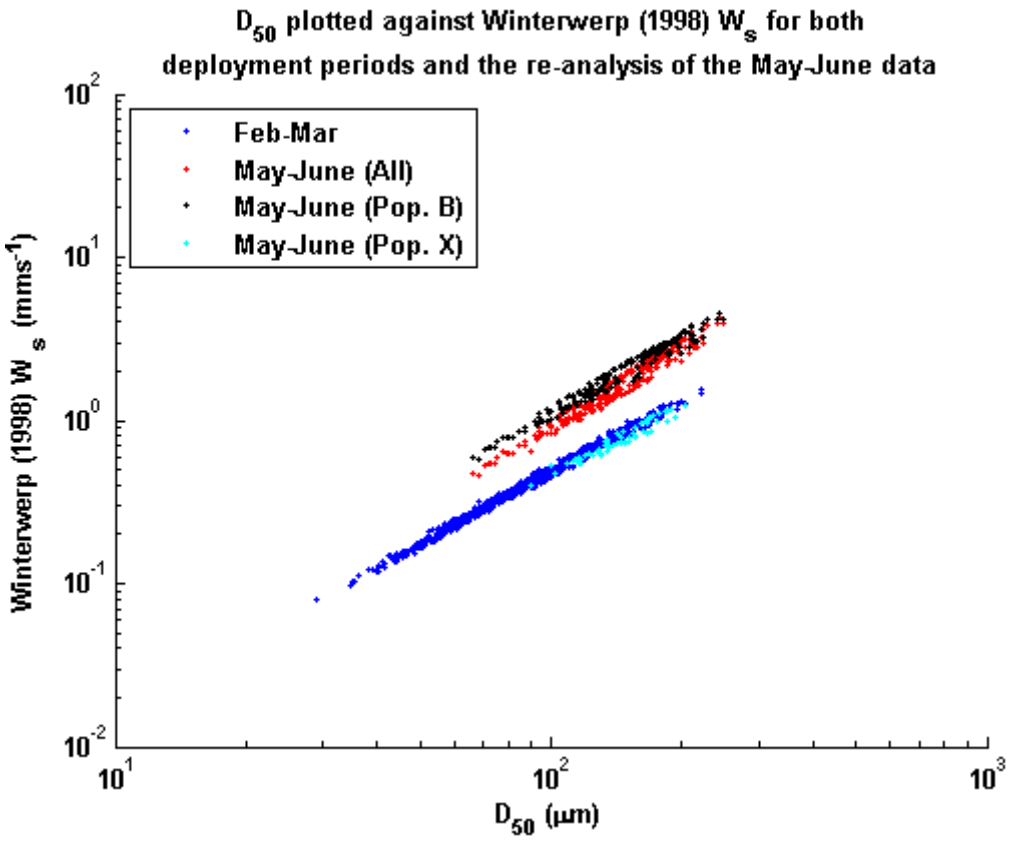

Fig. 8.17 – D_{50} plotted against Winterwerp (1998) settling velocities for the February-March data, original May-June analysis and the re-analysed May-June data split into populations B and X

Possibility of resuspension

Plotting the occurrences of the population X particles on the ADCP pressure curve (Fig. 8.20 top) and the ADCP-derived current speeds (Fig. 8.20 bottom) shows that the population X particles occurred predominantly during high current speed conditions during the flood and ebb tides, with only one occurrence during current speeds < 0.4 ms^{-1}. Occurrence during high current speed conditions suggests that the population X particles were resuspended from the sea bed. However, the population X particles were of lower density, but similar size, to the majority of the population B material which dominated the May-June deployment period (Fig. 8.14 bottom left), and therefore these particles should have been preferentially resuspended under low current speed conditions. However, as can be seen in

Fig. 8.21, the population X particles were not preferentially resuspended, with the particles at times not present until SPM concentrations exceeded 500 µll^{-1}.

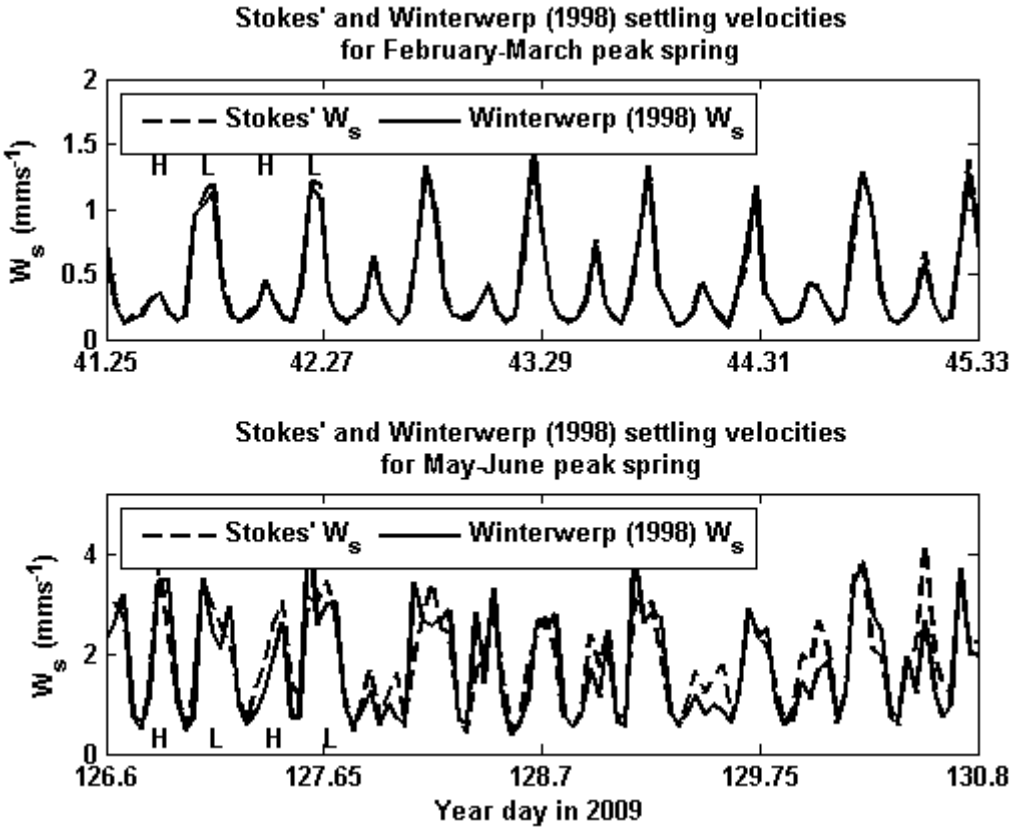

Fig. 8.18 – Comparison between the spring tide Stokes' and Winterwerp (1998) settling velocities for February-March (top). Bottom shows spring tide Winterwerp (1998) settling velocities following the reanalysis of the May-June data into populations B and X. H & L indicate high and low water periods

It is possible therefore that population X did resuspend, but that some characteristic of the population X particles increased the amount of energy required for suspension. A property of the particles such as an adhesive coating, in the form of polysaccharides or other similar substances, could hinder resuspension, even at times when particles of a similar size but higher density were being resuspended.

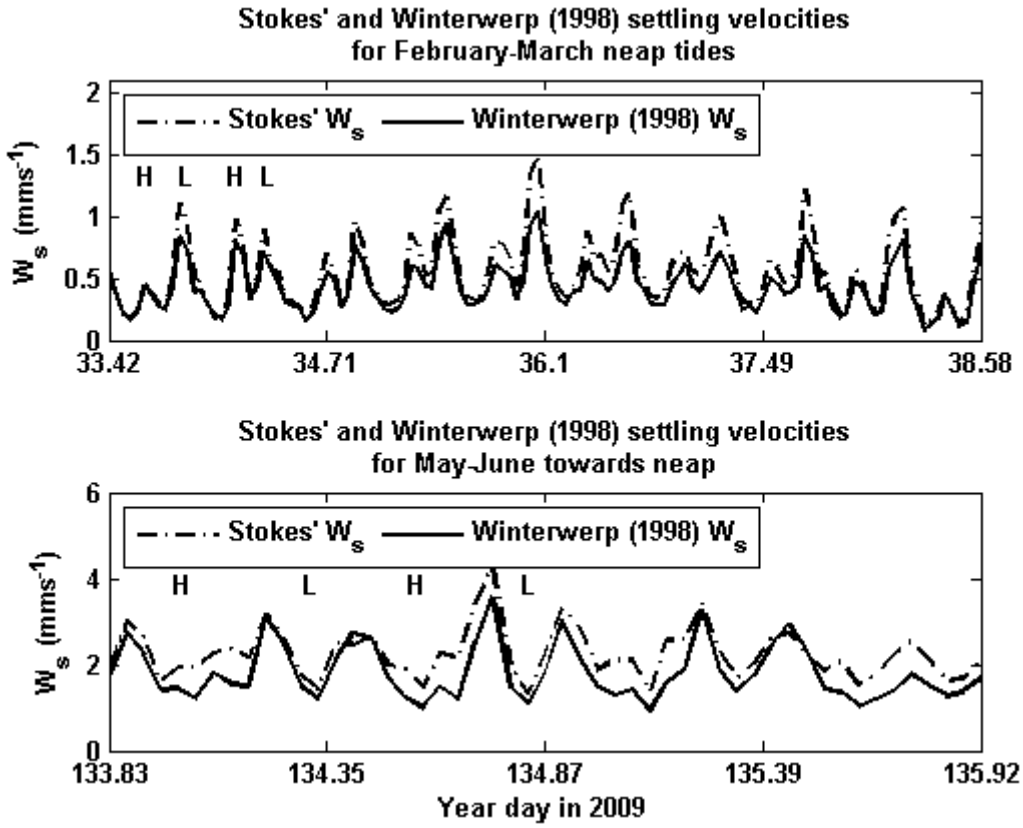

Fig. 8.19 – Comparison between the neap tide Stokes' and Winterwerp (1998) settling velocities for February-March (top). Bottom shows spring tide Winterwerp (1998) settling velocities following the reanalysis of the May-June data into populations B and X. H & L indicate high and low water periods

Possibility of advection

The population X particles may have been advected into the estuary from offshore or down the estuary from the salt marsh. As the particles occurred during peak spring conditions but were absent during neap tides (Fig. 8.20), it may be that the tidal range impacted upon the advection of population X past the mooring point. This would explain why the signal disappears towards neap tides, despite current speeds remaining > 0.4ms^{-1} and therefore seemingly high enough to resuspend these particles from the bed.

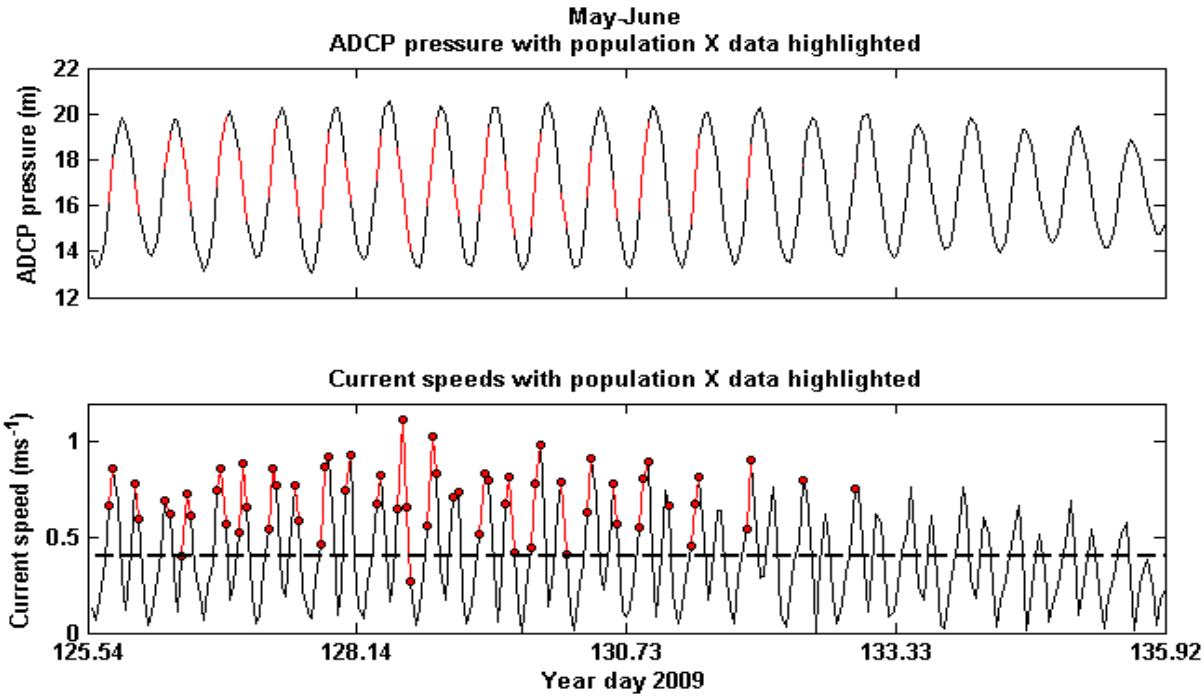

Fig. 8.20 – Tidal state (top) and current speed (bottom) for the first 250 hours of the May-June deployment with times that population X occurred highlighted with red dots and red lines

Composition of population X particles

The population X particles were of similar size and density to the larger February-March particles. It is conceivable therefore that the population X particles may have been composed of the same material as the February-March particles. However, investigation of the overlapping data shows that the February-March and population X particles occurred under differing tidal conditions. While the population X particles occurred predominantly during high current speed conditions (> 0.4 ms^{-1}) during both the flood and ebb tides (Fig. 8.20) and therefore during times of high turbulence and high shear stress, the overlapping particles during the February-March deployment occurred during low current speeds (Fig. 8.22), and therefore times of low turbulence and low stress, during high, and (predominantly) low water. These differing conditions indicate that despite the overlapping D_{50} and effective density ranges (Fig. 8.14 bottom left), the two signals do not represent the same type of particles.

The population X particles may have been diatoms – the size of which can vary while their effective density remains constant. Diatoms are generally found within the size range of 2 – 200 μm (Leng & Swann, 2010), and have effective densities of 100 to 300 kgm^{-3} (MacIntyre, et al., 1995; Celler, et al., 2014). The population X signal fits into the lower end of this effective density range, and the upper end of this size range (Fig. 8.14 bottom left). In addition, diatoms may secrete polysaccharides (Wright, et al., 1997; Sanford, 2008), binding them to sediment and making them harder to resuspend, a characteristic indicated in the previous section on resuspension which speculated that the population X particles may possess an adhesive coating.

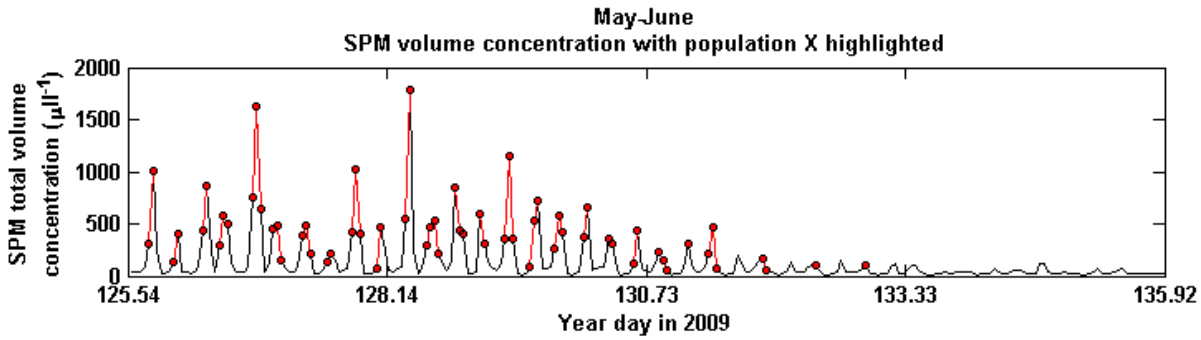

Fig. 8.21 – Volume concentration for the first 250 hours of the May-June deployment with the times at which the population X particles occurred highlighted

If population X does represent a diatom signal, then increased fluorescence response should have occurred when population X was present as diatoms are photosynthesizing plankton. Plotting the times of the occurrence of population X on the fluorescence response obtained from the May CTD casts (Fig. 8.23) shows that population X generally occurred during times of increased fluorescence response, with the exception of the third occurrence (around year day 126.3). However, any increased fluorescence response may be masked as these were already times of high fluorescence response (see Section 6.7.5) and it is therefore not possible to determine whether the presence of the population X particles led to a fluorescence response increase.

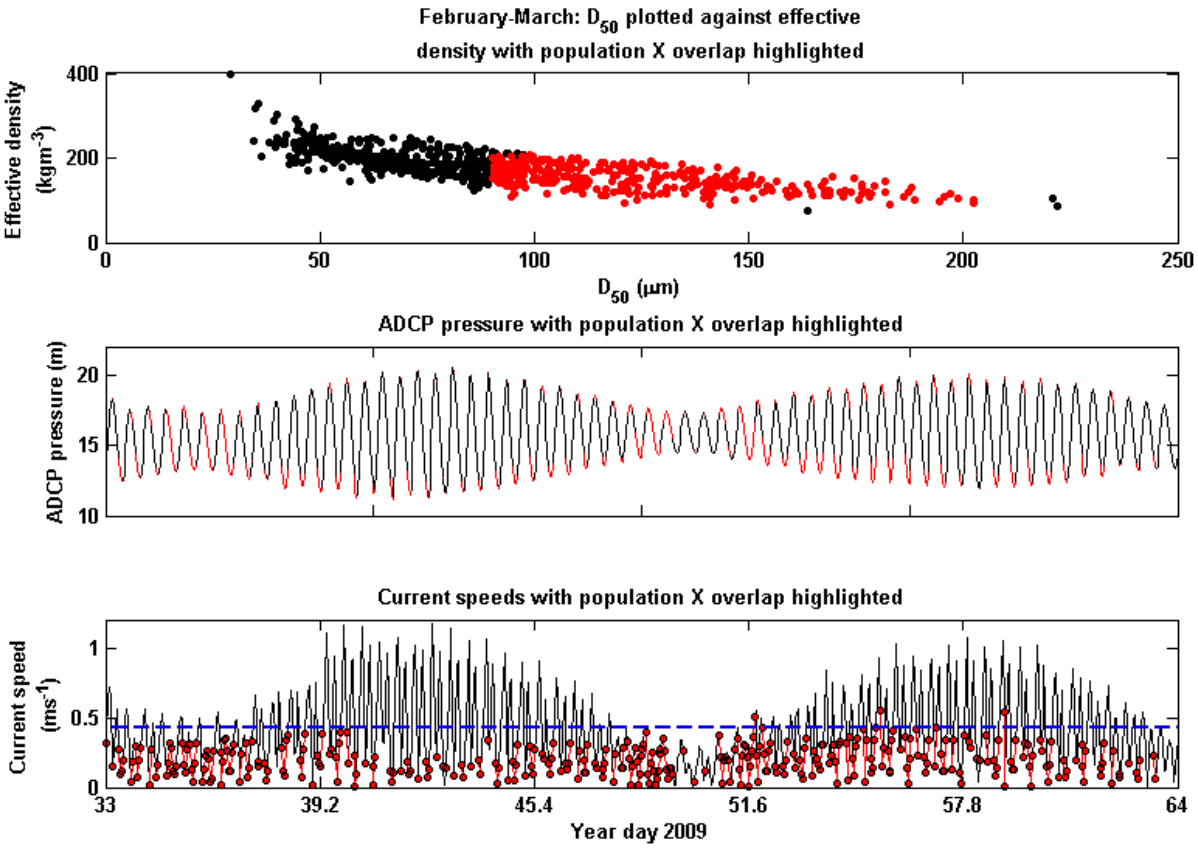

Fig. 8.22 – D_{50} plotted against effective density for the February-March deployment (top) with data that overlapped with the May-June population X data highlighted in red. ADCP pressure (middle) and current speed (bottom) are shown with times highlighted in red that the particles in the top panel, also highlighted in red, occurred

Source of population X

The February-March data has been shown to contain an advection signal with particles advected from the upper reaches of the estuary (Chapter 7). In addition, the reduction in the horizontal concentration gradient between deployment periods may have been caused by higher temperatures and higher solar radiation during May-June in combination with increased biological activity and sediment binding, causing an increase in the critical shear stress for erosion of the mudflat and salt marsh areas higher up the estuary, making them more resistant to erosion (see Section 7.6).

Sediment beds may be formed through the settling of particles onto the bed. The drying out of intertidal surface sediment during exposure to the air over the flood-ebb and spring-neap

cycles, and the increase in biological activity seen between winter and summer periods, can increase the shear strength of the surface sediment layer (Amos, et al., 1988; Decho, 1990). However, despite this increased shear strength, high shear stresses over these sediment beds may result in the erosion and suspension of pieces of these mudflats, known as aggregates (pieces of mudflat and / or other settled material not formed within the water column as flocs are). Aggregates are larger than individual particles and, being produced from a settled sediment bed, may have a constant density irrespective of size and, due to repeated exposure to atmospheric conditions during low water in summer, possess high yield strength (Amos, et al., 1988). The erosion of pieces of this aggregate during spring tide conditions could provide a source of particles of varying size with a constant density. These aggregate pieces could potentially also be coated in biological polysaccharide substances due to the biological activity on the intertidal areas, increasing the energy required for resuspension, fulfilling all of the criteria of the population X particles.

This presents two possible sources of the population X particles – resuspended and / or advected aggregates formed from dehydrated mudflat, or diatoms. With the data available it is not possible to ascertain which the correct source was and therefore both remain as valid potential sources of the population X particles.

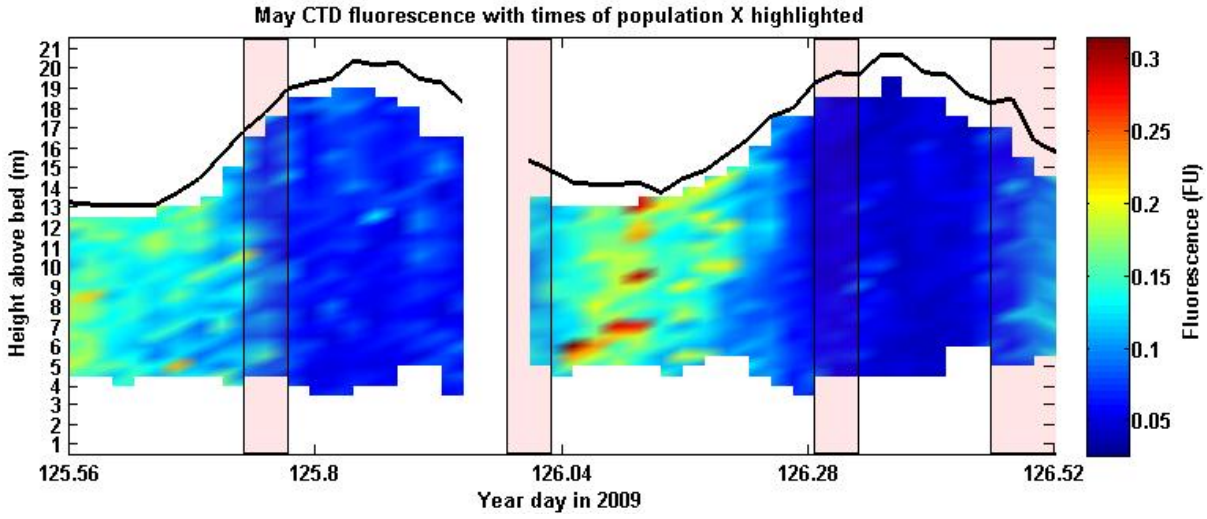

Fig. 8.23 – Fluorescence from the May CTD period with the occurrence times of population X highlighted

8.7.2 Estimation of the size of primary particles

By plotting and extrapolating trendlines fitted to the effective density plotted against D_{50} for both the February-March and May-June population B data (Fig. 8.24), it may be possible to identify a common primary particle from which both types of particles were formed. The population X data was not included in this analysis as the effective density of the population X particles does not vary with varying particle size (Fig. 8.14 bottom left) as that of the February-March and May-June population B particles does (Fig. 8.3 & Fig. 8.14 bottom left) and therefore these particles are unlikely to have been flocs. According to the extrapolated trendlines, the primary particle had a size of ~4 µm, with an effective density of ~700 kgm^3 (Fig. 8.24). This is consistent with the size of individual clay platelets (McAnally (1999)), and results from Maggi et al. (2006) in the Tamar, UK, and Verney et al. (2009) in the Seine, France who both reported primary particles of 4 µm. However, an effective density of ~700 kgm^{-3} does not correspond to any of the commonly occurring clay minerals including Kaolinite (effective density ~1600 kgm^{-3}), Montmorillonite (~1000 kgm^{-3})) or Illite (~1600 kgm^{-3}). It is therefore unlikely that the crossing point of these extrapolated trendline represents the true effective density of a potential primary particle, indicating that the flocs formed during one, or both, of the deployment periods were not fully composed of the same mineralic substance.

8.7.3 Relationship between populations B and X

Plotting the population X and B Winterwerp (1998) settling velocities separately with current speed (Fig. 8.25 top) shows that the settling velocities of population B generally decreased during high and low water, with higher settling velocities found during the flood and ebb periods for which data were available, while the settling velocities of population X generally decreased during peak flood and ebb, with higher settling velocities during the lower velocities on flood and ebb for which data were available. With the lack of data for population B during peak current speeds and the lack of data for population X during high and low water it is difficult to accurately determine the behavior of these particles. However, settling velocities for population B decreased during high and low water, which may indicate the settling of larger, faster settling flocs. This is supported by Fig. 8.25

(bottom) which shows that the effective density of the population B particles generally increased over high and low water, indicating the settling of low density macroflocs, while the effective density of the population X particles showed no relationship with current speed.

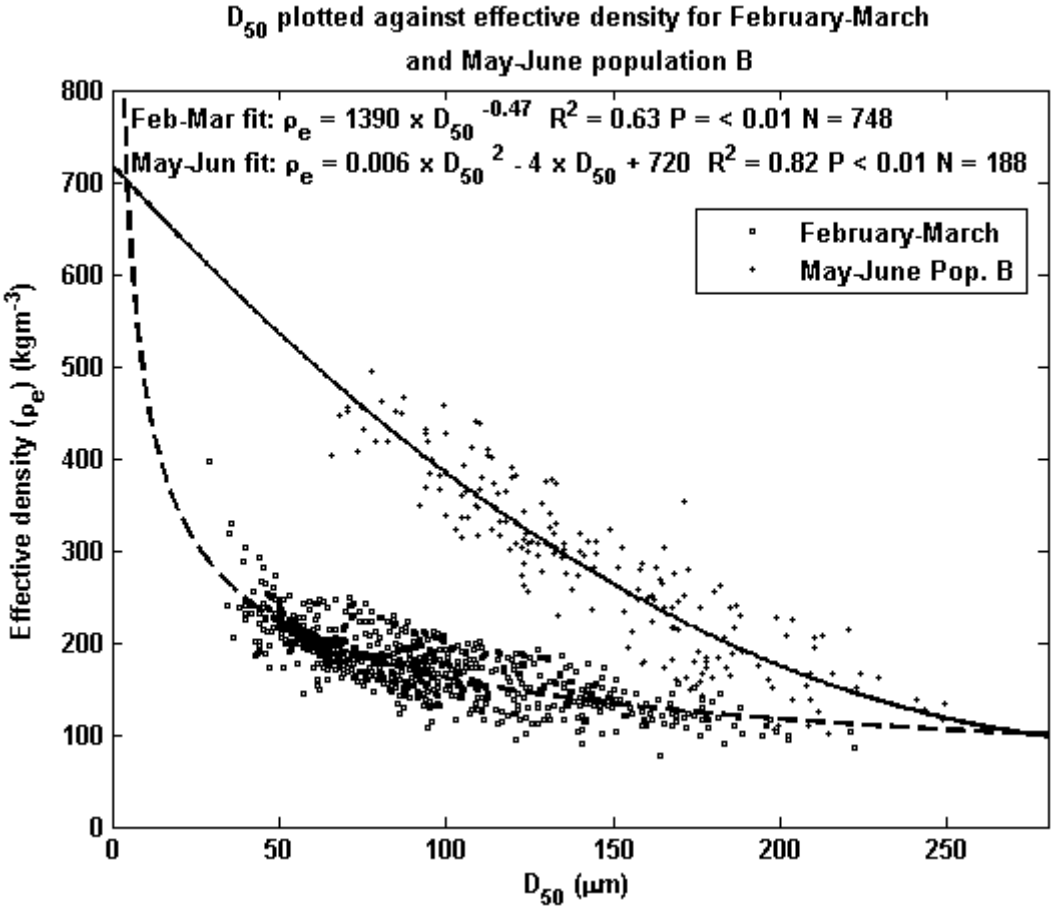

Fig. 8.24 – D_{50} plotted against effective density for the February-March and May-June population B data. The dashed trend line indicates the February-March regression, the solid trend line indicates the May-June population B regression

8.7.4 Reasons for the seasonal variations in particle characteristics and behaviour

Variations in biological productivity

Fluorescence may be used as a proxy for chlorophyll (Lorenzen, 1966), which is representative of photosynthetic activity and therefore the presence of plankton and other

photosynthetic organisms. These forms of organism generally produce polysaccharides, and levels of polysaccharides can be related to photosynthetic activity and are subsequently higher in summer than winter (Maerz & Wirtz, 2009). Therefore, in the context of this study, fluorescence is used to infer the presence of polysaccharides (see Section 3.3.5) and it is assumed that an increase in the levels of fluorescence, and therefore chlorophyll, should represent an increase in levels of polysaccharides. Polysaccharides coat particles, making them sticky and enhancing the success rates of particle collisions (Milligan & Hill, 1998) and bind particles together, increasing the yield strength of flocs, and making them harder to break (Dyer, 1986; Manning, et al., 2010).

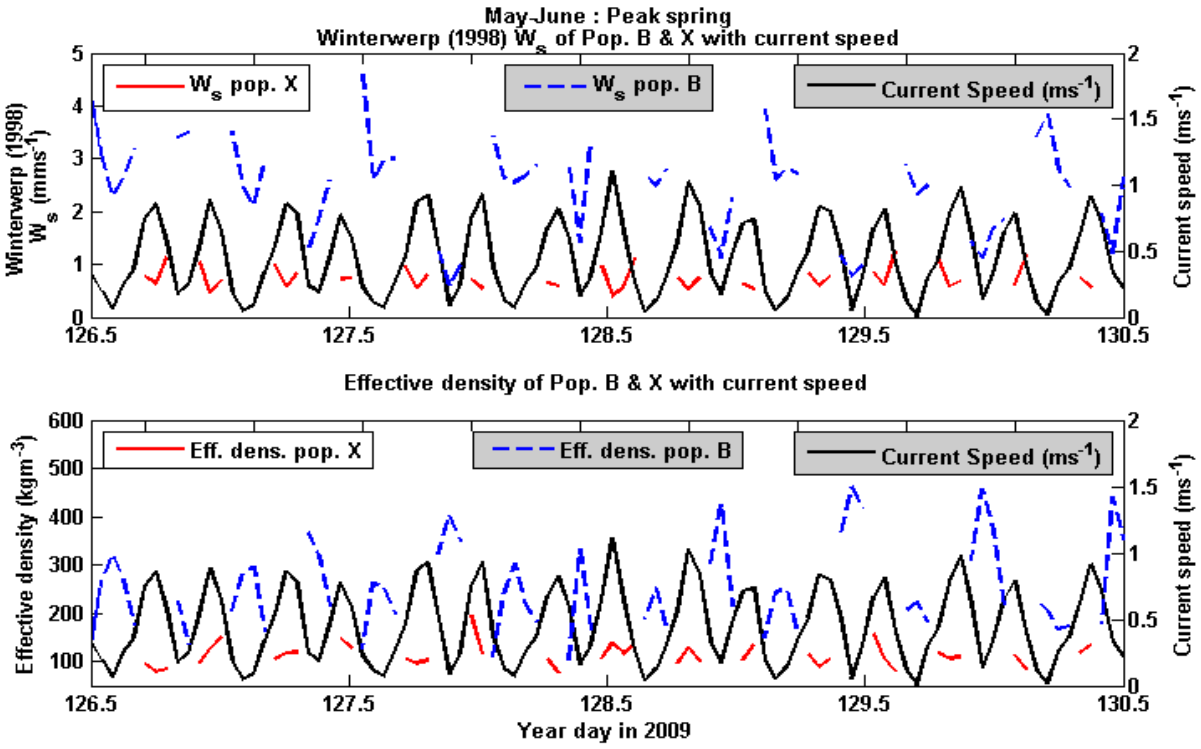

Fig. 8.25 – Winterwerp (1998) W_s (top) and effective density (bottom) of populations B & X plotted with current speed for peak spring during May-June

During the February and March CTD stations (Fig. 6.15a & b), fluorescence response was low and correlated with SPM mass concentrations (Fig. 6.25), indicating that fluorescing material was connected with, and likely carried by, SPM. Conversely, during the May anchor station (Fig. 6.15c), the predominant source of fluorescing material was high up the estuary (see Section 6.7.5), with fluorescence response elevated during the late ebb and over low water

(Fig. 6.15c), but uncorrelated with SPM concentrations (Fig. 6.25). Fluorescence response during May-June was up to three times higher than during February-March (Fig. 6.15c). It is postulated that biological material derived from the mud flat and salt marsh areas within the estuary was the source of the elevated fluorescence response during May-June (see Section 6.7.5) and delivered abundant levels of polysaccharides to the estuary system. These polysaccharides increased the yield strength of particles during May-June by comparison with February-March (Section 8.4). Higher floc strength would mean a higher transition threshold from flocculation to breakup and therefore flocculation occurring under more energetic conditions. Particles coming together under high energy conditions would experience higher energy collisions, and this may have resulted in the population B particles being denser (Fig. 8.3 & Fig. 8.14) and faster settling (Fig. 8.17) than the February-March particles.

Variations in the horizontal concentration gradient

Section 7.6 discusses reasons for the reduction in the strength of the horizontal concentration gradient between the February-March and May-June deployment periods. During February-March, the concentration gradient provided a constant stream of new particles to the system, while during May-June, the reduction of this gradient meant that new material was less common, and therefore the particles were likely to be formed from reworked existing material. This constant reworking of the same material, and repeated exposure to high levels of polysaccharides (see previous section), may have influenced the characteristics of the population B particles, with the constant resuspension, settling, and rolling of the particles on the bed without significant breakup causing the compaction of the flocs into denser particles over time.

Variations in river flow

Average river flow decreased between the February-March and May-June deployment periods (Fig. 6.4b & h). The influence of this decrease on the horizontal concentration gradient was considered in Section 7.6. It is unlikely that the reduction in river flow had a significant impact upon the particle characteristics observed. River flow makes up, on average, only 0.4% of the tidal prism (Moore, et al., 2009) and has been shown to be unimportant with regard to sediment supply to the estuary (Amoudry, et al., 2014).

8.7.5 Controls on particle behaviour

February-March

It is proposed that turbulence-mediated flocculation occurred during February-March. Concentrations of sticky polysaccharides were low, and low levels of turbulence brought particles together to form weak macroflocs (Fig. 8.2 top right), while strong turbulence resulted in floc breakup (Fig. 8.16). The longer timespan of low water (Fig. 7.11) gave flocs longer to form under low turbulence conditions and therefore the flocs formed during this time were larger and settled faster than those which formed during high water (Fig. 7.11). During the flood and ebb periods, these large flocs were broken into their constituent microflocs by high levels of turbulent shear (Fig. 8.16). A lack of biological activity meant that the flocs had a low yield strength (Section 8.4).

May-June population B

During May-June, when primary productivity is higher, polysaccharides present in the water column coated the particles, enhancing both the bond strength and stickiness of the flocs. Because the bonds were stronger, floc strength increased (see Section 8.6.2) and the higher transition threshold from flocculation to breakup meant flocculation occurred under more energetic conditions. Particles coming together under high energy conditions experienced higher energy collisions, resulting in the population B particles being denser (Fig. 8.3 & Fig. 8.14) and faster settling (Fig. 8.17) than the February-March particles, and resuspending on each tide without significant breakup (Fig. 7.12). The population B particles settled during high and low water, with the larger, faster settling macroflocs settling first, leading to an increase in the effective density, and a decrease in the settling velocity, of the suspension (Fig. 8.25). This can be seen during the run down to neap tides in May-June (Fig. 8.19 bottom) when no population X particles were present. This hypothesis is supported by the results of Jago, et al., (2007) from the Irish Sea, including the region seawards of the Dee Estuary, who found small, weak flocs in stratified areas of low turbulence and low biological activity – similar to the results obtained here for the February-March particles. Jago, et al., (2007) also found larger, stronger flocs in mixed waters under a high turbulence regime with abundant biological presence, which fits well with the flocs found in the present study for May-June population B. These new results show that the flocs in the estuary shared similar

properties to flocs in the mixed waters offshore from the Dee Estuary, and emphasise the importance of biological effects in estuarine systems, which have been shown to be greater than the physical effects during the May-June deployment period.

May-June population X

The population X particles were of similar size and density to the larger February-March particles (Fig. 8.3 & Fig. 8.14 bottom left), but did not occur under the same tidal conditions (Fig. 8.20 & Fig. 8.22). Based upon the characteristics of the population X particles such as size and effective density (Fig. 8.14 bottom left), it is likely that the population X particles were composed of either pieces of aggregate formed from pieces of mud flat or salt marsh, or a population of diatoms (see Section 8.7.1). However, with the available information it is not possible to determine which was the cause of the population X particles.

Differences between February-March and May-June population B

Fig. 8.26 visualises the differences between the February-March particles and those of population B during the May-June deployment, with the direction of the arrow indicating the direction of increase of each parameter. Flocs during February-March were weak (see Section 8.4), with low effective densities (Fig. 8.3) and, during this time of low biological activity (Fig. 6.15), were turbulence controlled (Fig. 8.16). In contrast, the May-June population B particles were stronger (see Section 8.6.2), denser (Fig. 8.3), and not limited by turbulence (Fig. 8.16) during this time of higher biological activity (Fig. 6.15). The differences between the deployment periods were large and likely the result of changes in the horizontal concentration gradient and seasonal variations in biological activity.

8.8 Conclusions

During February-March:

- Fluorescence and therefore chlorophyll and biological polysaccharide levels were low;
- Flocculation was controlled by the natural attractive forces between clay particles and levels of turbulent shear;

- Weak flocs were produced under low turbulence conditions during low and, to a lesser degree, high water;
- Flocs were broken up into smaller microflocs during high turbulence conditions on the flood and ebb tides.

During May-June:

- Fluorescence and therefore chlorophyll and biological polysaccharide levels were higher;
- Two particle populations were present: population B and population X;
- Floc size showed no relationship with turbulence for either population;
- Floc strength was increased, probably by the presence of polysaccharides, making the flocs more resistant to turbulence-induced breakup;
- Population B flocs were denser and settled faster by comparison with similarly-sized flocs during February-March;
- Population B flocs resuspended on each tide without breakup;
- Population X particles did not change density with changing size;
- Population X particles occurred predominantly during current speeds in excess of $0.4ms^{-1}$;
- It is likely that the population X particles had an adhesive coating enabling them to resist resuspension from the bed;
- The population X particles may have been composed of diatoms or pieces of aggregate from the intertidal areas high up the estuary.

It is thought that the settling velocity of SPM within the estuary was changed by these altering characteristics, emphasising the importance of modelling not only the physical, but the biological aspects of estuarine SPM in order to parameterize particle characteristics correctly. Modelling estuarine SPM with a constant settling velocity, or with a relationship based on shear alone, will be highly inaccurate for time periods in which biological processes have an impact upon SPM particle characteristics.

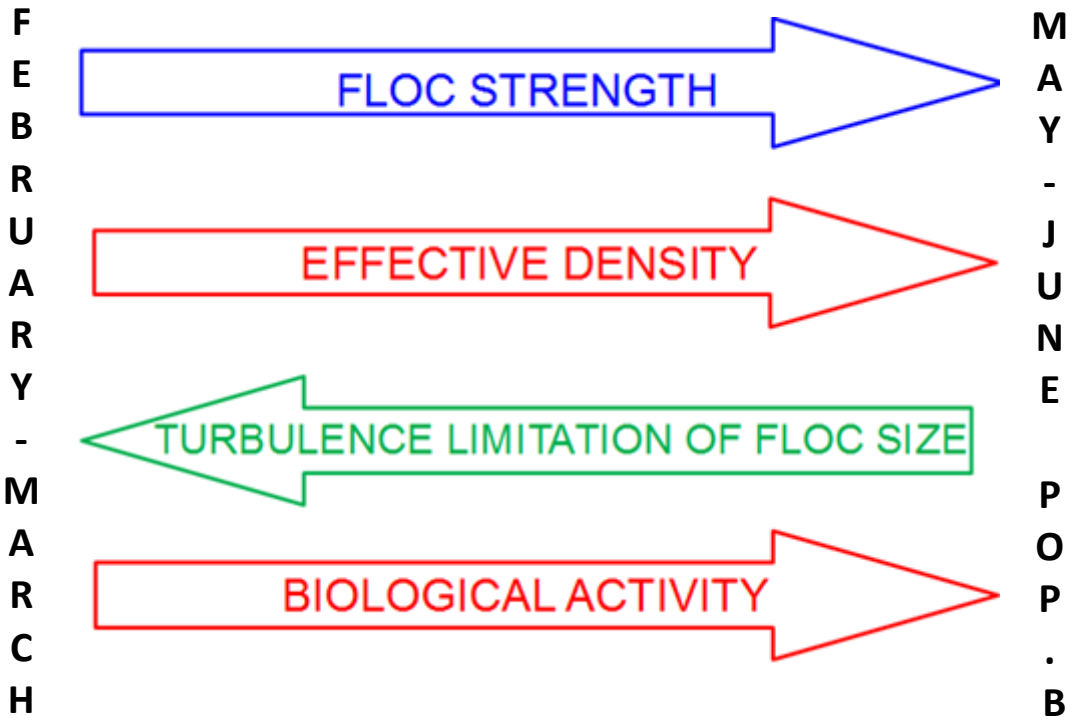

Fig. 8.26 – Changes in particle characteristics and controlling factors between the February-March and May-June population B particles

Chapter 9

Conclusions

9.1 Conclusions arising from the present study

The Dee Estuary is a highly energetic, hypertidal environment containing abundant cohesive SPM. Variations in SPM are strongly tidally modulated, impacted by the spring-neap cycle, and change greatly between February-March and May-June.

The original aim of this study was to investigate the turbulence and flocculation in a hypertidal estuarine system, by collecting a dataset of in-situ observational data and investigating both net SPM flux, and the trends in particle characteristics and behavior along tidal, spring-neap, and seasonal timescales. Motivation for these investigations came as part of the larger aims for the FORMOST Project (Field Observation and Modeling Of the Sediment Triad) – to better understand and successfully model sediment transport within the Dee Estuary.

Hydrodynamics

Tidal range varied during February-March from 9.4 m at the peak of springs, to 2.9 m at lowest neap, and during May-June from 8.1 m at the peak of springs, to 3.1 m at lowest neap. River flow decreased from an average of 19.5 m^3s^{-1} to 13.4 m^3s^{-1} between February-March and the first 250 hours of May-June – a decrease of 31 %.

The hydrodynamics of the water column were investigated using observations made during February-March and May-June 2009. Harmonic analysis of the depth-averaged currents and surface elevation showed the dominance of the M_2 and S_2 tidal harmonics. Some higher harmonics were also present, though their diurnal influence was weak. Currents within the Hilbre Channel were shown to be almost rectilinear.

Stratification occurred around low water. This was episodic and had different characteristics to the classical tidal straining suggested by Simpson et al., (1990). No stratification occurred during ebb; the water column was well mixed, and became gradually fresher. Density

stratification was prevalent during the early flood where the incoming tide intruded first at the sea bed while waters at the surface were still ebbing, resulting in density stratification. This difference from the classical regime was reflected in the temperatures, salinities and SPM concentrations which were vertically homogeneous during high water and ebb but showed stratification over low water and during the early flood in a manner similar to Giddings et al. (2011).

Particle dynamics

Flood-dominant resuspension occurred on most tides, reaching to the water surface. At high water, resuspended particles settled, while at low water, stratification resulted in a 2-layer system with fresher water containing a higher concentration of SPM lying over higher salinity, lower concentration water with a pycnocline separating the two areas.

During February-March, low turbulence levels during low and high water resulted in flocculation and large particles, while high turbulence during the flood and ebb caused breakup and resuspension and therefore an abundance of small particles. This was modulated by the semi-diurnal advection of a horizontal concentration gradient which brought small particles down the estuary.

During May-June, two populations of particles were found, termed population B and population X. Population B resuspended during the flood and ebb but did not break up under high turbulence conditions. Large flocs settled during high and low water, resulting in smaller particles dominating during low turbulence conditions. Population X, of lower density and lower settling velocity than the majority of the population B particles also resuspended during the flood and ebb, but was generally present only during high current speed ($> 0.4 ms^{-1}$) conditions. The identity of the population X particles is unknown, but they may have been either diatoms, or pieces of aggregate from the salt marsh and mud flat regions. A horizontal concentration gradient was present during the May-June deployment, but this time period was dominated by quarter-diurnal resuspension.

Seasonal particle characteristics

Fluorescence, used as a proxy for chlorophyll (Lorenzen, 1966) and therefore biological activity and the presence of biological polysaccharides, changed between deployments:

February and March displayed low fluorescence response, indicative of low biological productivity, which correlated well with SPM concentration while May and June showed high levels of fluorescence response during the late ebb and over low water that was not correlated with SPM concentration. Higher levels of chlorophyll were recorded during May-June by both satellite observations and an offshore buoy in Liverpool Bay by comparison with those levels recorded during February-March.

It is proposed that the increase in fluorescence response during the late ebb and over low water in May resulted from the export and advection of living organic material from the mud flat and salt marsh regions high up the estuary. This was due to the May CTD being undertaken on the run up to spring tides and therefore each tide covered areas of mud flat and salt marsh that had not been previously covered for several days, allowing time for biological production to occur on the surfaces of the mud flats and salt marshes. The tidal stage during the June CTD period (being around neap tides) resulted in less coverage of the salt marshes and mud flats, and the repeated coverage of areas that had been covered only hours previously. This resulted in less material being exported and advected down the estuary. The result of this was the June fluorescence signal, which displayed the same signal as the May data, but with reduced variability, concurrent with lower amounts of biologically active material entering the estuary.

It is surmised that abundant biological polysaccharides during May-June bound particles together and increased the yield strength of the flocs, changing the dominant SPM signal from flocculation and breakup to favour resuspension without breakup as flocs became strong enough to resist high levels of turbulence. Flocculation and breakup still occurred during May-June, but at much a reduced scale. The settling velocities of the SPM were changed by these altering characteristics, with settling velocities for similarly sized particles in excess of 2.5 times greater during May-June than February-March. It is therefore important to include the impacts of biological organisms in the numerical modelling of SPM processes as flocculation formulae which rely only on turbulent shear may be highly inaccurate.

The present study has shown that clear tidal, spring-neap, and seasonal signals are present in the SPM of the Dee Estuary. Tidal turbulence produces resuspension, while the strength

of the seasonally varying horizontal concentration gradient is likely to be controlled by a combination of river flow, the presence of biological organisms and the seasonally varying atmospheric processes. Seasonal variations in atmospheric processes and biological activity may also determine the characteristics of the flocs present within the estuary. A summary of the seasonal variations in particle characteristics and behaviour is presented in the summary table below:

SUMMARY	Peak flow	Slack water	Dominant process
February-March	Large, weak flocs ruptured by turbulence to generate small, dense, slow sinking particles. Small particles resuspended	Large, low density, weak flocs grow. Settling of larger flocs	Flocculation & breakup
May-June population B	Large, strong, denser flocs resuspended without rupture	Large, strong, denser flocs settle	Biological strengthening
May-June population X	Large, low density, strong particles resuspended or advected without rupture.	Unknown	Unknown

Seasonal volume flux

The spring-neap cycle had a large impact on the hydrodynamics of the estuary. During February-March, the quarter-diurnal resuspension signal was strong during spring tides. This quarter-diurnal signal was maintained throughout the spring-neap cycle; however, the amplitude of the signal reduced towards neap tides as lower current speeds resulted in less resuspension. A semi-diurnal advection signal was also present, bringing small particles down the estuary on the late ebb and over low water due to the presence of a horizontal concentration gradient.

During the May-June period, the horizontal concentration gradient and therefore the semi-diurnal advection signal was reduced. This was caused by the decrease in river flow coupled with the increase in biological activity, and therefore increased sediment binding, as well as the increase in air temperature and solar radiation, increasing the erosion threshold of salt marsh and mud flat material. Peaks in small particle concentration during May-June show a good relationship with peak current speeds during the spring-neap cycle indicating that the May-June period was predominantly resuspension controlled.

In the presence of strong tidal currents, the strong horizontal concentration gradient was able to affect the net volume flux of the estuary. In the case of the Dee Estuary, the gradient was not great enough to reverse the volume flux, but was able to reduce the flood dominance from 63% during May-June to just 16% during February-March. In an estuarine system with larger horizontal concentration gradients, it is hypothesized that the horizontal concentration gradient may be sufficient to alter the direction of the net volume flux of the estuary, even in the presence of flood dominant currents. The horizontal concentration gradient was mediated by the river flow, the presence of biological material stabilizing the sea bed, and the atmospheric conditions which may have acted to increase the shear strength of the intertidal bed sediment.

Flocculation also plays a role. Small particle volume flux was flood dominant during both February-March and May-June, while large particle volume flux was flood dominant during May-June, but ebb dominant during February-March. Flocculation during February-March was low-water dominant due to tidal asymmetry, with larger particles formed during the late ebb and over low water than formed at high water due to the increased time and concentrations of small particles available under the low current speed conditions of low water. The result of this was that the larger particles occurring during the late ebb and over low water in February-March settled faster than the large particles occurring during high water, resulting in a tidal pumping mechanism which may have accelerated infill of the estuary.

9.2 Future work

A number of differing research options could be undertaken to further this work. In order to build on this current research, further key observations should be made:

- Any investigations would require monitoring of SPM concentrations above the limit of saline intrusion to determine the riverine input into the system;
- Monitoring of SPM concentrations adjacent to the salt marshes and mud flats, as well as chlorophyll and polysaccharide levels within both the salt marsh channels, and in the main estuary channel;

- Investigations of the estuary carbon budget – if flocs are trapped in the estuary due to high flocculation on the late ebb and across low water during February-March then the estuary may be a carbon sink with carbon captured on the salt marsh, advected down the estuary and buried.

A number of observation methods could then be employed:

- Continual moored deployments between February and June to observe the transition between the two regimes in order to parameterise the changes;
- Investigations into other estuaries experiencing similar regimes to provide information on the universal application of this transition;
- Repetition of the observations during a larger range of river flow rates to parameterize the impact of flow rates on the regime;
- Repetition of the observations during a larger range of chlorophyll concentrations to determine the impact of the biological component on the regime;
- An estuary study of diatoms and other biostabilizing organisms;
- Use of a holographic camera or other floc camera system to more accurately capture the properties of the flocs including sizes, densities and settling velocities;
- 1D or full 3D modeling of the region including hydrodynamics, sediments and flocculation, allowing changing particle size rather than implementing separate particle classes as in Amoudry et al. (2014).

References

Abdel-Fattah, S., Amin, A. & van Rijn, L. C., 2004. Sand transport in Nile River, Egypt. *Journal of Hydraulic Engineering,* Volume 130, pp. 488-500.

Adler, P. M., 1981. Heterocoagulation in shear flow. *Journal of Colloid and Interface Science,* Volume 83, pp. 106-115.

Agrawal, Y. C. & Pottsmith, H. C., 1994. Laser diffraction particle sizing in STRESS. *Continental Shelf Research,* Volume 14, pp. 1101-1121.

Agrawal, Y. C. & Pottsmith, H. C., 2000. Instruments for particle size and settling velocity observations in sediment transport. *Marine Geology,* Volume 168, pp. 89-114.

Agrawal, Y. C. & Traykovski, P., 2001. Particles in the bottom boundary layer: concentration and size dynamics through events. *Journal of Geophysical Research,* Volume 106, pp. 9533-9542.

Amos, C. L., Grant, J., Daborn, G. R. & Black, K., 1992. Sea carousel - a benthic, annular flume. *Estuarine, Coastal and Shelf Science,* Volume 34, pp. 557-577.

Amos, C. L., van Wagonnet, N. A. & Daborn, G. R., 1988. The influence of subaerial exposure on the bulk properties of fine-grained intertidal sediment from Minas Basin, Bay of Fundy. *Estuarine, Coastal and Shelf Science,* Volume 27, pp. 1-13.

Amoudry, L. O. & Souza, A. J., 2011. Deterministic coastal morphological and sediment transport modeling: A review and discussion. *Reviews of Geophysics,* Volume 49, p. RG2002.

Amoudry, L. O., Souza, A. J., Brown, J. M. & Ramirez-Mendoza, R., 2014. Modelling-based assessment of suspended sediment dynamics in a hypertidal estuarine channel. *Ocean Dynamics,* 64(5), pp. 707-722.

Anderson, F. E. & Howell, B. A., 1984. Dewatering of an unvegetated muddy tidal flat during exposure - desiccation or drainage?. *Estuaries,* Volume 7, pp. 225-232.

Archer, A. W., 2013. World's highest tides: Hypertidal coastal systems in North America, South America and Europe. *Sedimentary Geology,* Volume 284, pp. 1-25.

Auffret, G., Khripounoff, A. & Vangriesheim, A., 1994. Rapid post-bloom resuspension in the northeastern Atlantic. *Deep-Sea Research,* Volume 41, pp. 925-939.

Baas, J., 2006. A flume study on the development and equilibrium morphology of current ripples in very fine sand. *Sedimentology,* Volume 41, pp. 185-209.

Baas, J., Best, J. L., Peakall, J. & Wang, M., 2009. A phase diagram for turbulent, transitional, and laminar clay suspension flows. *Journal of Sedimentary Research,* Volume 79, pp. 162-183.

Bagnold, R. A., 1966. An Approach to the Sediment Transport Problem for General Physics. *Physiographic and Hydraulic Studies of Rivers,* Issue Geological Survey Professional Paper 422-I, pp. 6-143.

Baugh, J. V. & Manning, A. J., 2007. An assessment of a new settling velocity parameterisation for cohesive sediment transport modeling. *Continental Shelf Research,* Volume 27, pp. 1835-1855.

Baumert, H. Z., Simpson, J. & Sundermann, J., 2005. *Marine turbulence: theories, observations, and models.* Cambridge: Cambridge University Press.

Berlamont, J., Ockenden, M., Toorman, E. & Winterwerp, J., 1993. The characterisation of cohesive sediment properties. *Coastal Engineering,* Volume 21, pp. 105-128.

Bianchi, T. S., Allison, M. A. & Cai, W.-J., 2014. *Biogeochemical dynamics at major river-coastal interfaces.* New York: Cambridge University Press.

Black, K. S., Tolhurst, T. J., Paterson, D. M. & Hagerthey, S. E., 2002. Working with natural cohesive sediments. *Journal of Hydraulic Engineering,* Volume 128, pp. 2-8.

Bolanos, R., Brown, J. M., Amoudry, L. O. & Souza, A. J., 2013. Tidal, riverine, and wind influences on the circulations of a macrotidal estuary. *Journal of Physical Oceanography,* Volume 43, pp. 29-50.

Bolanos, R., Brown, J. M. & Souza, A. J., 2014. Wave-current interactions in a tide dominated estuary. *Estuarine, Coastal and Shelf Science,* p. DOI: 10.1016/j.csr.2014.05.009.

Bolanos, R., Moate, B. D. & Souza, A. J., 2009. Measuring suspended sediment and its wave and turbulence forcing in the Dee Estuary. *Proceedings of Coastal Dynamics: Impacts of Human Activities on Dynamic Coastal Processes,* pp. 1-12.

Bolanos, R. & Souza, A. J., 2010. Measuring hydrodynamic and sediment transport processes in the Dee Estuary. *Earth System Science Data,* Volume 2, pp. 157-165.

Bowden, K. F., 1955. Some observations of turbulence near the sea bed in a tidal current. *Quarterly journal of the Royal Meteorological Society,* Volume 81, pp. 640-641.

Bowden, K. F., 1967. *Estuaries.* Washington D.C.: American Association for the Advancement of Science.

Bowden, K. F. & Proudman, J., 1949. Observations on the turbulent fluctuations of a tidal current. *Proceedings of the Royal Society of London,* Volume 199, pp. 311-327.

Bowers, D. G., Binding, C. E. & Ellis, K. M., 2007. Satellite remote sensing of the geographical distribution of suspended particle size in an energetic shelf sea. *Estuarine, Coastal and Shelf Science,* Volume 73, pp. 457-466.

Bowers, D. G. & Mitchelson-Jacob, E. G., 1996. Inherent optical properties of the Irish Sea determined from underwater irradiance measurements. *Estuarine, Coastal and Shelf Science,* Volume 43, pp. 433-447.

Bowers, D. & Simpson, J. H., 1987. Mean position of tidal fronts in European-shelf seas. *Continental Shelf Research,* Volume 7, pp. 35-44.

Bowles, P., Burns, R., Hudswell, F. & Whipple, R., 1958. *Sea disposal of low activity effluent.* 2nd Geneva, New York, U.N., pp. 376-389.

Braithwaite, K., Bowers, D., Nimmo-Smith, W. & Graham, G., 2012. Controls on floc growth in an energetic tidal channel. *Journal of Geophysical Research,* 117(C2), pp. 1-12.

Brown, J. M., Bolanos, R. & Souza, A. J., 2013. Process contribution to the time-varying residual circulation in tidally dominated estuarine environments. *Estuaries and Coasts,* pp. 1-17.

Brown, J. M., Bolanos, R. & Souza, A. J., 2014. Controls on the mid-term estuarine residuals: circulation and elevation. *Ocean Dynamics,* p. In Press.

Bruley, D. F., 1965. Predicting vertical film flow characteristics in the entrance region. *AIChE Journal,* Volume 11, pp. 945-950.

Buchan, S., Floodgate, G. D. & Crisp, D. J., 1967. Studies of the seasonal variation of the suspended matter of the Menai Strait I The inorganic fraction. *Limnology and Oceanography,* Volume 12, pp. 419-431.

Bunt, J. A. C., Larcombe, P. & Jago, C. F., 1999. Quantifying the response of optical backscatter devices and transmissometers to variations in suspended particulate matter. *Continental Shelf Research,* Volume 19, pp. 1199-1220.

Burchard, H. et al., 2008. Observational and numerical modelling methods for quantifying coastal ocean turbulence and mixing. *Progress in Oceanography,* Volume 76, pp. 399-442.

Burney, C. M., 1986. Bacterial utilization of total in situ dissolved carbohydrate in offshore waters. *Limnology and Oceanography,* Volume 31, pp. 427-431.

Cameron, W. M. & Pritchard, D. W., 1963. Estuaries. In: M. N. Hill, ed. *The Sea: Ideas and Observations on Progress in the Study of the Seas.* New York: Wiley-Interscience, pp. 306-324.

Cartwright, G. M., Friedrichs, C. T. & Sanford, L. P., 2011. In situ characterization of estuarine suspended sediment in the presence of muddy flocs and pellets. *Coastal Sediments,* pp. 642-655.

Celler, K. et al., 2014. A mass-spring model unveils the morphogenesis of phototrophic Diatoma biofilms (supplementary information). *Nature Scientific Reports,* Volume 4, pp. 1-7.

Chase, R. R. P., 1977. Transport dynamics and kinematic behavior of aquatic particulates. *PhD Thesis, University of Chicago, Chicago.*

Chase, R. R. P., 1979. Settling behavior of natural aquatic particulates. *Limnology and Oceanography,* Volume 24, pp. 417-426.

Clarke, S. & Elliot, A. J., 1998. Modelling Suspended Sediment Concentrations in the Firth of Forth. *Estuarine, Coastal and Shelf Science,* Volume 47, pp. 235-250.

Coriolis, G. G., 1835. Sur les équations du mouvement relatif des systèmes de corps. *Journal De l'Ecole Royale Polytechnique,* Volume 15, pp. 144-154.

Costerton, J. W., 1984. Mechanisms of microbial adhesion to surfaces. Direct ultrastructural examination of adherent bacterial populations in natural and pathogenic ecosystems. In: M. J. Klug & C. A. Reddy, eds. *Current perspectives in microbial ecology, Proceedings of the 3rd international symposium on microbial ecology.* Washington D.C.: American Society for Microbiology, pp. 115-123.

Cross, J., Nimmo-Smith, W., Torres, R. & Hosegood, P. J., 2013. Biological controls on resuspension and the relationship between particle size and the Kolmogorov lengthscale in a shallow coastal sea. *Marine Geology,* Volume 343, pp. 29-38.

Dankers, P. J. T. & Winterwerp, J. C., 2007. Hindered settling of mud flocs: Theory and validation. *Continental Shelf Research,* Volume 27, pp. 1893-1907.

Darwin, C., 1846. *Geological observations on South America: The geology of the voyage of the Beagle under the command of Capt. Fitzroy.* London: R.N., Smith, Elder and Co..

Davies, E. J., Nimmo-Smith, W. A. M., Agrawal, Y. C. & Souza, A. J., 2012. LISST-100 response to large particles. *Marine Geology,* Volume 307-310, pp. 117-122.

Dean, R. G. & Darymple, R. A., 1991. Water wave mechanics for engineers and scientists. *Advanced Series on Ocean Engineering,* Volume 2, p. 353.

Dearnaley, M. P., 1996. Direct measurements of settling velocities in the Owen tube: a comparison with agravimetric analysis. *Journal of Sea Research,* Volume 36, pp. 41-47.

Decho, A. W., 1990. Microbial exopolymer secretions in ocean environments: their role(s) in food webs and marine processes. *Oceanography and Marine Biology Annual Review,* Volume 28, pp. 73-153.

Doodson, A. T., 1921. The Harmonic Development of the Tide-Generating Potential. *Proceedings of the Royal Society of London,* Volume 100, pp. 305-329.

Droppo, I. G., 2000. Filtration in particle size analysis. In: R. A. Meyers, ed. *Encyclopedia of Analytical Chemistry.* Chichester: John Wiley & Sons, Ltd., pp. 5397-5413.

Droppo, I. G., Leppard, G. G., Flannigan, D. T. & Liss, S. N., 1997. The freshwater floc: a functional relationship of water and organic and inorganic floc constituents affecting suspended sediment properties. *Water, Air and Soil Pollution,* Volume 99, pp. 43-54.

Dyer, K., 2001. *Encyclopedia of Ocean Science.* London: Academic Press.

Dyer, K. P., 1986. *Coastal and estuarine sediment dynamics.* Chichester: John Wiley & Sons.

Dyer, K. R. et al., 1996. A comparison of in situ techniques for estuarine floc settling velocity measurements. *Journal of Sea Research,* Volume 36, pp. 15-29.

Dyer, K. R. & Manning, A. J., 1999. Observation of the size, settling velocity and effective density of flocs, and their fractal dimensions. *Journal of Sea Research,* Volume 41, pp. 87-95.

Edelvang, K. & Austen, I., 1997. The temporal variation of flocs and fecal pellets in a tidal channel. *Estuarine, Coastal and Shelf Science,* Volume 44, pp. 361-367.

Edzwald, J. K. & O'Melia, C. R., 1975. Clay distributions in recent estuarine sediments. *Clays and Clay Minerals,* Volume 23, pp. 39-44.

Eggleston, D. B., Armstrong, D. A., Ellis, W. E. & Patton, W. S., 1998. Estuarine fronts as conduits for larval transport: Hydrodynamics and the spatial distribution of Dungeness crab postlarvae. *Marine Ecology Progress Series,* Volume 164, pp. 73-82.

Einstein, A., 1905. Uber die von der molekularkinetischen Theorie der Warme geforderte Bewegung von in ruhenden Flussigkeiten suspendierten Teilchen. *Annalen der Physik,* Volume 17, pp. 549-560.

Eisma, D., 1986. Flocculation and de-flocculation of suspended matter in estuaries. *Netherlands Journal of Sea Research,* Volume 20, pp. 183-199.

Eisma, D. et al., 1991. Suspended-matter particle size in some west-European estuaries; Part 1: Particle-size distribution. *Netherlands Journal of Sea Research,* Volume 28, pp. 193-214.

Engel, A. et al., 2004. Polysaccharide aggregation as a potential sink of marine dissolved organic carbon. *Letters to Nature,* Volume 428, pp. 929-932.

Environment Agency, 2009. *Water for life and livelihoods: River Basin Management Plan Dee River Basin District.* Bristol: Environment Agency.

Essink, K. & Bos, A. H., 1985. Growth of three bivalve molluscs transplanted along the axis of the Ems estuary. *Netherlands Journal of Sea Research,* Volume 19, pp. 45-51.

Fairbanks, R. G., 1989. A 17,000-year glacio-eustatic sea level record: influence of glacial melting rates on the Younger Dryas event and deep-ocean circulation. *Nature,* Volume 342, pp. 637-642.

Feddersen, F., Trowbridge, J. H. & Williams, A. J. 3., 2006. Vertical Structure of Dissipation in the Nearshore. *Journal of Physical Oceanography,* Volume 37, pp. 1764-1777.

Fennessy, M. J., Dyer, K. R. & Huntley, D. A., 1994. Size and settling velocity distributions of flocs in the Tamar estuary during a tidal cycle. *Netherlands Journal of Aquatic Ecology,* Volume 28, pp. 275-282.

Fitzpatrick, C. S. B., Fradin, E. & Gregory, J., 2004. Temperature effects on flocculation using different coagulants. *Water, Science and Technology,* Volume 50, pp. 171-175.

Fleming, J., 1818. Observations on the junction of fresh water of rivers with the salt water of the sea. *Transactions of the Royal Society Edinburgh,* Volume 8, pp. 507-513.

Flesch, J. C., Spicer, P. T. & Pratsinis, S. E., 1999. Laminar and turbulent shear-induced flocculation of fractal aggregates. *Materials, Interfaces and Electrochemical Phonomena,* Volume 45, pp. 1114-1124.

Friedrichs, C. T., Cartwright, G. M. & Dickhudt, P. J., 2008. Quantifying benthic exchange of fine sediment via continuous, noninvasive measurements of settling velocity and bed erodability. *Oceanography,* Volume 21, pp. 168-172.

Fryirs, K. A. & Brierley, G. J., 2013. *Geomorphic analysis of river systems.* Chichester: Wiley & Sons.

Fugate, D. C. & Friedrichs, C. T., 2002. Determining concentration and fall velocity of estuarine particle populations using ADV, OBS and LISST. *Continental Shelf Research,* Volume 22, pp. 1867-1886.

Fugate, D. C. & Friedrichs, C. T., 2003. Controls on suspended aggregate size in partially mixed estuaries. *Estuarine, Coastal and Shelf Science,* Volume 58, pp. 389-404.

Fugate, D. C., Friedrichs, C. T. & Sanford, L. P., 2007. Lateral dynamics and associated transport of sediment in the upper reaches of a partially mixed estuary, Chesapeake Bay, USA. *Continental Shelf Research,* Volume 27, pp. 679-698.

Garcia-Soto, C. & Pingree, R. D., 2009. Spring and summer blooms of phytoplankton (SwaWiFS/MODIS) along a ferry line in the Bay of Biscay and western English Channel. *Continental Shelf Research,* Volume 29, pp. 1111-1122.

Gargett, A. E., 1988. A ‘‘large-eddy’’ approach to acoustic remote sensing of turbulence kinetic energy dissipation rate ε. *Atmosphere–Ocean,* Volume 26, pp. 483-508.

Gargett, A. E., 1994. Observing turbulence with a modified acoustic Doppler current profiler. *Journal of Atmospheric and Oceanic Technology,* Volume 11, pp. 1592-1610.

Gartner, J. W., Cheng, R. T., Wang, P.-F. & Richter, K., 2001. Laboratory and field evaluations of the LISST-100 instrument for suspended particle size determinations. *Marine Geology,* Volume 175, pp. 199-219.

Geyer, W. R., 2010. Estuarine salinity structure and circulation. In: *Contemporary issues in estuarine physics, transport and water quality.* New York: Cambridge University Press, pp. 12-26.

Geyer, W. R., Hill, P. S. & Kineke, G. C., 2004. The transport, transformation and dispersal of sediment by buoyant coastal flows. *Continental Shelf Research,* Volume 24, pp. 927-949.

Gibbs, R. J., 1985. Estuarine flocs: their size, settling velocity and density. *Journal of Geophysical Research,* Volume 90, pp. 3249-3251.

Gibbs, R. J., Tshudy, D. M., Konwar, L. & Martin, J. M., 1989. Coagulation and transport of sediments in the Gironde estuary. *Sedimentology,* Volume 36, pp. 987-999.

Giddings, S. N., Fong, D. A. & Monismith, S. G., 2011. Role of straining and advection in the intratidal evolution of stratification, vertical mixing, and longitudinal dispersion of a shallow, macrotidal, salt wedge estuary. *Journal of Geophysical Research,* Volume 116, p. C03003.

Gitelson, A. A., Buschmann, C. & Lichtenthaler, H. K., 1999. The chlorophyll fluorescence ratio F735/F700 as an accurate measure of the chlorophyll content in plants. *Remote Sensing of Environment,* Volume 3, pp. 296-302.

Godin, G., 1972. *The Analysis of Tides.* Toronto: Toronto Press.

Graf, G. et al., 1982. Benthic Response to Sedimentation of a Spring Phytoplankton Bloom: Process and Budget. *Marine Biology,* Volume 67, pp. 201-208.

Graf, W. H., 1971. *Hydraulics of sediment transport.* New York: McGraw-Hill.

Graham, G. W. & Nimmo-Smith, W. A. M., 2010. The application of holography to the analysis of size and settling velocity of suspended cohesive sediments. *Limnology and Oceanography Methods,* Volume 8, pp. 1-15.

Gratiot, N. & Manning, A. J., 2007. A laboratory study of dilute suspension mud floc characteristics in an oscillatory diffusive turbulent flow. *Journal of Coastal Research,* Volume 50, pp. 1142-1146.

Greenwood, N. et al., 2011. Spatial and temporal variability in nutrient concentrations in Liverpool Bay, a temperate latitude region of freshwater influence. *Ocean Dynamics,* Volume 61, pp. 2181-2199.

Gregory, J., 1997. The density of particle aggregates. *Water Science and Technology,* Volume 36, pp. 1-13.

Gross, T. F. & Dade, W. B., 1991. Suspended sediment storm modeling. *Marine Geology,* Volume 99, pp. 343-360.

Gross, T. F. & Nowell, A. R. M., 1983. Mean flow and turbulence scaling in a tidal boundary layer. *Continental Shelf Research,* Volume 2, pp. 109-126.

Grove, K. G., 1914. *The transportation of debris by running water.* Washington: Government Printing Office.

Gust, G. & Walger, E., 1976. The influence of suspended cohesive sediments on boundary-layer structure and erosive activity of turbulent seawater flow. *Marine Geology,* Volume 22, pp. 189-206.

Hallermeier, R. J., 1981. Terminal settling velocity of commonly occurring sand grains. *Sedimentology,* Volume 28, pp. 859-865.

Hannah, C. G. & Wright, D. G., 1995. Depth dependent analytical and numerical solutions for wind-driven flow in the coastal ocean. *Coastal and Estuarine Studies,* Volume 47, pp. 125-152.

Hansen, D. V. & Rattray, M., 1965. Gravitational circulation in straits and estuaries. *Journal of Marine Research,* Volume 23, pp. 104-122.

Hansen, D. V. & Rattray, M., 1966. New dimensions in estuary classification. *Limnology & Oceanography,* Volume 11, pp. 319-326.

Hanson, A. & Cleasby, J., 1990. The effects of temperature on turbulent flocculation: Fluid dynamics and chemistry. *Journal of the American Water Works Association,* Volume 82, pp. 56-72.

Harland, B. J., Taylor, D. & Wither, A., 2000. The distribution of mercury and other trace metals in the sediments of the Mersey Estuary over 25 years 1974-1998. *The Science of the Total Environment,* Volume 253, pp. 45-62.

Hayter, E. J., 1983. *Prediction of cohesive sediment movements in estuarial waters.* Ph.D Thesis: University of Florida.

Hayter, E. J. & Mehta, A. J., 1986. Modelling cohesive sediment transport in estuarial waters. *Applied Mathematical Modelling,* Volume 10, pp. 294-303.

Hearn, C. J., 2008. *The dynamics of coastal models.* New York: Cambridge University Press.

Heip, C. H. R. et al., 1995. Production and consumption of biological particles in temperate tidal estuaries. *Oceanography and Marine Biology an Annual Review,* Volume 33, pp. 1-150.

Hill, P. S., Syvitski, J. P., Cowan, E. A. & Powell, R. D., 1998. In situ observations of floc settling velocities in Glacier Bay, Alaska. *Marine Geology,* Volume 145, pp. 85-94.

Hill, P. S., Voulgaris, G. & Trowbridge, J. H., 2001. Controls on floc size in a continental shelf bottom boundary layer. *Journal of Geophysical Research,* Volume 106, pp. 9543-9549.

Hoitink, A. J. F., Hoekstra, P. & van Maren, D. S., 2003. Flow asymmetry associated with astonomical tides: Implications for the residual transport of sediments. *Journal of Geophysical Research,* Volume 108, pp. 13-1 - 13-8.

Holland, A. F., Zingmark, R. G. & Dean, J. M., 1974. Quantitative evidence concerning the stabilization of sediments by marine benthic diatoms. *Marine Biology,* Volume 27, pp. 191-196.

Holt, J., Icarus Allen, J., Proctor, R. & Gilbert, F., 2005. Error quantification of a high-resolution coupled hydrodynamic-ecosystem coastal-ocean model: Part 1 model overview and assessment of the hydrodynamics. *Journal of Marine Systems,* Volume 57, pp. 167-188.

Holt, J. & Umlauf, L., 2008. Modelling the tidal mixing fronts and seasonal stratification of the Northwest European Continental Shelf. *Continental Shelf Research,* Volume 28, pp. 887-903.

Hopkins, J. & Polton, J. A., 2012. Scales and structure of frontal adjustment and freshwater export in a region of freshwater influence. *Ocean Dynamics,* Volume 62, pp. 45-62.

Howarth, J., 1998. The effect of stratification on tidal current profiles. *Continental Shelf Research,* Volume 18, pp. 1235-1254.

Howarth, M. J. & Souza, A. J., 2005. Reynolds stress observations in continental shelf seas. *Deep-Sea Research II,* Volume 52, pp. 1075-1086.

Huang, J., Hilldale, R. C. & Greimann, B. P., 2006. Cohesive sediment transport. In: *Erosion and sedimentation manual.* Denver, Colorado: Bureau of Reclamation, pp. 4-1 - 4-46.

Huijts, K. M. H., Schuttelaars, H. M., de Swart, H. E. & Valle-Levison, A., 2006. Lateral entrapment of sediment in tidal estuaries: An idealized model study. *Journal of Geophysical Research,* Volume 111, p. C12016.

Huschke, R. E., 1959. *Glossary of meteorology.* Boston, USA: American Meteorological Society.

Hutchinson, S. M., 1994. Cs in saltmarsh sediments in the Dee Estuary. *Marine Pollution Bulletin,* Volume 28, pp. 262-265.

Hutchinson, S. M. & Prandle, D., 1994. Siltation in the saltmarsh of the Dee Estuary derived from 137Cs analysis of shallow cores. *Estuarine, Coastal and Shelf Science,* Volume 38, pp. 471-478.

Islam, M. R. & Chaudry, M. H., 1997. Numerical solution of transport equation for applications in environmental hydraulics and hydrology. *Journal of Hydrology,* Volume 191, pp. 106-121.

Ives, K. J., 1977. *The scientific basis of flocculation.* Alphen aan den Rijn, The Netherlands: Sijthoff & Noordhoff.

Jago, C. F. et al., 1993. Resuspension processes and seston dynamics, southern North Sea. *Philosophical Transactions of the Royal Society London,* Volume 343, pp. 475-491.

Jago, C. F. & Bull, C. F. J., 2000. Quantification of errors in transmissometer-derived concentration of suspended particulate matter in the coastal zone: implications for flux determinations. *Marine Geology,* Volume 169, pp. 273-286.

Jago, C. F. & Jones, S. E., 1998. Observation and modelling of the dynamics of benthic fluff resuspended from a sandy bed in the southern North Sea. *Continental Shelf Research,* Volume 18, pp. 1255-1282.

Jago, C. F. & Jones, S. E., 2002. Diagnostic criteria for reconstruction of tidal continental shelf regimes: changing the paradigm. *Marine Geology,* Volume 191, pp. 95-117.

Jago, C. F. et al., 2002. Resuspension of benthic fluff by tidal currents in deep stratified waters, northern North Sea. *Journal of Sea Research,* Volume 48, pp. 259-269.

Jago, C. F., Jones, S. E., Sykes, P. & Rippeth, T., 2006. Temporal variation of suspended particulate matter and turbulence in a high energy, tide-stirred, coastal sea: Relative contributions of resuspension and disaggregation. *Continental Shelf Research,* Volume 26, pp. 2019-2028.

Jago, C. F., Kennaway, G. M., Novarino, G. & Jones, S. E., 2007. Size and settling velocity of suspended flocs during a Phaeocystis bloom in the tidally stirred Irish Sea, NW European shelf. *Marine Ecology Progress Series,* Volume 345, pp. 51-62.

Jerlov, N. G., 1976. *Marine Optics.* Amsterdam: Elsevier.

Johnson, C. P., Li, X. & Logan, B. E., 1996. Settling velocities of fractal aggregates. *Environmental Science and Technology,* Volume 30, pp. 1911-1918.

Jones, N. L. & Monismith, S. G., 2008a. The Influence of Whitecapping Waves on the Vertical Structure of Turbulence in a Shallow Estuarine Embayment. *Journal of Physical Oceanography,* Volume 38, pp. 1563-1580.

Jones, N. L. & Monismith, S. G., 2008b. Modeling of the influence of wave-enhanced turbulence in a shallow tide- and wind-driven water column. *Journal of Geophysical Research,* Volume 113, p. C03009.

Jones, S. E. et al., 1998. Aggregation and resuspension of suspended particulate matter at a seasonally stratified site in the southern North Sea: physical and biological controls. *Continental Shelf Research,* Volume 18, pp. 1283-1309.

Junk, W. J., Bayley, P. B. & Sparks, R. E., 1989. The flood pulse concept in river-floodplain systems. *Special Publications in Fish and Aquatic Science,* Volume 106, pp. 110-127.

Kac, M., 1947. Random walk and the theory of Brownian motion. *The American Mathematical Monthly,* Volume 54, pp. 369-391.

Kajihara, M., 1971. Settling velocity and porosity of large suspended particles. *Journal of the Oceanographical Society of Japan,* Volume 27, pp. 158-162.

Karleskint Jr, G., Turner, R. & Small Jr, J. W., 2006. *Introduction to Marine Biology.* Belmont, Canada: Brooks/Cole.

Khorsandi, B., Mydlarski, L. & Gaskin, S., 2012. Noise in turbulence measurements using acoustic Doppler velocimetry. *Journal of Hydraulic Engineering,* Volume 138, pp. 829-838.

Kolmogorov, A. N., 1991. The local structure of turbulence in incompressible viscous fluid for very large Reynolds numbers. *Proceedings of the Royal Society of London,* Volume 434, pp. 9-13.

Kranck, K. & Milligan, T., 1988. Macroflocs from diatoms - in situ photography of particles in Bedford basin, Nova-Scotia. *Marine Ecology Progress Series,* Volume 44, pp. 183-189.

Kranenberg, C., 1994. On the fractal structure of cohesive sediment aggregates. *Estuarine, Coastal and Shelf Science,* Volume 39, pp. 451-460.

Krivtsov, V., Howarth, M. J. & Jones, S. E., 2009. Characterising observed patterns of suspended particulate matter and relationships with oceanographic and meteorological variables: Studies in Liverpool Bay. *Environmental Modelling & Software,* Volume 24, pp. 677-685.

Krivtsov, V. et al., 2008. Monitoring and modelling of the Irish Sea and Liverpool Bay: An overview and an SPM case study. *Ecological Modelling,* Volume 212, pp. 37-52.

Krivtsov, V., Sigee, D. C. & Bellinger, E. G., 2001. A one-year study of the Rostherne Mere ecosystem: seasonal dynamics of water chemistry, plankton, internal nutrient release, and implications for long-term trophic status and overall functioning of the lake. *Hydrological Processes,* Volume 15, pp. 1489-1506.

Krone, R. B., 1962. *Flume studies in the transport of sediment in estuarine shoaling processes.* Berkeley: University of California.

Kusters, K. A., Wijers, J. G. & Thoenes, D., 1997. Aggregation kinetics of small particles in agitated vessels. *Chemical Engineering Science,* Volume 52, pp. 107-121.

Lambert, A., 1988. Regulation of the River Dee. *Regulated Rivers Research and Management,* Volume 2, pp. 293-308.

Lavelle, J. W. & Mofjeld, H. O., 1987. Do critical stresses for incipient motion and erosion really exist?. *Journal of Hydraulic Engineering,* Volume 113, pp. 370-385.

Lavelle, J. W., Mofjeld, H. O. & Baker, E. T., 1984. An in situ erosion rate for a fine-grained marine sediment. *Journal of Geophysical Research,* Volume 89, pp. 6543-6552.

Leng, M. J. & Swann, G. E. A., 2010. Stable isotopes in diatom silica. In: J. P. Smol & E. F. Stoermer, eds. *The diatoms: applications for the environmental and earth sciences.* Cambridge, UK: Cambridge University Press, pp. 127-143.

Lesourd, S. et al., 2001. Morphosedimentary Evolution of the Macrotidal Seine Estuary Subjected to Human Impact. *Estuaries,* Volume 24, pp. 940-949.

Lick, W., Huang, H. & Jepsen, R., 1993. Flocculation of fine-grained sediments due to differential settling. *Journal of Geophysical Research,* Volume 98, pp. 279-288.

Li, D.-H. & Ganczarczyk, J., 1987. Stroboscopic determination of settling velocity, size and porosity of activated sludge flocs. *Water Research,* Volume 21, pp. 257-262.

Lim-Seok, K. & Cleasby, J. L., 1995. Temperature effects on flocculation kinetics using FE(III) coagulant. *Journal of Environmental Engineering,* Volume 121, pp. 893-901.

Li, M. Z. & Amos, C. L., 2001. SEDTRANS96: the upgraded and better calibrated sediment-transport model for continental shelves. *Computers and Geosciences,* Volume 27, pp. 619-645.

Lindahl, M. T., 1983. Drag reduction by polymer additions in the northern intertidal: Seasonal factors controlling erosion and deposition - a review. *Canadian Journal of Fish and Aquatic Science,* Volume 40, pp. 143-159.

Linden, P. F. & Simpson, J. E., 1988. Modulated mixing and frontogenesis in shallow seas and estuaries. *Continental Shelf Research,* Volume 8, pp. 1107-1127.

Lindsay, P., Balls, P. W. & West, J. R., 1996. Influence of Tidal Range and River Discharge on Suspended Particulate Matter Fluxes in the Forth Estuary (Scotland). *Estuarine, Coastal and Shelf Science,* Volume 42, pp. 63-82.

Lintern, D. G., 2003. *Influences of flocculation on bed form properties for fine-grained cohesive sediment.* Ph.D Thesis: Oxford University.

Liu, Z., 2001. *Sediment Transport.* Havnebygning: Aalborg Universitet.

Lohrmann, A., Hackett, B. & Roed, L. P., 1990. High resolution measurements of turbulence, velocity and stress using a pulse to-pulse coherent sonar. *Journal of Atmospheric and Oceanic Technology,* Volume 7, pp. 19-37.

Lorenzen, C. J., 1966. A method for the continuous measurement of in vivo chlorophyll concentration. *Deep-Sea Research,* Volume 13, pp. 223-227.

Lorke, A. & Wüest, A., 2005. Application of Coherant ADCP for Turbulence Measurements in the Bottom Boundary Layer. *Journal of Atmospheric and Oceanic Technology,* Volume 22, pp. 1821-1828.

Lu, Y. & Lueck, R. G., 1999. Using a Broadband ADCP in a Tidal Channel. Part II: Turbulence. *Journal of Atmospheric and Oceanic Technology,* Volume 16, pp. 1568-1579.

Maa, J. P.-Y. & Kwon, J.-I., 2007. Using ADV for cohesive sediment settling velocity measurements. *Estuarine, Coastal and Shelf Science,* Volume 73, pp. 351-354.

MacIntyre, S., Alldredge, A. L. & Gotschalk, C. C., 1995. Accumulation of marine snow at density discontinuities in the water column. *Limnology and Oceanography,* Volume 40, pp. 449-468.

Maerz, J. & Wirtz, K., 2009. Resolving physically and biologically driven suspended particulate matter dynamics in a tidal basin with a distribution-based model. *Estuarine, Coastal and Shelf Science,* Volume 84, pp. 128-138.

Maggi, F., Manning, A. J. & Winterwerp, J. C., 2006. Image separation and geometric characterisation of mud flocs. *Journal of Hydrology,* Volume 326, pp. 325-348.

Maggi, F., Mietta, F. & Winterwerp, J. C., 2007. Effect of variable fractal dimension on the floc size distribution of suspended cohesive sediment. *Journal of Hydrology,* Volume 343, pp. 43-55.

Manning, A. J., 2004. The observed effects of turbulence on estuarine flocculation. *Journal of Coastal Research,* Volume 41, pp. 90-104.

Manning, A. J., 2006. *LabSFLOC - a laboratory system to determine the spectral characteristics of flocculating cohesive sediment.* Wallingford, UK: HR Wallingford Technical Report TN156.

Manning, A. J. & Bass, S. J., 2006. Variability in cohesive sediment settling fluxes: Observations under different estuarine tidal conditions. *Marine Geology,* Volume 235, pp. 177-192.

Manning, A. J., Bass, S. J. & Dyer, K. R., 2006. Floc properties in the turbidity maximum of a mesotidal estuary during neap and spring tidal conditions. *Marine Geology,* Volume 235, pp. 193-211.

Manning, A. J. et al., 2011. Cohesive sediment flocculation and the application to settling flux modelling. In: S. S. Ginsberg, ed. *Sediment Transport.* Rijeka, Croatia: Intech, pp. p91-116.

Manning, A. J. & Dyer, K., 2002. The use of optics for the in-situ determination of flocculated mud characteristics. *Journal of Optics A: Pure and Applied Optics,* Volume 4, pp. 71-81.

Manning, A. J., Langston, W. J. & Jonas, P. J. C., 2010. A review of sediment dynamics in the Severn Estuary: Influence of flocculation. *Marine Pollution Bulletin,* Volume 61, pp. 37-51.

Marker, M. E., 1967. The Dee Estuary – its progressive silting and salt marsh development. *Transactions of the Institute of British Geographers,* Volume 41, pp. 65-71.

Martino, M., Turner, A., Nimmo, M. & Millward, G. E., 2002. Resuspension, reactivity and recycling of trace metals in the Mersey Estuary, UK. *Marine Chemistry,* Volume 77, pp. 171-186.

McAnally, W., 1999. Aggregation and deposition of estuarine sediment. *Ph.D Thesis, University of Florida, USA.*

McAnally, W. H. et al., 2007. Management of fluid mud in estuaries, bays, and lakes. I: Present state of understanding on character and behavior. *Journal of Hydraulic Engineering,* Volume 133, pp. 9-22.

McGranaham, D. A., Balk, D. & Anderson, B., 2007. The Rising Tide: Assessing the risks of climate change and human settlements in low elevation coastal zones. *Environment and urbanization,* Volume 19, pp. 17-37.

McLusky, D. S. & Elliott, M., 2004. *The Estuarine Ecosystem: Ecology, Threats and Management.* New York: Oxford University Press.

Meakin, P., 1989. *Simulations of aggregation processes, the fractal approach the heterogeneous chemistry.* New York: John Wiley & Sons.

Mehta, A. J., 1986. Characterization of cohesive sediment properties and transport processes in estuaries. *Estuarine Cohesive Sediment Dynamics,* Volume 14, pp. 290-325.

Mehta, A. J., 1988. *Physical Processes in Estuaries.* Berlin: Springer-Verlag.

Mehta, A. J. & Partheniades, E., 1982. Resuspension of deposited cohesive sediment beds. *Coastal Engineering Proceedings,* Volume 1, pp. 1569-1588.

Meral, R., 2008. Laboratory Evaluation of Acoustic Backscatter and LISST Methods for Measurements of Suspended Sediments. *Sensors,* Volume 8, pp. 979-993.

Meyer-Peter, E. & Mueller, R., 1948. *Formulas for bed-load transport.* Stockholm, Sweden, Proceedings of the international association of hydraulic research, 2nd congress.

Mikkelsen, O. A., Hill, P. S., Milligan, T. G. & Chant, R. J., 2005. In situ particle size distributions and volume concentrations from a LISST-100 laser particle sizer and a digital floc camera. *Continental Shelf Research,* Volume 25, pp. 1959-1978.

Mikkelsen, O. A. et al., 2008. The influence of schlieren on in situ optical measurements used for particle characterization. *Limnology & Oceanography Methods,* Volume 6, pp. 133-143.

Mikkelsen, O. A. & Pejrup, M., 2000. In situ particle size spectra and density of particle aggregates in a dredging plume. *Marine Geology,* Volume 170, pp. 443-459.

Mikkelsen, O. A. & Perjup, M., 2001. The use of a LISST-100 laser particle sizer for in-situ estimates of floc size, density and settling velocity. *Geo-Marine Letters,* Volume 20, pp. 187-195.

Milligan, T. G. & Hill, P. S., 1998. A laboratory assessment of the relative importance of turbulence, particle composition, and concentration in limiting maximal floc size and settling behavior. *Journal of Sea Research,* Volume 39, pp. 227-241.

Mirlean, N., Andrus, V. E. & Baisch, P., 2003. Mercury pollution sources in sediments of Patos Lagoon Estuary, Southern Brazil. *Marine Pollution Bulletin,* Volume 46, pp. 331-334.

Mitchener, H. & Torfs, H., 1996. Erosion of mud / sand mixtures. *Coastal Engineering,* Volume 29, pp. 1-25.

Moore, R. D., 2009. Hydrodynamic and morphometric modelling of a macro-tidal estuary: the Dee Estuary of NW England. *Ph.D Thesis, Univeristy of Liverpool, UK.*

Moore, R. D., Wolf, J., Souza, A. J. & Flint, S. S., 2009. Morphological evolution of the Dee Estuary, Eastern Irish Sea, UK: A tidal asymmetry approach. *Geomorphology,* Volume 103, pp. 588-596.

Nagano, T., Yanase, N., Tsuduki, K. & Nagao, S., 2003. Particulate and dissolved elemental loads in the Kuji River related to discharge rate. *Environmental International,* Volume 28, pp. 649-658.

Neumann, A. C., Gebelein, C. D. & Scoffin, G. P., 1970. The composition, structure, and erodability of sub-tidal mats, Abaco, Bahamas. *Journal of Sedimentary Petrology,* Volume 40, pp. 274-297.

Newton, I., 1687. Philosophiæ Naturalis Principia Mathematica. In: *De mundi systemate.* London: Philosophical Transactions of the Royal Society.

Nikuradse, J., 1932. Gesetzmassigkeiten der turbulenten Stromung in glatten Rohren: mit 9 Zahlentafeln. *VDI-Verlag.*

Nikuradse, J., 1933. Stromungsgestze in rauhen Rohren.

Osborn, T. R. & Crawford, W. R., 1980. An Airfoil Probe for Measuring Turbulent Velocity Fluctuations in Water. In: F. Dobson, L. Hasse & R. Davis, eds. *Air–Sea Interactions: Instruments and Methods.* New York, USA: Plenum Press, pp. 369-386.

Oseen, C., 1927. *Hydrodynamik.* Leipzig: Akademische Verlagsgesellschaft.

Paintal, A. S., 1971. Concept of critical shear stress in loose boundary open channels. *Journal of Hydraulic Research,* Volume 9, pp. 91-113.

Parchure, T. M. & Mehta, A. J., 1995. Erosion of soft cohesive sediment deposits. *Journal of Hydraulic Engineering,* Volume 11, pp. 1308-1326.

Parker, D. S., Kaufman, W. J. & Jenkins, D., 1972. Floc breakup in turbulent flocculation processes. *Journal of the Sanitary Engineering Division,* 98(1), pp. 79-99.

Patchineelam, S. M. & Kjerfve, B., 2004. Suspended sediment variability on seasonal and tidal time scales in the Winyah Bay estuary, South Carolina, USA. *Estuarine, coastal and shelf science,* Volume 59, pp. 307-318.

Paterson, D. M., 1989. Short-term changes in the erodibility of intertidal cohesive sediments related to the migratory behavior of epipelic diatoms. *Limnology and Oceanography,* Volume 34, pp. 223-234.

Pawlowicz, R., Beardsley, B. & Lentz, S., 2002. Classical tidal harmonic analysis including error estimates in MATLAB using T_Tide. *Computers and Geosciences,* Volume 28, pp. 929-937.

Prandle, D., 1982. The vertical structure of tidal currents and other oscillatory flows. *Continental Shelf Research,* Volume 1, pp. 191-207.

Prandle, D., Lane, A. & Souza, A. J., 2011. Coastal Circulation in Treatise on Estuarine and Coastal Science. In: E. Wolanski & D. McLusky, eds. Oxford: Elsevier, pp. 237-266.

Pritchard, D. W., 1952. Advances in Geophysics. In: *Estuarine hydrography.* New York: Academic Press, pp. 243-280.

Pritchard, D. W., 1954. A study of the salt balance in a coastal plain estuary. *Journal of Marine Research,* Volume 13, pp. 133-144.

Pritchard, D. W., 1956. The dynamic structure of a coastal plain estuary. *Journal of Marine Research,* Volume 15, pp. 33-42.

Proudman, J., 1928. On a general expansion in the theory of the tides. *London Mathematical Society,* Volume 29, pp. 527-536.

Pugh, D. T., 1987. *Tides, surges and mean sea-level: a handbook for engineers and scientists.* Chichester: Wiley.

Pye, K., 1996. Estuarine shores: evolution, environments and human alterations. In: K. F. Nordstrom & C. T. Roman, eds. *Evolution of the shoreline of the Dee Estuary, United Kingdom.* New York: Wiley, pp. 14-37.

Ralston, D. K. & Geyer, W. R., 2009. Episodic and long-term sediment transport capacity in the Hudson river estuary. *Estuaries and Coasts,* Volume 32, pp. 1130-1151.

Ramirez-Mendoza, R., Souza, A. J. & Amoudry, L. O., 2014. Flocculation in Hypertidal Estuaries. *Ocean Dynamics,* Volume January, pp. 1-13.

RDI, 1996. Acoustic Doppler Current Profiler: Principles of Operation, A Practical Primer. *Second Edition.*

Reynolds, O., 1883. An experimental investigation of the circumstances which determine whether the motion of water shall be direct or sinuous, and the law of resistance in parallel channels. *Philosophical Transactions of the Royal Society,* Volume 174, pp. 935-982.

Rhoads, D. C. & Boyer, L. F., 1982. *Animal sediment relations: the biogenic alteration of sediments.* New York: Plenum Press.

Richard, J.-B., Thomson, J., Polagye, B. & Bard, J., 2013. Method for identification of Doppler noise levels in turbulent flow measurements dedicated to tidal energy. *International Journal of Marine Energy,* Volume 3, pp. 52-64.

Ridgway, J. & Shimmield, G., 2002. Estuaries as repositories of historical contamination and their impact on shelf seas. *Estuarine, Coastal and Shelf Science,* Volume 55, pp. 903-928.

Riemann, F., 1989. Gelatinous phytoplankton detritus aggregates on the Atlantic deep-sea bed. *Marine Biology,* Volume 100, pp. 533-540.

Rippeth, T. P., Williams, E. & Simpson, J. H., 2002. Reynolds stress and turbulent energy production in a tidal channel. *Journal of Physical Oceanography,* Volume 32, pp. 1242-1251.

Rosen, M. W. & Cornford, N. E., 1971. Fluid friction of fish slimes. *Nature,* Volume 234, pp. 49-51.

Ross, M. A. & Mehta, A. J., 1989. On the mechanics of lutoclines and fluid mud. *Journal of Coastal Research,* Volume 5, pp. 51-61.

Sahin, C., 2014. Investigation of the variability of floc sizes on the Louisiana Shelf using acoustic estimates of cohesive sediment properties. *Marine Geology,* Volume 353, pp. 55-64.

Sanford, L. P., 1994. Wave-forced resuspension of upper Chesapeake bay muds. *Estuaries,* Volume 17, pp. 148-165.

Sanford, L. P., 2008. Modelling a dynamically varying mixed sediment bed with erosion, deposition, bioturbation, consolidation, and armoring. *Computers & Geoscience,* Volume 34, pp. 1263-1283.

Sanford, L. P. & Halka, J. P., 1993. Assessing the paradigm of mutually exclusive erosion and deposition of mud, with examples from upper Chesapeake Bay. *Marine Geology,* Volume 114, pp. 37-57.

Sanford, L. P., Panageotou, W. & Halka, J. P., 1991. Tidal resuspensions of sediments in northern Chesapeake Bay. *Marine Geology,* Volume 97, pp. 87-103.

Sanford, L. P., Suttles, S. E. & Halka, J. P., 2001. Reconsidering the physics of the Chesapeake Bay estuarine turbidity maximum. *Estuaries,* Volume 24, pp. 655-669.

Schiller, L. & Naumann, A., 1933. Uber die grundlegenden Berechnungen bei der Schwerkraft Aufbereitung. *Z. VDI,* Volume 77.

Sfriso, A., Marcomini, A. & Zanette, M., 1995. Heavy Metals in Sediments, SPM and Phytozoobenthos of the Lagoon of Venice. *Marine Pollution Bulletin,* Volume 30, pp. 116-124.

Sherman, D. J. & Greenwood, B., 1984. Boundary roughness and bedforms in the surf zone. *Marine Geology,* Volume 60, pp. 199-218.

Simpson, J. H., Brown, J., Matthews, J. & Allen, G., 1990. Tidal straining, density currents and stirring in the control of estuarine stratification. *Estuaries,* Volume 13, pp. 125-132.

Simpson, J. H., Fisher, N. R. & Wiles, P., 2004. Reynolds stress and TKE production in an estuary with a tidal bore. *Estuary, Coastal and Shelf Science,* Volume 60, pp. 619-627.

Simpson, J. H. & Hunter, J. R., 1974. Fronts in the Irish Sea. *Nature,* Volume 250, pp. 404-406.

Simpson, J. H. & Souza, A. J., 1995. Semidiurnal switching of stratification in the region of freshwater influence of the Rhine. *Journal of Geophysical Research,* 100(C4), pp. 7037-7044.

Smith, S. J. & Friedrichs, C. T., 2011. Size and settling velocities of cohesive flocs and suspended sediment aggregates in a trailing suction hopper dredge plume. *Continental Shelf Research,* Volume 31, pp. 50-63.

Smyth, W. D. & Moum, J. N., 2000a. *Ocean Turbulence, College of Oceanic & Atmospheric Processes.* Corvallis: Oregon State University.

Smyth, W. D. & Moum, J. N., 2000b. Anisotropy of turbulence in stably stratified mixing layers. *Physics of Fluids,* Volume 12, pp. 1343-1362.

Sollas, W. J., 1883. The Estuaries of the Severn and its Tributaries; an Inquiry into the Nature and Origin of their Tidal Sediment and Alluvial Flats. *Quarterly Journal of the Geological Society,* Volume 39, pp. 611-626.

Soulsby, R., 1997. *Dynamics of Marine Sands.* UK: Thomas Telford Publishing.

Soulsby, R. L., 2000. *Methods for predicting suspensions of mud.* Wallingford: HR Wallingford Report TR104.

Soulsby, R. L. & Wainwright, B. L. S. A., 1987. A criterion for the effect of suspended sediment on near-bottom velocity profiles. *Journal of Hydraulic Research,* Volume 25, pp. 341-356.

Souza, A. J., 2007. The use of ADCPs to measure turbulence and SPM in shelf seas. *2nd International Conference & Exhibition on Underwater Acoustic Measurements: Technologies & Results.*

Souza, A. J., 2013. On the use of the Strouhal/Stokes number to explain the dynamics and water column structure on shelf seas. *Ocean Science,* Volume 9, pp. 391-398.

Souza, A. J., Alvarez, L. G. & Dickey, T. D., 2004. Tidally induced turbulence and suspended sediment. *Geophysical Research Letters,* Volume 31, p. L20309.

Souza, A. J. et al., 2012. *Coupled Coastal Wind, Wave and Current Dynamics.* Cambridge: Cambridge University Press.

Souza, A. J., Dickey, T. D. & Chang, G. C., 2001. Modeling water column structure and suspended particulate matter on the Middle Atlantic continental shelf during the passages of Hurricanes Edouard and Hortense. *Journal of Marine Research,* Volume 59, pp. 1021-1045.

Souza, A. J. & Friedrichs, C. T., 2005. *Near-bottom boundary layers, Marine Turbulence: Theories, Observations, and Models.* Cambridge: Cambridge University Press.

Souza, A. J., Holt, J. T. & Proctor, R., 2007. Modelling SPM on the NW European shelf seas. *Geological Society of London,* Volume 274, pp. 147-158.

Souza, A. J. & Howarth, M. J., 2005. Estimates of Reynolds Stress in a highly energetic shelf sea. *Ocean Dynamics,* Volume 55, pp. 490-498.

Spearman, J. R., Manning, A. J. & Whitehouse, R. J. S., 2011. The settling dynamics of flocculating mud and sand mixtures: part 2 - numerical modelling. *Ocean Dynamics,* Volume 61, pp. 351-370.

Stacey, M. T., 1996. Turbulent mixing and residual circulation in a partially stratified estuary. *Ph.D Thesis, Stanford University, USA.*

Stacey, M. T., Monismith, S. G. & Burau, J. R., 1999. Observations of turbulence in a partially stratified estuary. *Journal of Physical Oceanography,* Volume 29, pp. 1950-1970.

Steers, J. A., 1967. *Estuaries.* Washington D.C.: American Association for the Advancement of Science.

Sternberg, R. W., Berhane, I. & Ogston, A. S., 1999. Measurement of size and settling velocity of suspended aggregates on the northern California continental shelf. *Marine Geology,* Volume 154, pp. 43-53.

Sternberg, R. W., Larsen, L. H. & Miao, Y. T., 1985. Tidally driven transport on the East China Sea continental shelf. *Continental Shelf Research,* Volume 4, pp. 105-120.

Stokes, G. G., 1844. On the theories of internal friction of fluids in motion and of the equilibrium and motion of elastic solids. *Transactions of the Cambridge Philosophical Society,* Volume 8, pp. 287-319.

Stokes, G. G., 1851. On the effect of the internal friction of fluids on the motion of pendulumns. *Transactions of the Cambridge Philosophical Society,* Volume 9.

Stolzenbach, K. D. & Elimelich, M., 1994. The effect of density on collisions between sinking particles: implications for particle aggregation in the ocean. *Journal of Deep Sea Research,* Volume 41, pp. 469-483.

Stramski, D., Boss, E., Bogucki, D. & Voss, K. J., 2004. The role of seawater constituents in light backscattering in the ocean. *Progress in Oceanography,* Volume 61, pp. 27-56.

Suzuki, Y., Sugimura, Y. & Itoh, T., 1985. A catalytic oxidation method for the determination of total nitrogen dissolved in seawater. *Marine Chemistry,* Volume 16, pp. 83-97.

Sverdrup, H. U., Johnson, M. W. & Fleming, R. H., 1942. *The oceans: Their physics, chemistry, and general biology.* New York: Prentice-Hall.

Syvitski, J. P. M. & Murray, J. W., 1981. Particle interaction in fjord suspended sediment. *Marine Geology,* Volume 39, pp. 215-242.

Tambo, N. & Watanabe, Y., 1979. Physical characteristics of flocs – I. The floc density function and aluminium floc. *Water Research,* Volume 13, pp. 409-419.

Ten Brinke, W. B. M., 1994. In situ aggregate size and settling velocity in the Oosterschelde tidal basin (The Netherlands). *Netherlands Journal of Sea Research,* Volume 32, pp. 23-35.

Tennekes, H. & Lumley, J. L., 1972. *A first course in turbulence.* Cambridge, MA: MIT Press.

Thomas, D. N., Judd, S. J. & Fawcett, N., 1999. Flocculation Modelling: A Review. *Water Research,* Volume 33, pp. 1579-1592.

Thomson, W., 1879. On gravitational oscillations of rotating water. *Proceedings of the Royal Society of Edinburgh,* Volume 10, pp. 92-100.

Thomson, W., 1881. The tide gauge, tidal harmonic analyser, and tide predicter. *Proceedings of the Institution of Civil Engineers,* Volume 65, pp. 3-24.

Thorne, P. D. et al., 1991. Measuring suspended sediment concentrations using acoustic backscatter devices. *Marine Geology,* Volume 98, pp. 7-16.

Thorpe, S. A., 2007. *An introduction to ocean turbulence.* Cambridge: Cambridge University Press.

Thurston, W., 2009. Turbulence as a mediator of processes in a macrotidal estuary. *Ph.D Thesis, University of Leeds, UK.*

Tian, T. et al., 2009. Importance of resuspended sediment dynamics for the phytoplankton spring bloom in a coastal marine ecosystem. *Journal of Sea Research,* Volume 62, pp. 214-228.

Tockner, K. & Stanford, J. A., 2002. Riverine flood plains: present state and future trends. *Environmental Conservation,* Volume 3, pp. 308-330.

Traykovski, P., Geyer, W. R., Irish, J. D. & Lynch, J. F., 2000. The role of wave-induced density-driven fluid mud flows for cross-shelf transport on the Eel River continental shelf. *Continental Shelf Research,* Volume 20, pp. 2113-2140.

Turner, A. & Millward, G. E., 2002. Suspended particles: Their role in estuarine biogeochemical cycles. *Estuarine, Coastal and Shelf Science,* Volume 55, pp. 857-883.

Turner, A., Millward, G. E. & Tyler, A. O., 1994. The distribution and chemical composition of particles in a macrotidal estuary. *Estuarine, Coastal and Shelf Science,* Volume 38, pp. 1-17.

Uncles, R. J., Stephens, J. A. & Harris, C., 2013. Estimating estuarine turbidity: An application to estuaries of the Isle of Man and northeast Irish Sea. *Ocean & Coastal Management,* Volume 79, pp. 42-51.

Uncles, R. J., Stephens, J. A. & Smith, R. E., 2002. The dependence of estuarine turbidity on tidal intrusion length, tidal range and residence time. *Continental Shelf Research,* Volume 22, pp. 1835-1856.

Valle-Levison, A., 2008. Density-driven exchange flows in terms of the Kelvin and Ekman numbers. *Journal of Geophysical Research,* Volume 113, p. C04001.

Valle-Levison, A., 2010. *Definition and classification of estuaries, in Contemporary issues in estuarine physics.* Cambridge: Cambridge University Press.

van de Hulst, H. C., 1957. *Light scattering by small particles.* New York: Wiley.

van der Lee, M. E., Bowers, D. G. & Kyte, E., 2009. Remote sensing of temporal and spatial patterns of suspended particle size in the Irish Sea in relation to the Kolmogorov microscale. *Continental Shelf Research,* Volume 29, pp. 1213-1225.

van der Lee, W. T. B., 2000. Temporal variation of floc size and settling velocity in the Dollard estuary. *Continental Shelf Research,* Volume 20, pp. 1495-1511.

van der Perk, M., 2006. *Soil and water contamination.* Leiden, The Netherlands: Taylor & Francis.

van Leussen, W., 1994. Estuarine macroflocs: their role in fine-grained sediment transport. *Ph.D Thesis, University of Utrecht, The Netherlands.*

van Leussen, W., 1997. The kolmogorov microscale as a limiting value for the floc sizes of suspended fine-grained sediments in estuaries. In: N. Burt, R. Parker & J. Watts, eds. *Cohesive Sediments.* New York: John Wiley & Sons, pp. 45-62.

van Rijn, L. C., 1984. Sediment transport, Part II: Suspended load transport. *Journal of Hydraulic Engineering,* Volume 110, pp. 1613-1641.

Vanoni, V. A., 2006. *Sedimentation Engineering.* Reston, VA: American Society of Civil Engineers.

Velegrakis, A. F. et al., 1997. Resuspension and advection processes affecting suspended particulate matter concentrations in the central English Channel. *Journal of Sea Research,* Volume 38, pp. 17-34.

Verney, R., Lafite, R. & Brun-Cottan, J. C., 2009. Flocculation potential of estuarine particles: The importance of environmental factors and of the spatial and seasonal variability of suspended particulate matter. *Estuaries and Coasts,* Volume 32, pp. 678-693.

Verney, R., Lafite, R., Brun-Cottan, J. C. & Le Hir, P., 2011. Behaviour of a floc population during a tidal cycle: Laboratory experiments and numerical modelling. *Continental Shelf Research,* Volume 31, pp. 64-83.

Voulgaris, G. & Meyers, S. T., 2004. Temporal variability of hydrodynamics, sediment concentration and sediment settling velocity in a tidal creek. *Continental Shelf Research,* Volume 24, pp. 1659-1683.

Wang, Z. Y. & Larsen, P., 1994. Turbulence structure of flows of water and clay suspensions with bedload. *Journal of Hydraulic Engineering,* Volume 120, pp. 577-600.

Wan, Z. H. & Wang, Z. Y., 1994. *Hyperconcentrated Flow.* Rotterdam: A A Balkema.

Weekes, A. R., Simpson, J. H. & Bowers, D. G., 1993. The relationship between concentrations of Suspended particulate material and tidal processes in the Irish sea. *Continental shelf research,* Volume 13, pp. 1325-1334.

Weisse, T. W. et al., 1990. Response of the microbial loop to the phytoplankton spring bloom in a large prealpine lake. *Limnology and Oceanography,* Volume 35, pp. 781-794.

Wentworth, C. K., 1922. A scale of grade and class terms for clastic sediments. *Journal of Geology,* Volume 30, pp. 377-392.

Werdell, P. J. et al., 2013. Retrieving marine inherent optical properties from satellites using temperature and salinity-dependent backscattering by seawater. *Optics Express,* 21(26), pp. p32611-32622.

Whitehouse, R., 1995. Observations of the boundary layer characteristics and the suspension of sand at a tidal site. *Continental Shelf Research,* Volume 15, pp. 1549-1567.

Whitehouse, R. J. S., Soulsby, R., Roberts, W. & Mitchener, H., 2000. *Dynamics of Estuarine Muds.* London: Thomas Telford Publishing.

Wiles, P. J., Rippeth, T. P., Simpson, J. H. & Hendricks, P. J., 2006. A novel technique for measuring the rate of turbulent dissipation in the marine environment. *Geophysical Research Letters,* Volume 33, pp. 21-25.

Williams, E. & Simpson, J. H., 2004. Uncertainties in estimates of Reynolds stress and TKE production rate using the ADCP variance method. *Journal of Atmospheric and Oceanic Technology,* Volume 21, pp. 347-357.

Williams, J. J., Humphery, J. D., Hardcastle, P. J. & Wilson, D. J., 1998. Field observations of hydrodynamic conditions and suspended particulate matter in the southern North Sea. *Continental Shelf Research,* Volume 18, pp. 1215-1233.

Willis, B., 1893. Conditions of Sedimentary Deposition. *The Journal Of Geology,* Volume 1, pp. 476-520.

Wilson, I. G., 1972. Aeolian bedforms - their development and origins. *Sedimentology,* Volume 19, pp. 173-210.

Winkler, M., Kopf, G., Hauptvogel, C. & Neu, T., 1998. Fate of artificial musk fragrances associated with suspended particulate matter (SPM) from the river Elbe (Germany) in comparison to other organic contaminants. *Chemosphere,* Volume 37, pp. 1139-1156.

Winterwerp, J. C., 1998. A simple model for turbulence induced flocculation of cohesive sediment. *Journal of Hydraulic Research,* Volume 36, pp. 309-326.

Winterwerp, J. C., 2002. On the flocculation and settling velocity of estuarine mud. *Continental Shelf Research,* Volume 22, pp. 1339-1360.

Winterwerp, J. C., 2011. The physical analyses of muddy sedimentation processes. In: *Treatise on Estuarine and Coastal Science.* Oxford: Elsevier, pp. 311-360.

Winterwerp, J. C. et al., 2006. A heuristic formula for turbulence-induced flocculation of cohesive sediment. *Estuarine, Coastal and Shelf Science,* Volume 68, pp. 195-207.

Winterwerp, J. C. & van Kesteren, W. G. M., 2004. *Introduction to the physics of cohesive sediment in the marine environment.* Amsterdam: Elsevier.

Wright, L. D., Friedrichs, C. T. & Hepworth, D. A., 1997. Effects of benthic biology on bottom boundary layer processes, Dry Tortugas Bank, Florida Keys. *Geo-Marine Letters,* Volume 17, pp. 291-298.

Yasumoto, M. & Nambi, S., 1976. Biochemical and physical properties of an activated sludge on settling characteristics. *Water Research,* Volume 10, pp. 71-77.

Yeung, A. K. C. & Pelton, R., 1996. Micromechanics: A new approach to studying the strength and break-up of flocs. *Journal of Colloid and Interface Science,* Volume 184, pp. 579-585.

Ziegler, C. K. & Lick, W., 1988. The Transport of Fine-Grained Sediments in Shallow Waters. *Environmental Geology and Water Sciences,* Volume 11, pp. 123-132.

Zonta, R., Collavini, F., Zaggia, L. & Zuliani, A., 2005. The effect of floods on the transport of suspended sediments and contaminants: A case study from the estuary of the Dese River (Venice Lagoon, Italy). *Environment International,* Volume 31, pp. 948-958.